THE UNIVERSITY of EDINBURGH

This thesis has been submitted in fulfilment of the requirements for a postgraduate degree (e.g. PhD, MPhil, DClinPsychol) at the University of Edinburgh. Please note the following terms and conditions of use:

A Study of MIMO Techniques for Optical Wireless Communications

HAMMED GBOLAHAN OLANREWAJU

A thesis submitted for the degree of Doctor of Philosophy
The University of Edinburgh
November 2019

Dedication

Dedicated to The Almighty God and my darling mother, Mrs Taiwo Adejoke Olanrewaju.

Lay summary

The trends of communication technology in recent years have shown widespread deployment of wireless communication systems, with a plethora of devices and web-based applications. As network capacity expands, so does the utilisation. The imagined future is that of a networked society in which data and applications are accessible to everyone and everything, universally and continually. The realisation of such level of pervasiveness is bound to stimulate enormous demand for more capacity and availability. Present wireless based technologies are largely provisioned using the spectral resource in the radio frequency (RF) window of the electromagnetic spectrum. However, the scale of deployments using the RF resources points to the saturation of this band and its inadequacy to solely satisfy the growing demand for more capacity. In addition, the future networked society is expected to erupt with greatly diversified use cases and specifications. It is therefore conceivable that new technologies will be incorporated to complement the existing RF based systems in order to meet future needs.

In the context of the above projections, the technology of using light for wireless connectivity, known as Optical wireless communication (OWC), has attracted growing interest. OWC offers a vast spectral resource and it is therefore being explored as a promising solution to the massive connectivity demand of future networks. The adoption of OWC technology is further fostered by the widespread deployment of light emitting diodes (LEDs) as efficient and cost-effective illumination devices. These LEDs are used as optical transmitter for OWC. The small form factor and dense deployment of these light sources provide an opportunity to use a number of them synergistically in order to improve transmission capacity and/or reliability. Such applications are however not without challenges that need to be investigated.

The focus of thesis is to study and evaluate techniques that can apply multiple light sources for data transmission in indoor environments. First, multiple-source techniques with reduced complexity are employed to improve the transmission rate of energy efficient modulation schemes. This way, an attractive trade-off can be achieved between system capacity and energy requirement. Furthermore, these techniques are investigated in terms of their need for synchronisation and the impact of interference experienced as transmitted signal propagates in the indoor environments. Finally, multiple-source techniques that can support high date rate are studied. Methods of mitigating the bandwidth-limitation of off-the-shelf light sources and the inadequacies of indoor environment to support parallel data transmission, are proposed and demonstrated experimentally.

Abstract

With its huge spectral resource, optical wireless communication (OWC) has emerged as a promising complementary technology to the radio frequency (RF) communication systems. OWC provides data communications for a variety of user applications and it can be deployed using simple, low-cost, low-power and energy-efficient component. In order to enhance capacity, reliability and/or coverage of OWC, multiple-input-multiple-output (MIMO) systems are employed to exploit additional degrees of freedom, such as the location and angular orientation of optical sources and detectors. However, the implementation of MIMO systems is faced with challenges such as the strong correlation and multipath propagation in indoor OWC channels, system synchronisation, as well as inter-channel interference (ICI) due to multiple parallel data transmission. This dissertation investigates MIMO OWC systems which utilises transmission techniques with reduced complexity. A detailed study and performance evaluation of the techniques in terms of capacity, spectral efficiency and error rates is conducted through theoretical analysis, simulation and experiments. The system performance is investigated under different constraints imposed by impairments such as interference, synchronization and channel correlation.

Optical spatial modulation (OSM) is studied as a low complexity technique using multiple light sources to enhance system capacity. A generalised framework for implementing OSM with energy efficient pulse position modulation scheme is devised. This framework supports other variants of OSM, and it can be adapted to satisfy varying system requirement such as spectral and energy efficiencies. The performance of the OWC system is investigated in indoor line-of-sight (LOS) propagation. The error performance of the system is analysed theoretically and matched by simulation results. Also, the system performance is evaluated with experiments to demonstrate feasibility. Furthermore, the performance of OSM MIMO techniques in the realistic indoor scenario is considered by taking into account the multiple reflections of the transmitted signal from room surfaces. This is motivated by the recent drive towards high-speed Gigabits per second (Gbps) data communication, where the inter-symbol interference (ISI) caused by the multipath propagation may pose a major bottleneck. A model of the multipath-induced ISI is presented to account for signal spreading and then applied to formulate the error performance analysis. The impact of multipath-induced power penalty and delay spread on system performance is demonstrated using their spatial distributions across the coverage area.

Additionally, the impact of timing synchronization problems on the error performance of different variants of the OSM MIMO techniques is investigated. While most works related to SM have assumed a perfect synchronization among the multiple transmitter and receiver elements, such assumption pose a challenge in practical deployment. Hence, the need to examine the impact of synchronisation error that can result from clock jitters and variations in propagation delay. Synchronisation error analyses of OSM schemes are presented, and the tolerance of each scheme to timing synchronization errors is demonstrated. To further enhance system capacity, this thesis also explores spatial multiplexing MIMO technique with orthogonal frequency division multiplexing (OFDM). The central objective is to propose and apply techniques to address the correlation of the indoor optical wireless channel and the frequency selectivity due to the limited bandwidth of LEDs. To address these two effects, a joint coding of paired information symbols was applied in a technique termed pairwise coding (PWC). This technique is based on rotated symbol constellation and it offers significant performance improvement. The error performance of the proposed system is evaluated through simulation and experimental demonstration. PWC proved to be effective over varying degrees of bandwidth limitation and under different channel conditions.

Acknowledgements

Declaration

I declare that this thesis has been composed solely by myself and that it has not been submitted, either in whole or in part, in any previous application for a degree. Except where otherwise acknowledged, the work presented is entirely my own.

25/11/2019

Hammed Gbolahan Olanrewaju

Contents

List of tables

List of figures

List of abbreviations

A/D   Analog-to-digital

AWG   Arbitrary waveform generator

AWGN   Additive white Gaussian noise

BER   Bit error rate

CAGR   Compound annual growth rate

CIR   Channel impulse response

CP   Cyclic prefix

CSI   Channel state information

D2D   Device-to-device (D2D) communications

dB   decibel

DPWC   dual pairwise coding

D/A   Digital-to-analog

DC   Direct current

DD   Direct detection

EGC   Equal gain combining

EM   Electromagnetic

FFT   Fast Fourier transform

FOV   Field of view

GSPPM   Generalised spatial pulse position modulation

GSSK   Generalised space shift keying

ICI   Inter-channel interference

IEEE   Institute of Electrical and Electronics Engineers

IFFT   Inverse fast Fourier transform

i.i.d   Independent identically distributed

IM   Intensity modulation

IM/DD   Intensity modulation and direct detection

IoT   Internet of Things (IoT)

IR   Infrared

ISI   Inter-symbol interference

LED   Light emitting diode

LOS   Line-of-sight

LPF   Low-pass filter

LTE   Long-Term Evolution

M2M   Machine-to-machine

MF   Matched filter

MIMO   Multiple-input-multiple-output

MISO   Multiple-input-single-output

ML   Maximum likelihood

MMSE   Minimum mean squared error

NLOS   Non line-of-sight

O/E   Optical-to-electrical

OFDM   Orthogonal frequency division multiplexing

O-OFDM   Optical orthogonal frequency division multiplexing

OOK   On-off keying

OSM   Optical spatial modulation

OWC   Optical wireless communication

P/S   Parallel-to-serial

PAM   Pulse amplitude modulation

PAPR   Peak-to-average-power ratio

PEP   Pairwise error probability

PIN   p-type intrinsic n-type

PD   Photodetector

PDF   Probability density function

PSD   Power spectral density

PPM   Pulse position modulation

PWC   Pairwise coding

QAM   Quadrature amplitude modulation

RC   Repetition coding

RF   Radio frequency

RLS   Recursive least square

RMS   Root mean square

RX   Receiver

SC   Single carrier

SC-PWC   Subcarrier pairwise coding

SCH-PWC   Subchannel pairwise coding

SCP   Spatial constellation point

SER   Symbol error rate

SISO   Single-input-single-output

SNIR   Signal-to-noise-and-interference ratio

SM   Spatial modulation

SMP   Spatial multiplexing

SNR   Signal-to-noise ratio

SPPM   Spatial pulse position modulation

SSK   Space shift keying space-time

SSL	Solid state lighting
SVD	Singular value decomposition
S/P	Serial-to-parallel
TIA	Transimpedance amplifier
TX	Transmitter
VL	Visible light
VLC	Visible light communications
ZF	Zero-forcing

List of mathematical symbols

E_s	electrical energy per symbol
γ_b	signal-to-noise ratio per bit
γ_s	signal-to-noise ratio per symbol
σ^2	noise variance
R_spec	spectral efficiency, bit/s/Hz
$(\cdot)^*$	Hermitian transposition
$\mathbf{I}_n$	$n \times n$ identity matrix
$\hat{\mathbf{1}}_{N_\text{t}}$	a $(1 \times N_\text{t})$ unit vector
$\Re(\cdot)$	real part of a complex argument
$\Im(\cdot)$	imaginary part of a complex argument
$\widetilde{i}$	unit imaginary number
$\cos(\cdot)$	cosine function
$\sin(\cdot)$	sine function
$\exp(\cdot)$	natural exponential function
$[\,\cdot\,]^\dagger$	matrix/vector transpose operation.
$a \in [1, L]$	$a \in \{1, 2, \ldots, L\}$
$\delta(\cdot)$	Dirac delta function
m	Lambertian mode number of transmitter source
$\Phi_{1/2}$	semi-angle at half power
$\mathcal{S}$	configurations of the transmitter source
$\mathcal{R}$	configurations of the receiver detector
h	channel gain

$h(t)$ channel impulse response

ρ reflectivity

B signal bandwidth

$h^{(0)}(t; \mathcal{S}; \mathcal{R}))$ LOS channel impulse response

$h^{(k)}(t; \mathcal{S}; \mathcal{R}))$ NLOS channel impulse response after k reflections

$\hat{\mathbf{u}}_s$ unit-length orientation vector of transmitter source

$\hat{\mathbf{u}}_r$ unit-length orientation vector of receiver detector

$\mathcal{A}_r$ active collection area of receiver detector

$\mathbf{p}_s$ transmitter source position (coordinates) vector

$\mathbf{p}_r$ receiver detector position (coordinates) vector

τ_{rms} root mean square (RMS) delay spread

$\overline{\tau}$ mean delay spread

R responsivity of photodetector (A/W)

$\otimes$ convolution operation

$\odot$ Hadamard (entry-wise) product

$\eta(t)$ noise (AWGN) variable

$\boldsymbol{\eta}$ noise (AWGN) vector

P_{ave} average transmitted optical power

L size of signal constellation diagram

N_{s} size of spatial constellation diagram

T symbol duration

T_{c} PPM slot/chip duration

$\mathbf{H}$ MIMO channel matrix

N_{t} number of transmitter sources

N_{r} number of receiver detectors

$\arg\max$ argument of the maximum

$\arg\min$	argument of the minimum
$\lvert\cdot\rvert$	absolute value
$\lVert.\rVert$	vector norm operation
$\lVert\cdot\rVert_{\mathrm{F}}$	Frobenius (matrix) norm
$f(\cdot)$	probability density function
$\mathcal{M}$	number of transmitted bits per symbol
$\mathcal{A}_{j,m}$	GSPPM symbol
$\widehat{\mathcal{A}}_{\hat{j},\hat{m}}$	estimated GSPPM symbol
$\log_2(\cdot)$	logarithm to base 2
P_{t}	peak transmitted optical power
$\mathbf{v}_j$	LED activation vector
λ_j	pulse-inversion constant
$\mathcal{D}(\cdot)$	Euclidean distance metric
τ	duty cycle of GSSK scheme
$P_{\mathrm{c,sym}}^{\mathrm{GSPPM}}$	probability of correct symbol detection for GSPPM
$P_{\mathrm{e,sym}}^{\mathrm{GSPPM}}$	probability of error in symbol detection for GSPPM
$P_{\mathrm{c,ppm}}^{\mathrm{GSPPM}}$	probability of correct pulse position detection for GSPPM
$P_{\mathrm{e,ppm}}^{\mathrm{GSPPM}}$	probability of error in pulse position detection for GSPPM
$P_{\mathrm{c,scp}}^{\mathrm{GSPPM}}$	probability of correct spatial constellation point detection for GSPPM
$P_{\mathrm{e,scp}}^{\mathrm{GSPPM}}$	probability of error in spatial constellation point detection for GSPPM
$Q(\cdot)$	Q-function
$\mathrm{PEP}_{m\rightarrow q}^{j}$	PEP that receiver decides in favour of slot q instead of slot m
$\mathrm{PEP}_{m}^{j\rightarrow k}$	PEP that receiver decides in favour of SCP k instead of j
$\mathbb{P}(\cdot)$	probability of occurrence
N_0	noise power spectral density
Δh	difference between the channel gain pair

Δ_{n_t} timing offsets introduced into signal from LED n_t

ϵ_{n_t} normalised timing offsets introduced into signal from LED n_t

$\boldsymbol{\epsilon}$ vector of normalised timing offsets

$\mathcal{C}_d$ condition number

Chapter 1

Introduction

1.1 Motivation

Major technological developments in recent times have set the pace for pervasive connectivity and a networked society in which information is accessible to everyone and everything. People's ideas about communication have evolved altogether, with mobile and wireless technologies taking the centre stage. The growth of wireless communications stands out as one of the great achievements in technological advancement [1]. This is mirrored by the rapid evolution of mobile communications from the second generation (2G) system launched in 1991 into the current fourth generation (4G) and the imminent fifth generation (5G) networks. Each generation has provided significant performance enhancements in response to the ever-increasing demand for capacity due to massive growth in digital applications and web-based services. At inception, mobile networks were designed to provide voice services with basic data solutions, however, they have since emerged into high-speed data networks for ubiquitous connectivity. As network capacity improves, so does the use cases and the demands for wireless applications grow. This creates a recurring trend in which increase in capacity leads to increase in utilisation, which in turn drives the demand for additional capacity. Thus, resulting in an insatiable demand.

In the last decade, wireless network traffic has grown at an unprecedented rate, and this trend is expected to continue beyond the next decade [2]. As shown in Figure 1.1, according to Cisco's *Global Mobile Data Traffic Forecast*, the global IP traffic is projected to triple from 2017 to 2022 at a compound annual growth rate (CAGR) of 26%, with traffic from wireless and mobile devices accounting for 71% of total IP traffic by 2022 [3]. These projections align with similar forecast obtained from the 2018 Ericsson mobility report [4], where the total mobile
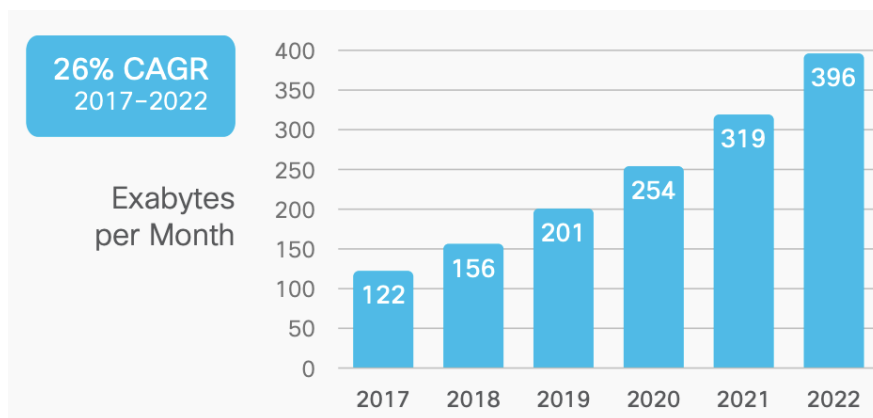
Figure 1.1: *Global mobile data traffic forecast. Source: Cisco Visual Networking Index [3].*

data traffic is predicted to rise at a CAGR of 31% between 2018 and 2024. Mobile devices such as smartphones and tablets are equipped with cutting-edge features like high-density displays and powerful processors that provide users with data-intensive applications such as high-definition (HD) – 4K and 8K – videos applications. Furthermore, a growing number of objects are being digitized through Internet of Things (IoT) and machine-to-machine (M2M) applications such as smart meters, video surveillance, healthcare devices and transportation. These contributes significantly to the growth of devices and connections. In the global device and connection forecast shown in Figure 1.2, by 2022, M2M connections will be more than half (51%) of the global connected devices and connections, up from 34% in 2017, with about 14.6 billion M2M connections by 2022 [3].
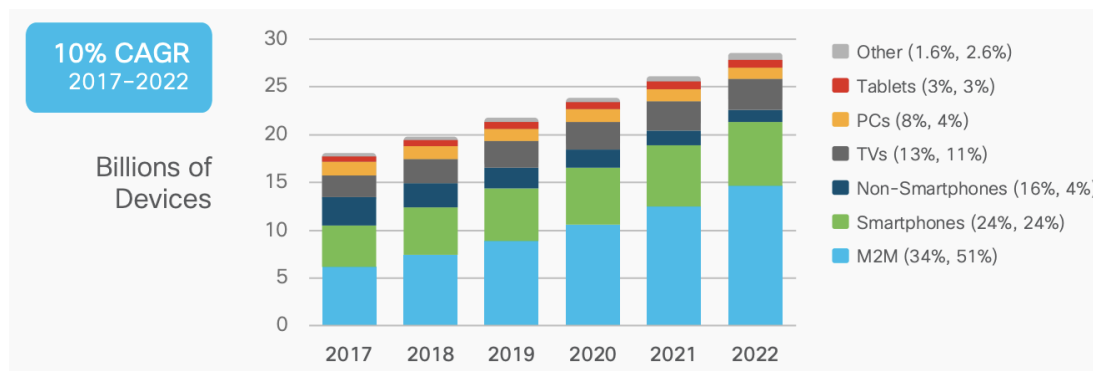
Figure 1.2: *Global devices and connections growth. Source: Cisco Visual Networking Index [3].*

Based on the foregoing projections, it is conceivable that the demand for connectivity and the

influx of applications will continue to drive the scale and capacity of the network infrastructure at extreme rates. With the actualization of IoT and M2M technologies, it is reasonable to assume that this data growth will persist beyond the next decade [5]. Currently, these diverse wireless applications and services are predominantly provisioned using the radio frequency (RF) band of the electromagnetic (EM) spectrum, with frequencies between 30 kHz and 300 GHz. Here, the term "radio" is inclusive of the EM frequency bands that are often referred to as "radio frequency," "microwave," and "millimeter wave." However, the spectral efficiency of wireless network continues to saturate despite the introduction of new standards and technological advancements [6]. The United Kingdom Ofcom licensed spectrum estimates show that by 2020 the currently awarded and planned awards of mobile broadband spectrum in the UK may become insufficient to keep pace with mobile data demand [7, 8]. With the current RF spectrum already in near saturation, coupled with the expected increase in mobile data traffic, the limitations of RF-only wireless communications has become more apparent. It is therefore imaginable that provision for the future wireless connectivity will require using an alternative spectrum [5, 9]. Consequently, in recent times, a strong case has been made for expansion into additional complementary spectrum, and the research community has began the pursuit of solutions that target adjunct portions of the EM spectrum for wireless communications. In particular, the optical range of spectrum including infrared (IR), visible light (VL) and ultraviolet (UV) bands offers a huge bandwidth which can be used to augment the current RF-based communications [1].

The technology of using the optical band of the EM spectrum for wireless data transmission is termed optical wireless communications (OWC). The wavelengths of the optical spectrum are: the IR band – from 750 nm to 2.5 μm, the VL band – between 380 nm to 750 nm, and the UV band – from 10 nm to 380 nm. As shown in Figure 1.3, the size of the combined IR and VL spectrum alone is approximately 780 THz, which is about 2,600 times the size of the entire RF spectrum of 300 GHz. With its available vast and license-free bandwidth, OWC can support a diverse range of applications. Besides, OWC provides robustness to EM interference, which makes it safe for use in environments where RF is undesirable such as the aviation industry, healthcare facilities, and petrochemical plants [5, 10]. Furthermore, since OWC does not interfere with RF communications, its can be used as a complementary technology in an hybrid RF/OWC system. Moreover, the last couple of years have witnessed increasing
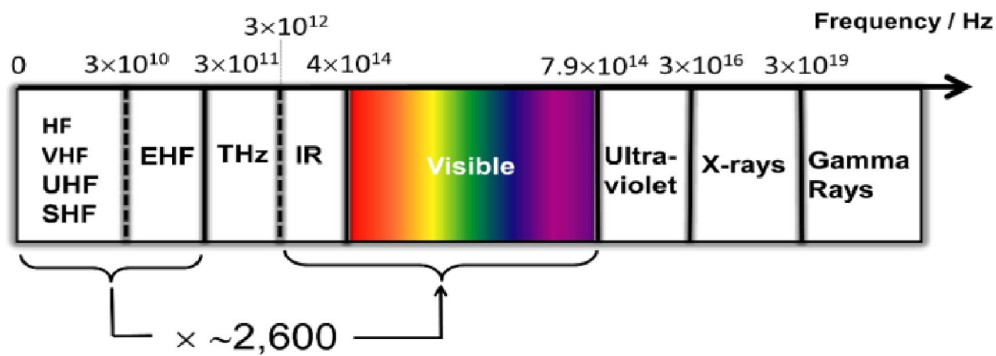
Figure 1.3: *The RF spectrum (∼300 GHz) is only a fraction of the combined VL and IR spectrum (∼780 THz) [5]. HF: High frequency, VHF: Very high frequency, UHF: Ultra high frequency, SHF: Super high frequency, EHF: Extremely high frequency.*

interest in OWC systems operating in the visible band commonly referred to as visible light communication (VLC). The utilisation of VLC for simultaneously providing illumination, data communications, and indoor localization has further expanded the potentials of OWC [1]. Interest in VLC has been inspired by the widespread adoption of solid state lighting (SSL) using high brightness light emitting diodes (LEDs). SSL offers attractive features such as a long life expectancy, lower power consumption, energy efficiency, compact form factor and lower heat dissipation [10]. With these benefits, SSL through LEDs is projected to continue to rise in the years ahead. The United States Department of Energy estimates that LEDs will hold 86% of all lighting installation by 2035 [11]. This indicates an inevitable proliferation of LED devices along with the associated VLC technology.

The applications of OWC cut across both the indoor and outdoor environments including underwater. The transmission of data is achieved by light propagation through free space over distances of few metres (indoor) to few kilometres (outdoor terrestrial) [1]. The application areas are numerous, including short-range device-to-device (D2D) communications, broadband access in homes and offices, indoor localization, vehicular communications, among others [12]. Given its impressive advantages and the wide range of potential application areas, OWC is considered a key component of future wireless communications [5]. The proliferation of OWC has already begun, and being a relatively recent technology, its deployment is expected to face a number of challenges. However, since many of those constraints may have already been addressed in RF through decades of research, OWC is expected to follow a much accelerated path [13].

A seamless realization of optical wireless network necessitates the utilisation of a wide variants of modulation formats and data transmission techniques. This is particularly important in order to support a large number of applications. One of such methods is the use of multiple optical sources and detectors at the transmitter and receiver, respectively, a technique termed multiple-input and multiple-output (MIMO) transmission. In MIMO systems, a serial input data stream is sent via multiple optical sources and is collected by an array of detectors, each with different signal strengths according to the geometric configuration [14]. MIMO technique in OWC can be used to create parallel communication channels by exploiting additional degrees of freedom, such as the space and viewing angle of optical sources, as well the space and field of view of optical detectors. The application of MIMO techniques in OWC is to a large extent motivated by the success it has recorded in RF communications, where it has been used to enhance the capacity and/or reliability of wireless communication links. For instance, the IEEE 802.11n wireless-networking standard [15] and Long-Term Evolution (LTE) technology [16–18] are designed to use multiple antennas to increase data rate. Similarly, optical MIMO systems offer the potential to enhance spectral efficiency by providing higher capacity without the need for additional power or bandwidth. Besides, MIMO systems can also be configured to increase link range and to relax the requirement for source-detector alignment by the way of diversity [12, 19].

Moreover, in indoor VLC applications which combines illumination with communications, a large number of optical sources (LEDs) are deployed within a confined area in order to meet the illumination requirements. Thus, VLC can take advantage of these multiple LEDs to enable optical MIMO communication [20]. Furthermore, given the small form factor of the optical sources coupled with the chip-on-board technology [21], an array of sources could be compactly packed into fixtures, and these sources can be employed in a MIMO setup. MIMO technique is particularly beneficial to VLC system. The finite bandwidth of front-end devices, mainly the off-the-shelf phosphor-based white LEDs [22] limits the speed of the communication system. In this context, MIMO is an attractive solution for achieving high data rates.

Integrating MIMO technique into OWC is faced with a number of challenges. For instance, due to low differentiability of the indoor optical wireless channel [12, 23], MIMO systems is

more difficult to realize in OWC compared to RF communications. The performance gains in MIMO systems rely on the existence of diverse multiple spatial paths in nature. This introduces a unique "channel signature" to differentiate the multiple wireless links. However, in OWC, the paths between the transmitter and receiver are less diverse as light intensity does not show significant changes with close distance [24]. Besides, there is need to examine the synchronisation requirement and address the inter-channel interference (ICI) due to parallel data transmission. Another areas of investigation is the performance of MIMO systems indoor multipath optical channels, particularly when considering user mobility.

There are a number of approaches to implementing MIMO technique for OWC, and each has its unique features, advantages and limitations. Some of the common ones considered in this thesis include repetition coding (RC) used mainly for diversity gain, spatial multiplexing (SMP) which offers capacity gains, and spatial modulation (SM) with provides a trade-off between capacity and reliability [23]. Each of these MIMO schemes are further discussed in Chapter 2. The rest of the thesis is focused on exploring the potentials of the last two MIMO schemes, and also evaluating their performance in the presence of some the aforementioned challenges of MIMO systems.

1.2 Contributions

This research work is aimed at investigating the performance of MIMO techniques in OWC system, in an effort to understand their benefits and limitations. State-of-the-art optical MIMO schemes are studied, and novel schemes are proposed to improve system performance such as throughput and energy efficiency. In view of the unique features of each MIMO technique, our investigation of MIMO in OWC systems is in two folds. First, in Chapters 3-5, SM-MIMO is investigated as low complexity technique in combination with energy-efficient pulse position modulation (PPM). This is targetted at OWC applications such as sensor networks and IoT devices with limited energy and processing capacity. The second part of our investigation in Chapter 6 explores SMP-MIMO for high data rate VLC system such as internet access in homes. Techniques are applied to address the sensitivity of SMP-MIMO to the high similarity of optical wireless channel and the small bandwidth of off-the-shelf optical sources (white LEDs). The error performance analyses and evaluation of the MIMO schemes are presented, considering constraints and impairments such as channel path loss,

channel differentiability, multipath-induced interference and system synchronisation. Results are obtained via theoretical analysis, simulation and experimental demonstration. In this work, the emphasis is on OWC systems utilising the IR and VL spectrum, particularly in the indoor environments. Within this context, the contributions of this research work are summarised as follows:

- A novel optical MIMO scheme exploiting the concept of SM in combination with PPM is presented. The proposed scheme termed generalised spatial pulse position modulation (GSPPM) enhances the spectral efficiency of classical PPM by conveying additional information bits via the spatial domain (index) of optical sources. This scheme benefits from both the reduced complexity of SM technique and the energy efficiency of PPM. Additionally, the GSPPM scheme is used as reference to devise a general framework for implementing PPM-based SM-MIMO schemes. The framework supports three other variants of SM, thus making it valid for a wide range of scenarios. Furthermore, analysis of the error performance of the schemes in the presence of indoor line-of-sight (LOS) channel path loss and additive white Gaussian noise (AWGN) is presented and verified via simulations. Besides, the system performance is evaluated with proof-of-concept experimental demonstrations to illustrate the feasibility of the proposed scheme.

- Most works on SM-MIMO technique have assumed an ideal scenario in which synchronisation between transmitter and receiver elements is perfect. However, such assumption present challenges for practical deployment. Hence, the second contribution of this research work is to examine the impact of timing synchronisation error on SM schemes by deriving the error analysis for SM technique using the four variants of SM considered in the preceding contribution item as case study. Analytical expression of the attainable symbol error rate (SER) considering the energy loss and intersymbol interference (ISI) caused by timing synchronisation error is presented. Finally, we present results to demonstrate the tolerance of each SM scheme to synchronisation errors.

- Furthermore, for high-speed Gigabits per second (Gbps) data communication and mobile OWC network, the performance of SM technique in realistic indoor optical wireless channel with LOS and multipath propagation is investigated. The system model is devised to account for the ISI experienced in the dispersive non-LOS (NLOS) channel by

taking into account the multiple reflections of the transmitted signal from room surfaces. Based on the system model, the error performance analysis of SM technique in multipath channel is derived to validate simulation results. Using the spatial distributions of the multipath-induced power penalty and the delay spread, we demonstrate their impact on error performance.

- Finally, considering the finite bandwidth of LEDs, in order to enhance system capacity, this research also explores SMP MIMO technique with multi-carrier modulation – orthogonal frequency division multiplexing (OFDM) – for multiplexing gains. First, given that SMP based MIMO systems are less robust to channel similarity compared to SM, singular value decomposition (SVD) precoding is applied to decompose the MIMO channel into independent parallel sub-channels. Then, dual pairwise coding (DPWC) technique is proposed for the MIMO-OFDM VLC system to enhance performance. DPWC technique is employed to combat the signal-to-noise ratio (SNR) imbalance created in the received information symbols due to the limited LED bandwidth and the high similarity of typical indoor VLC MIMO channels. The error performance of the proposed DPWC technique is investigated in detail via simulation and experimental demonstration. Its effectiveness over varying degrees of bandwidth limitation and different channel conditions is presented. Experimental results show that SNR savings of more 10 dB can be achieved at a data rate of 496 Mbps from two white LEDs with bandwidth of 12 MHz and 15 MHz.

1.3 List of publications

The foregoing contributions have resulted in the following publications.

Book chapter

1. H. G. Olanrewaju, F. B. Ogunkoya and W. O. Popoola, "Spatial Modulation – A Low Complexity Modulation Technique for Visible Light Communications", *Visible Light Communications*, IntechOpen, July 26th, 2017.

Journals

1. H. G. Olanrewaju, J. Thompson and W. O. Popoola, "Performance of Optical Spatial Modulation in Indoor Multipath Channel," in *IEEE Transactions on Wireless Communications*, vol. 17, no. 9, pp. 6042-6052, Sept. 2018.

2. H. G. Olanrewaju and W. O. Popoola, "Effect of Synchronization Error on Optical Spatial Modulation," in *IEEE Transactions on Communications*, vol. 65, no. 12, pp. 5362-5374, Dec. 2017.

3. H. G. Olanrewaju, J. Thompson and W. O. Popoola, "Performance Analysis of Optical Spatial Modulation in Atmospheric Turbulence Channel," **Invited paper** *Photonic*s. vol. 5. no. 4. Multidisciplinary Digital Publishing Institute, 2018.

4. H. G. Olanrewaju, J. Thompson and W. O. Popoola, "Pairwise Coding for MIMO-OFDM Visible Light Communication," in *IEEE Transactions on Wireless Communications*, [**Submitted**].

Conference papers

1. H. G. Olanrewaju, J. Thompson and W. O. Popoola, "Impact of Timing Offset on Optical Spatial Pulse Position Modulation," *2018 IEEE 88th Vehicular Technology Conference (VTC-Fall)*, Chicago, USA, 2018.

2. H. G. Olanrewaju, J. Thompson and W. O. Popoola, "Generalized Spatial Pulse Position Modulation for Optical Wireless Communications," *2016 IEEE 84th Vehicular Technology Conference (VTC-Fall)*, Montreal, QC, 2016, pp. 1-5.

3. H. G. Olanrewaju, J. Thompson and W. O. Popoola, "On spatial pulse position modulation for optical wireless communications," *2016 IEEE Photonics Society Summer Topical Meeting Series (SUM)*, Newport Beach, CA, 2016, pp. 44-45.

1.4 Thesis outline

The remainder of this thesis is structured as follows:

Chapter 2 details an overview of OWC technology, where the salient features along with the current and emerging application areas are presented. The basic blocks of a typical OWC system are introduced with the key characteristics of the transmitter, receiver and the optical wireless channel. The digital modulation formats employed in OWC, including MIMO techniques are discussed in the concluding part of the chapter.

Chapter 3 presents the generalised systems model and the error performance analysis PPM-based SM-MIMO technique in LOS and AWGN optical wireless channel. Four variants of the SM technique are considered and their performances are evaluated using derived analytical expressions, computer simulations, and experiments. Also, the SM schemes are compared in terms of their spectral and energy efficiencies, highlighting their merits and limitations.

Chapter 4 examines the impact of timing synchronisation error on the performance of SM-based OWC system. The signal energy loss and energy spillover (ISI) caused by timing offset are modelled. Thereafter, the performances of four SM schemes are analysed, evaluated and compared under the condition of imperfect timing synchronisation. The analytical and simulation results are presented for varying values of timing offset and channel gain.

Chapter 5 presents the analysis of the performance of SM technique in indoor optical wireless channel with LOS and multipath propagation. A model of the multipath-induced ISI is devised and then applied to derive an analytical upper bound on the SER of SM technique in multipath channel. The chapter is concluded with an investigation into the impact of multipath-induced power penalty and delay spread on error performance.

Chapter 6 presents a pairwise coding (PWC) technique for MIMO-OFDM based VLC system to mitigate the effect of LEDs' bandwidth limitations and the VLC channel correlation. SVD-based precoding is applied with three different implementations of PWC, and their performances are compared under different bandwidth-limitation scenarios and MIMO channel conditions. Finally, the performances of the PWC schemes are investigated with experimental demonstration.

Chapter 7 summarises and concludes the presented work, highlighting the main findings. In addition, the limitations of the research work are discussed and potential future work is identified.

Chapter 2
An overview of optical wireless communications

Since originating in the ancient era in the form of optical telegraphs via torches, smoke signals, beacon fires and semaphore lines [25], optical wireless communication (OWC) has evolved into a promising technology for data communication. The potential applications of OWC are numerous, and the use cases are growing massively. In recent decades, OWC has been successfully deployed for outdoor terrestrial point-to-point communication, also known as the free space optical (FSO) systems. Areas where FSO has been used include high bit-rate inter-building links over distances up to several kilometers, back-haul for cellular network, enterprise/campus connectivity and last-mile access network [26, 27]. With regards to indoor applications, the commercialisation of OWC received a major boost in the 1990s with the formation of the Infrared Data Association (IrDA) in 1993 to promote the development and growth of IR enabled products and services. IrDA became a highly successful short-range communications solution for file transfer between mobile phones and personal computers, and for remote controls in television and video players [28].

The use of white LEDs for data communication and illumination emerged in the early 2000s with the pioneering work of Tanaka et al. [29, 30] at Keio University to demonstrate the feasibility of indoor optical data transmission. In 2003, the Visible light communication consortium (VLCC) [31] was formed, with the objective of proposing standards for VLC and promoting the technology. The organization proposed two standards – Visible Light Communication System Standard and Visible Light ID System Standard – by 2007 [10]. The VLCC alliance later metamorphosed into Visible Light Communications Associations (VLCA) in 2014. As part of the European Union's (EU) vision for future internet, the Gigabit Home Access Networks (OMEGA) project [32] was commissioned in 2008 to develop a standard for

ultra broadband in home networks. The interdisciplinary project, with a team from the industry and academia, was aimed at enabling gigabit data rates using heterogeneous technologies such as power communications (PLC), RF communications and OWC. Results from the OMEGA project include an 803 Mbps VLC system with wavelength division multiplexing (WDM) [33]. The first Institute of electrical and electronics engineers (IEEE) standard for VLC was published in 2011 as IEEE 802.15.7-2011 [34]. This standard covers the link layer and physical layer design specifications for short-range wireless optical communication using visible light.

In the recent past, research projects on VLC have been carried out on different fronts. In 2013, researchers at Oxford university reported an experimental demonstration of an indoor VLC transmission at 1 Gbps [19]. Also, the LiFi research group at the University of Edinburgh presented a 3 Gbps VLC system using Gallium Nitrate μLED and OFDM [35]. Other notable research groups working on OWC include the Smart Lighting Engineering Research Centre [36] at Boston University and the Center for Ubiquitous Communication by light (UC-Light) [37] at the University of California, Riverside. In general, OWC has evolved into a promising transmission technique for wireless communications and it can serve to augment the existing RF communications. In view of the enormous benefits of OWC, consolidated research efforts are increasingly being directed towards realizing its full potential.

In OWC, information is transmitted by modulating the intensity, phase or frequency of radiations emitted by the optical sources such as LED and laser diode (LD). The optical radiation act as the carrier signal conveying information by propagating through unguided optical channel to the receiver, where it is collected by a photodetector (PD). Mostly, OWC employs intensity modulation and direct detection (IM/DD) technique which entails modulating information on the intensity (power) of light waves at the transmitter, and using a PD to transform instantaneous power into proportional current at the receiver. IM/DD is used due to its reduced cost and complexity, as adopting the coherent scheme in OWC will require accurate wave-front matching between the incoming signal and the local oscillator [27, 38].

An overview of OWC technology is presented in this chapter with the aim of capturing its prominent features, including the advantages, limitations and some areas of current and emerging applications. The chapter also describes the system blocks of a typical OWC link,

where the key characteristics of the transmitter, the receiver and the optical wireless channel are introduced. Finally, the digital modulation formats employed for OWC are presented along with the application of MIMO technique to maximize the throughput and enhance system performance.

2.1 Features of OWC

The OWC technology has a number of attractive benefits and application areas, some of which were introduced in Chapter 1. In the following, these features are further discussed alongside the challenges/limitations of OWC.

2.1.1 Advantages of OWC

Some of the compelling advantages of OWC technology are summarized below.

- **Broad bandwidth**: the optical band on the EM spectrum is orders of magnitude wider than that of RF. The usable bandwidth in the IR and VL bands alone is about 2,600 times the usable frequencies in RF band [5].

- **Simplicity and cost effectiveness**: OWC utilizes baseband digital technology which makes transmission and reception simpler than in RF communication where coherent methods such as heterodyne reception increases the system complexity [38]. Moreover, OWC can be implemented using relatively low-cost front-end devices such as commercially available LEDs and PD [6, 12]. Also, the deployment cost of OWC is reduced since the spectrum used is largely license-free, and in the case of VLC, existing lighting infrastructure can be reused.

- **Energy efficiency**: the optical sources, such as LEDs, are highly energy efficient. LEDs requires 80% less power compared to the conventional lights [12]. Furthermore, in VLC applications, since data transmission is piggy-backed on illumination, the energy used by LEDs is mainly needed for illumination. Besides, when illumination is not required, energy-efficient VLC techniques exist that enable data communication even when the light appears dark or off [39].

- **Security and spatial reuse**: optical radiations do not penetrate opaque objects, as such, they can be confined to well-defined coverage zones. This makes OWC an inherently secure means of communications. In addition, the high degree of spatial confinement

allows for the OWC to operate with coexistence of proximal and non-interfering links. This enables greater data density.

- **Interference avoidance**: optical signal does not interfere with RF signals, which makes it suitable as a complimentary solution to RF as in hybrid system RF/OWC system. Also, OWC is robust against EM interference and it does not interfere with the operation of sensitive electronic equipment. This feature makes OWC, particularly VLC, safe for use in environments where RF is prohibited such as aerospace, healthcare and petrochemical facilities [5, 10].

2.1.2 Challenges of OWC

Despite the attractions listed above, OWC also has limitations which are relevant for its implementation, including the following:

- **Non-negativity of transmit signal**: the realization of OWC through IM/DD means that the modulating signal has to be both real-valued and non-negative since the channel input represents instantaneous optical power [6, 38]. This poses additional constraints on the modulation techniques that can be employed in OWC, thus, limiting the application of the well-researched modulation formats in RF communications.

- **Transmitter bandwidth**: the finite bandwidth (about 2.5 MHz for white-light response and 14 MHz for blue-light response [22]) of off-the-shelf high brightness phosphor-converted-LEDs (pc-LEDs) limits the achievable data rate, particularly in VLC [40].

- **Mobility**: LOS link is the best option for OWC systems as it offers higher SNR, low error rate and high data rates. However, LOS links are susceptible to blockage and thus, they restrict mobility, especially in indoor environment. On the order hand, non-LOS (NLOS) links are more robust to blocking and can provide better support for user mobility, but for high-speed applications, the data rate is limited by the path loss and multi-path induced dispersion.

- **Transmission distance**: for OWC system using LEDs as optical source, the transmission distance is limited due to the sharp decrease in illumination with distance. While LDs can be used as light sources to obtain directional beam with limited power loss, their

usage however is subjected to stringent eye safety regulations due to their high radiant power.

2.1.3 Areas of application of OWC

The features listed above make OWC an attractive option in many application areas. An overview of some the use cases for OWC is given as follows.

- **wireless internet access and smart lighting**: indoor OWC can be used to provide wireless connectivity in homes and offices. The lighting fixtures illuminating the room also can act as optical access points (APs), with power, data and multi-point coordination realised using power-over-ethernet (PoE) or PLC technology [41]. In such deployment, VL spectrum is used for the downlink transmission to devices, while uplink transmission can be established using IR spectrum [5, 24]. Besides, indoor OWC can also be used to provide intelligent lighting solution which monitors factors such as light intensity and colour to regulate the level of illumination in a space while saving power [42].

- **Indoor localisation**: with the increasing number of LED luminaires in a typical indoor building, the unique identification of each LED source is being exploited to provide VLC-based positioning with higher accuracy and resolutions of a few centimeters [43, 44]. This system can be deployed in retail store, shopping malls and museums.

- **In-flight communications**: in aircraft where the use of RF radiation is undesirable, the LED-based lighting used in aircraft cabins are potentials VLC transmitters to provide both illumination and communication services for passengers [45, 46].

- **Vehicular communication**: LED-based traffic lights, street light and car lights can be exploited to establish OWC. Traffic lights can send traffic conditions and road safety notifications to the car. In the same vein, cars can also communicate with each other using head and tail lights to prevent accidents [24].

Other use cases for OWC include in smart-display signboards in shopping malls, airports and bus stops using arrays of LEDs to convey information to user devices. Besides, as increasing number of objects are being digitized through the IoT technology, OWC can be used to provide connectivity via low-power LED technologies [9]. In addition, since light propagates through water with lesser attenuation than RF, higher data rate underwater communications between

divers or remote operated vehicles are possible via OWC [6].

2.2 The OWC system blocks

The description of the fundamental blocks of an OWC system is presented in this section. The block diagram of a typical OWC system is shown in Figure 2.1. Customary of any other communication system, an OWC system consist of three major blocks: the transmitter, the receiver and the channel. Each of these blocks is further discussed below.
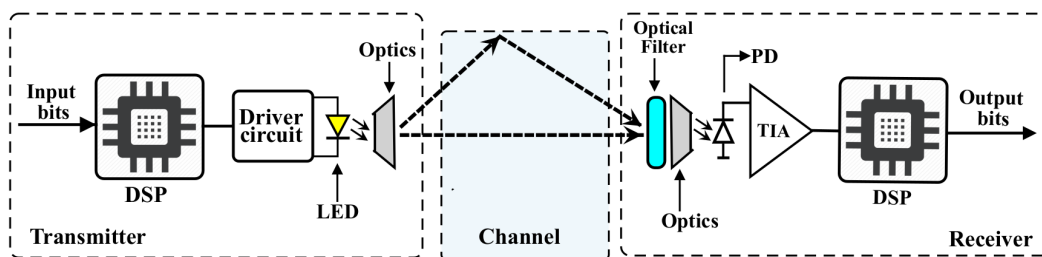
Figure 2.1: *Block diagram of a typical OWC system, illustrating the transmitter, receiver and channel blocks.*

2.2.1 Optical transmitter

The optical transmitter modulates the data/information onto the optical carrier via intensity modulation (IM). This entails varying the power (intensity) of the light emitted by the optical source in accordance to the modulating information signal. The transmitter includes a digital signal processor (DSP) which carries out the digital modulation of the information bits, and a digital-to-analog converter (DAC) that transforms the DSP output into an analog modulating signal. A driver circuit is then employed to control current flow through the optical source in proportion to the modulating signal. The optical source in turn converts the information-carrying current signal into optical intensity. An optical system made of a lens, a collimator, or a diffuser can then be employed to collect and concentrate or broaden the optical beam towards the receiver. The most commonly used optical sources are the LEDs (incoherent sources) and the LDs (coherent sources). The choice of the optical source to use depends on the target application. LEDs generally emit a broader beam compared to LDs, typical value of spectral width for LEDs is about $40\,\mathrm{nm}$ and for LDs is about $1\,\mathrm{nm}$ [47, 48]. Thus, LEDs are mainly used for indoor applications. But they can also be used for short-range outdoor OWC link up to a kilometre. LDs are mostly used for outdoor long distance OWC links due to their

highly directional beam profile which limits channel power loss. They are however subject to stringent eye safety regulations due to high radiant power [49]. For application in VLC, the rate of intensity variation for the optical source is much faster than the response time of the human eye, such that the emitted light is actually perceived as a steady glow [12].

2.2.2 Optical receiver

The primary function of the receiver is to recover the transmitted data from the incident light. Direct detection (DD) is employed, in which the PD produces an electrical signal proportional to the received instantaneous optical power [38]. An optical systems, e.g. collimator lenses, is used to collect and concentrate the incoming light unto the PD. An optical filter can also be applied to select a portion (e.g. wavelength) of interest in the optical spectrum, and also to minimise or reject the unwanted noise from ambient light. Thereafter, a PD or an array of PDs generates photo-current that is proportional to incident optical power. A post-detection circuit provides signal amplification and filtering to remove unwanted signals. This includes a transimpedance amplifier (TIA) which amplifies and converts the photo-current from the PD into voltage signal. Finally, an analog-to-digital converter (ADC) is employed to transform the signal from analog into digital form, and a DSP block carries out the demodulation required to retrieve the transmitted information bits. The two common PD types are the p-type intrinsic n-type (PIN) PD or avalanche photodiode (APD). The PIN PD has smaller gain compared to the APD, but it is simpler in structure, cheaper and offers a larger active area. These features make PIN PDs the most predominantly used PD for OWC. Using DD at the receiver allows simpler and low-cost implementation of transceiver devices without the need for complex high-frequency circuit designs used in coherent systems. However, the simplicity of DD comes at the cost of losing the optical carrier's frequency and phase information [38]. The two primary sources of noise in the receiver are the shot noise in the received photocurrent caused by ambient lights like the sun and other artificial lights, and the thermal noise generated from the receiver electronics (e.g. amplifier). Both shot and thermal noises can be modelled by Gaussian distribution [38, 49].

2.2.3 Indoor optical wireless channel

The nature of the indoor optical wireless channel is dependent on the link properties such as the position, orientation and radiation/detection characteristics of the transmitter and receiver, as well the dimension and features of the environment and intervening objects. Based on the propagation path of the light from the transmitter to the receiver, the OWC link can be classified into LOS and NLOS communications. In LOS links, the signal travels via a direct uninterrupted path between the transmitter and the receiver, while the NLOS links rely on the reflection of light signals from surfaces and intervening objects in order to reach the receiver [6, 38]. To model a generalised case, we consider the non-directed LOS optical wireless link in which the transmitted signal propagates through not only the LOS direct path, but also via multiple reflected (NLOS) paths between the transmitter and the receiver. An illustration of the geometry of this scenario is given in Figure 2.2. The parameters (angles and distances) describing the geometry of the transmitter, receiver and reflecting surfaces are shown. The figure also depicts the LOS path between the LED and the PD, and the NLOS path from the LED through the first and k-th surface reflector to the PD.
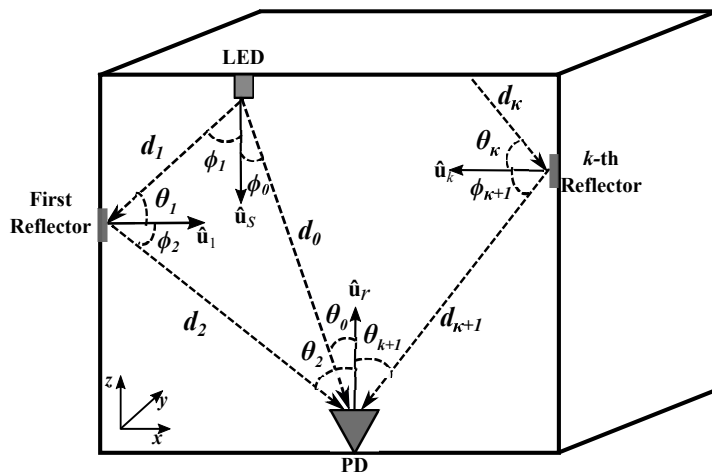
Figure 2.2: *Geometry of ray-tracing in an indoor OWC channel.*

The IM/DD-based indoor optical wireless channel can be characterised by the impulse response $h(t)$, which relates the optical power that is transmitted to that incident on the PD. The channel impulse response (CIR) consists of LOS and multipath components, and it models the effect of both optical path loss and multipath dispersion [49, 50]. Numerically, the CIR of an optical

wireless channel can be obtained using the ray-tracing algorithm developed by Barry et al. [51] which calculates the path loss and time delay for every path through which the transmitted signal travels from the source to the receiver. Considering an optical source and a detector in a room as shown in Figure 2.2, let the configurations of the source and the receiver be denoted by $\mathcal{S}$ and $\mathcal{R}$, respectively, the CIR, $h(t)$ can be expressed as sum of the LOS response and K multipath responses [51]:

$$h(t) = h^{(0)}(t; \mathcal{S}; \mathcal{R}) + \sum_{k=1}^{K} h^{(k)}(t; \mathcal{S}; \mathcal{R}) \tag{2.1}$$

where $h^{(0)}(t; \mathcal{S}; \mathcal{R})$ is the LOS response, while $h^{(k)}(t; \mathcal{S}; \mathcal{R})$ is the response of the light after undergoing k reflections. For the source, $\mathcal{S} = \{\mathbf{p}_s, \hat{\mathbf{u}}_s, m\}$, where $\mathbf{p}_s = [x_{p_s}, y_{p_s}, z_{p_s}]$ is the position (coordinates) vector, $\hat{\mathbf{u}}_s = [x_{u_s}, y_{u_s}, z_{u_s}]$ is the unit-length orientation vector, and m is the Lambertian mode number which specifies the directionality of the source beam. In the same vein, for the receiver, $\mathcal{R} = \{\mathbf{p}_r, \hat{\mathbf{u}}_r, A_r, \Psi_r\}$, where $\mathbf{p}_r = [x_{p_r}, y_{p_r}, z_{p_r}]$ is the position vector, $\hat{\mathbf{u}}_r = [x_{u_r}, y_{u_r}, z_{u_r}]$ is the unit-length orientation vector, $\mathcal{A}_r$ is active collection area and Ψ_r is the FOV of the receiver.

According to [51], by modelling the transmitter and receiver with generalized Lambertian radiation and detection pattern, respectively [38, 52], the LOS CIR is approximated as a scaled and delayed Dirac delta function:

$$h^{(0)}(t; \mathcal{S}; \mathcal{R}) = \frac{(m+1)\mathcal{A}_r}{2\pi d_0^2} \cos^m(\phi_0) \cos(\theta_0) \operatorname{rect}\left(\frac{\theta_0}{\Psi_r}\right) \delta(t - d_0/c) \tag{2.2}$$

where $d_0 \gg \mathcal{A}_r$ and $\delta(\cdot)$ is the Dirac delta function which specifies the signal propagation delay. The distance between the source and the receiver, $d_0 = \|\mathbf{p}_s - \mathbf{p}_r\|$. The angle of emission at the source $\phi_0 = \arccos(\hat{\mathbf{u}}_s \cdot (\mathbf{p}_r - \mathbf{p}_s))/d_0$, while the angle of incidence at the receiver is $\theta_0 = \arccos(\hat{\mathbf{u}}_r \cdot (\mathbf{p}_s - \mathbf{p}_r))/d_0$. The mode number of the source, $m = \frac{-\ln 2}{\ln \cos(\Phi_{1/2})}$, where $\Phi_{1/2}$ is the semi-angle at half power. The scalar c denotes the speed of light, and the rectangular function is defined as:

$$\operatorname{rect}(a) = \begin{cases} 1; & \text{for } |a| \leq 1 \\ 0; & \text{for } |a| > 1. \end{cases} \tag{2.3}$$

The multipath component of the CIR is obtained by partitioning the reflecting surfaces of the

environment into multiple reflector elements, each with area $\mathcal{A}_{\mathrm{ref}}$, and then computing the impulse response in a recursive multi-bounce method. Based on the algorithm proposed in [51], the impulse response after k reflections is given by:

$$h^{(k)}(t; \mathcal{S}; \mathcal{R}) = \frac{(m+1)}{2\pi} \sum_{i=1}^{N} \frac{\rho_i \mathcal{A}_{\mathrm{ref}}}{d_i^2} \cos^m(\phi_i) \cos(\theta_i) \operatorname{rect}\left(\frac{2\theta_i}{\pi}\right) h^{(k-1)}(t - d_i/c; \mathcal{E}_i; \mathcal{R})$$

(2.4)

where N is the total number of reflector elements across all reflecting surfaces, ρ_i is the reflection coefficient of the i-th element, and d_i is the distance between the i-th element and the source, the receiver or another reflector elements as shown in Figure 2.2. The parameter $\mathcal{E}_i$ denotes the configuration of the i-th element. The recursive algorithm expressed by (2.4) decomposes the multi-bounce method into two step: first, it considers each reflector element, $\mathcal{E}_i$, as a receiver, with area $\mathcal{A}_{\mathrm{ref}}$, and FOV of $180°$ that collect an incoming light from the an optical source or from another reflector. Second, the reflector element act as a source with ideal Lambertian radiation intensity pattern, i.e., $m = 1$.

Multipath propagations cause time spreading of the received signal. A common measure for quantifying the time-dispersive properties of multipath propagation is the root mean square (RMS) delay spread, τ_{rms}, which can be calculated using the following expression [38]:

$$\tau_{\mathrm{rms}} = \sqrt{\frac{\int_{-\infty}^{\infty} (t - \overline{\tau})^2 \, h^2(t) \, \mathrm{d}t}{\int_{-\infty}^{\infty} h^2(t) \, \mathrm{d}t}}$$

(2.5)

where the mean delay spread, $\overline{\tau}$, is obtained from:

$$\overline{\tau} = \frac{\int_{-\infty}^{\infty} t \, h^2(t) \, \mathrm{d}t}{\int_{-\infty}^{\infty} h^2(t) \, \mathrm{d}t}.$$

(2.6)

2.3 Optical digital modulation techniques

This section reviews digital modulation schemes that are widely used for OWC. Emphasis is placed on modulations formats which are related to the focal point of this research work. They include pulsed modulation schemes such as on-off-keying (OOK), PPM and pulse amplitude modulation (PAM), as well as multi-carrier techniques, specifically, OFDM. As stated previously, in an IM/DD based optical wireless system, the modulating signal controls

the drive current which in turn changes the intensity of the optical source proportionally. The equivalent baseband model for the IM/DD system is expressed by [38]:

$$r(t) = Rh(t) \otimes s(t) + \eta(t) \tag{2.7}$$

where $\otimes$ denotes convolution, $s(t)$ is the intensity of the optical source, $r(t)$ is the photocurrent generated by the PD and R is the responsivity of the PD. The noise is represented by $\eta(t)$, and is assumed to be the sum of thermal noise and shot noise due to ambient light. It can be modelled as real-valued AWGN with zero mean and variance σ^2 [26, 38]. As shown in (2.7), the channel input $s(t)$ represents instantaneous optical power, therefore, it is non-negative, i.e., $s(t) \geq 0$. The average transmitted optical power P_{ave} is obtained as [38]:

$$P_{\text{ave}} = \lim_{T \to \infty} \frac{1}{2T} \int_{-T}^{T} s(t) \, \mathrm{d}t \tag{2.8}$$

where T is the period for transmitted light wave. The average received optical power, P_{r} is related to P_{ave} by $P_{\text{r}} = hP_{\text{ave}}$, where the direct-current (DC) channel gain, $h = \int_{-\infty}^{\infty} h(t) \, \mathrm{d}t$. Eye safety requirements on the radiation of the optical sources can be satisfied by limiting P_{ave} such that it does not exceed the maximum permissible radiant power level.

The choice of modulation schemes for OWC systems plays a vital role in determining important system parameters such as power and spectral efficiency, as well as error performance. Power efficient modulation schemes are considered for energy-constrained applications such as sensors and IoT devices, whereas bandwidth efficient scheme are preferred for high data rates applications such as video streaming via home/office internet access. Further discussion on popular modulation schemes is given below.

2.3.1 Pulsed modulation techniques

Pulsed modulation techniques utilize discrete intensity levels to represent the information symbols. Widely used techniques for IM/DD optical wireless systems include the following.

2.3.1.1 On-off-keying

OOK is the most basic pulsed scheme for IM/DD in optical communication due to its simplicity [49]. However, as a binary modulation scheme, OOK transmits only one bit per

symbol interval, hence it provides limited spectral efficiency. As its name suggests, OOK represents binary information in the form of high intensity (on) and low intensity (off). A high intensity represents bit '1' while a low intensity signifies bit '0'. Typically, OOK is implemented using the non-return to zero (NRZ) pulse format, where an optical pulse is transmitted for the entire symbol duration T. However, OOK can also be designed with return to zero (RZ) pulse format by transmitting the optical pulse for a fraction of the symbol interval, thereby offering an improved power efficiency over NRZ-OOK, though at the cost of increased bandwidth requirement. Figure 2.3 illustrates a NRZ-OOK optical signal. $P_{\mathrm{on}}^{\mathrm{OOK}}$ and $P_{\mathrm{off}}^{\mathrm{OOK}}$, respectively denote high and low intensity power level emitted by the optical source. Related works on OOK include NRZ-OOK modulation with post-equalisation and blue filtering to achieve data rates of 100 Mbps and 340 Mbps in [22] and [53], respectively.
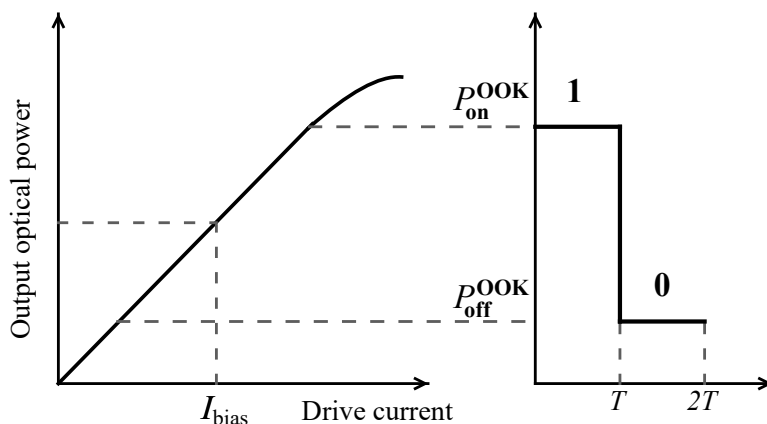
Figure 2.3: *Optical OOK signal.*

2.3.1.2 Pulse amplitude modulation

An L-ary PAM scheme transmits information using multiple intensity levels, where L denotes the size of signal constellation diagram, i.e., the number of optical intensity levels. Thus, $\log_2(L)$ bits are mapped to each PAM constellation transmitted per symbol interval. Given the non-negativity constraints on optical transmit signals, unipolar L-PAM is used in OWC, and the intensity levels are given by [23]: $P_{\ell}^{\mathrm{PAM}} = \frac{2P_{\mathrm{ave}}}{L-1}$ for $\ell = 0, 1, \ldots, (L-1)$. As an illustration, a 4-PAM optical signal is shown in Figure 2.4. By transmitting $\log_2(L)$ bits/symbol as against 1 bits/symbol in OOK, PAM provides a higher bandwidth efficiency compared to OOK. However, using multiple intensity levels means that the PAM scheme could be affected by the LED's non-linear operation and colour temperature (chromaticity) due to variation in

drive current [54].
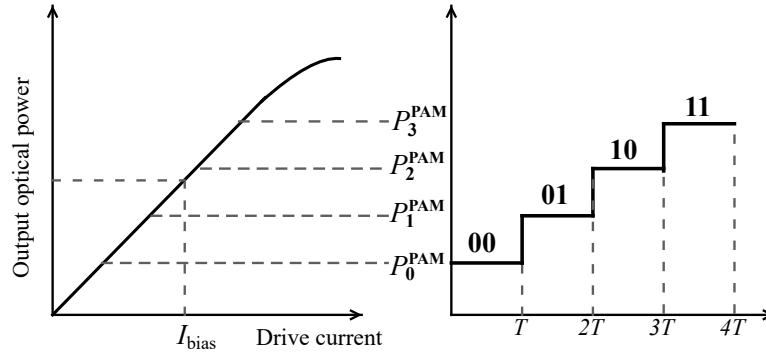
Figure 2.4: *Optical 4-PAM signal.*

2.3.1.3 Pulse position modulation

In an L-ary PPM, the symbol duration is divided into L time subintervals/slots, each with duration $T_c = T/L$. Information is transmitted by varying the temporal offset (position) of the optical pulse in each symbol duration. A filled time slot has an intensity level (pulse amplitude) of P_{on}^{PPM}, while the remaining $(L-1)$ empty slots have low intensity level P_{off}^{PPM}. An L-ary PPM scheme has a signal constellation size of L. The transmitted constellation (symbol) is identified by the position of the pulse, and $\log_2(L)$ bits are mapped to each of the L constellations. Figure 2.5 illustrates a 4-PPM optical signal. As L increases, the power efficiency and error performance of L-PPM modulation improves. The average power requirement for PPM is smaller than OOK and PAM. However, PPM has shorter pulse interval which implies higher bandwidth requirement. As such, PPM is less bandwidth efficient than PAM [12, 55]. Different variants of PPM have been proposed in order to improve spectral efficiency. For instance, Overlapping PPM (OPPM) [56] and Multipulse PPM (MPPM) [57] use longer pulse duration than the conventional PPM. This is achieved by allowing more than one pulse to be transmitted during the symbol duration. Part of our investigation in this research work include the use of MIMO techniques to enhance the spectral efficiency of conventional PPM (see Chapter 3) by encoding additional information bits on the spatial domain of optical sources.
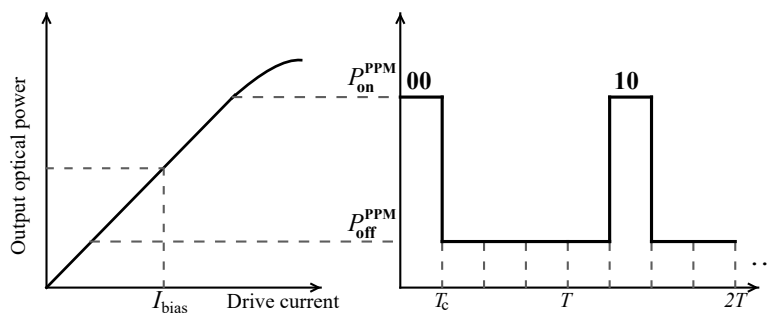
Figure 2.5: *Optical 4-PPM signal.*

2.3.2 Optical OFDM

As communication speed increases, the frequency selectivity caused by the LED's response and the multipath propagation of transmitted signal leads to ISI. The data rate that is achievable from the pulsed modulation techniques presented above is constrained by the presence of ISI. Hence, multi-carrier modulation techniques such as OFDM have a become prime candidate for high data rate OWC systems. OFDM is a bandwidth efficient transmission technique that is robust against ISI [58]. In OFDM, a wideband channel is subdivided into multiple narrowband and orthogonal subchannels which are used to transmit independent data streams in parallel. Each subchannel is called a subcarrier (SC). A conventional modulation scheme, typically, M-ary quadrature amplitude modulation (QAM), is employed to modulate information onto each SC. Figure 2.6 illustrates the system blocks for an optical OFDM. The information bits are mapped into M-QAM symbol constellations. Then, a serial-to-parallel (S/P) block converts the QAM symbol stream into parallel blocks of symbols which are assigned to the SCs in each OFDM frame. An inverse fast Fourier transform (IFFT) operation is applied to multiplex the parallel streams and generate a time domain OFDM signal.

For IM/DD based OWC, the time domain OFDM signal modulates the intensity of the light emitted by the optical source. As such, the signal is confined to be real-valued and unipolar. Real-valued time domain signal is obtained by imposing Hermitian symmetry when mapping symbol onto the SCs such that the negative frequency SCs are set to the complex conjugate of the data on the positive SCs. The Hermitian symmetry operation is denoted by "$*$" in the block diagram in Figure 2.6. With Hermitian symmetry applied, the IFFT block produces bipolar real-valued signals. Based on how the bipolar signals are converted to unipolar, there
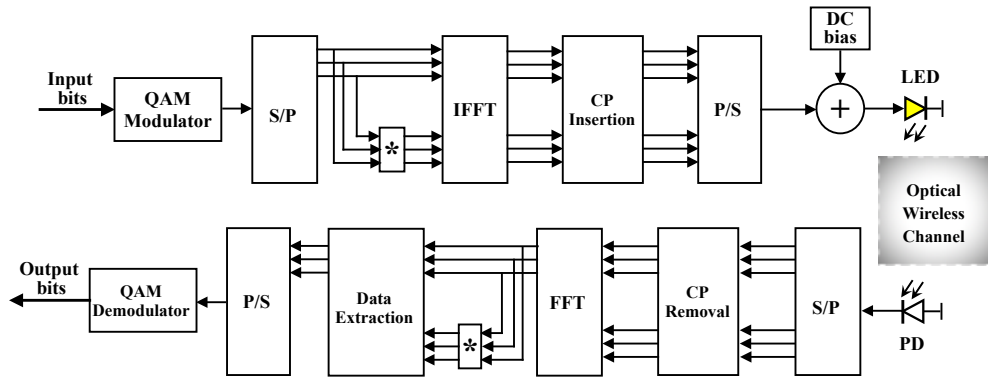
Figure 2.6: *Block diagram of an optical OFDM system. The symbol "∗" denotes the the Hermitian symmetry operation*

are different implementations of optical OFDM. One approach is the DC-biased optical (DCO) OFDM [59, 60]. With DCO, a DC offset is added to the IFFT output to obtain positive valued signals. Another approach is the Asymmetrically-clipped optical (ACO) OFDM in which information is modulated onto only the odd indexed SCs at the IFFT input. Then, the bipolar IFFT output is converted to unipolar by simply clipping the time domain symbol at zero. It has been shown in [61] that this clipping introduces noise only on the non-information carrying even indexed SCs. Details of the implementation and performance comparison of DCO-OFDM and ACO-OFDM is provided in [62]. In order to mitigate ISI and ICI, cyclic prefix (CP) is appended to the start of each time domain OFDM frame before sending it through the optical source [63]. At the receiver, a copy of the transmitted frames which have been distorted by the channel and receiver's AWGN is passed through the serial to parallel (S/P) block. After the S/P conversion of the received data stream into sets of OFDM frames, the CP extension of each frame is removed. Fast Fourier transform (FFT) operation is then applied to demultiplex the OFDM frame and recover the data modulated onto each SC. With a sufficiently large number of SCs, each of them is considered as a narrowband non-frequency-selective subchannels. Thus, single-tap frequency domain equalisation can be employed on each SCs to retrieve the transmitted M-QAM symbol before demodulation is performed to recover the information bits in each symbols.

2.4 Optical MIMO techniques

The utilisation of multiple elements at the transmitter and receiver in MIMO systems constitute a key technology for improving the capacity and/or reliability of wireless

communications. MIMO techniques have been widely researched and implemented in RF based communications systems to enable multiplexing gain, diversity gain, or antenna gain, and hence to enhance the bit rate, error performance, or the signal-to-noise-plus-interference ratio of wireless systems, respectively [58, 64, 65]. Motivated by the success achieved in RF systems, MIMO techniques have also been proposed for OWC systems. An optical transmitter can employ an array of optical sources which can be configured for MIMO data transmission. Optical MIMO technique are designed to exploit additional degrees of freedom, such as the location and viewing angle of optical sources, as well as the location and field of view of optical detectors [21, 23, 66, 67]. These techniques are promising solutions to efficiently utilize the available bandwidth for data rate, and to improve coverage and reliability of the communication system.

MIMO techniques rely on the wireless channel to introduce specific channel signatures (signal strengths) on the multiple links. These signatures enable the receiver to distinguish the signals from different transmitter sources. A simplified schematic of a MIMO system for OWC is shown in Figure 2.7. Considering an OWC system with N_t optical sources and N_r detectors, using the baseband channel model given in (2.7), the MIMO system can be expressed as:

$$\mathbf{r} = R\mathbf{H}\mathbf{s} + \boldsymbol{\eta} \tag{2.9}$$

where $\mathbf{r} = [r_1 \dots r_{N_r}]^\dagger$ is the received signal vector, $\mathbf{s} = [s_1 \dots s_{N_t}]^\dagger$ is the transmitted signal vector and $\boldsymbol{\eta}$ is the N_r-dimensional real-valued AWGN vector, where $[\cdot]^\dagger$ denote the transpose operation. The entries of vector $\mathbf{s}$ indicate which signal is emitted by each optical source, i.e. s_{n_t} denotes the signal emitted by source n_t. The $N_r \times N_t$ MIMO channel matrix is denoted by $\mathbf{H}$. Assuming maximum-likelihood (ML) detection at the receiver, with perfect knowledge of the channel, the decoder decides in favour of the signal vector $\widehat{\mathbf{s}}$ which minimises the Euclidean distance between the actual received signal vector $\mathbf{r}$ and all the possible received signals. That is:

$$\widehat{\mathbf{s}} = \arg\max_{\mathbf{s}} f_{\mathbf{r}}(\mathbf{r}|\mathbf{H}, \mathbf{s}) = \arg\min_{\mathbf{s}} \|\mathbf{r} - R\mathbf{H}\mathbf{s}\|^2 \tag{2.10}$$

where $\|.\|$ denotes the vector norm operation. The probability density function of $\mathbf{r}$ conditioned
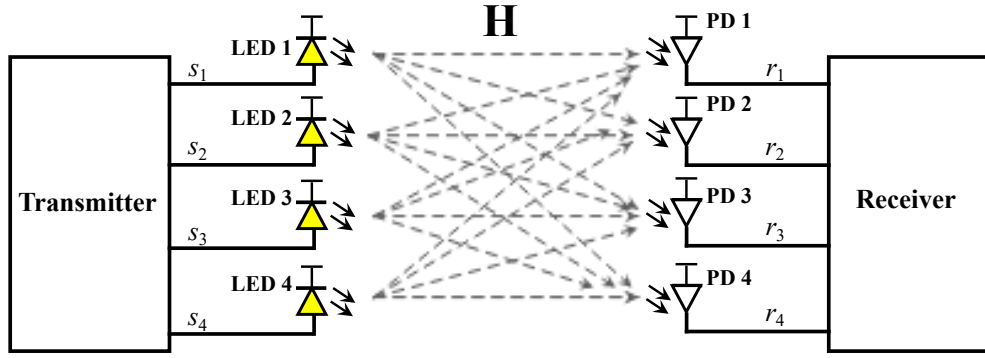
Figure 2.7: *Illustration of optical MIMO system.*

on $\mathbf{H}$ and $\mathbf{s}$ is given by:

$$f_{\mathbf{r}}(\mathbf{r}|\mathbf{H}, \mathbf{s}) = \frac{1}{(2\pi\sigma^2)^{N_{\mathrm{r}}L/2}} \exp\left(-\frac{\|\mathbf{r} - R\mathbf{H}\mathbf{s}\|^2}{2\sigma^2}\right). \tag{2.11}$$

Various MIMO techniques have been proposed for OWC in indoor and outdoor environment, each technique with its own unique features and advantages. In outdoor FSO systems, MIMO system using spatially separated optical wireless channels with LOS alignment have been employed to improve system performance. FSO systems using MIMO diversity techniques are explored in [68–71] to combat the effect of turbulence-induced fading by providing redundancy. Besides, in [72], the authors investigated the deployment of orthogonal space-time block codes (OSTBCs) and RC MIMO scheme, demonstrating that both schemes can achieve full diversity over turbulence-induced fading channels. To increase the bandwidth efficiency of FSO systems, in [73], SMP MIMO scheme is considered, where each transmitter sends independent information to its corresponding receiver's aperture. The impact of the number of transceiver pairs and beam waist on the performance of the FSO system is investigated, and proposed SMP scheme is compared with spatial diversity FSO system. Also, the use of SM as a MIMO scheme with reduced complexity has been explored to enhance the spectral efficiency of FSO systems using different statistical distributions to model the channel fading in [74–80]. Different variants of the aforementioned MIMO schemes have also been investigated in indoor optical wireless environment. The performance of MIMO technique in diffuse optical wireless systems employing Space Time Block Coding (STBC) is investigated in [81]. It is shown that STBC techniques can be used to increase the capacity and

improve their coverage. Furthermore, detailed performance analysis and comparison of indoor MIMO optical wireless system using RC, SMP and SM schemes are presented in [23, 82]. It was shown that RC is less restrictive in terms of its requirement for channel decorrelation (transmitter-receiver alignment) but its bandwidth efficiency is limited. As such, RC used mainly for achieving diversity gain or improving link range. In contrast, SMP MIMO provides capacity gains, but is highly sensitive to channel correlation. SM technique provides an attractive trade-off between capacity and reliability. SM is more robust to correlated channels than SMP, and it offers higher spectral efficiency than RC. These three widely adopted MIMO techniques are further discussed as follows.

2.4.1 Repetition coding

In RC MIMO technique, the same information signal is transmitted from all the optical sources. That is, they are modulated with the same data streams, such that in (2.9), $s_1 = s_2 = \cdots = s_{N_t}$. The transmitted signals from all optical sources add up constructively at the receiver with different signal strength, depending on the link characteristics. The RC MIMO system is illustrated in Figure 2.8a. An RC scheme can be used to provide wider coverage. In [83], transmitter angle diversity is employed using optical source with limited divergence angle but pointed in different directions to achieve room scale coverage. Besides, spatial diversity can be employed at the receiver using multiple detectors to achieve wider FOV and robustness against blocking [84, 85]. Maximum ratio combining (MRC) is considered in [85] to improve error performance, while selection combining is combined with angle diversity to for coverage and mobility [84]. Moreover, [72] show that FSO systems using RC can outperform OSTBC scheme.
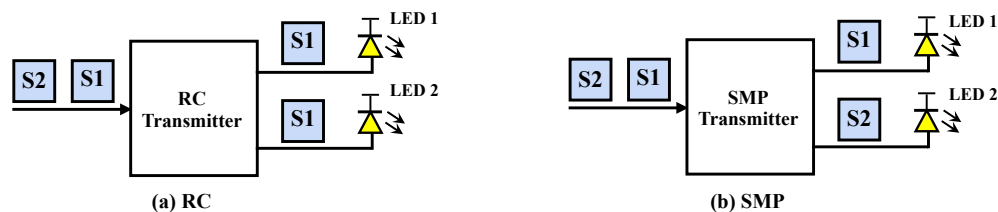
Figure 2.8: *Illustration of (a) RC and (b) SMP optical MIMO systems.*

2.4.2 Spatial multiplexing

SMP technique entails simultaneously transmitting independent data stream over multiple optical sources. Using N_t sources, the overall data rate (spectral efficiency) is enhanced by a factor of N_t compared to single optical source system without requiring extra bandwidth. The SMP MIMO system is illustrated in Figure 2.8b. Since the individual data streams are superimposed during transmission, ICI cancellation is required at the receiver in order to separate the data streams. Besides, to facilitate detection, a rich scattering environment is very important and the number of detectors should be equal to or larger than number of transmitter sources ($N_r \geq N_t$) [21]. SMP technique is applied in [86, 87] using zero forcing (ZF) to cancel the signal interferences among the transmitter sources. An experimental demonstration of four-channel MIMO-OFDM VLC transmission system using SMP technique with nine-channel imaging receiver to achieve Gigabit data rate is reported in [19].

2.4.3 Spatial modulation

In SM, the symbol constellation space in the conventional digital modulation scheme is extended to the spatial dimension of the multiple optical sources in a MIMO setup. Thus, additional information bits are transmitted by encoding them on the spatial index of the sources. SM is proposed in [88] and further investigated in [80, 89–96]. The fundamental concept optical SM (OSM) is to utilize spatially separated optical sources as spatial constellation points to convey additional information bits. The difference in optical source placement imprints different channel signature (pathloss). This enables the receiver to distinguish the signals of each source from the others. Using the ML detection algorithm as expressed by (2.10), the receiver estimates the data symbol as a combination of the activated transmitter source and the transmitted signal constellation.

In OWC, OSM technique has been implemented in a variety of forms, using different signal modulation methods, and activating single or multiple optical sources in a symbol duration. In this thesis, we refer to the SM schemes that activate only one optical source per symbol interval as the classical SM schemes [23, 90, 92, 97], while those activating more than one source are termed the generalised SM (GSM) schemes [94, 98–100]. The simplest implementation of OSM technique is the optical space shift keying (SSK) [90, 97] in which only a single LED is

activated in a symbol duration and information bits are encoded solely on the spatial index of the activated optical source. Other variants of SM entail encoding some information bits in the indices of the sources while the rest of the information bits are conveyed by the transmitted digital modulation such as PPM [92, 94], PAM [23] and OFDM [101].

The encoding process for classical OSM schemes is as follows. Considering an optical MIMO system with N_t LEDs, at the transmitter, the information bits to be transmitted are grouped into data symbols, and the bits that make up each data symbol are divided into two parts: spatial bits and signal bits. The spatial bits form the spatial constellation point (SCP) which determines the index (spatial position) of the LED that will be activated, while the signal bits constitute the signal constellation point which determines the electrical signal (digital constellation) that modulates the intensity of the activated LED. Let the sizes of the spatial and signal constellation diagrams be denoted by N_s and L, respectively. Then, there are $(N_\text{s} \times L)$ possible data symbols and thus, the number of bits transmitted per symbol is given by $\mathcal{M} = \log_2(LN_\text{s})$. As an illustration, the encoding mechanism for an OSM scheme with $N_\text{t} = 4$, $L = 4$ and $\mathcal{M} = 4$ bits/symbol is shown in Figure 2.9. To transmit the first data symbol which consist of bits '1101', LED 4 is selected to be activated based on the first two most significant bits, '11', while remaining two bits, '01', are encoded in the signal constellation point 'S$_2$'.
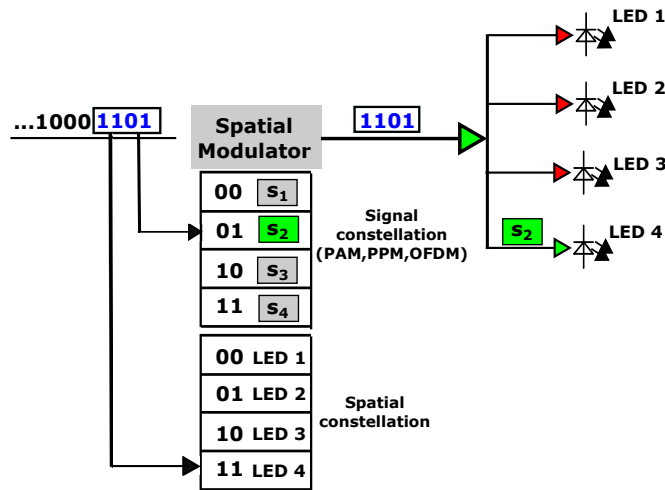
Figure 2.9: *Illustration of OSM encoding mechanism using $N_\text{t} = 4$ LEDs.*

In the classical SM schemes, by allowing only one of N_t optical sources to be activated during a symbol interval, the ICI from multiple transmitter sources can be eliminated. However, the size of the spatial constellation and thus, the achievable capacity gain is limited. Besides, the

total number of sources is constrained to a power of two. These limitations can be addressed by allowing the activation of more than one optical source during a symbol period. This is the approach employed in GSM schemes. This way, the spatial constellation size and hence, the number of bits per symbol can be increased, albeit, at the cost of increasing ICI and synchronisation requirement [99, 100]. GSM technique has been implemented in different formats. In the approach presented in [99], the number of activated LEDs in any given symbol interval is fixed at N_a where $1 < N_\mathrm{a} < N_\mathrm{t}$. Each active LED transmits different L-ary PAM symbols simultaneously. In contrast, the GSM schemes in [100] entails varying both the number of activated sources and their transmit powers in order to satisfy illumination constraints. In the GSM schemes considered in [93, 94, 102], the number and indices of the activated sources are varied based on the spatial bits of the data symbol. All the activated sources transmit the same signal constellation. By transmitting the same signal constellation from more than one source at a time, this latest variant of GSM benefits from spatial diversity gains and reduced ICI at the receiver. This is the implementation of GSM considered in this thesis. Further description of the four OSM variants covered in this work is provided as follows.

2.4.3.1   Space shift keying (SSK)

In SSK, only one LED is activated to send an optical data signal during a given symbol duration, while the rest of the LEDs are idle. Therefore, with a total of N_t LEDs, there are $N_\mathrm{s} = N_\mathrm{t}$ possible spatial constellations. Also, the activated LED does not transmit any digital signal constellation. Rather, it simply transmits a rectangular optical pulse of constant peak power, P_t, for the entire symbol duration T. Since no signal modulation is used, then $L = 1$ and the data symbol is encoded solely in the SCP, i.e., the index of the activated LED. Therefore, a total of $\mathcal{M} = \log_2(N_t)$ bits are transmitted per SSK symbol. An illustration of SSK scheme with 4 LEDs is depicted in Fig. 2.10. Two information bits are transmitted per symbol, and the first pair of bits, '01', is transmitted by activating 'LED 2'. The achieved transmission rate in SSK can be increased by adding signal modulation and/or activating multiple LEDs concurrently, as employed in the SM schemes discussed next.
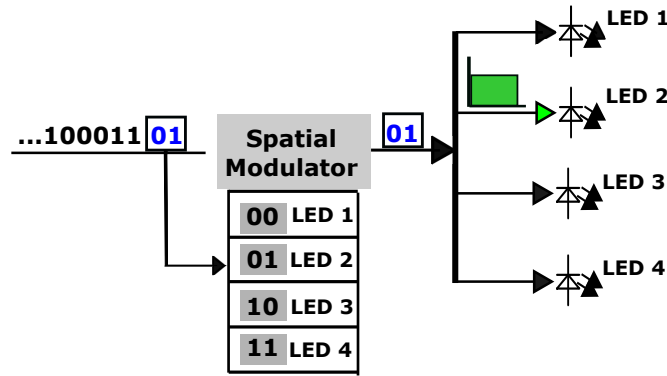
Figure 2.10: *An illustration of SSK modulation using $N_t = 4$ LEDs.*

2.4.3.2 Generalised space shift keying (GSSK)

Unlike SSK in which only one LED is activated in any given symbol duration, in optical GSSK [102, 103], one or more LEDs can be activated concurrently. However, signal modulation is also not used in GSSK, i.e., $L = 1$. Hence, the data symbol is encoded solely in the SCP. Using N_t LEDs, $N_s = 2^{N_t}$, and $\mathcal{M} = N_t$ bits/symbol. The position of ones (1s) in the binary representation of each data symbol determines the indices of the LEDs that will be activated to convey the symbol. For any given data symbol, except when all the bits are zeros, the LEDs whose positions correspond to a bit value of one are activated to transmit a RZ pulse with duty cycle τ and peak power P_t, while all the other LEDs are idle, where $0 < \tau \leq 1$. However, when all the bits of the data symbol are zeros, all the LEDs are activated, but they transmit RZ pulse pattern that is orthogonal to the all ones data symbol (i.e., with a duty cycle $(1 - \tau)$. An illustration of GSSK is shown in Fig. 2.11 with the pulse pattern for a 2-LED GSSK scheme. Without the loss of generality, in this thesis, $\tau = 1$ is considered for the GSSK scheme [98, 102].

2.4.3.3 Spatial pulse position modulation (SPPM)

SPPM combines SSK with PPM. As such, only one of the N_t LEDs is activated during a given symbol duration. The activated LED transmits an L-PPM optical signal. The size of the signal constellation, L, is equal to the number of PPM time slots (pulse position) in each symbol period. Hence, in SPPM, $N_s = N_t$ and total number of bits transmitted per symbol is $\mathcal{M} = \log_2(LN_t)$. At the transmitter, the first $\log_2(N_t)$ most significant bits of each data symbol constitute the spatial bits, while the remaining $\log_2(L)$ bits constitute the signal bits.

Figure 2.11: *Illustration of the pulse pattern for optical GSSK scheme with $N_t = 2$ LEDs.*

The signal bits determine the time slot in which a pulse will be placed in the L-PPM signal transmitted by the activated LED. SPPM is illustrated in Fig. 2.12 for the case of $N_t = 4$, $L = 2$ and $\mathcal{M} = 3$ bits/symbol. As an example, data symbol '3' with binary representation '011', is transmitted by activating 'LED 2' to transmit a pulse in the second time slot.

Figure 2.12: *An illustration of the pulse pattern for SPPM scheme with $N_t = 4$, $L = 2$ and $\mathcal{M} = 3$ bits/symbol. The sample PPM patterns represent the pulse pattern for the data bits indicated in the square brackets.*

2.4.3.4   Generalised spatial pulse position modulation (GSPPM)

In a GSPPM scheme, one or more LEDs can be activated to concurrently transmit data signals [94] (as in GSSK). Thus, the spatial constellation size is $N_s = 2^{N_t}$. Also, the activated LEDs transmit the same L-PPM pulse pattern just as in SPPM. LED activation in GSPPM [94] is done in a similar way to the GSSK scheme, albeit with a slight modification. That is, the number of ones (1s) in the spatial bits still determines the number and the indices of the active LEDs, but a pulse-inversion technique [104] is employed in GSPPM in place of the RZ pulse coding used in GSSK. The pulse-inversion technique in GSPPM is such that when the spatial bits are all zeros, all the LEDs are activated, but they are driven by an electrical pulse signal of amplitude $-V$ volts. For all other SCPs, the LEDs whose indices correspond to the bit value '1' in the spatial bits are activated, and they are driven by an electrical pulse signal of amplitude V volts. By using bipolar signal of amplitude $\pm V$ volts, GSPPM requires a DC bias equivalent to V volts to convert the bipolar signal to unipolar signal. However, for applications in VLC, this DC bias will be available anyway to turn on the LEDs for illumination purposes. In GSPPM, a total of $\mathcal{M} = (N_t + \log_2(L))$ bits are transmitted per symbol. The most significant N_t bits of each symbol constitute the spatial bits, while the remaining $(\log_2 L)$ bits constitute the signal bits which are conveyed by the transmitted PPM signal. GSPPM scheme is further illustrated in Fig. 2.13 using $N_t = 2$, $L = 2$ and $\mathcal{M} = 3$ bits/symbol. To transmit symbol '3', with binary equivalent, '011', the first two bits, '01' are used to select the 'LED 1' for activation while 'LED 2' remains idle. The last bit of the symbol, '1', indicates that the pulse will be transmitted in the second time slot.

2.4.4   Computation complexity analysis

Based on the ML detection algorithm expressed in (2.10), the computation complexity of aforementioned optical MIMO techniques at the receiver is analysed as follows. The RC technique is not considered here, as it can be implemented with a much simpler detection algorithm compared to the other MIMO techniques. The computational complexity of detection algorithm is defined in terms of the total number of floating point operations (FLOPs), i.e., multiplications, additions and subtractions, needed. Accordingly, with $R = 1$ A/W in (2.10), the FLOPs count and the number bits transmitted per symbol interval for each optical MIMO scheme are provided in Table 2.1. For the classical SM schemes such
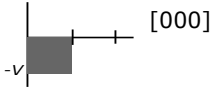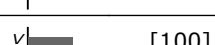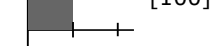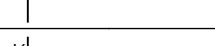
Data symbol	Binary equivalent	Spatial Constellation	Signal Constellation	Activated LEDs	Sample PPM Signal Pattern
0	000	00	0	1 and 2	[000]
1	001	00	1		
2	010	01	0	1	[011]
3	011	01	1		
4	100	10	0	2	[100]
5	101	10	1		
6	110	11	0	1 and 2	[111]
7	111	11	1		

Figure 2.13: *An illustration of the pulse pattern for GSPPM scheme with $N_t = 2$, $L = 2$ and $\mathcal{M} = 3$ bits/symbol. The sample PPM patterns represent the pulse pattern for the data bits indicated in the square brackets.*

as OSSK and SPPM, the FLOP count is reduced because only one optical source is activated in given symbol interval. As such, the transmit signal vector, **s** has only one non-zero entry. In the case of GSM schemes such as the GSSK and GSPPM implementations described above, the number of activated sources depends on the symbol constellation. With GSPPM, considering all the possible SCPs, the average number of activated sources per symbol is $N_e = N_t(2^{N_t-1} + 1)/2^{N_t}$. The receiver computation complexity for SMP, SM and GSM techniques for different configurations are shown in Figure 2.14. Using an illustrative example with $N_t = 4$, $N_r = 4$ and $\mathcal{M} = 8$ bits/symbol, the FLOPs count values for each MIMO scheme is shown in the last column of Table 2.1. Clearly, the detection processes for SM and GSM are less computationally expensive compared that of SMP. While SM and GSM require 3840 and 6400 FLOPs, respectively, SMP utilizes 9984 FLOPs. The SM technique has the least number of FLOPs as it eliminates ICI by activating only one source in a given symbol period. The derivations of the FLOPs count expressions in Table 2.1 are provided in Appendix A. Furthermore, it should be noted that while ML detection has been assumed in these analyses for a fair comparison and as applied throughout this thesis, each of the MIMO schemes can also be implemented using detection algorithms with lower complexity.

MIMO technique	Bit/stmbol, $\mathcal{M}$	FLOPs count	Sample FLOPs count $(N_\text{t} = 4, N_\text{r} = 4, \mathcal{M} = 8)$
SMP	$N_\text{t} \log_2(L)$	$2^{\mathcal{M}}(2N_\text{r}N_\text{t} + 2N_\text{r} - 1)$ $= L^{N_\text{t}}\left(2N_\text{r}N_\text{t} + 2N_\text{r} - 1\right)$	9984
SM (SPPM)	$\log_2(LN_\text{t})$	$2^{\mathcal{M}}(4N_\text{r} - 1)$ $= LN_\text{t}\left(4N_\text{r} - 1\right)$	3840
GSM (GSPPM)	$N_\text{t} + \log_2(L)$	$2^{\mathcal{M}}(2N_\text{r}N_\text{e} + 2N_\text{r} - 1)$ $= 2^{N_\text{t}}L\left(2N_\text{r}N_\text{e} + 2N_\text{r} - 1\right)$	6400

Table 2.1: *Comparison of computational complexity at the receiver for different MIMO techniques. L is the size of the transmitted signal constellation, e.g. L-PPM, N_e is the average number of activated sources per symbol in GSPPM. Note that each technique can also be implemented with lower complexity detection algorithms.*
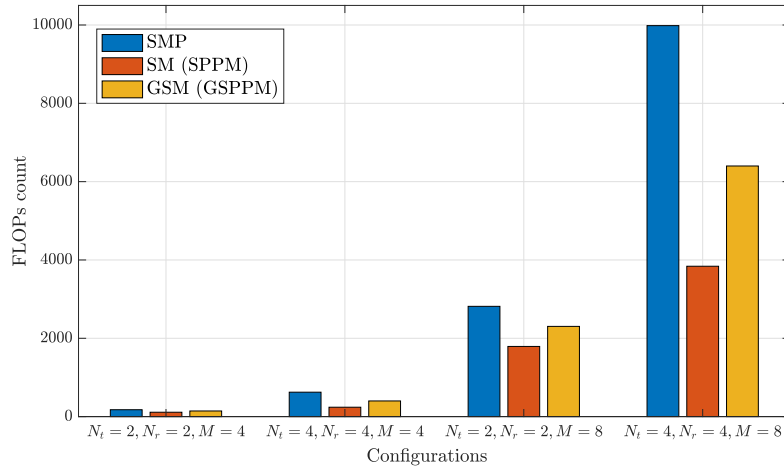
Figure 2.14: *Receiver computation complexity for SMP, SM and GSM MIMO techniques, using different configurations.*

2.5 Summary

In this chapter, the background on OWC technology has been presented. A brief account of how OWC has evolved into the spotlight of ongoing research in wireless communication is provided. The chapter also discussed the features of OWC, highlighting the advantages, challenges and promising areas of application. Moreover, the primary blocks of a typical OWC system are introduced, where the key components of the transmitter and receiver blocks were described. Besides, the propagation characteristics and modelling of the indoor optical wireless

channel has been reviewed. The geometry of the LOS and NLOS communication scenarios is defined, including the simulation of the channel impulse response based on ray-tracing algorithm. Furthermore, the chapter presented an overview of the common digital modulation format in OWC, with emphasis on pulsed modulation techniques such as OOK, PPM and PAM, as well multi-carrier modulation using OFDM. In the concluding part of the chapter, we reviewed MIMO techniques for OWC, highlighting the specific features, advantages and limitations of each technique. MIMO techniques can be used to improve the capacity and/or reliability of OWC system by designing the system to provide multiplexing gain, diversity gain, or an attractive trade-off between both. Due to the use of multiple transmit and receive elements in MIMO transmission, there is need to examine the synchronisation requirement and the impact of interference in such deployment. These will be studied in detail in subsequent chapters as outlined in Section 1.4 of the introductory chapter.

Chapter 3

Performance evaluation of optical spatial modulation in LOS channel

Optical spatial modulation (OSM) is a promising MIMO technique which provides an attractive trade-off between spatial multiplexing and diversity gains. The overall gain achieved in an OSM scheme is also dependent on the digital modulation methods used. For instance, in the PAM-based OSM scheme [97] the use of varying transmit power levels to convey additional bits offers spectral efficiency gains. However, the detection of PAM levels is susceptible to the channel states. The channel gain and the noise level can make the differentiation between the activated LED and the received power level less apparent [92]. In contrast, the optimal detector for pulse-position modulation (PPM) is less reliant on information about the channel state [105]. The optical receiver detects the transmitted symbol by determining time slot with the maximal energy. Moreover, the superior power efficiency of PPM makes it an attractive modulation technique for OWC systems. The drawback of PPM however lies in its higher bandwidth requirement due to shorter pulse duration. Within this context, PPM can be combined with OSM concept to improve spectral efficiency. Thus, PPM-based OSM schemes harness the power efficiency of PPM and the spectral efficiency gain of OSM. Furthermore, since the detection of PPM is not reliant on the channel states, the complexity of the detection algorithm for PPM-based OSM can be reduced by decomposing it into two separate processes: one to determine the transmitted PPM signal and the other to detect the activated transmitter.

In this chapter, a generalised framework for PPM-based OSM is presented using the novel GSPPM [94] scheme described in Chapter 2 as a reference. Furthermore, assuming that complete synchronisation is maintained between the transmitter and receiver, the system performance is evaluated in an indoor OWC environment with LOS characteristics. Subsequently, performance evaluation in the presence imperfect synchronisation and multipath

distortion are considered in Sections 4 and 5, respectively. By appropriately choosing the system parameters such as the number of active LEDs and whether or not digital modulation is employed, the general formulation for GSPPM is adaptable to any of the following OSM schemes: SSK, SPPM and GSSK. Thus, making a single OSM framework valid for a wide range of applications. This approach allows for flexibility in designing an OSM-MIMO system that can satisfy the requirements of the target application such as data rate, reliability (in terms of error performance) and energy efficiency.

Analytical expressions for evaluating the symbol error rate (SER) of these PPM-based OSM scheme are derived in the presence of OWC LOS channel impairments and AWGN. These derivations, which are obtained using the union bound approximations [106], match the results from computer-based simulations. Furthermore, the impact of channel gain values, i.e., the position/alignment of the LEDs and detectors, on system performance is demonstrated. We show how the individual values of the channel gains as well as the disparity between the gains affects error performance. In addition, the spectral and energy efficiencies of the four OSM scheme are compared to show the benefits and limitations of each scheme. Finally, using the SPPM scheme as a case study, the performance of PPM-based OSM technique is demonstrated experimentally. Results are presented at different data rates and under different channel conditions (LED/PD alignment).

The rest of this chapter is organised as follows: using GSPPM as a reference scheme, Section 3.1 provides a general system model for PPM-based OSM, and in Section 3.2, the theoretical error performance analyses of GSPPM and the other three OSM schemes are presented. Section 3.3 provides the analytical and simulation results of the performance evaluation of the schemes. An experimental demonstration of the SPPM as a representative scheme is reported in Section 3.4, while concluding remarks are given in Section 3.5.

3.1 System model

The system model for PPM-based OSM schemes is presented in this section. First, GSPPM is used as a reference and the process of transmitting and detecting the data symbol is described. Later, we show how the system parameters can be changed to obtain the system model of the other three OSM schemes.

3.1.1 System model of GSPPM

Using the description of GSPPM given in Chapter 2, we consider a MIMO OWC system equipped with N_t LED units at the transmitter and N_r PDs at the receiver. The number of PPM time slots in each symbol duration, L, is equal to the size of the signal constellations, while the size of the spatial constellations $N_s = 2^{N_t}$. Let $\mathcal{A}_{j,m}$, for $j \in [1, N_s]$ and $m \in [1, L]$, denote the GSPPM symbol that is transmitted by activating one or more of LEDs according to the j-th SCP to simultaneously transmit PPM signals with a pulse in the m-th time slot. The signal emitted by the activated LEDs propagates through the OWC channel to the receiver. Due to the difference in the spatial locations of the LEDs, each of them introduces a specific "channel signature" i.e., the channel gain, that makes their emitted signal unique at the receiver. The more differentiable the channel signatures are from each other, the more identifiable the signal from each LED become at the receiver [23,91]. The detection unit at the receiver exploits these unique channel signatures to retrieve the transmitted symbol. Typical of communication systems, especially in MIMO systems where a knowledge of the channel state is required, the channel gains of the N_t LEDs are assumed to be known at the receiver. This can be obtained from pilot symbols that are sent ahead of the data transmission. Based on the channel gains, the demodulator performs a ML detection to estimate the transmitted symbol.

The transmitted L-PPM waveform with a pulse of peak transmit optical power, P_t, located in m-th time slot can be defined as:

$$\phi_m(t) = P_t \operatorname{rect}\left(\frac{t - (m-1)T_c}{T_c}\right), \quad 0 \leq t \leq T \tag{3.1}$$

where T is the duration of each symbol, $T_c = T/L$ is the duration of each time slot, and the rectangular function $\operatorname{rect}(a)$ is given by:

$$\operatorname{rect}(a) = \begin{cases} 1; & \text{for } 0 \leq a < 1 \\ 0; & \text{elsewhere.} \end{cases} \tag{3.2}$$

Therefore, the $N_t \times 1$ dimensional vector of the transmitted signals for symbol $\mathcal{A}_{j,m}$ can be expressed as:

$$\mathbf{s}_{j,m}(t) = \mathbf{v}_j \phi_m(t) \tag{3.3}$$

where $\mathbf{v}_j = [v_1, \ldots, v_{N_t}]^\dagger$ is the LED activation vector that determines the indices (position) of the LEDs that will be activated if the symbol to be transmitted contains the j-th SCP. The entries of $\mathbf{v}_j$ are binary digits, with '1's' at the indices of activated LEDs, and '0's' at the indices of idle LEDs.

For symbol $\mathcal{A}_{j,m}$, the $N_r \times 1$ vector of the received electrical signal, neglecting any applied direct current (DC) bias, is therefore given by:

$$\begin{aligned} \mathbf{r}(t) &= \lambda_j R \mathbf{H} \mathbf{s}_{j,m}(t) + \eta(t) \\ &= RP_t \lambda_j \mathbf{H} \mathbf{v}_j \phi_m(t) + \eta(t), \quad 0 \leq t \leq T. \end{aligned} \tag{3.4}$$

where R is the responsivity of the PDs and λ_j is the pulse-inversion constant associated with the j-th SCP. For GSPPM, as described in Chapter 2, if the spatial bits are all zeros, then $\lambda_j = -1$, otherwise $\lambda_j = +1$. The $N_r \times N_t$ LOS MIMO channel gain matrix is denoted by $\mathbf{H}$. Considering a Silicon PIN photodetector with negligible signal shot noise and dark current [49, 107], the scalar $\eta(t)$ is the sum of the ambient light shot noise and the thermal noise in the receiver. Thus, $\eta(t)$ is modelled as independent and identically distributed (i.i.d) AWGN [26, 38, 68]. As an illustration, using a 2-LED set-up consisting of LED1 and LED2, the received electrical signal for all the N_s possible SCP is obtained as shown in Table 3.1. The $1 \times N_r$ vector $\mathbf{h}_{n_t}$ for $n_t = 1, \ldots, N_t$, denotes the n_t-th column of $\mathbf{H}$.

SCP (j)	Spatial bits	$\mathbf{v}_j^\dagger$	Activated LEDs	λ_j	$\mathbf{r}(t)$
1	00	$[1,1]$	LEDs 1 & 2	-1	$-(\mathbf{h}_1 + \mathbf{h}_2)RP_t\phi_m(t) + \eta(t)$
2	01	$[0,1]$	LED 1	1	$\mathbf{h}_1 RP_t\phi_m(t) + \eta(t)$
3	10	$[1,0]$	LED 2	1	$\mathbf{h}_2 RP_t\phi_m(t) + \eta(t)$
4	11	$[1,1]$	LEDs 1 & 2	1	$(\mathbf{h}_1 + \mathbf{h}_2)RP_t\phi_m(t) + \eta(t)$

Table 3.1: *LED Activation and received electrical signal for a 2-LED GSPPM scheme*

At the receiver, a matched filter (MF) architecture is employed, where the applied unit energy receive filter is given by:

$$\alpha(t) = \frac{1}{\sqrt{T_c}} \text{rect}\left(\frac{t}{T_c}\right), \quad 0 \leq t \leq T_c. \tag{3.5}$$

The MF outputs of the PDs are sampled at the chip rate $1/T_c$ to obtain the samples of the

received PPM signal in each time slot. Thus, the $N_r \times L$ array of the MF outputs in each time slot and for all PDs is written as:

$$\mathbf{Y} = \lambda_j \mathbf{H} \mathbf{v}_j \mathbf{x}_m + \mathbf{Z}. \tag{3.6}$$

The vector $\mathbf{x}_m = [x_{m,\ell}]$ for $\ell = 1, \ldots, L$, is a $1 \times L$ dimensional vector whose entries are given by:

$$x_{m,\ell} = \begin{cases} RP_t \sqrt{T_c}; & \text{if } \ell = m \\ 0 ; & \text{otherwise.} \end{cases} \tag{3.7}$$

$\mathbf{Z}$ is the $N_r \times L$ dimensional noise matrix whose entries are i.i.d Gaussian variables with variance $\sigma_z^2 = \frac{N_0}{2}$, where N_0 represents the one-sided noise power spectral density.

Based on the ML criterion, the estimate of the transmitted symbol, $\widehat{\mathcal{A}}_{\hat{j},\hat{m}}$, is obtained from the combination of the pulse position and the SCP which gives the minimum Euclidean distance from the received signal [92, 94]. That is,

$$\widehat{\mathcal{A}}_{\hat{j},\hat{m}} = [\hat{j}, \hat{m}] = \arg \max_{j,m} f(\mathbf{Y}|\lambda_j \mathbf{v}_j \mathbf{x}_m, \mathbf{H})$$

$$= \arg \min_{j,m} \mathcal{D}(\mathbf{Y}, \lambda_j \mathbf{H} \mathbf{v}_j \mathbf{x}_m). \tag{3.8}$$

The conditional probability density function (PDF), $f(\mathbf{Y}|\lambda_j \mathbf{v}_j \mathbf{x}_m, \mathbf{H})$ is defined as:

$$f(\mathbf{Y}|\lambda_j \mathbf{v}_j \mathbf{x}_m, \mathbf{H}) = \frac{1}{(2\pi\sigma_n^2)^{N_r L/2}} \exp\left(-\frac{\|\mathbf{Y} - \lambda_j \mathbf{H} \mathbf{v}_j \mathbf{x}_m\|_F^2}{2\sigma_n^2}\right), \tag{3.9}$$

where $\|\cdot\|_F$ denotes the Frobenius (matrix) norm, and the distance metric, $\mathcal{D}(\mathbf{Y}, \lambda_j \mathbf{H} \mathbf{v}_j \mathbf{x}_m)$, is expressed as:

$$\mathcal{D}(\mathbf{Y}, \lambda_j \mathbf{H} \mathbf{v}_j \mathbf{x}_m) = \|\mathbf{Y} - \lambda_j \mathbf{H} \mathbf{v}_j \mathbf{x}_m\|_F^2. \tag{3.10}$$

3.1.2 System model of SSK, SPPM and GSSK

The system models for SSK, GSSK and SPPM are similar to that of GSPPM described above, and they can be obtained by re-defining certain system parameters. Based on the description of each scheme in Chapter 2, a summary of how the system parameters are defined for each

scheme is provided in Table 3.2. The pulse-inversion constants, λ, is employed only in GSPPM, hence it is equal to one for all other schemes. As an example, a GSPPM scheme can be converted to a GSSK scheme if the signal modulation, i.e. PPM, in GSPPM is removed by setting $L=1$. Additionally, a return-to-zero pulse pattern is used for the transmitted signal. The pulse duration T_c depends on the SCP of the data symbol, and this is defined in terms of the duty cycle, τ. Similarly, the SPPM scheme can be obtained from the GSPPM scheme if only one LEDs is activated during any symbol duration. As such, in SPPM, the LED activation vector, $\mathbf{v}$, will have only one non-zero entry which will be positioned at the index of the activated LED.

Scheme	N_s	L	$\mathcal{M}$ (bits/symbol)	T_c	λ
SSK	N_t	1	$\log_2(N_t)$	T	1
GSSK	2^{N_t}	1	N_t	$\{\tau T, (1-\tau)T\}$	1
SPPM	N_t	L	$\log_2(LN_t)$	T/L	1
GSPPM	2^{N_t}	L	$N_t + \log_2(L)$	T/L	± 1

Table 3.2: *Summary of system parameters for the different OSM schemes*

3.2 Error performance analysis

Following the detection process in Section 3.1, the error performance analyses of the four variants of OSM technique are formulated in this section. First, the symbol error probability of GSPPM is derived, then the analysis is extended to obtain the corresponding expressions for the error probability of SSK, GSSK and SPPM.

The error performance analysis involves evaluating the probability of a correct symbol detection, $P_{\text{c,sym}}^{\text{GSPPM}}$, from which the symbol error probability can then be derived as [92, 94]:

$$P_{\text{e,sym}}^{\text{GSPPM}} = 1 - P_{\text{c,sym}}^{\text{GSPPM}} \tag{3.11}$$

Considering a symbol which is transmitted by activating the LEDs based on SCP j, with the pulse in slot m, the symbol is correctly detected if both the pulse position and the SCP are determined correctly. Thus, the probability of correct symbol detection is given by

$$\begin{aligned} P_{\text{c,sym}}^{\text{GSPPM}} &= P_{\text{c,scp}}^{\text{GSPPM}} \times P_{\text{c,ppm}}^{\text{GSPPM}} \\ &= \mathbb{P}(\hat{j} = j | \hat{m} = m) \times \mathbb{P}(\hat{m} = m) \end{aligned} \tag{3.12}$$

where $P_{\text{c,ppm}}^{\text{GSPPM}} = \mathbb{P}(\hat{m} = m)$, is the probability of a correctly detected pulse position, and $P_{\text{c,scp}}^{\text{GSPPM}} = \mathbb{P}(\hat{j} = j | \hat{m} = m)$, is the probability of correctly detecting the SCP given that the pulse position has been correctly detected. The notation $\mathbb{P}(\cdot)$ represents the probability of occurrence. The expressions for $P_{\text{c,scp}}^{\text{GSPPM}}$ and $P_{\text{c,ppm}}^{\text{GSPPM}}$ are derived as follows.

3.2.1 Probability of correct SCP detection in GSPPM

In order to obtain $P_{\text{c,scp}}^{\text{GSPPM}}$, first, the pairwise error probabilities (PEP) is evaluated. For a symbol which is transmitted by activating the LEDs based on SCP j, with the pulse in slot m, the pairwise error probability (PEP) that the receiver decides in favour of SCP k instead of j, $j \neq k$, is given by:

$$\text{PEP}_m^{j \to k} = \mathbb{P}\left(\mathcal{D}(\mathbf{Y}, \lambda_j \mathbf{H} \mathbf{v}_j \mathbf{x}_m) > \mathcal{D}(\mathbf{Y}, \lambda_k \mathbf{H} \mathbf{v}_k \mathbf{x}_m)\right) \tag{3.13}$$

By applying (3.6) and (3.7) in (3.10), we obtain:

$$\mathcal{D}(\mathbf{Y}, \lambda_j \mathbf{H} \mathbf{v}_j \mathbf{x}_m) = \|\lambda_j \mathbf{H} \mathbf{v}_j \mathbf{x}_m + \mathbf{Z} - \lambda_j \mathbf{H} \mathbf{v}_j \mathbf{x}_m\|_{\text{F}}^2 = \|\mathbf{Z}\|_{\text{F}}^2 \tag{3.14}$$

Similarly,

$$\begin{aligned}
\mathcal{D}(\mathbf{Y}, \lambda_k \mathbf{H} \mathbf{v}_k \mathbf{x}_m) &= \|\lambda_j \mathbf{H} \mathbf{v}_j \mathbf{x}_m + \mathbf{Z} - \lambda_k \mathbf{H} \mathbf{v}_k \mathbf{x}_m\|_{\text{F}}^2 \\
&= \sum_{\substack{\ell=1 \\ \ell \neq m}}^{L} \|\mathbf{z}_\ell\|^2 + \left\|\mathbf{z}_m + (\lambda_j \mathbf{H} \mathbf{v}_j - \lambda_k \mathbf{H} \mathbf{v}_k) R P_{\text{t}} \sqrt{T_{\text{c}}}\right\|^2.
\end{aligned} \tag{3.15}$$

where $\mathbf{z}_\ell$ is the ℓ-th column of the noise matrix $\mathbf{Z}$. By applying (3.14) and (3.15) in (3.13), we obtain:

$$\begin{aligned}
\text{PEP}_m^{j \to k} &= \mathbb{P}\left(\mathbf{z}_m^\dagger (\lambda_k \mathbf{H} \mathbf{v}_k - \lambda_j \mathbf{H} \mathbf{v}_j) > \frac{1}{2}(R P_{\text{t}} \sqrt{T_{\text{c}}}) \|\lambda_j \mathbf{H} \mathbf{v}_j - \lambda_k \mathbf{H} \mathbf{v}_k\|^2\right) \\
&= Q\left(\|\lambda_k \mathbf{H} \mathbf{v}_k - \lambda_j \mathbf{H} \mathbf{v}_j\| \sqrt{\frac{\gamma_{\text{s}}}{2}}\right)
\end{aligned} \tag{3.16}$$

where the electrical signal-to-noise ratio (SNR), $\gamma_{\text{s}} = \frac{E_{\text{s}}}{N_0}$, energy per symbols $E_{\text{s}} = R P_{\text{t}} \sqrt{T_{\text{c}}}$, and the Q-function, $Q(\cdot)$ is defined as $Q(a) = \frac{1}{2\pi} \int_a^\infty \exp\left(-\frac{u^2}{2}\right) \mathrm{d}u$. The variable $\mathbf{z}_m^\dagger (\lambda_j \mathbf{H} \mathbf{v}_j - \lambda_k \mathbf{H} \mathbf{v}_k)$ is a Gaussian variable with zero mean and a variance of $\frac{1}{2} N_0 \|\lambda_k \mathbf{H} \mathbf{v}_k - \lambda_j \mathbf{H} \mathbf{v}_j\|^2$.

For K equally likely SCPs, using the union bound approximation [106], the probability of error in detecting the SCP j, is given by:

$$P_{\text{e,scp}}^{\text{GSPPM}}(j) \leq \sum_{\substack{k=1 \\ k \neq j}}^{N_{\text{s}}} \text{PEP}_m^{j \to k} = \sum_{\substack{k=1 \\ k \neq j}}^{N_{\text{s}}} Q\left(\|\lambda_k \mathbf{H} \mathbf{v}_k - \lambda_j \mathbf{H} \mathbf{v}_j\| \sqrt{\frac{\gamma_{\text{s}}}{2}}\right) \tag{3.17}$$

Therefore, the probability of correctly detecting SCP j, conditioned on the pulse occupying time slot m, is expressed as:

$$P_{\text{c,scp}}^{\text{GSPPM}}(j) \approx 1 - P_{\text{e,scp}}^{\text{GSPPM}}(j) = 1 - \sum_{\substack{k=1 \\ k \neq j}}^{N_{\text{s}}} Q\left(\|\lambda_k \mathbf{H} \mathbf{v}_k - \lambda_j \mathbf{H} \mathbf{v}_j\| \sqrt{\frac{\gamma_{\text{s}}}{2}}\right) \tag{3.18}$$

3.2.2 Probability of correct pulse position detection in GSPPM

Again, for a symbol which is sent by activating LEDs using SCP j, to transmit a pulse in slot m of the PPM signal, and the PEP that the receiver decides in favour of slot q instead of slot m, $m \neq q$, is given by:

$$\text{PEP}_{m \to q}^{j} = \mathbb{P}\left(\mathcal{D}(\mathbf{Y}, \lambda_j \mathbf{H} \mathbf{v}_j \mathbf{x}_m) > \mathcal{D}(\mathbf{Y}, \lambda_j \mathbf{H} \mathbf{v}_j \mathbf{x}_q)\right) \tag{3.19}$$

where $\mathcal{D}(\mathbf{Y}, \lambda_j \mathbf{H} \mathbf{v}_j \mathbf{x}_m)$ is given by (3.14), while $\mathcal{D}(\mathbf{Y}, \lambda_j \mathbf{H} \mathbf{v}_j \mathbf{x}_q)$ is expressed as

$$\begin{aligned}
\mathcal{D}(\mathbf{Y}, \lambda_j \mathbf{H} \mathbf{v}_j \mathbf{x}_q) &= \|\lambda_j \mathbf{H} \mathbf{v}_j \mathbf{x}_m + \mathbf{Z} - \lambda_j \mathbf{H} \mathbf{v}_j \mathbf{x}_q\|_{\text{F}}^2 \\
&= \sum_{\substack{\ell=1 \\ \ell \neq \{m,q\}}}^{L} \|\mathbf{z}_\ell\|^2 + \left\|\lambda_j \mathbf{H} \mathbf{v}_j R P_{\text{t}} \sqrt{T_{\text{c}}} + \mathbf{z}_m\right\|^2 + \left\|\mathbf{z}_q - \lambda_j \mathbf{H} \mathbf{v}_j R P_{\text{t}} \sqrt{T_{\text{c}}}\right\|^2.
\end{aligned} \tag{3.20}$$

By using (3.14) and (3.20) in (3.19), we obtain:

$$\begin{aligned}
\text{PEP}_{m \to q}^{j} &= \mathbb{P}\left((\mathbf{z}_q - \mathbf{z}_m)^\dagger \lambda_j \mathbf{H} \mathbf{v}_j > R P_{\text{t}} \sqrt{T_{\text{c}}} \|\lambda_j \mathbf{H} \mathbf{v}_j\|^2\right) \\
&= Q\left(\|\lambda_j \mathbf{H} \mathbf{v}_j\| \sqrt{\gamma_{\text{s}}}\right)
\end{aligned} \tag{3.21}$$

where $(\mathbf{z}_q - \mathbf{z}_m)^\dagger \lambda_j \mathbf{H} \mathbf{v}_j$ is a zero-mean Gaussian variable with a variance of $N_0 \|\lambda_j \mathbf{H} \mathbf{v}_j\|^2$. For L equiprobable pulse positions, the probability for correct pulse position detection for the

transmitted symbol with SCP j, is given by:

$$P_{\text{c,ppm}}^{\text{GSPPM}}(j) \;=\; 1 \;-\; (L-1)\, Q\left(\|\lambda_j \mathbf{H} \mathbf{v}_j\| \sqrt{\gamma_{\text{s}}}\right). \tag{3.22}$$

By combining (3.18) with (3.22) according to (3.11) and (3.12), the error probability for the symbol with SCP j and PPM time slot m, is obtained as:

$$P_{\text{e,sym}}^{\text{GSPPM}}(j) \;\le\; 1 \;-\; \left[1 \;-\; \sum_{\substack{k=1 \\ k \ne j}}^{N_{\text{s}}} Q\left(\|\lambda_k \mathbf{H}\mathbf{v}_k - \lambda_j \mathbf{H}\mathbf{v}_j\|\sqrt{\frac{\gamma_{\text{s}}}{2}}\right)\right]$$
$$\times \left[1 \;-\; (L-1)Q\left(\|\lambda_j \mathbf{H}\mathbf{v}_j\|\sqrt{\gamma_{\text{s}}}\right)\right]. \tag{3.23}$$

Now, the average symbol error probability for the GSPPM scheme in LOS channel is evaluated from the expectation of the $P_{\text{e,sym}}^{\text{GSPPM}}(j)$ as:

$$\begin{aligned}
P_{\text{e,sym}}^{\text{GSPPM}} \;=\;&\; \mathbb{E}\left[P_{\text{e,sym}}^{\text{GSPPM}}(j)\right] \;=\; \frac{1}{N_{\text{s}}} \sum_{j=1}^{N_{\text{s}}} P_{\text{e,sym}}^{\text{GSPPM}}(j) \\
\le\;&\; 1 - \frac{1}{N_{\text{s}}} \sum_{j=1}^{N_{\text{s}}} \left[\left[1 \;-\; \sum_{\substack{k=1 \\ k \ne j}}^{N_{\text{s}}} Q\left(\|\lambda_k \mathbf{H}\mathbf{v}_k - \lambda_j \mathbf{H}\mathbf{v}_j\|\sqrt{\frac{\gamma_{\text{s}}}{2}}\right)\right] \right. \\
&\; \left. \times \left[1 \;-\; (L-1)Q\left(\|\lambda_j \mathbf{H}\mathbf{v}_j\|\sqrt{\gamma_{\text{s}}}\right)\right]\right]
\end{aligned} \tag{3.24}$$

where $\mathbb{E}\left[\,\cdot\,\right]$ denotes the expectation operator, and $N_{\text{s}} = 2^{N_{\text{t}}}$ for the GSPPM scheme.

The symbol error probability given by (3.24) can also be approximated by assuming the independent detection of the pulse position and SCP for the transmitted symbol. This approach involves independently evaluating the probability of correct pulse position and SCP detection. The approach is demonstrated in Appendix B and a similar one can be applied to the error performance analyses of OSM schemes in the subsequent Chapters 4 and 5.

3.2.3 Error probability for SSK

Using Table 3.2, the symbol error probability of the SSK scheme, $P_{\text{e,sym}}^{\text{SSK}}$, is obtained by substituting $L=1$, $N_{\text{s}}=N_{\text{t}}$, $T_{\text{c}}=T$ and $\lambda_j=1, \forall j$, in (3.24). Furthermore, since in SSK only

one LED is activated during any symbol duration, then for the j-th SCP, the vector $\mathbf{v}_j$ $\forall j$, has only one non-zero entry. This non-zero entry is positioned at the index of the activated j-th LED. Hence, the terms $\mathbf{Hv}_k$ and $\mathbf{Hv}_j$ in (3.24) yield $\mathbf{h}_k$ and $\mathbf{h}_j$, respectively, where $\mathbf{h}_k$ and $\mathbf{h}_j$, are respectively the k-th and j-th columns of channel matrix $\mathbf{H}$. Therefore,

$$P_{\text{e,sym}}^{\text{SSK}} \leq \frac{1}{N_\text{t}} \sum_{j=1}^{N_\text{t}} \sum_{\substack{k=1 \\ k \neq j}}^{N_\text{t}} Q\left(\|\mathbf{h}_k - \mathbf{h}_j\|\sqrt{\frac{\gamma_\text{s}}{2}}\right). \tag{3.25}$$

3.2.4 Error probability for GSSK

For a GSSK scheme with $\tau = 1$, according to Table 3.2, the symbol error probability of GSSK, $P_{\text{e,sym}}^{\text{GSSK}}$, is obtained by substituting the following in (3.24): $L = 1$, $N_\text{s} = 2^{N_\text{t}}$, $T_\text{c} = T$ and $\lambda_j = 1, \forall j$. Hence,

$$P_{\text{e,sym}}^{\text{GSSK}} \leq \frac{1}{2^{N_\text{t}}} \sum_{j=1}^{2^{N_\text{t}}} \sum_{\substack{k=1 \\ k \neq j}}^{2^{N_\text{t}}} Q\left(\|\mathbf{Hv}_k - \mathbf{Hv}_j\|\sqrt{\frac{\gamma_\text{s}}{2}}\right) \tag{3.26}$$

Since the symbol information is encoded solely on the SCP in GSSK, then the symbol error probability of GSSK in (3.26) is equivalent to the probability of error in detecting the SCP of GSPPM in (3.17).

3.2.5 Error probability for SPPM

The symbol error probability of an SPPM scheme, $P_{\text{e,sym}}^{\text{SPPM}}$, is obtained from (3.24) by applying the following: $N_\text{s} = N_\text{t}$, and $\lambda_j = 1, \forall j$. Also, since only a single LED is activated in any given symbol duration, then $\mathbf{h}_j = \mathbf{Hv}_j$, $\forall j$. Therefore,

$$\begin{aligned}
P_{\text{e,sym}}^{\text{SPPM}} \leq 1 &- \frac{1}{N_\text{t}} \sum_{j=1}^{N_\text{t}} \left[\left[1 - \sum_{\substack{k=1 \\ k \neq j}}^{N_\text{t}} Q\left(\|\mathbf{h}_k - \mathbf{h}_j\|\sqrt{\frac{\gamma_\text{s}}{2}}\right)\right] \right. \\
&\left. \times \left[1 - (L-1) \times Q\left(\|\mathbf{h}_j\|\sqrt{\gamma_\text{s}}\right)\right]\right]. \tag{3.27}
\end{aligned}$$

3.3 Simulation and analytical results

This section presents the analytical and simulation results of the performance evaluation of the OSM schemes considered in this chapter. The simulation procedure is outlined in Algorithm 1 of Appendix C.1. An OWC system with $N_r = 4$ PDs and $N_t = 4$ LEDs is considered in this evaluation. For the sake of simplicity, the responsivity of the PD, R is assumed to be 1 A/W in all the simulation results presented in this thesis. The channel path gains are obtained from the simulation of the indoor OWC channel as described in Chapter 2. The simulation parameters are given in Table 3.3. It is assumed that the LEDs as well as the PDs are in close proximity such that only a small path difference exist between the transmitter-receiver MIMO links. Consequently, the OWC links represent LOS channels without any temporal dispersion. The normalized channel gain matrix for the 4×4 MIMO setup is:

$$\mathbf{H} = \begin{bmatrix} 0.8847 & 0.4298 & 0.3587 & 0.2001 \\ 0.9314 & 0.4592 & 0.3736 & 0.2113 \\ 0.9491 & 0.4556 & 0.3879 & 0.2140 \\ 1.0000 & 0.4872 & 0.4043 & 0.2262 \end{bmatrix} \tag{3.28}$$

Parameter	Value	Parameter	Value
Room dimension	$(5 \times 5 \times 3)$ m	PD Area (cm^2)	1.0
LED half angle, $\Phi_{1/2}$	$60°$	PD field of view	$70°$
LED separation	0.6 m	PD separation	0.05 m
LEDs orientation vector, $\hat{\mathbf{u}}_s$ (facing downward)	$[0, 0, -1]$	PDs orientation vector, $\hat{\mathbf{u}}_r$ (facing upward)	$[0, 0, 1]$
LEDs' coordinates (m)	(2.2,2.2,3), (2.2,2.8,3), (2.8,2.2,3), (2.8,2.8,3)		
PDs' coordinates (m)	(0.675,1.075,0.8), (0.675,1.125,0.8) (0.725,1.075,0.8), (0.725,1.125,0.8)		

Table 3.3: *OWC channel simulation parameters for OSM in LOS environment.*

3.3.1 Symbol error rate performance

The error performance plots from both the theoretical analysis and simulations are obtained by plotting the achieved SER against the SNR per bit $\gamma_b = \gamma_s/\mathcal{M}$, where $\mathcal{M}$ is the number of bits per symbol. The SER plots for GSPPM are shown in Figure 3.1 using $N_t = \{2, 4\}$ and $L = \{2, 8\}$. These error performance plots show that the analytical bound in (3.24) is very tight on the simulation results. The slight deviation observed at SER > 0.1 (for $N_t = 4$) is due to

the union bound techniques used in the analysis which can permit an error rate greater than 1. Moreover, Figure 3.1 shows that as L increased from 2 to 8, the SNR required to achieve an SER of 10^{-6} reduced by about 2 dB and 1.5 dB for $N_\mathrm{t} = 2$ and $N_\mathrm{t} = 4$, respectively. This highlights the power efficiency benefit of PPM that is harnessed in GSPPM. Additionally, using $L = 8$, the SNR required to achieve an SER of 10^{-6} is reduced by about 14 dB for $N_\mathrm{t} = 2$ compared to $N_\mathrm{t} = 4$. This is expected because using more LEDs results in a denser spatial constellation and a less disperse channel gain values. Thus, a higher SNR is required to reduce the error rates. We however note that using higher number of LEDs increases the spectral efficiency of the systems by increasing the number of bits transmitted per symbol. By varying the number of LEDs and PPM time slots, an attractive trade-off between spectral and energy efficiencies can be achieved in GSPPM. Similar performance trends to GSPPM are obtained for SPPM, GSSK and SSK. For instance, the SER plots for SPPM is shown in Figure 3.2. As in the case of GSPPM, the analytical expression for the SER of SPPM in (3.27) also gives tight upper bound on the simulation results.
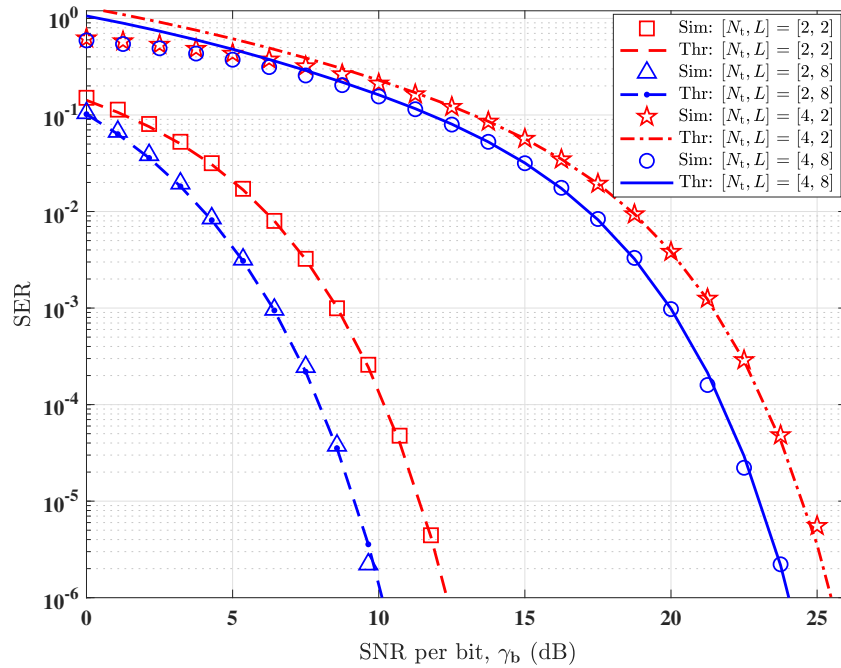
Figure 3.1: *Error performance of GSPPM, $N_\mathrm{t} = \{2, 4\}$ and $L = \{2, 8\}$. Sim: Simulation, Thr: Theory*
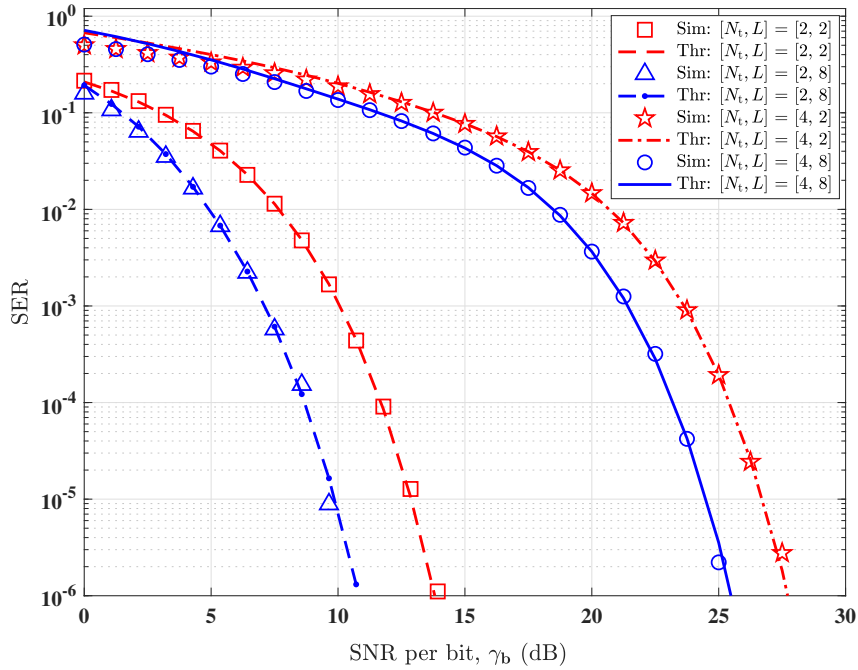
Figure 3.2: *Error performance of SPPM, $N_\mathrm{t} = \{2, 4\}$ and $L = \{2, 8\}$. Sim: Simulation, Thr: Theory*

3.3.2 Impact of channel gain on performance

Given that SM is predicated on the disparity of channel gain values for the spatially separated LEDs, having a wide difference between the channel gains should naturally connote a better error performance. However, a wide disparity in channel gain values may also imply smaller channel gain values for some LEDs. This will result in a reduction in the received SNR and consequently a worse error performance. Using the SPPM as a case study, the impact of channel gains on the performance of OSM technique is illustrated in Figure 3.3. To show how the individual values of the channel gain affect performance, we consider a pair of LEDs at a time using $L = 2$ and $N_\mathrm{r} = 1$, i.e. the first row of matrix **H** in (3.28). The error performance plots for different channel gain values (LED/PD position/alignment) are depicted in Figure 3.3. Also, Table 3.4 provides a summary of the channel gain values of the LED pairs as well as the difference between the channel gain of each pair, Δh, and the SNR required to achieve SER of 10^{-6}. It is observed that the smaller the value of Δh, the higher the SNR required to achieve a given SER. For instance, to achieve an SER of 10^{-6} the pair LEDs-$\{1, 2\}$ with $\Delta h = 0.4549$ requires about 6.5 dB, 9.5 dB and 16.5 dB less than the pairs
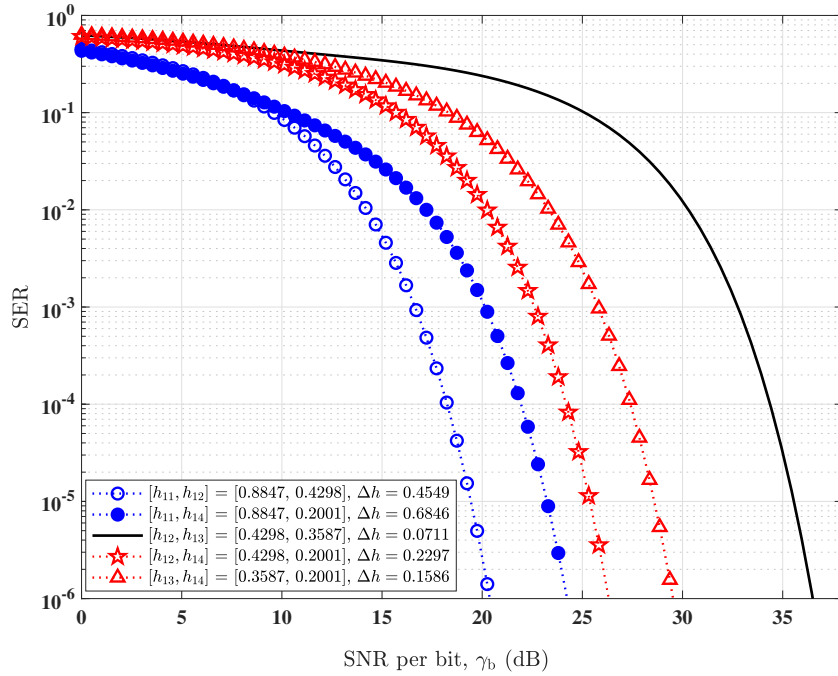
Figure 3.3: *Impact of channel gain values (LED/PD alignment) on the error performance of SPPM. $N_t = 2$, $L = 2$. Channel gains: $\{h_{1,i}\}_{i=1}^{N_t} = [0.8847, 0.4298, 0.3587, 0.2001]$.*

LED pair	Channel gain values	Δh	γ_b (dB) $\left(\text{@ SER} = 10^{-6}\right)$
LEDs-$\{1, 2\}$	$[h_{11}, h_{12}] = [0.8847, 0.4298]$	0.4549	20.0
LEDs-$\{1, 4\}$	$[h_{11}, h_{14}] = [0.8847, 0.2001]$	0.6846	24.0
LEDs-$\{2, 3\}$	$[h_{12}, h_{13}] = [0.4298, 0.3587]$	0.0711	36.5
LEDs-$\{2, 4\}$	$[h_{12}, h_{14}] = [0.4298, 0.2001]$	0.2297	26.5
LEDs-$\{3, 4\}$	$[h_{13}, h_{14}] = [0.3587, 0.2001]$	0.1586	29.5

Table 3.4: *Summary of the channel gain values of the LED pairs, the difference between the channel gain of each pair, Δh, and the SNR required to achieve a representative SER of 10^{-6}.*

LEDs-$\{2,4\}$ ($\Delta h = 0.2297$), LEDs-$\{3,4\}$ ($\Delta h = 0.1586$) and LEDs-$\{2,3\}$ ($\Delta h = 0.0711$), respectively. However, according to (3.27), the SER of SPPM also depends on the absolute value of the individual channel gains. This can be seen in the case of LEDs-$\{1,2\}$ and LEDs-$\{1,4\}$, where the former LED pair performs better than the latter even though the latter pair has a higher value of Δh. This particularly important at higher SNR values as shown in the SER plots of Figure 3.3.

To further illustrate the impact of channel gain values, a pair of normalised channel gain values $[h_A, h_B]$ is considered. We set $h_A = 1$, and the value of h_B is varied between 0 and 1. Thus, as h_B increases, the values of $\Delta h = (h_A - h_B)$ decreases. In Figure 3.4, for SSK, SPPM, GSSK, and GSPPM, the SER achieved at a representative SNR, $\gamma_b = 20$ dB, is plotted against the value of h_B. For SSK, as h_B increases and Δh decreases, SER performance becomes worse.
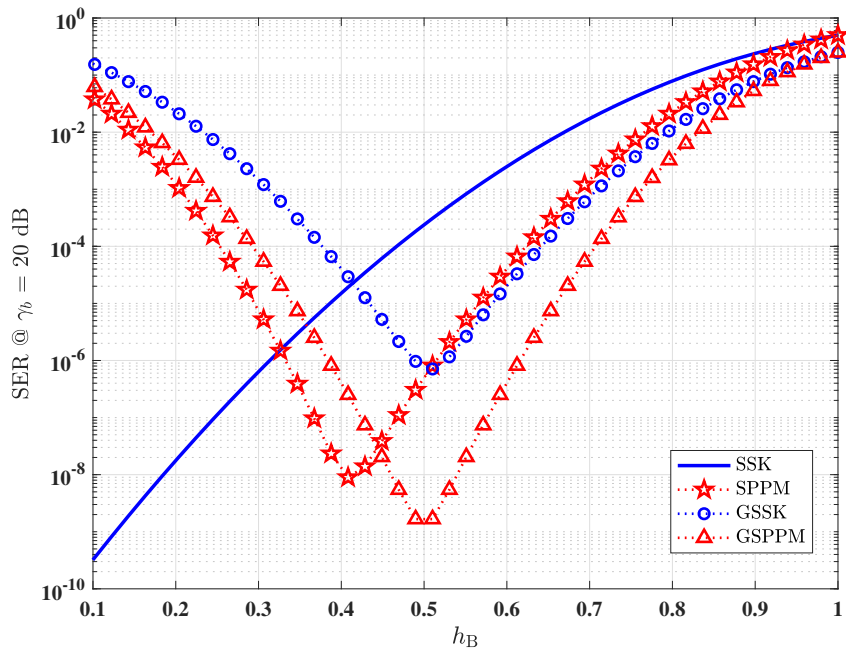
Figure 3.4: *Impact of channel gain values and disparity on the error performance of OSM schemes. $N_t = 2$, $L = 2$. Channel gains: $h_A = 1$*

This is expected since symbol detection in SSK is dependent on the disparity of the channel gains but not on the individual values of the channel gains as shown by (3.25). On the contrary, for SPPM, as h_B increases from 0 to 0.4, Δh decreases and the SER becomes smaller. This is because increasing the value of h_B also increases the effective SNR which aids the correct detection of the transmitted digital modulation i.e., the PPM signal. As h_B increases from 0.4 to

1, while the effective SNR becomes higher, the value of Δh also reduces. This makes the LED indices (path gain) becomes less differentiable at the receiver, and thus the SER grows higher. Similar trend is observed in the plots for GSSK and GSPPM. In particular, for GSSK and GSPPM, the figure shows that the lowest SER is achieved when $h_{\mathrm{B}} = 0.5$. This corresponds to a channel condition in which the spatial constellation points (i.e., the associated channel gain values) are evenly spaced-out at the receiver. For instance, with $[h_{\mathrm{A}}, h_{\mathrm{B}}] = [1, 0.5]$, using Table 3.1, the possible channel gain values for the SCPs are: $\{1.5, 1.0, 0.5\}$. These results show that while SER of SPPM, GSSK and GSPPM are dependent on both Δh and the individual values of the channel gains, that of SSK is influenced by only the value of Δh. The information is useful when setting the alignment of the LEDs and PDs for optimal system performance.

3.3.3 Performance comparison of OSM schemes

A performance comparison of the different OSM schemes considered in this chapter is provided in Table 3.5. These schemes are compared in terms of the average transmitted optical power P_{ave}, spectral efficiency, R_{spec} (bit/s/Hz), and the number of bits per symbol, $\mathcal{M}$. Spectral efficiency is defined as the ratio of the bit rate to the bandwidth requirement of the scheme, where bandwidth requirement is equivalent to the reciprocal of the pulse duration in each scheme. From this table, the superior spectral efficiency of GSSK over the other OSM schemes is obvious. Although GSPPM transmits more bits/symbol compared to GSSK, the use of PPM increases the bandwidth requirement due to shorter pulse duration. Hence, the reason for the lower value of R_{spec} for GSPPM compared to GSSK. Similar explanation holds for the comparison SPPM with SSK. However, the shorter pulse duration in GSPPM and SPPM also implies that smaller average transmitted optical power is used compared to GSSK and SSK. Hence, what GSPPM and SPPM suffers in spectral efficiency, is gained in terms of energy efficiency. Furthermore, the schemes are compared in terms of energy efficiency in Figure 3.5, where energy efficiency is expressed in terms of the SNR required to achieve an illustrative SER of 10^{-6}. For a fair comparison, all the OSM schemes are implemented with the same P_{ave} as that of GSPPM for the corresponding values of L - number of PPM slots. Using $N_{\mathrm{t}} = 4, N_{\mathrm{r}} = 4$, the SNR at SER $= 10^{-6}$ is plotted in Figure 3.5. This result shows that GSSK and SSK are less energy efficient when compared with SPPM and GSPPM. The SNR requirement of GSSK for $L = 4$ exceeds those of SPPM and GSPPM by up to 18 dB and 13

dB, respectively. This can be attributed to the energy efficiency benefit that PPM adds to both SPPM and GSPPM.

OSM Scheme	Bit/symbol, $\mathcal{M}$	R_{spec} (bit/s/Hz)	P_{ave}
SSK	$\log_2(N_{\text{t}})$	$\log_2(N_{\text{t}})$	P_{t}
SPPM	$\log_2(LN_{\text{t}})$	$\frac{1}{L}\log_2(LN_{\text{t}})$	$\frac{P_{\text{t}}}{L}$
GSSK	N_{t}	N_{t}	$N_{\text{t}}P_{\text{t}}\left(\frac{\tau}{2} + \frac{1-\tau}{2^{N_{\text{t}}}}\right)$
GSPPM	$N_{\text{t}} + \log_2(L)$	$\frac{1}{L}(N_{\text{t}} + \log_2(L))$	$\frac{N_{\text{t}}P_{\text{t}}}{L}\left(\frac{1}{2} + \frac{1}{2^{N_{\text{t}}}}\right)$

Table 3.5: *Comparison of OSM schemes in terms of bit per symbol $\mathcal{M}$, spectral efficiency R_{spec} and average optical power P_{ave}.*

Together, Table 3.5 and Figure 3.5 therefore, show clearly how the SPPM and GSPPM combine the energy efficiency of the PPM with the spectral efficiency and low complexity of SM to provide an attractive performance trade-offs. This permits a flexible implementation based on the data rate and error performance requirements of the target application. For instance, in wireless sensor networks which are constrained by energy resource and processing capacity, GSPPM or SPPM with energy efficiency and improved spectral efficiency (over PPM) are a viable technique. For applications in VLC, where there is less constraint on the energy as the LEDs are also used for the illumination purposes, the GSSK scheme with its high spectral efficiency can be used to achieve high throughput.

3.4 Experimental demonstration of OSM technique

This experimental demonstration of the OSM MIMO technique is conducted using the SPPM scheme as a case study. The performance of SPPM as viable modulation technique for OWC is demonstrated at varying data rates.

3.4.1 Experimental setup

The experimental OWC link consists of 2 LEDs and a single PD over a distance of one metre as shown in Figure 3.6. Each LED is driven at a maximum average drive current of 20mA (i.e. maximum average consumed power of 76mW). The coordinates of two LEDs in centimetres are (0,0) and (0,30), respectively, while that of the receiver is (100,15) [108]. The transmission signal is generated by a vector signal generator (Keysight E4428C) which is
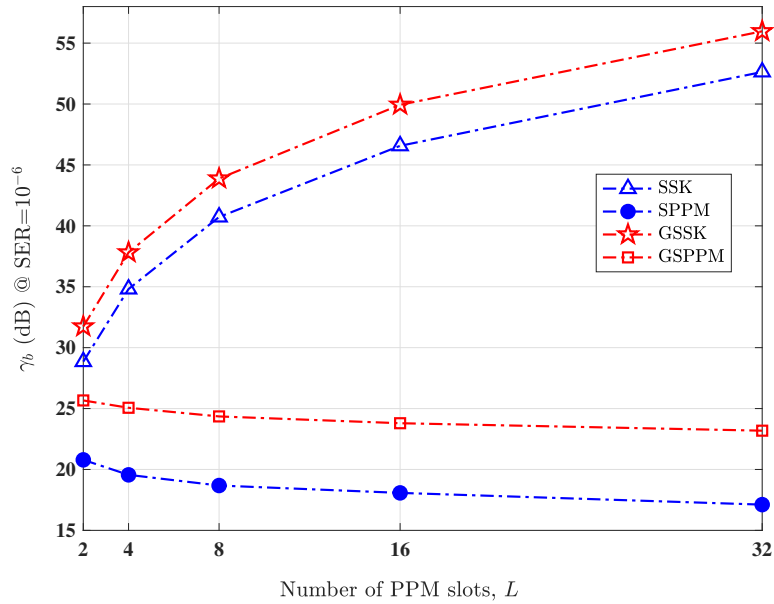
Figure 3.5: *Energy efficiency comparison of SSK, SPPM, GSSK and GSPPM.* $N_\mathrm{t} = 4, N_\mathrm{r} = 4$.

controlled via MATLAB software installed on a personal computer. The signal from the vector signal generator is routed through its input ports to drive two infrared LEDs (SFH 4550). The receiver consist of a PIN-PD (S6967), a trans-impedance amplifier (AD8015), and a two pole Sallen Key configured low pass filter which is used to limit noise and eliminate out of band signals. The received signal strength is enhanced by a 13.9 dB post-detection amplifier. The output of the receiver is captured on an oscilloscope (MSOX2024A) from which the acquired data is fed back into MATLAB software for offline processing. Finally, the channel path gains are estimated using known channel estimation symbols, and the transmitted data symbols are estimated based on the ML criterion described in Section 3.1.

A sample of the received signal is shown in Figure 3.7. The signal frame structure consists of the header (synchronisation and channel estimation symbols) and the data symbols. The synchronisation part of the header includes a pulse whose magnitude is made to be significantly higher than any other pulse in the signal frame in order to denote the beginning of the transmission. The channel estimation symbols consist of two sets of pseudo-random symbols. The first set consists of symbols that are transmitted by only LED 1 while LED 2 is inactive, and the second set consists of symbols that are transmitted by LED 2 while LED 1 is inactive.
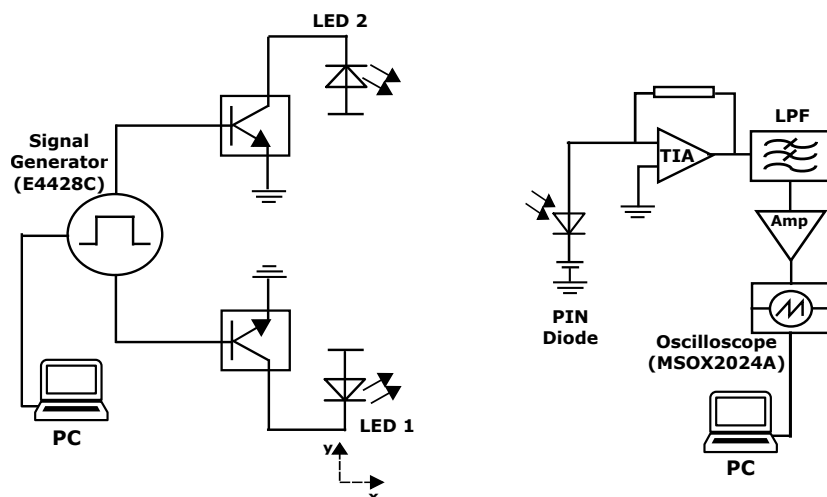
Figure 3.6: *Experimental set-up of SPPM. Coordinates (in cm): LED 1 - (0,0), LED 2 - (0,30), and PD - (100,15).*

In this way, each LED takes turn to transmit channel estimation symbols which are then used to estimate the path gain associated with each LED-PD link.
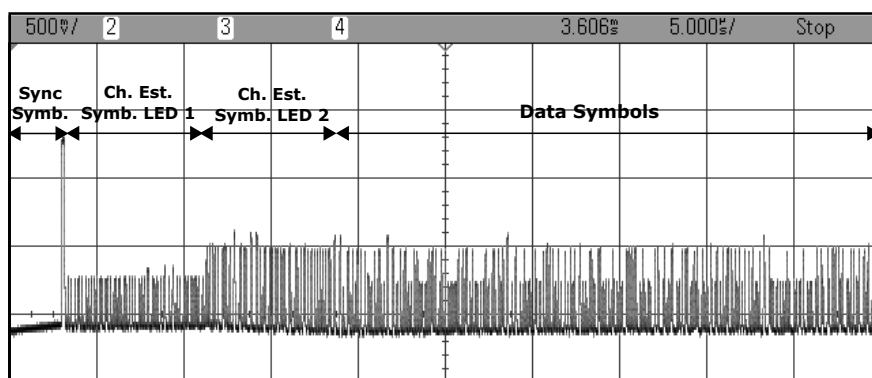
Figure 3.7: *Sample received signal captured on the oscilloscope. The signal frame structure include: the synchronization symbols, channel estimation symbols and data symbols.*

3.4.2 Experimental results

With the 2-LEDs SPPM setup, we consider the cases for $L = 2$ and $L = 4$. The normalized channel gains for LED 1 and LED 2 is $\mathbf{h} = [1, 0.59]$. Figure 3.8 shows the achieved SER plotted against the average received electrical power per bit (P_{eb}). To achieve different received power levels, the optical power transmitted by each LED is varied by changing the magnitude of the modulating signal from the vector signal generator. Additionally, we considered two different data rates by varying the number of samples per symbol in the transmitted signal.

The maximum number of transmitted symbols is 10^5 (this is limited by the sampling rate of the signal generator, 100Msa/s). Results of the different scenarios investigated in the experiment are provided in Table 3.6. It should be noted that these results are without any forward error correction codes.
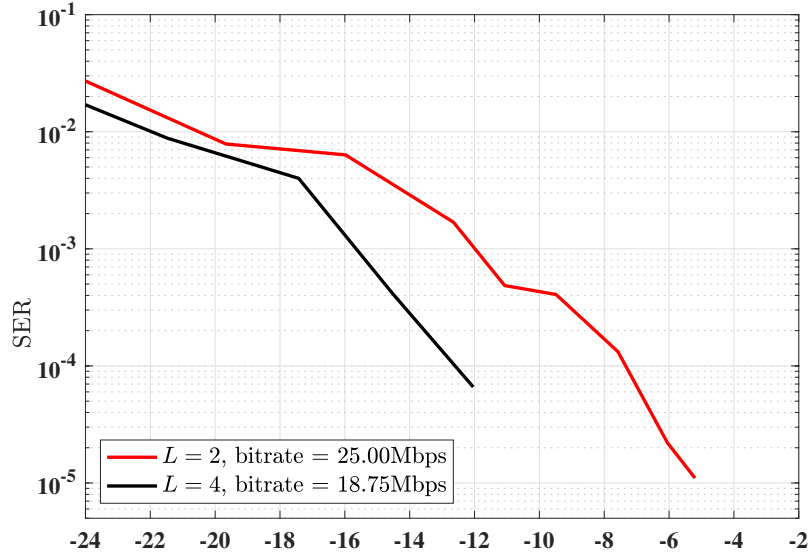
Figure 3.8: *Experimental error performance of SPPM, $N_t = 2, L = 2, 4$, Normalized channel gain, $\mathbf{h} = [1, 0.59]$.*

PPM slots L	Samples per symbol	Bit/symbol $\mathcal{M}$	Bitrate (Mbps)	SER (@ $P_{eb} = -10$ dBm)
2	8	2	25.00	4×10^{-4}
	6	2	33.33	4×10^{-2}
4	16	3	18.75	below 10^{-5}
	12	3	25.00	2×10^{-2}

Table 3.6: *Experimental setup cases and results.*

From Figure 3.8, for the case of $L = 2$, at data rate of 25.00 Mbps, an SER of 4×10^{-4} is achieved with $P_{eb} = -10$ dBm. Similarly, for $L = 4$, at the data rate of 18.75 Mbps and $P_{eb} = -12$ dBm, the achieved SER is 6×10^{-5}, but no error was recorded in the transmission at $P_{eb} > -12$ dBm. As L increased from 2 (at 25.00 Mbps) to 4 (at 18.75 Mbps), the P_{eb} required to achieve an SER of 10^{-4} reduced by about 5 dB. This highlights the energy efficiency benefit that PPM adds to SPPM. Similarly, the achieved data rate is improved because SPPM transmits more bits per symbol compared to classical PPM. Thus, by combining SSK

with PPM, SPPM has improved the data rate and thus the spectral efficiency of PPM while retaining its energy efficiency. These results demonstrates SPPM as a viable modulation technique capable of providing data rate and energy-efficient OWC, particularly in applications with limited energy budget.

3.5 Summary

In this chapter, a generalised framework for PPM-based OSM schemes is presented using a novel scheme termed GSPPM as a reference. GSPPM harnesses the power efficiency of PPM and the spectral efficiency provided by the OSM technique. The general formulation for GSPPM is valid for a wide range of applications as it can be adapted to other OSM schemes namely: SSK, SPPM and GSSK. Thus, the framework permits flexibility in designing an OSM-MIMO system based on the requirements of the target applications. In addition, the impact of channel gain values, i.e., LED/PD alignment on system performance is analysed. The results obtained illustrate how the individual values of the channel gains as well as the disparity of the gains affects error performance. This analysis is useful in the system setup in order to ensure that the LED/PD alignment is optimised for the best error performance (reliability). Moreover, since the developed generalised framework can be adapted to any of the four schemes of OSM, a comparison of these scheme is provided in order to show the benefits and limitations of each scheme. Finally, the performance of SPPM as a signalling technique for OWC is demonstrated experimentally. Error performance results are presented at different data rates. Thus far, the analyses and results obtained in this chapter assumes an ideal system in which a complete synchronisation is maintained between the transmitter and receiver. In the next chapter, we eliminate this assumption, and examine the impact of timing synchronisation error on the performance of the OSM schemes considered herein.

Chapter 4

Impact of timing synchronisation error on the performance of optical spatial modulation

As in most works related to SM [97, 99, 101], in the analysis and performance evaluation of optical SM-MIMO technique presented in the preceding chapter, synchronisation is assumed to be perfect among the array of transmitter sources and between the transmitter and receiver. However, such an assumption represents an ideal condition which is not valid for practical deployment. Even in the proof-of-concept experiments conducted in the laboratory, the need to consider the synchronisation of the system is recognised [91, 109]. Timing synchronisation error can result from the clock jitters in the transmitter and variation in path length due to spatial separation of the transmitter sources, multipath propagation in OWC channel and the mobility or orientation of the receiver [95]. Therefore, in this chapter, we examine the impact of timing synchronisation error on the performance of SM technique in OWC systems. Specifically, the receiver clock is used as reference, and timing errors are modelled as timing offset/displacement in the signals received from each source. As a result of the timing offset, only a portion of the signal energy is obtained by integrating over the time interval for each pulse, while the rest of the signal energy is contributed as ISI in the adjacent pulse interval in the form of energy spillover. By considering the energy loss and spillover phenomena, the performance of the four OSM schemes considered in the preceding chapter is analysed and evaluated under the condition of imperfect timing synchronisation. The theoretical bound on the SER of each scheme is derived and verified with closely-matching simulation results. Error performance results are presented for varying values of timing offset. Expectedly, system performance degrades with increase in timing synchronisation error. Furthermore, the impact of timing errors on each of the four OSM schemes are compared. While SSK is tolerant for a small range of timing synchronisation error, GSSK, SPPM and GSPPM are significantly

impaired. Results obtained also highlight the influence of channel gain values. We observe that the smaller the channel gain value of the LED-PD in which synchronisation error occurs, the lesser the impact of the synchronisation error on the system performance.

The rest of the chapter is organised as follows: illustrations on the impact timing synchronisation error are given in Section 4.1. Then, using GSPPM as a reference scheme, Section 4.2 provides a general model for timing offsets in the OSM schemes, and in Section 4.3, the theoretical analysis of the effects timing offsets on the performance of GSPPM is presented. Thereafter, the timing error analysis is extended to SSK, GSSK, and SPPM in Section 4.4. The analytical and simulation results of the performance evaluation of the four schemes are presented in Section 4.5 while the concluding remarks are given in Section 4.6.

4.1 Timing synchronisation in SM-MIMO

Timing synchronisation plays an important role in communications systems [110, 111] as imperfect synchronisation causes the receiver to read a mixture of interfering signals at its sampling instant. These interfering signals constitute ISI in the received data streams. This compromises the data symbol, and thus, increases the error rate. Hence, synchronisation problems, including performance analysis, timing estimation, and correction, must be addressed in order to avoid performance degradation in practical networks.

As a MIMO technique, SM requires the deployment of spatially separated multiple transmit elements, and it exploits their spatial domain to convey information. As established in Chapter 3, the performance of SM technique is highly dependent on the disparity of the channel gains of the transmit-receive paths [23, 93, 112]. Physically separating the MIMO transmit-receive paths in order to achieve channel gain dissimilarity can cause each path to experience different propagation characteristics such as channel delay. Consequently, multiple timing offsets are generated between the transmitter sources and the receiver. A similar variation in channel characteristics is expected in a system with receiver mobility. Therefore, in OSM schemes, even though the LEDs are not activated concurrently, synchronisation error can occur if the signal transmitted by each LED experiences different channel delay. In the case of generalised SM schemes, timing synchronisation is even more essential since multiple LEDs transmit data signals concurrently [113].

As an illustration, considering a 2-LED and single-PD set-up in a $(5 \times 5 \times 3)$-m room, with the PD at the centre of the room: $(x, y, z) = (2.5, 2.5, 0.85)$-m, the LEDs can be placed at any two of 64 possible locations on the ceiling, where each location is separated by a distance of 0.6 m along the x and y axes as depicted in Figure 4.1a. For multipath propagation with first order reflections from the room surfaces, the RMS delay spread, τ_{rms} experienced at each LED location is depicted in Figure 4.1b. It can be seen in Figure 4.1b that τ_{rms} varies among all the possible locations of the LEDs. To determine the optimum placements of the two LEDs: LED1 and LED2, given the symmetry of the configuration, we focus on one of the quadrants of the ceiling enclosed in the red square as shown in Figure 4.1a. With LED1 placed at one of the nearest positions to the receiver: $(x, y, z) = (2.2, 2.2, 3)$ m, the position of LED2 is varied among the remaining 15 possible locations. Let h_1 and h_2 denote the DC channel gain for LED1 and LED2. Without loss of generality, considering one of the variants of optical SM discussed in Chapter 3, i.e., SPPM, using the normalised values of h_1 and h_2, the achieved SER at an SNR of 20 dB are plotted against the euclidean distance, d, between LED1 and LED2, in Figure 4.1c. Also, the ratio of the channel gains, h_2/h_1 are shown on the right y-axis of Figure 4.1c.
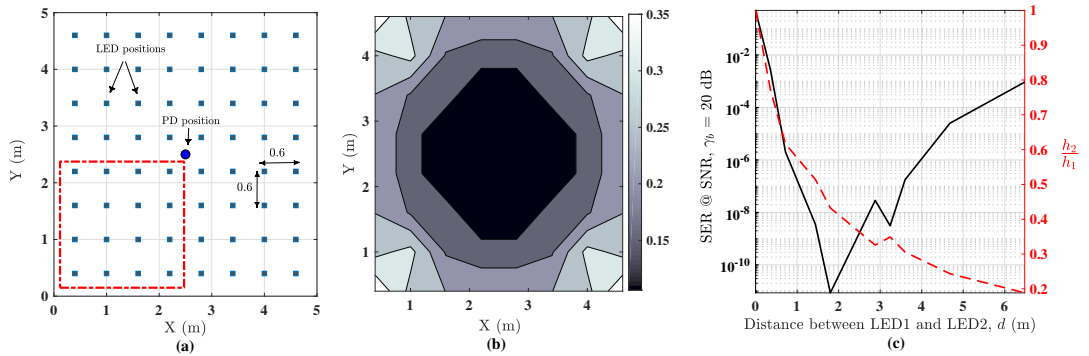
Figure 4.1: *Effect of LED placement/separation on system performance. (a) Placement of LEDs and PD, (b) τ_{rms} (nsec) at different LED positions, and (c) plot of achieved SER at SNR=20 dB and channel gain ratio against LED separation.*

It can be seen from Figure 4.1c that the optimum distance between LED1 and LED2, for which the minimum SER is achieved, is $d = 1.8$ m. This correspond to locating LED1 and LED2 at $(2.2, 2.2, 3)$ m and $(1, 1.6, 3)$ m, respectively. At these locations, the normalised DC gain is about $[h_1, h_2] = [1, 0.42]$, and τ_{rms} is about 0.11 ns and 0.2 ns for LED1 and LED2, respectively. This represents a difference in delay of about 0.09 ns. For high-speed optical communication system with a data rate of least 1 Gbps [35, 114, 115], a delay of about 0.09 ns represent about

9% of the bit duration. Therefore, placing the LEDs at these specified locations for optimum error performance can create a timing offset due to their differences in propagation delay. In terms of receiver mobility, if LED1 and LED2 are fixed at their respective locations as obtained above, and the receive terminal moves across the room, a similar trend to those highlighted above is observed in the values of τ_{rms}. Figure 4.2a and 4.2b show the contour plots of τ_{rms} for LED1 and LED2, respectively. The differences observed in these plots show that the signals transmitted from each LED will experience different path delays thereby introducing timing offsets with respect to the receiver's clock.
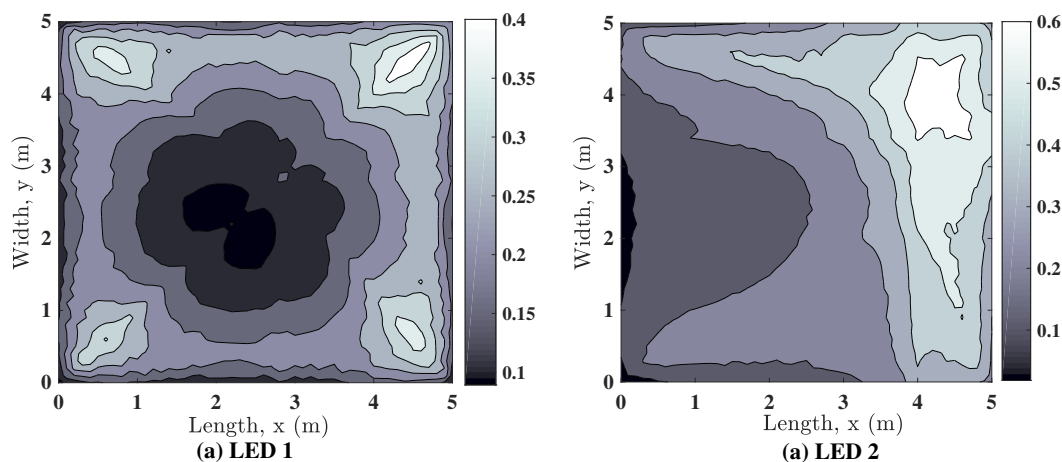
Figure 4.2: *Plot of τ_{rms} (nsec) at different receiver positions for (a) LED1 and (b) LED2*

Moreover, since additional information bits are encoded in the signal transmitted by the activated LED(s) in SM techniques, the synchronisation requirement of the employed signal modulation is also relevant. The effect of synchronisation error on the modulating digital signal constellations that are widely used for optical communication has previously been studied in [116–120]. The theoretical analysis of the effect of synchronisation error on OOK and PPM are presented in [116]. Similarly, an inverse pulse position modulation (IPPM) method is proposed for visible light communication in [117], and the models derived show the effect of clock time shift and jitter on the error performance. References [119] and [120] studied the impact of imperfect synchronisation on optical OFDM systems and they present techniques to mitigate its effect. In this work, we consider the effect of synchronisation error on OSM techniques, which entails both spatial and signal constellations.

The assumption that timing is perfectly synchronised among the multiple transmit and receive

units in the SM scheme implies that the signals received from the transmitter sources have the same clock timing without deviation, and they experience the same propagation delay. However, the aforementioned factors have motivated the need to examine this assumption by analysing the effect of timing synchronisation error on the performance of OSM schemes as follows.

4.2 System Model

In Section 3.1, the system model for an ideal OSM setup assuming a perfect timing synchronisation is presented. However, in this section, we discard this assumption, and we consider a non-ideal system in which the received signal is impaired by errors in timing synchronisation between the LEDs and the receiver. With reference to the receiver clock, such errors introduce timing offset/displacement in the received signal. Due to this offset, some samples of a given data symbol will form part of another data symbol. Hence, the receiver reads a mixture of interfering signals at its sampling instant. In this section, the GSPPM scheme is used as a reference to present a model to account for the pulse energy loss and energy spread caused by error in timing synchronisation.

Without the loss of generality, we consider an OWC system equipped with N_t LEDs and a single PD. Let $\mathcal{A}_{j,m}$ for $j = 1, 2, \ldots, N_\mathrm{s}$, $m = 1, 2, \ldots, L$, denote the GSPPM symbol that is transmitted by activating a number of LEDs according to j-th spatial constellation point (SCP), to simultaneously transmit a pulse in the m-th time slot of the PPM signal. The size of the spatial constellation is denoted by N_s, while L is the number of PPM sime slots/chips. Assuming a perfect timing synchronisation between the LEDs and the receiver, from (3.4), the received electrical signal for symbol $\mathcal{A}_{j,m}$ in a single-PD system is given by:

$$r(t) = RP_\mathrm{t}\lambda_j\mathbf{h}\mathbf{v}_j\phi_m(t) + \eta(t), \quad 0 \leq t \leq T. \tag{4.1}$$

where T is the symbol duration, R is the responsivity of the photodetector (PD) and the vector $\mathbf{h} = [h_1 \ldots h_{N_\mathrm{t}}]$ is the LOS channel gain between the LEDs and the receiver. The noise term $\eta(t)$ is the sum of the ambient light shot noise and the thermal noise in the receiver, modelled as i.i.d AWGN with variance $\sigma^2 = \frac{N_0}{2}$ [26, 38]. The LED activation, $\mathbf{v}_j$, vector is defined as in (3.3), while the pulse-inversion constant, $\lambda_j = \pm 1$ as explained in 3.1.1.

Using a MF receiver architecture, where the receive filter, $\alpha(t)$, is given by:

$$\alpha(t) = RP_t \operatorname{rect}\left(\frac{t}{T_c}\right), \quad 0 \leq t \leq T_c, \tag{4.2}$$

T_c is the duration of each PPM slot/chip. The MF output in each time slot, obtained by sampling at the rate $1/T_c$, is given by:

$$\mathbf{y} = \mathbf{x}_{j,m} + \mathbf{z} \tag{4.3}$$

where $\mathbf{y} = [y_1, \ldots, y_\ell]$ is a $(1 \times L)$-dimensional vector of MF samples, $\mathbf{x}_{j,m} = [x_{j,m}^{(1)}, \ldots, x_{j,m}^{(L)}]$ is the vector of MF samples without noise, given by:

$$x_{j,m}^{(\ell)} = \begin{cases} \lambda_j \mathbf{h} \mathbf{v}_j E_s; & \text{if } \ell = m \\ 0; & \text{otherwise,} \end{cases} \tag{4.4}$$

and $\mathbf{z} = [z_1, \ldots, z_\ell]$ consists of the L Gaussian noise values at the output of the MF in each time slot, with variance $\sigma_z^2 = \frac{N_0}{2} E_s$. The energy per symbol $E_s = (RP_t)^2 T_c$.

The expressions in (4.3) and (4.4) indicate that the MF output in any filled time slot (i.e., the PPM pulse position) is a factor of the transmitted signal energy. Thus, any signal displacement due to synchronisation error is manifested in two ways: (1) the reduction in the pulse energy because there is energy spread into neighbouring time slot, and (2) intra or inter-symbol-interference (ISI) in neighbouring time slot or symbol in the form of pulse energy spillover. These energy loss and energy spread phenomena created by synchronisation error are accounted for as follows.

Consider a non-ideal system in which the received signal is impaired by errors in timing synchronisation between the LEDs and the receiver. Let $\mathcal{A}_{i,\mu}$ and $\mathcal{A}_{j,m}$ denote two consecutively transmitted symbols, such that $\mathcal{A}_{i,\mu}$ and $\mathcal{A}_{j,m}$ are sent in the previous and current symbol duration, respectively. Also, using the receiver clock as reference, let the timing offsets introduced into the signal received from each transmit unit (LED) be denoted by Δ_{n_t} for $n_t = 1, \ldots, N_t$. Positive timing offsets, i.e., $0 < \Delta_{n_t} < T_c$, are considered here, but the interpretation also holds for negative offsets. A positive offset implies that the received signal is lagging with respect to the receiver's clock. If any of the LEDs that are activated to

send symbol $\mathcal{A}_{j,m}$ experiences synchronisation error, then only a portion of the pulse energy is included in the MF output for slot m, while the remaining pulse energy is spilled over into the next time slot. By using (4.4), the portion of symbol $\mathcal{A}_{j,m}$'s energy that is captured in the MF sample in each time slot is expressed as [95]:

$$
\widetilde{x}_{j,m}^{(\ell)} = \begin{cases} E_{\mathrm{s}}\lambda_j \left(\mathbf{h} \odot \left(\hat{\mathbf{1}}_{N_{\mathrm{t}}} - \boldsymbol{\epsilon}\right)\right) \mathbf{v}_j; & \text{if } \ell = m \\ 0; & \text{otherwise,} \end{cases}
\tag{4.5}
$$

while the the energy lost as ISI from slot m into the neighbouring time slot $\ell = (m+1)$ is given by:

$$
\xi_{j,m}^{(\ell)} = \begin{cases} E_{\mathrm{s}}\lambda_j \left(\mathbf{h} \odot \boldsymbol{\epsilon}\right) \mathbf{v}_j; & \text{if } \ell = m+1 \\ 0; & \text{otherwise,} \end{cases}
\tag{4.6}
$$

where $\odot$ denotes the Hadamard (entry-wise) product, while $\hat{\mathbf{1}}_{N_{\mathrm{t}}}$ represents $(1 \times N_{\mathrm{t}})$ unit vector. The vector $\boldsymbol{\epsilon} = [\epsilon_1 \ldots \epsilon_{n_{\mathrm{t}}} \ldots \epsilon_{N_{\mathrm{t}}}]$ represents the timing offsets normalised by the pulse (slot) duration T_{c}, that is, $\epsilon_{n_{\mathrm{t}}} = \Delta_{n_{\mathrm{t}}}/T_{\mathrm{c}}$. Furthermore, if symbol $\mathcal{A}_{i,\mu}$ is impaired by timing offset, then energy is lost from slot μ into the adjoining time slot. If slot μ is the last time slot in symbol $\mathcal{A}_{i,\mu}$, then the energy loss is contributed as ISI into the first time slot in symbol $\mathcal{A}_{j,m}$. This energy spread is given by:

$$
\xi_{i,\mu}^{(\ell)} = \begin{cases} E_{\mathrm{s}}\lambda_i \left(\mathbf{h} \odot \boldsymbol{\epsilon}\right) \mathbf{v}_i; & \text{if } \mu = L \text{ and } \ell = 1 \\ 0; & \text{otherwise,} \end{cases}
\tag{4.7}
$$

Using the definitions above for the energy loss and energy spillover due to timing synchronisation error, the MF sample in each time slots of symbol $\mathcal{A}_{j,m}$ consists of Gaussian noise z_ℓ and of one or more of three signal components:

(i) the pulse energy transmitted in each time slot, which is denoted by $\widetilde{x}_{j,m}^{(\ell)}$, and given by (4.5)

(ii) energy due to intra-symbol interference from neighbouring slots within symbol $\mathcal{A}_{j,m}$, which is denoted by $\xi_{j,m}^{(\ell)}$, and given by (4.6)

(iii) energy due to inter-symbol interference from neighbouring slots within symbol $\mathcal{A}_{i,\mu}$,

which is denoted by $\xi_{i,\mu}^{(\ell)}$, and given by (4.7)

Therefore, the MF sample of symbol $\mathcal{A}_{j,m}$ in the presence of ISI is expressed as:

$$\widetilde{y}_\ell = \widetilde{x}_{j,m}^{(\ell)} + \xi_{j,m}^{(\ell)} + \xi_{i,\mu}^{(\ell)} + z_\ell, \quad \ell = 1, ..., L \tag{4.8}$$

It is clear from the expressions above that the amount and the impact of the ISI caused by the energy loss and spreading described above depends on the pulse position of both symbols $\mathcal{A}_{i,\mu}$ and $\mathcal{A}_{j,m}$. In the following analysis, by considering all the possible pulse position combinations, we derive the upper bound on the symbol error probability of a GSPPM scheme that is impaired by timing offset.

4.3 Synchronisation error analysis of GSPPM

As explained in Section 3.2, a correct detection of transmitted symbol is achieved if both the pulse position and the SCP are correctly detected. Thus, in order to obtain the symbol error probability a GSPPM scheme that is impaired by timing offsets as defined in (3.11), we first obtain the probabilities of correctly detecting the SCP, $\overline{P}_{\text{c,scp}}^{\text{GSPPM}}$, and the PPM pulse position, $\overline{P}_{\text{c,ppm}}^{\text{GSPPM}}$, as follows.

4.3.1 Impact of timing offset on spatial constellation point detection in GSPPM

For symbol $\mathcal{A}_{j,m}$ which is transmitted by activating LEDs based on SCP j, assuming a correctly detected pulse position, i.e., $\hat{m} = m$, the PEP that the receiver decides in favour of SCP k instead of j, $j \neq k$, is given by:

$$\overline{\text{PEP}}_m^{j \to k} = \mathbb{P}\left(\mathcal{D}(\widetilde{y}_m, x_{j,m}^{(m)}) > \mathcal{D}(\widetilde{y}_m, x_{k,m}^{(m)})\right) \tag{4.9}$$

where $\widetilde{\mathbf{y}} = [\widetilde{y}_\ell]_{\ell=1}^L$, and the distance metric, $\mathcal{D}(\widetilde{y}_m, x_{j,m}^{(m)}) = \left|\widetilde{y}_m - x_{j,m}^{(m)}\right|^2$. Using (4.4) and (4.8), (4.9) becomes:

$$\text{PEP}_m^{j \to k} = \mathbb{P}\left((\widetilde{y}_m - \lambda_j \mathbf{h}\mathbf{v}_j E_\text{s})^2 > (\widetilde{y}_m - \lambda_k \mathbf{h}\mathbf{v}_k E_\text{s})^2\right) \tag{4.10}$$

As mentioned earlier, the value of $\widetilde{y}_m$ in (4.10) depends on the pulse position of symbols $\mathcal{A}_{i,\mu}$ and $\mathcal{A}_{j,m}$. For the two symbols with L-PPM pulse pattern, there are L^2 possible pulse

position combinations which are grouped under two cases as follows. An illustrative example of the these two cases for a 4-PPM pulse pattern is shown in Figure 4.3. A summary of the parameters and expressions for the various pulse position combinations in the SCP detection of GSPPM are provided in Table 4.1. The cases are further discussed as follows.
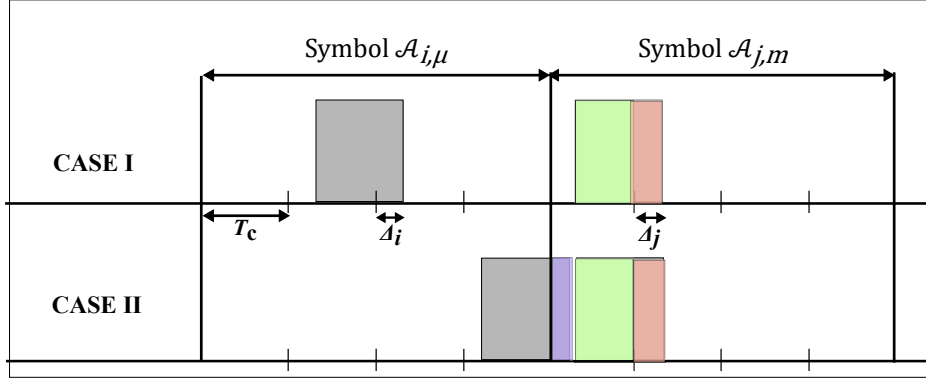
Figure 4.3: *Pulse position combinations for two consecutive symbols $\mathcal{A}_{i,\mu}$ and $\mathcal{A}_{j,m}$, in a GSPPM scheme using 4-PPM. The scalars Δ_i and Δ_j are the timing offsets in the received signal from one of the LEDs activated to send $\mathcal{A}_{i,\mu}$ and $\mathcal{A}_{j,m}$, respectively. The colour scheme used indicates the signal component according to (4.8).*

Case I

If the pulse position of symbol $\mathcal{A}_{i,\mu}$ is not its last time slot, that is, $1 \leq \mu < L$, or that of symbol $\mathcal{A}_{j,m}$ is not its first time slot, that is, $1 < m \leq L$, then, there is no energy spread from $\mathcal{A}_{i,\mu}$ into the pulse position of $\mathcal{A}_{j,m}$. Therefore,

$$\widetilde{y}_m = \widetilde{x}_{j,m}^{(m)} + z_m = E_s \lambda_j \left(\mathbf{h} \odot (\hat{\mathbf{1}}_{N_t} - \boldsymbol{\epsilon}) \right) \mathbf{v}_j + z_m, \tag{4.11}$$

and the PEP for this case is obtained as:

$$\begin{aligned}
\overline{\mathrm{PEP}}_m^{\mathrm{I},j \to k} &= \mathbb{P} \left(z_m \left(\lambda_k \mathbf{h} \mathbf{v}_k - \lambda_j \mathbf{h} \mathbf{v}_j \right) > E_s \mathcal{U}_{j,k}^{\mathrm{I}} \right) \\
&= \int_{\frac{E_s \mathcal{U}_{j,k}^{\mathrm{I}}}{2 \left| \lambda_k \mathbf{h} \mathbf{v}_k - \lambda_j \mathbf{h} \mathbf{v}_j \right|}}^{\infty} \frac{1}{\sqrt{2\pi\sigma_z^2}} \exp \left(-\frac{a^2}{2\sigma_z^2} \right) \, \mathrm{d}a \\
&= Q \left(\frac{\mathcal{U}_{j,k}^{\mathrm{I}}}{\left| \lambda_k \mathbf{h} \mathbf{v}_k - \lambda_j \mathbf{h} \mathbf{v}_j \right|} \sqrt{\frac{\gamma_s}{2}} \right)
\end{aligned} \tag{4.12}$$

where

$$\mathcal{U}_{j,k}^{\mathrm{I}} = (\lambda_j \mathbf{h} \mathbf{v}_j) \Big[\lambda_j \mathbf{h} \mathbf{v}_j \ - \ 2\lambda_j \left(\mathbf{h} \odot \boldsymbol{\epsilon} \right) \mathbf{v}_j \Big]$$
$$+ (\lambda_k \mathbf{h} \mathbf{v}_k) \Big[\lambda_k \mathbf{h} \mathbf{v}_k \ - \ 2\lambda_j \left(\mathbf{h} \odot \left(\hat{\mathbf{1}}_{N_{\mathrm{t}}} - \boldsymbol{\epsilon} \right) \right) \mathbf{v}_j \Big], \quad (4.13)$$

and the symbol SNR is $\gamma_{\mathrm{s}} = E_{\mathrm{s}}/N_0$. Out of the L^2 possibilities, there are $(L^2 - 1)$ possible combinations of slots μ and m for this case, therefore, the probability of occurrence of this case is $\Phi_{\mathrm{I}} = (1 - (1/L^2))$.

Case II

If the pulse position of symbol $\mathcal{A}_{i,\mu}$ is its last time slot, i.e., $\mu = L$, and that of symbol $\mathcal{A}_{j,m}$ is its first time slot, i.e, $m = 1$, then, the energy spread from $\mathcal{A}_{i,\mu}$ is contributed into the slot m of $\mathcal{A}_{j,m}$. Hence,

$$\widetilde{y}_m = \widetilde{x}_{j,m}^{(m)} + \xi_{i,\mu}^{(m)} + z_m$$
$$= E_{\mathrm{s}} \left[\lambda_j \left(\mathbf{h} \odot \left(\hat{\mathbf{1}}_{N_{\mathrm{t}}} - \boldsymbol{\epsilon} \right) \right) \mathbf{v}_j + \lambda_i \left(\mathbf{h} \odot \boldsymbol{\epsilon} \right) \mathbf{v}_i \right] + z_m. \quad (4.14)$$

The probability of occurrence of this case is $\Phi_{\mathrm{II}} = 1/L^2$. Given that symbol $\mathcal{A}_{i,\mu}$ can contain any of the N_{s} eqiprobable SCPs, the PEP for this case is obtained by taking the average over N_{s} equiprobable SCPs, and it is given by:

$$\overline{\mathrm{PEP}}_m^{\mathrm{II},j\to k} = \frac{1}{N_{\mathrm{s}}} \sum_{i=1}^{N_{\mathrm{s}}} \mathbb{P} \left(z_m \left(\lambda_k \mathbf{h} \mathbf{v}_k - \lambda_j \mathbf{h} \mathbf{v}_j \right) > E_{\mathrm{s}} \mathcal{U}_{i,j,k}^{\mathrm{II}} \right)$$
$$= \frac{1}{N_{\mathrm{s}}} \sum_{i=1}^{N_{\mathrm{s}}} Q \left(\frac{\mathcal{U}_{i,j,k}^{\mathrm{II}}}{|\lambda_k \mathbf{h} \mathbf{v}_k - \lambda_j \mathbf{h} \mathbf{v}_j|} \sqrt{\frac{\gamma_{\mathrm{s}}}{2}} \right) \quad (4.15)$$

where

$$\mathcal{U}_{i,j,k}^{\mathrm{II}} = (\lambda_j \mathbf{h} \mathbf{v}_j) \Big[\lambda_j \mathbf{h} \mathbf{v}_j - 2\lambda_j \left(\mathbf{h} \odot \boldsymbol{\epsilon} \right) \mathbf{v}_j + 2\lambda_i \left(\mathbf{h} \odot \boldsymbol{\epsilon} \right) \mathbf{v}_i \Big]$$
$$+ (\lambda_k \mathbf{h} \mathbf{v}_k) \Big[\lambda_k \mathbf{h} \mathbf{v}_k \ - \ 2\lambda_j \left(\mathbf{h} \odot \left(\hat{\mathbf{1}}_{N_{\mathrm{t}}} - \boldsymbol{\epsilon} \right) \right) \mathbf{v}_j - 2\lambda_i \left(\mathbf{h} \odot \boldsymbol{\epsilon} \right) \mathbf{v}_i \Big]. \quad (4.16)$$

Case	μ	m	$\widetilde{x}_{j,m}^{(m)}$	$\xi_{j,m}^{(m)}$	$\xi_{i,\mu}^{(m)}$
Case I	$1 \leq \mu < L$	$1 < m \leq L$	$E_\mathrm{s}\lambda_j \left(\mathbf{h} \odot (\hat{\mathbf{1}}_{N_\mathrm{t}} - \boldsymbol{\epsilon}) \right) \mathbf{v}_j$	0	0
Case II	L	1	$E_\mathrm{s}\lambda_j \left(\mathbf{h} \odot (\hat{\mathbf{1}}_{N_\mathrm{t}} - \boldsymbol{\epsilon}) \right) \mathbf{v}_j$	0	$\lambda_i \left(\mathbf{h} \odot \boldsymbol{\epsilon} \right) \mathbf{v}_i$

Table 4.1: *Summary of the parameters and expressions for various pulse position combinations in the SCP detection of GSPPM.*

By combining (4.12) and (4.15), the PEP of decoding the SCP is given by:

$$\overline{\mathrm{PEP}}_m^{j \to k} = \Phi_\mathrm{I} \times \overline{\mathrm{PEP}}_m^{\mathrm{I}, j \to k} + \Phi_\mathrm{II} \times \overline{\mathrm{PEP}}_m^{\mathrm{II}, j \to k}. \tag{4.17}$$

With the union bound approximation [106], the probability of correctly detecting the SCP j, of the transmitted symbol, conditioned on a correctly detected pulse position m, is given by:

$$\begin{aligned}
\overline{P}_{\mathrm{c,scp}}^{\mathrm{GSPPM}}(j) &\leq 1 - \sum_{\substack{k=1 \\ k \neq j}}^{N_\mathrm{s}} \overline{\mathrm{PEP}}_m^{j \to k} \\
&= 1 - \frac{1}{L^2} \sum_{\substack{k=1 \\ k \neq j}}^{N_\mathrm{s}} \left[(L^2 - 1)\, Q\left(\frac{\mathcal{U}_{j,k}^{\mathrm{I}}}{|\lambda_k \mathbf{h}\mathbf{v}_k - \lambda_j \mathbf{h}\mathbf{v}_j|} \sqrt{\frac{\gamma_\mathrm{s}}{2}} \right) \right. \\
&\qquad\qquad\qquad\qquad \left. \frac{1}{N_\mathrm{s}} \sum_{i=1}^{N_\mathrm{s}} Q\left(\frac{\mathcal{U}_{i,j,k}^{\mathrm{II}}}{|\lambda_k \mathbf{h}\mathbf{v}_k - \lambda_j \mathbf{h}\mathbf{v}_j|} \sqrt{\frac{\gamma_\mathrm{s}}{2}} \right) \right]. \tag{4.18}
\end{aligned}$$

where $\mathcal{U}_{j,k}^{\mathrm{I}}$ and $\mathcal{U}_{i,j,k}^{\mathrm{II}}$ are defined in (4.13) and (4.16), respectively.

4.3.2 Impact of timing offset on pulse position detection in GSPPM

For the transmitted symbol $\mathcal{A}_{j,m}$, the activated LEDs transmit a pulse in slot m of the PPM signal, and the PEP that the receiver decides in favour of slot q instead of slot m, $m \neq q$, is expressed as:

$$\overline{\mathrm{PEP}}_{m \to q}^{j} = \mathbb{P} \left(\mathcal{D}(\widetilde{\mathbf{y}}, \mathbf{x}_{j,m}) > \mathcal{D}(\widetilde{\mathbf{y}}, \mathbf{x}_{j,q}) \right) \tag{4.19}$$

where

$$\mathcal{D}(\widetilde{\mathbf{y}}, \mathbf{x}_{j,m}) = \left(\widetilde{y}_m - x_{j,m}^{(m)}\right)^2 + \left(\widetilde{y}_q - x_{j,m}^{(q)}\right)^2 \tag{4.20}$$

$$\mathcal{D}(\widetilde{\mathbf{y}}, \mathbf{x}_{j,q}) = \left(\widetilde{y}_m - x_{j,q}^{(m)}\right)^2 + \left(\widetilde{y}_q - x_{j,q}^{(q)}\right)^2 \tag{4.21}$$

As in Section 4.3.1, the values of $\overline{y}_m$ and $\overline{y}_q$, and hence $\overline{\mathrm{PEP}}_{m \to q}^j$, depend on the index of slot m and q in the PPM signal of symbol $\mathcal{A}_{j,m}$, and on the index of slot μ in the PPM signal of symbol $\mathcal{A}_{i,\mu}$. All the possible pulse position combinations are grouped into five different cases, and the diagrammatic illustration of these cases for a 4-PPM pulse pattern is shown in Figure 4.4. A summary of the parameters and the expressions for $\overline{y}_m$ and $\overline{y}_q$ for each case is provided in Table 4.2. These parameters and expressions are used to evaluate (4.19), and to compute the probability of correctly detecting the pulse position as follows.
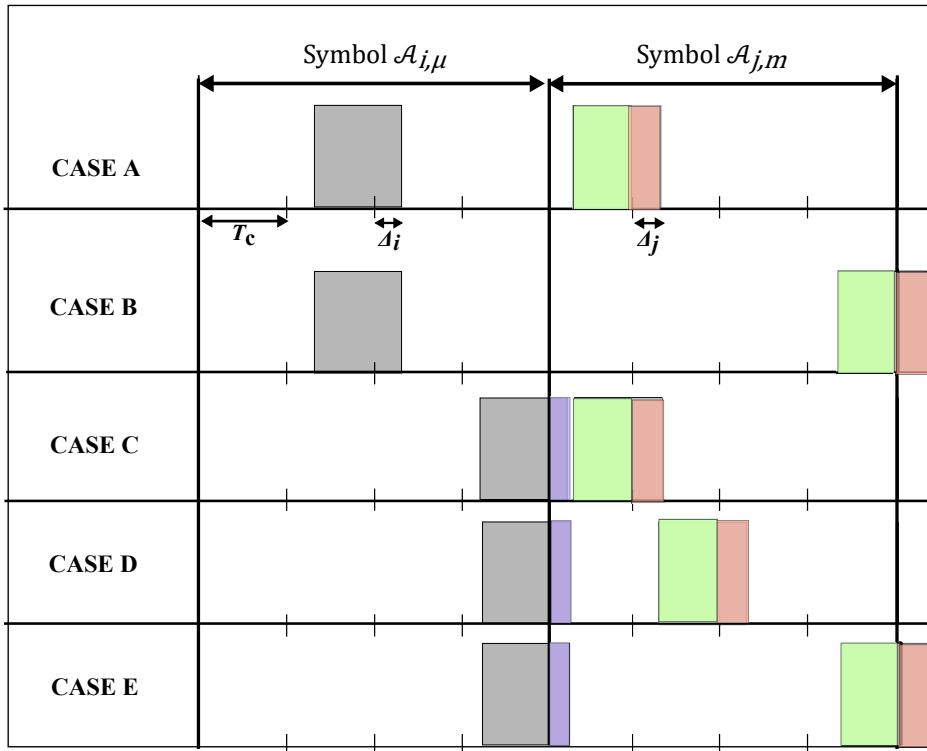
**Figure 4.4:** *Illustration of different pulse position combinations for two consecutive symbols $\mathcal{A}_{i,\mu}$ and $\mathcal{A}_{j,m}$, in a GSPPM scheme using 4-PPM. The scalars Δ_i and Δ_j are the timing offsets in the received signal from one of the LEDs activated to send $\mathcal{A}_{i,\mu}$ and $\mathcal{A}_{j,m}$, respectively. The colour scheme used indicates the signal component according to (4.8).*

Case A

For this case, $1 \leq \mu < L$ and $1 \leq m < L$. Hence, no energy loss from $\mathcal{A}_{i,\mu}$ is contributed to the MF output in the first slot of $\mathcal{A}_{j,m}$. Using Table 4.2, the probability of error in decoding the pulse position in this case is:

$$\mathcal{P}_{j,\,\mathrm{A}} = \Phi_{\mathrm{A}} \times \left(\mathrm{PEP}^{j}_{m \to (m+1)} + (L-2)\, \mathrm{PEP}^{j}_{m \to q} \right), \tag{4.22}$$

where Φ_{A} is the probability of occurrence for this case, and it is obtained as:

$$\Phi_{\mathrm{A}} = \mathbb{P}\left(1 \leq \mu < L\right) \times \mathbb{P}\left(1 \leq m < L\right) = (L-1)^2/L^2. \tag{4.23}$$

$\mathrm{PEP}^{j}_{m \to (m+1)}$ is the PEP between slot m and the adjacent slot $(m+1)$, while $\mathrm{PEP}^{j}_{m \to q}$, for $\{1 \leq q \leq L, q \neq m, q \neq (m+1)\}$, is the PEP between slot m and any of the other $(L-2)$ empty slots in $\mathcal{A}_{j,m}$.

Case B

As in case A above, For symbol $\mathcal{A}_{i,\mu}$, the index of slot μ lies in the range $1 \leq \mu < L$. But, for symbol $\mathcal{A}_{j,m}$, $m = L$. Hence, the energy loss in $\mathcal{A}_{j,m}$ is from slot m into first time slot of the next symbol. Therefore, the probability of error in detecting the pulse position in this case is given by:

$$\mathcal{P}_{j,\,\mathrm{B}} = \Phi_{\mathrm{B}} \times (L-1)\, \overline{\mathrm{PEP}}^{j}_{m \to q} \tag{4.24}$$

where $\overline{\mathrm{PEP}}^{j}_{m \to q}$ for $1 \leq q \leq (L-1)$, is the PEP between slot m and any of the other $(L-1)$ empty slots. The probability of occurrence for this case is:

$$\Phi_{\mathrm{B}} = \mathbb{P}\left(1 \leq \mu < L\right) \times \mathbb{P}\left(m = L\right) = (L-1)/L^2. \tag{4.25}$$

Case C

In this case, the pulse position for symbol $\mathcal{A}_{i,\mu}$ is its last time slot, that is, $\mu = L$, while that of symbol $\mathcal{A}_{j,m}$ is its first time slot, that is, $m = 1$. Hence, any energy loss from $\mathcal{A}_{i,\mu}$, is added to the MF output in slot m of symbol $\mathcal{A}_{j,m}$, while the energy loss from slot m in $\mathcal{A}_{j,m}$ is captured

in the MF output of the next slot, $(m + 1)$. Given that symbol $\mathcal{A}_{i,\mu}$ can contain any of the N_s eqiprobable SCPs, the error probability for this case is obtained by taking the average over these N_s equiprobable SCPs. This also applies to cases D and E below. Thus, the probability of error in detecting the pulse position for case C is:

$$\mathcal{P}_{j,\,\mathrm{C}} = \frac{\Phi_\mathrm{C}}{N_\mathrm{s}} \sum_{i=1}^{N_\mathrm{s}} \left[\overline{\mathrm{PEP}}^{\,j}_{m \to (m+1)} \; + \; (L-2)\, \overline{\mathrm{PEP}}^{\,j}_{m \to q} \right] \tag{4.26}$$

where $\overline{\mathrm{PEP}}^{\,j}_{m \to (m+1)}$ is the PEP between slot m and the next slot $(m+1)$, while $\overline{\mathrm{PEP}}^{\,j}_{m \to q}$, for $3 \leq q \leq L$, is the PEP between slot m and any of the other $(L-2)$ empty slots. This scenario can occur with the probability:

$$\Phi_\mathrm{C} = \mathbb{P}\left(\mu = L\right) \times \mathbb{P}\left(m = 1\right) = 1/L^2, \tag{4.27}$$

Case D

For symbol $\mathcal{A}_{i,\mu}$, $\mu = L$, while the pulse position of symbol $\mathcal{A}_{j,m}$ is neither its first nor its last time slot, i.e, $1 < m < L$. As a result, any spillover energy from $\mathcal{A}_{i,\mu}$ is contributed to the MF output in the first slot of $\mathcal{A}_{j,m}$, while the spillover from slot m in $\mathcal{A}_{j,m}$ is captured in the MF output of slot $(m + 1)$. This case can occur with the probability:

$$\Phi_\mathrm{D} = \mathbb{P}\left(\mu = L\right) \times \mathbb{P}\left(2 \leq m < (L-1)\right) = (L-2)/L^2, \tag{4.28}$$

and the probability of error in detecting the pulse position in this case is:

$$\mathcal{P}_{j,\,\mathrm{D}} \;=\; \frac{\Phi_\mathrm{D}}{N_\mathrm{s}} \sum_{i=1}^{N_\mathrm{s}} \left[\overline{\mathrm{PEP}}^{\,j}_{m \to 1} + \overline{\mathrm{PEP}}^{\,j}_{m \to (m+1)} + (L-3)\overline{\mathrm{PEP}}^{\,j}_{m \to q} \right] \tag{4.29}$$

where $\overline{\mathrm{PEP}}^{\,j}_{m \to 1}$ is the PEP between slot m and the first slot, while $\overline{\mathrm{PEP}}^{\,j}_{m \to q}$ for $\{2 \leq q \leq L,\ q \neq m, q \neq (m+1)\}$, is the PEP between slot m and any of the other $(L-3)$ empty slots.

Case E

For symbol $\mathcal{A}_{i,\mu}$, $\mu = L$, and for symbol $\mathcal{A}_{j,m}$, $m = L$. As a result, while the spillover energy from $\mathcal{A}_{i,\mu}$ is contributed to the MF output in the first slot of $\mathcal{A}_{j,m}$, that of slot m in $\mathcal{A}_{j,m}$ is captured in the MF output in the first time slot of the next symbol. This case can occur with

the probability:

$$\Phi_{\mathrm{E}} = \mathbb{P}\left(\mu = L\right) \times \mathbb{P}\left(m = L\right) = 1/L^2, \tag{4.30}$$

and the probability of error in detecting the pulse position in this case is:

$$\mathcal{P}_{j,\,\mathrm{E}} = \frac{\Phi_{\mathrm{E}}}{N_{\mathrm{s}}} \sum_{i=1}^{N_{\mathrm{s}}} \left[\overline{\mathrm{PEP}}^{j}_{m \to 1} + (L-2)\overline{\mathrm{PEP}}^{j}_{m \to q} \right] \tag{4.31}$$

where $\overline{\mathrm{PEP}}^{j}_{m \to 1}$ is the PEP between slot m and the first slot, and $\overline{\mathrm{PEP}}^{j}_{m \to q}$ for $1 < q < L$, is the PEP between slot m and any of the other $(L-2)$ empty slots.

The PEP terms in (4.22), (4.24), (4.26), (4.29) and (4.31), are obtained by using the corresponding expressions for $\widetilde{y}_m$ and $\widetilde{y}_q$ as summarised in Table 4.2 to evaluate the PEP definition in (4.19). The resulting expressions for these PEP terms are shown in the last column of Table 4.2. The probability of correctly decoding the pulse position of the transmitted data symbol with SCP j, is given by:

$$\overline{P}^{\mathrm{GSPPM}}_{\mathrm{c,ppm}}(j) = 1 - \left(\mathcal{P}_{j,\,\mathrm{A}} + \mathcal{P}_{j,\,\mathrm{B}} + \mathcal{P}_{j,\,\mathrm{C}} + \mathcal{P}_{j,\,\mathrm{D}} + \mathcal{P}_{j,\,\mathrm{E}} \right). \tag{4.32}$$

By applying (4.18) and (4.32) in (3.11) and (3.12), when the transmitted symbol is impaired by errors in timing synchronisation, the error probability for the symbol with SCP j, is:

$$\overline{P}^{\mathrm{GSPPM}}_{\mathrm{e,sym}}(j) \leq 1 - \overline{P}^{\mathrm{GSPPM}}_{\mathrm{c,scp}}(j) \times \left[1 - \left(\mathcal{P}_{j,\,\mathrm{A}} + \mathcal{P}_{j,\,\mathrm{B}} + \mathcal{P}_{j,\,\mathrm{C}} + \mathcal{P}_{j,\,\mathrm{D}} + \mathcal{P}_{j,\,\mathrm{E}} \right) \right]. \tag{4.33}$$

Therefore, the average symbol error probability for a GSPPM scheme that is impaired by timing synchronisation error is calculated from the expectation of $\overline{P}^{\mathrm{GSPPM}}_{\mathrm{e,sym}}(j)$, as

$$\begin{aligned}
\overline{P}^{\mathrm{GSPPM}}_{\mathrm{e,sym}} &= \mathbb{E}\left[\overline{P}^{\mathrm{GSPPM}}_{\mathrm{e,sym}}(j) \right] = \frac{1}{N_{\mathrm{s}}} \sum_{j=1}^{N_{\mathrm{s}}} \overline{P}^{\mathrm{GSPPM}}_{\mathrm{e,sym}}(j) \\
&\leq 1 - \frac{1}{N_{\mathrm{s}}} \sum_{j=1}^{N_{\mathrm{s}}} \left[\overline{P}^{\mathrm{GSPPM}}_{\mathrm{c,scp}}(j) \times \left[1 - \left(\mathcal{P}_{j,\,\mathrm{A}} + \mathcal{P}_{j,\,\mathrm{B}} + \mathcal{P}_{j,\,\mathrm{C}} + \mathcal{P}_{j,\,\mathrm{D}} + \mathcal{P}_{j,\,\mathrm{E}} \right) \right] \right].
\end{aligned}$$
$$\tag{4.34}$$

Note that for GSSPM scheme, $N_{\mathrm{s}} = 2^{N_{\mathrm{t}}}$. Furthermore, by setting the normalised timing offsets

to zero, that is, $\{\epsilon_\kappa\}_{\kappa=1}^{N_{\rm t}} = 0$, the derived expression in (4.34) reduces to the standard SER expression for a GSPPM scheme without timing errors, as presented in (3.24).

4.4 Extension of synchronisation error analysis of GSPPM to other OSM Schemes

Following the approach in Section 3.2, the synchronisation error analysis derived for GSPPM in Section 4.3 is used as a reference case from which similar analyses for SSK, GSSK and SPPM are derived. These analyses are obtained by using the appropriate parameters' specifications for each OSM scheme provided in Table 3.2 to modify the derivation for GSPPM.

4.4.1 Synchronisation Error Analysis of SSK

For an SSK scheme that is affected by timing error in transmitter-receiver synchronisation, the symbol error probability of the scheme, $\overline{P}_{\rm e,sym}^{\rm SSK}$, is obtained by using the following parameters from Table 3.2 in (4.34): $L=1$, $N_{\rm s}=N_{\rm t}$, $T_{\rm c}=T$ and $\lambda_j=1, \forall j$. With $L=1$, then $m=q$, and according to (4.19), all the PEP terms in Table 4.2 return as zero. Thus, the error probabilities $\mathcal{P}_A = \mathcal{P}_A \cdots = \mathcal{P}_E = 0$. Furthermore, in SSK, $\mathbf{v}_j \, \forall j$, has only one non-zero entry. Consequently, the terms in (4.18) involving the vector $\mathbf{v}$ can be further simplified. For example, $\mathbf{h}\mathbf{v}_j = h_j$, and $(\mathbf{h} \odot \boldsymbol{\epsilon})\mathbf{v}_j = h_j\epsilon_j, \forall j$. Therefore,

$$\overline{P}_{\rm e,sym}^{\rm SSK} \le \frac{1}{(N_{\rm t})^2} \sum_{j=1}^{N_{\rm t}} \sum_{\substack{k=1 \\ k \neq j}}^{N_{\rm t}} \sum_{i=1}^{N_{\rm t}} Q\left(\frac{\mathcal{X}_{i,j,k}}{|h_k - h_j|}\sqrt{\frac{\gamma_{\rm s}}{2}}\right) \tag{4.35}$$

where

$$\mathcal{X}_{i,j,k} = h_j^2(1 - 2\epsilon_j) + 2h_jh_k(\epsilon_j - 1) + h_k^2 + 2h_i\epsilon_i(h_j - h_k). \tag{4.36}$$

If the system is perfectly synchronised, then the normalised timing offset associated with each LED becomes zero, that is, $\{\epsilon_{n_{\rm t}}\}_{n_{\rm t}=1}^{N_{\rm t}} = 0$, and (4.35) reduces to the standard SER expression for SSK which can be obtained from (3.25) by considering a single receiver.

Case	μ	m	$\tilde{y}_m$	q	$\tilde{y}_q$	Φ	$\overline{\mathrm{PEP}}^{j}_{m\to q}$
A	$1 \le \mu < L$	$1 \le m < L$	$E_{\mathrm{s}}\lambda_j\big(\mathbf{h}\odot(\hat{\mathbf{1}}_{N_{\mathrm{t}}} - \boldsymbol{\epsilon})\big)\mathbf{v}_j + z_m$	$m+1$	$E_{\mathrm{s}}\lambda_j(\mathbf{h}\odot\boldsymbol{\epsilon})\mathbf{v}_j + n_q$	$\left(\dfrac{L-1}{L}\right)^2$	$Q\!\left(\sqrt{\gamma_{\mathrm{s}}}\,\lambda_j\big(\mathbf{h}\odot(\hat{\mathbf{1}}_{N_{\mathrm{t}}} - 2\boldsymbol{\epsilon})\big)\mathbf{v}_j\right)$
				$\begin{array}{c}1 \le q \le L\\ q \ne m,\, q \ne m+1\end{array}$	n_q		$Q\!\left(\sqrt{\gamma_{\mathrm{s}}}\,\lambda_j\big(\mathbf{h}\odot(\hat{\mathbf{1}}_{N_{\mathrm{t}}} - \boldsymbol{\epsilon})\big)\mathbf{v}_j\right)$
B		L	$E_{\mathrm{s}}\lambda_j\big(\mathbf{h}\odot(\hat{\mathbf{1}}_{N_{\mathrm{t}}} - \boldsymbol{\epsilon})\big)\mathbf{v}_j + z_m$	$1 \le q \le (L-1)$	n_q	$\dfrac{L-1}{L^2}$	$Q\!\left(\sqrt{\gamma_{\mathrm{s}}}\,\lambda_j\big(\mathbf{h}\odot(\hat{\mathbf{1}}_{N_{\mathrm{t}}} - \boldsymbol{\epsilon})\big)\mathbf{v}_j\right)$
C	L	1	$\begin{array}{l}E_{\mathrm{s}}\lambda_j\big(\mathbf{h}\odot(\hat{\mathbf{1}}_{N_{\mathrm{t}}} - \boldsymbol{\epsilon})\big)\mathbf{v}_j\\ {}+ E_{\mathrm{s}}\lambda_i(\mathbf{h}\odot\boldsymbol{\epsilon})\mathbf{v}_i + z_m\end{array}$	$m+1$	$E_{\mathrm{s}}\lambda_j(\mathbf{h}\odot\boldsymbol{\epsilon})\mathbf{v}_j + n_q$	$\dfrac{1}{L^2}$	$Q\!\left(\sqrt{\gamma_{\mathrm{s}}}\big[\lambda_j\big(\mathbf{h}\odot(\hat{\mathbf{1}}_{N_{\mathrm{t}}} - 2\boldsymbol{\epsilon})\big)\mathbf{v}_j + \lambda_i(\mathbf{h}\odot\boldsymbol{\epsilon})\mathbf{v}_i\big]\right)$
				$3 \le q \le L$	n_q		$Q\!\left(\sqrt{\gamma_{\mathrm{s}}}\big[\lambda_j\big(\mathbf{h}\odot(\hat{\mathbf{1}}_{N_{\mathrm{t}}} - \boldsymbol{\epsilon})\big)\mathbf{v}_j + \lambda_i(\mathbf{h}\odot\boldsymbol{\epsilon})\mathbf{v}_i\big]\right)$
D		$1 < m < L$	$E_{\mathrm{s}}\lambda_j\big(\mathbf{h}\odot(\hat{\mathbf{1}}_{N_{\mathrm{t}}} - \boldsymbol{\epsilon})\big)\mathbf{v}_j + z_m$	1	$E_{\mathrm{s}}\lambda_i(\mathbf{h}\odot\boldsymbol{\epsilon})\mathbf{v}_i + n_q$	$\dfrac{L-2}{L^2}$	$Q\!\left(\sqrt{\gamma_{\mathrm{s}}}\big[\lambda_j\big(\mathbf{h}\odot(\hat{\mathbf{1}}_{N_{\mathrm{t}}} - \boldsymbol{\epsilon})\big)\mathbf{v}_j - \lambda_i(\mathbf{h}\odot\boldsymbol{\epsilon})\mathbf{v}_i\big]\right)$
				$m+1$	$E_{\mathrm{s}}\lambda_j(\mathbf{h}\odot\boldsymbol{\epsilon})\mathbf{v}_j + n_q$		$Q\!\left(\sqrt{\gamma_{\mathrm{s}}}\big[\lambda_j\big(\mathbf{h}\odot(\hat{\mathbf{1}}_{N_{\mathrm{t}}} - 2\boldsymbol{\epsilon})\big)\mathbf{v}_j\big]\right)$
E		L	$E_{\mathrm{s}}\lambda_j\big(\mathbf{h}\odot(\hat{\mathbf{1}}_{N_{\mathrm{t}}} - \boldsymbol{\epsilon})\big)\mathbf{v}_j + z_m$	$\begin{array}{c}2 \le q \le L\\ q \ne m,\, q \ne m+1\end{array}$	$E_{\mathrm{s}}\lambda_i(\mathbf{h}\odot\boldsymbol{\epsilon})\mathbf{v}_i + n_q$	$\dfrac{1}{L^2}$	$Q\!\left(\sqrt{\gamma_{\mathrm{s}}}\big[\lambda_j\big(\mathbf{h}\odot(\hat{\mathbf{1}}_{N_{\mathrm{t}}} - \boldsymbol{\epsilon})\big)\mathbf{v}_j - \lambda_i(\mathbf{h}\odot\boldsymbol{\epsilon})\mathbf{v}_i\big]\right)$
				$1 < q < L$	n_q		$Q\!\left(\sqrt{\gamma_{\mathrm{s}}}\,\lambda_j\big(\mathbf{h}\odot(\hat{\mathbf{1}}_{N_{\mathrm{t}}} - \boldsymbol{\epsilon})\big)\mathbf{v}_j\right)$

Table 4.2: *Summary of the parameters and expressions for different pulse position combinations in a GSPPM scheme impaired by timing synchronisation error*

4.4.2 Synchronisation Error Analysis of GSSK

Considering a GSSK scheme with $\tau = 1$ [98, 102], according to Table 3.2, the symbol error probability of GSSK impaired by timing offset, $\overline{P}_{\text{e,sym}}^{\text{GSSK}}$, is obtained by substituting the following in (4.34): $L = 1$, $N_{\text{s}} = 2^{N_{\text{t}}}$, $T_{\text{c}} = T$ and $\lambda_j = 1, \forall j$. Thus, we obtain:

$$\overline{P}_{\text{e,sym}}^{\text{GSSK}} \leq \frac{1}{2^{2N_{\text{t}}}} \sum_{j=1}^{2^{N_{\text{t}}}} \sum_{\substack{k=1 \\ k \neq j}}^{2^{N_{\text{t}}}} \sum_{i=1}^{2^{N_{\text{t}}}} Q\left(\frac{\mathcal{U}_{i,j,k}^{\text{II}}}{|\mathbf{hv}_k - \mathbf{hv}_j|} \sqrt{\frac{\gamma_{\text{s}}}{2}} \right), \tag{4.37}$$

where $\mathcal{U}_{i,j,k}^{\text{II}}$ is defined by (4.16). Again, by setting $\{\epsilon_{n_{\text{t}}}\}_{n_{\text{t}}=1}^{N_{\text{t}}} = 0$, equation (4.37) reduces to the standard expression for the SER of an optical GSSK scheme without timing errors, as presented in (3.26).

4.4.3 Synchronisation Error Analysis of SPPM

From Table 3.2, the symbol error probability of an SPPM scheme with timing offsets, $\overline{P}_{\text{e,sym}}^{\text{SPPM}}$, can be obtained from that of GSPPM by setting $N_{\text{s}} = N_{\text{t}}$, and $\lambda_j = 1, \forall j$. Moreover, the cases considered in Section 4.3.1 for the detection of SCP in GSPPM also hold for the detection of the transmitter index in SPPM. Hence, from (4.18), the probability of correctly detecting the LED index (SCP) j, in SPPM is given by:

$$\overline{P}_{\text{c,scp}}^{\text{SPPM}}(j) = 1 - \frac{1}{L^2} \sum_{\substack{k=1 \\ k \neq j}}^{N_{\text{t}}} \left[(L^2 - 1)Q\left(\frac{\mathcal{Y}_{j,k}^{\text{I}}}{|h_k - h_j|} \sqrt{\frac{\gamma_{\text{s}}}{2}} \right) + \frac{1}{N_{\text{t}}} \sum_{i=1}^{N_{\text{t}}} Q\left(\frac{\mathcal{Y}_{i,j,k}^{\text{II}}}{|h_k - h_j|} \sqrt{\frac{\gamma_{\text{s}}}{2}} \right) \right], \tag{4.38}$$

where

$$\mathcal{Y}_{j,k}^{\text{I}} = h_j^2(1 - 2\epsilon_j) + 2h_j h_k(\epsilon_j - 1) + h_k^2 \tag{4.39}$$

$$\mathcal{Y}_{i,j,k}^{\text{II}} = h_j^2(1 - 2\epsilon_j) + 2h_j h_k(\epsilon_j - 1) + h_k^2 + 2h_i \epsilon_i(h_j - h_k). \tag{4.40}$$

Furthermore, the cases considered in the analysis of pulse position detection in GSPPM (in Section 4.3.2) also hold for the pulse position detection in SPPM. The expressions for the probabilities $\mathcal{P}_{j,\text{A}}, \ldots, \mathcal{P}_{j,\text{E}}$, in the case of GSPPM, are simplified for SPPM, and are denoted by $\widetilde{\mathcal{P}}_{j,\text{A}}, \ldots, \widetilde{\mathcal{P}}_{j,\text{E}}$, as presented in Table 4.3. From (4.32), the probability of correct pulse

Table 4.3: *Probability of error in pulse position detection for different pulse position combinations in SPPM with synchronisation errors.*

CASE	Probability of error in pulse position detection, $\widetilde{\mathcal{P}}$
A	$\widetilde{\mathcal{P}}_{j,\,\mathrm{A}} = \dfrac{(L-1)^2}{L^2}\left[Q\Big(h_j(1-2\epsilon_j)\sqrt{\gamma_\mathrm{s}}\Big) + (L-2)Q\Big(h_j(1-\epsilon_j)\sqrt{\gamma_\mathrm{s}}\Big)\right]$
B	$\widetilde{\mathcal{P}}_{j,\,\mathrm{B}} = \dfrac{(L-1)^2}{L^2}\,Q\Big(h_j(1-\epsilon_j)\sqrt{\gamma_\mathrm{s}}\Big)$
C	$\widetilde{\mathcal{P}}_{j,\,\mathrm{C}} =$ $\dfrac{1}{N_\mathrm{t}L^2}\sum\limits_{i=1}^{N_\mathrm{t}}\left[Q\Big(\big(h_j(1-2\epsilon_j)+h_i\epsilon_i\big)\sqrt{\gamma_\mathrm{s}}\Big) + (L-2)Q\Big(\big(h_j(1-\epsilon_j)+h_i\epsilon_i\big)\sqrt{\gamma_\mathrm{s}}\Big)\right]$
D	$\widetilde{\mathcal{P}}_{j,\,\mathrm{D}} = \dfrac{L-2}{N_\mathrm{t}L^2}\sum\limits_{i=1}^{N_\mathrm{t}}\left[Q\Big(\big(h_j(1-\epsilon_j)-h_i\epsilon_i\big)\sqrt{\gamma_\mathrm{s}}\Big) \quad + \quad Q\Big(h_j(1-\epsilon_j)\sqrt{\gamma_\mathrm{s}}\Big) \quad + \right.$ $\left. (L-3)Q\Big(h_j(1-2\epsilon_j)\sqrt{\gamma_\mathrm{s}}\Big)\right]$
E	$\widetilde{\mathcal{P}}_{j,\,\mathrm{E}} = \dfrac{1}{N_\mathrm{t}L^2}\sum\limits_{i=1}^{N_\mathrm{t}}\left[Q\Big(\big(h_j(1-\epsilon_j)-h_i\epsilon_i\big)\sqrt{\gamma_\mathrm{s}}\Big) + (L-2)Q\Big(h_j(1-\epsilon_j)\sqrt{\gamma_\mathrm{s}}\Big)\right]$

position detection in SPPM with LED index (SCP) j, can be expressed as:

$$\overline{P}_{\mathrm{c,ppm}}^{\mathrm{SPPM}}(j) = 1 - \left(\widetilde{\mathcal{P}}_{j,\,\mathrm{A}} + \widetilde{\mathcal{P}}_{j,\,\mathrm{B}} + \widetilde{\mathcal{P}}_{j,\,\mathrm{C}} + \widetilde{\mathcal{P}}_{j,\,\mathrm{D}} + \widetilde{\mathcal{P}}_{j,\,\mathrm{E}}\right) \tag{4.41}$$

Combining (4.38) and (4.41), the average symbol error probability for an SPPM scheme impaired by timing error is given by:

$$\begin{aligned}
\overline{P}_{\mathrm{e,sym}}^{\mathrm{SPPM}} &= \mathbb{E}\left[\overline{P}_{\mathrm{e,sym}}^{\mathrm{SPPM}}(j)\right] = \frac{1}{N_\mathrm{t}}\sum_{j=1}^{N_\mathrm{t}}\overline{P}_{\mathrm{e,sym}}^{\mathrm{SPPM}}(j) \\
&= \frac{1}{N_\mathrm{t}}\sum_{j=1}^{N_\mathrm{t}}\left[1 - \overline{P}_{\mathrm{c,scp}}^{\mathrm{SPPM}}(j) \times \overline{P}_{\mathrm{c,ppm}}^{\mathrm{SPPM}}(j)\right] \\
&= 1 - \frac{1}{N_\mathrm{t}}\sum_{j=1}^{N_\mathrm{t}}\left[\overline{P}_{\mathrm{c,scp}}^{\mathrm{SPPM}}(j) \times \left(1 - \widetilde{\mathcal{P}}_{j,\,\mathrm{A}} + \widetilde{\mathcal{P}}_{j,\,\mathrm{B}} + \widetilde{\mathcal{P}}_{j,\,\mathrm{C}} + \widetilde{\mathcal{P}}_{j,\,\mathrm{D}} + \widetilde{\mathcal{P}}_{j,\,\mathrm{E}}\right)\right]
\end{aligned}$$

$$\tag{4.42}$$

4.5 Simulation and analytical results

In this section, we present the simulation results of the effect of timing synchronisation error on the four SM schemes studied in the previous sections, and we verify these results with the analytical expressions. The simulation procedure is outlined in Algorithm 1 of Appendix C.1. The achieved SER is plotted against the SNR per bit γ_{b}. The channel path gains are obtained from the simulation of indoor OWC channel using the ray-tracing algorithm [38, 121] as described in Chapters 2. The normalized channel gain values for four transmitters are $[h_{n_{\mathrm{t}}}]_{n_{\mathrm{t}}=1}^{N_{\mathrm{t}}} = [1, 0.409, 0.232, 0.143]$.

4.5.1 SER results

The error performance plots for SSK and GSSK schemes (using $N_{\mathrm{t}} = 2$), for five different values of timing offsets, are depicted in Figure 4.5 and Figure 4.6, respectively. Similar plots for SPPM and GSPPM (using $N_{\mathrm{t}} = 2, L = 2$) are depicted Figure 4.7 and Figure 4.8 respectively. Note that these results represent the scenario in which synchronisation error occurs in both transmitter sources. These results show that the analytical approximations in (4.34), (4.35), (4.37), (4.42) bound the simulation results very tightly. The performance degradation caused by error in timing synchronisation is obvious from the figures. For example, at SER $= 10^{-5}$, compared to the perfectly synchronised case ($\epsilon = 0$), a timing offset of 10% of the pulse duration T, results in about 2 dB SNR penalty for SSK and a about 9 dB SNR penalty for GSSK. Similarly, for SPPM a timing offset of 10% of the pulse duration T_{c}, results in SNR penalty of about 3 dB.

4.5.2 Performance comparison of OSM schemes

To compare the effect of synchronisation error on the four SM schemes, using $N_{\mathrm{t}} = 2, L = 2$, we estimate the achieved SER at $\gamma_{\mathrm{b}} = 15$ dB, for different timing offsets as shown in Figure 4.9. For a fair comparison, each modulation scheme is implemented with the same average energy per symbol and the timing offset is normalised to the symbol duration, T. The specified timing offsets are assigned to both LEDs concurrently. It is observed in Figure 4.9 that SPPM and GSPPM are more sensitive to the effect of timing offset compared to SSK and GSSK, respectively. This is clearly shown by the slope of the plot for each scheme. The results show a relatively rapid increase in the SER of SPPM and GSPPM as timing offset increases, in contrast
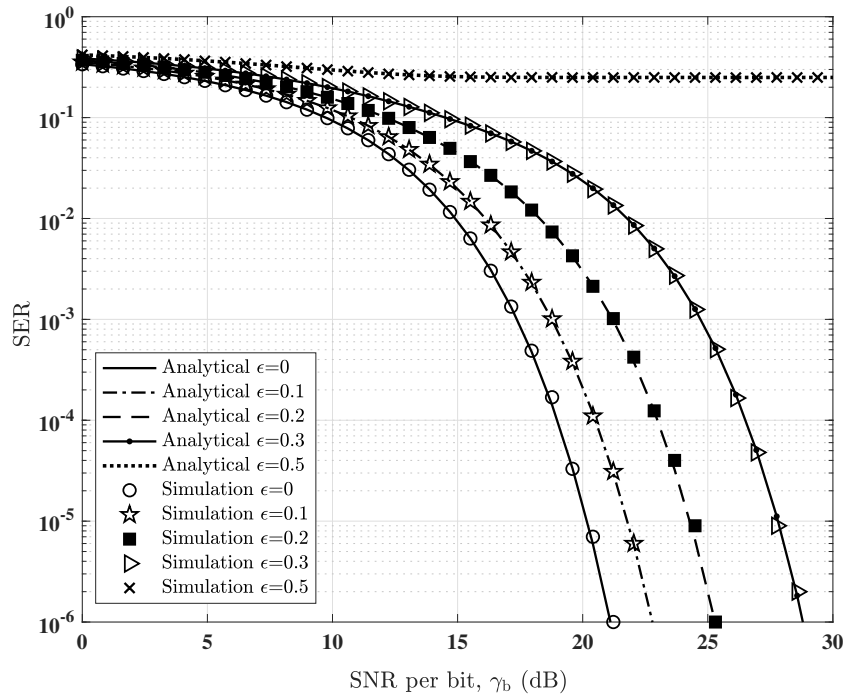
Figure 4.5: *Error performance of SSK impaired by timing synchronisation error.* $N_{\rm t} = 2$. *Channel gains:* $[h_1, h_2] = [1, 0.409]$. *Normalised offset:* $\epsilon_1 = \epsilon_2 = \epsilon$, $\epsilon = \Delta/T$.
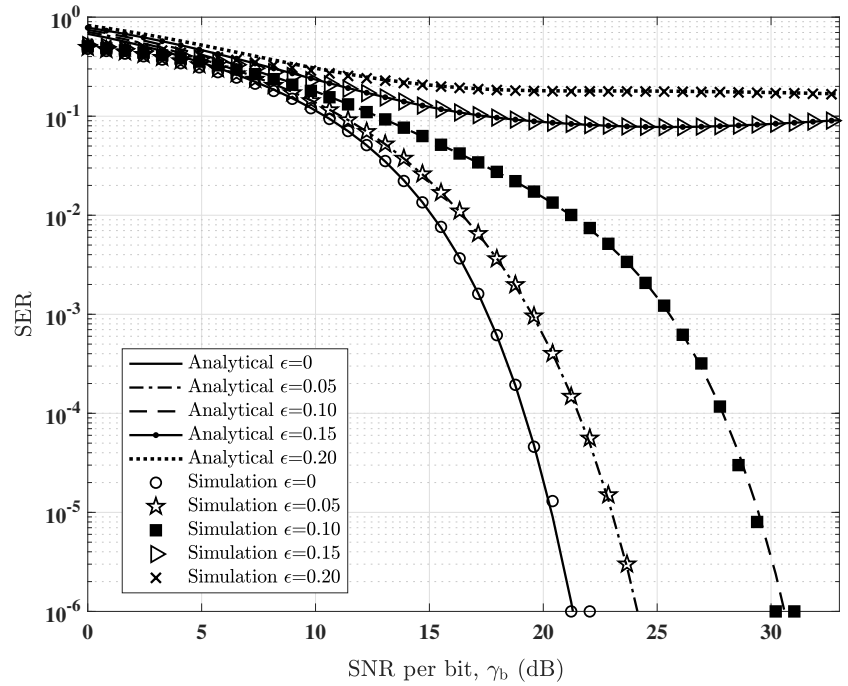
Figure 4.6: *Error performance of GSSK impaired by timing synchronisation error.* $N_{\rm t} = 2$. *Channel gains:* $[h_1, h_2] = [1, 0.409]$. *Normalised offset:* $\epsilon_1 = \epsilon_2 = \epsilon$, $\epsilon = \Delta/T$.
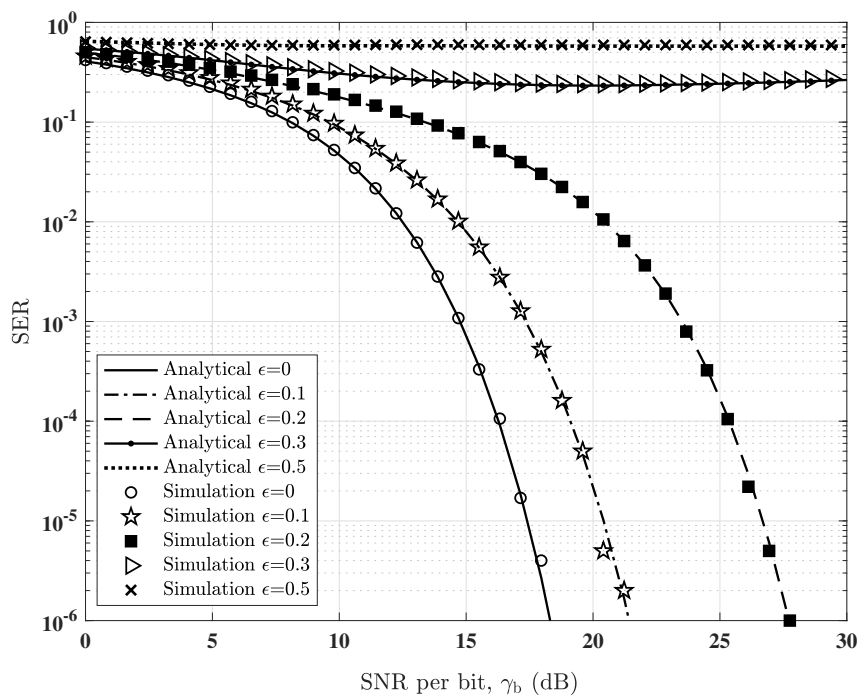
Figure 4.7: *Error performance of SPPM impaired by timing synchronisation error. $N_t = 2$, $L = 2$. Channel gains: $[h_1, h_2] = [1, 0.409]$. Normalised offset: $\epsilon_1 = \epsilon_2 = \epsilon$, $\epsilon = \Delta/T_c$.*
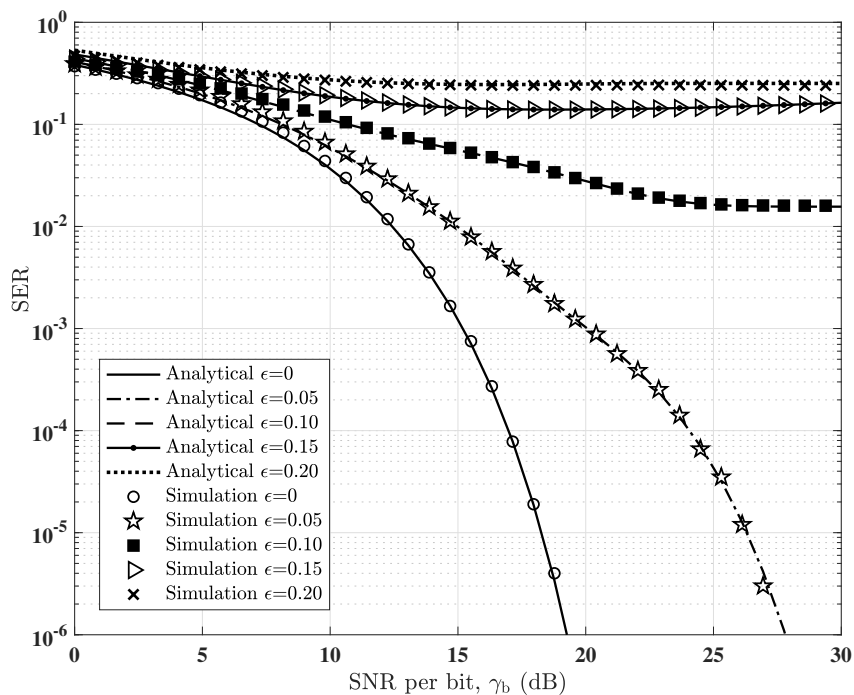
Figure 4.8: *Error performance of GSPPM impaired by timing synchronisation error. $N_t = 2$, $L = 2$. Channel gains: $[h_1, h_2] = [1, 0.409]$. Normalised offset: $\epsilon_1 = \epsilon_2 = \epsilon$, $\epsilon = \Delta/T_c$.*

to SSK and GSSK, respectively. For example, with reference to the zero-offset case ($\epsilon = 0$), a timing offset of 10% increases the SER from 10^{-6} to 3×10^{-4} in SPPM, whereas the SER of SSK increased from 7×10^{-3} to 10^{-2}. Though SPPM still achieved a better SER than SSK within the range: $0 \leq \tau \leq 0.18$, the energy efficiency gain that it harnessed from PPM is also rapidly lost to timing offset due to the sensitivity of PPM to synchronisation error [116, 117]. We also note that for $L = 2$, in SPPM and GSPPM, the duration of each PPM time slot is half
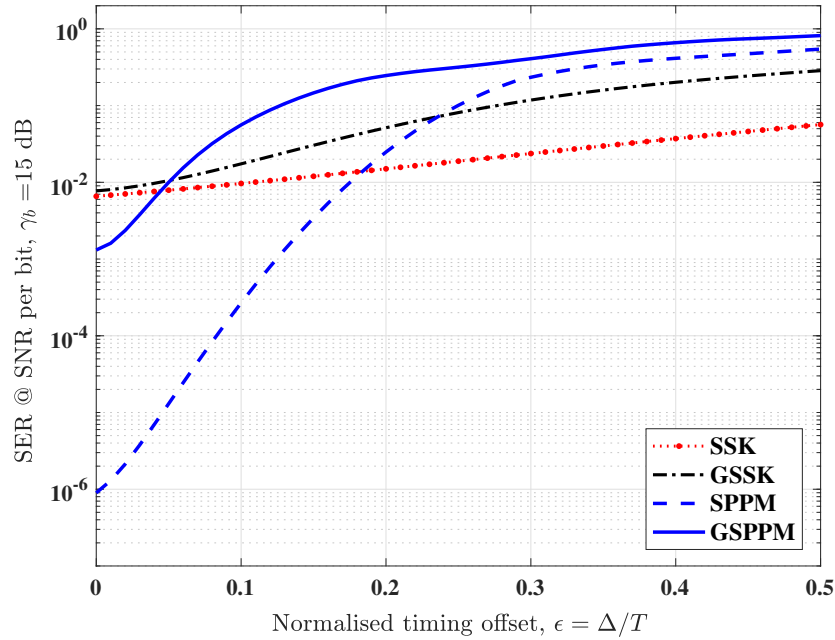
Figure 4.9: *Comparison of the effect of timing offset on SSK, SPPM, GSSK and GSPPM.* $N_{\mathrm{t}} = 2$, $L = 2$. *Channel gains:* $[h_1, h_2] = [1, 0.409]$.

of the symbol duration, hence, an offset of 10% of the symbol duration represent an offset of 20% of the pulse/slot duration and consequently, a 20% spillover in signal energy in SPPM and GSPPM as against a 10% energy spillover in SSK and GSSK. Besides, in SSK and GSSK, timing offset result in intersymbol interference while in SPPM and GSPPM, timing offset can result in both intersymbol interference and intrasymbol interference between PPM time slots. Furthermore, in Figure 4.9, as a result of multiple LEDs activation in GSSK against single-LED activation in SSK, the effect of timing errors is more pronounced in GSSK compared to SSK.

4.5.3 Impact of channel gain on performance

In Figure 4.10, we illustrate the impact of channel gain values (LED position) on the system performance using the GSPPM scheme as a case study. Using four LEDs, first, we introduce

timing offset in only one LED at a time, while the offsets in the other LEDs are set to zero. Then, equal timing offset is set in all the four LEDs concurrently. In all the cases, we estimate the achieved SER at $\gamma_b = 40$ dB. Note that the SER values higher than 1 are as result of the union bound approximation employed in the analytical derivation. It is observed in Figure 4.10 that the smaller the channel gain value of the LED in which synchronisation error occurs, the lesser the impact of the timing offset on the system performance. As an example, a timing offset of 10% of the slot duration, results in an increase in SER from 10^{-8} for the zero-offset case, to an error floor of SER ≈ 0.6 if the offset occurs in LED 1 ($h_1 = 1$), and an error floor of 0.2 if the offset occurs in LED 2 ($h_2 = 0.409$). While the achieved SER is 4×10^{-3} if the offset occurs in LED 3 ($h_3 = 0.232$) and 5×10^{-4} if the offset occurs in LED 4 ($h_4 = 0.143$). These results highlights the impact of channel gains values on the performance of SM technique. For instance, if timing offset is mainly due to difference in propagation delay, then by the inverse-square law of light radiation, the LEDs with larger delay (offset) are more likely to have the smaller channel gain, and thus lesser impact on performance.
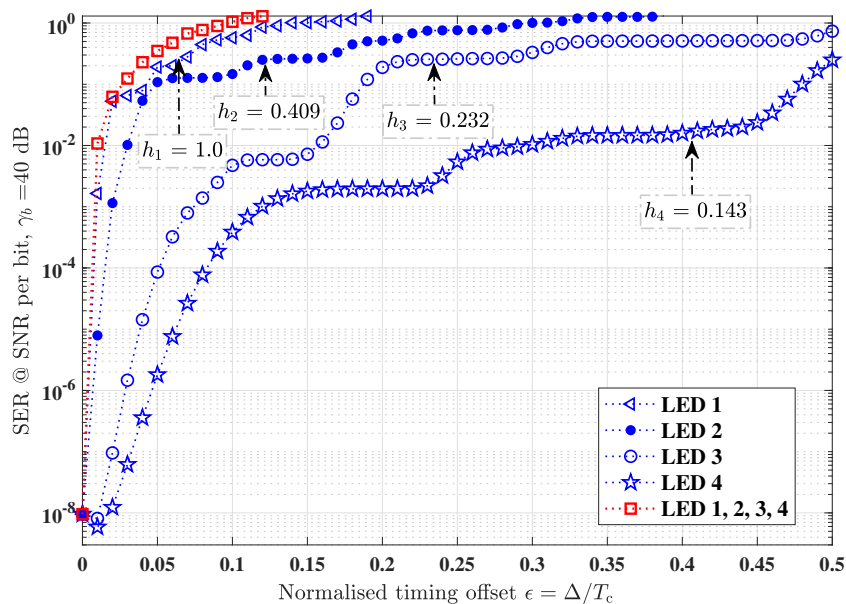
Figure 4.10: *Impact of channel gain values (transmitter location) on the error performance of GSPPM with timing offsets. $N_t = 4$, $L = 2$. Channel gains: $\{h_i\}_{i=1}^{N_t} = [1, 0.409, 0.232, 0.143]$.*

4.6 Summary

The effect of synchronisation error on SM based OWC systems has been investigated in this chapter. As a MIMO technique, SM exploits the physical deployment of multiple transmit

and receive elements. Synchronisation error between these multiple elements causes ISI which increases error rates. The analytical expressions for SER is derived for four different variants of SM, namely SSK, GSSK, SPPM and GSPPM, under the condition of imperfect timing synchronisation. These expressions validates the closely-matched simulation results, and they provide insight into how error in synchronisation affect the performance of SM techniques. Results show that error performance degrades with increasing synchronisation error. A comparison of the impact of timing offset on the performance of four OSM schemes highlights the tolerance of SSK to small range of synchronisation error compared to GSSK, SPPM, and GSPPM, though the former offers the lowest system capacity. The results obtained can be used to specify the threshold/tolerance level of each scheme to timing errors. Though SM technique relaxes synchronisation requirement by reducing the number of parallel data stream, these results have shown that accurate synchronisation is still critical, particularly for OSM schemes in which digital modulation is employed to enhance throughput. It worth mentioning that the results obtained here considers a scenario in which timing synchronisation error occurs in multiple transmitter-receiver paths. Also, the influence of channel gain values on the system performance is shown, and we observe that if timing synchronisation error occurs in the transmitter sources having smaller channel gain values, the impact on system performance is reduced.

Chapter 5

Performance of optical spatial modulation in indoor multipath channel

Most investigations on SM-based indoor OWC have considered performance evaluation in additive white Gaussian noise channel using LOS channel impulse response (CIR) only [102, 122, 123]. That is, the CIR has just a single tap. The assumption of LOS channel is suitable for low-speed transmission systems, where the symbol duration is long enough to capture the delayed signals arriving after multiple reflections from the room surfaces. However, in recent times, high-speed Gigabits per second (Gbps) optical wireless data communications have been demonstrated [35, 114]. Due to the shorter symbol duration in high-speed communication, the multipath propagation of the transmitted signal causes temporal dispersion, otherwise known as pulse spreading. The spreading of the transmitted pulse constitutes ISI which degrades system performance [49, 124]. Moreover, several works on indoor optical channel modelling have reported the significance of multiple reflections from room surfaces [51, 121, 125]. Thus, the assumption of an LOS channel represents an incomplete estimation of the system performance metric such a SNR and error rates. It is therefore imperative to explore the neglected effect of higher order reflections. Consequently, having conducted an evaluation of OSM schemes in LOS environment in Chapter 3, we now proceed in this chapter to investigate their performance in indoor multipath optical wireless channel by considering two OSM variants as representative schemes, namely: SSK and SPPM. In this chapter, the bandwidth limitation caused by the front-end devices, particularly the LEDs, is ignored. We focus solely on examining the impact of the multipath propagation of the transmitted signal.

First, a model of the multipath-induced ISI in SPPM is presented to account for the spreading of the transmitted signal due to multiple reflections. Using this ISI model, we then formulate the error performance analysis of SPPM in indoor multipath channel by deriving an analytical

approximation of the SER. In addition, we show that the SER for the LOS propagation of SPPM given by (3.27) in Chapter 3 can be obtained as a special case from the SER expression for multipath propagation. Furthermore, the analysis is extended to derive the SER of SSK for multipath and LOS propagations. As indoor OWC networks are to provide full coverage and mobility, we explore the spatial distribution of system performance parameters such as channel path gain, delay spread and multipath-induced power penalty. The rest of the chapter is organized as follows: the system model is provided in Section 5.1, while Section 5.2 presents a model to account for the multipath-induced ISI in SPPM. The error performance analyses in multipath and LOS indoor optical wireless channels are given in Section 5.3. The results of performance evaluation of the OSM schemes are presented and discussed in Section 5.4, and concluding remarks are given in Section 5.5.

5.1 SPPM system model

Using the description of SPPM given in Chapter 2, we consider an SPPM scheme with N_t LEDs and L time slots/chips in each symbol duration. Let $\mathbf{s} = [\mathbf{c}_1, \ldots, \mathbf{c}_N]$ denote a sequence of N consecutively transmitted SPPM symbols. The nth symbol, $\mathbf{c}_n$, is transmitted by activating LED Λ_n to transmit a pulse in slot ℓ_n of the L-PPM signal, where $\Lambda_n \in [1, N_\text{t}]$ and $\ell_n \in [0, L-1]$. Each SPPM symbol is a length-L binary chip sequence written as $\mathbf{c}_n = [c_n^{(0)}, \ldots, c_n^{(q)}, \ldots, c_n^{(L-1)}]$. The chip rate is $1/T_\text{c}$, where the duration of each PPM time slot $T_\text{c} = T/L$, and T is the SPPM symbol period. The entries of $\mathbf{c}_n$ are such that $c_n^{(q)} = 1$ if $q = \ell_n$, i.e., the pulse is transmitted in slot ℓ_n, otherwise $c_n^q = 0$. Therefore, the serialised sequence of LN chips for the N sequentially transmitted symbols is written as [96]:

$$
\begin{aligned}
\mathbf{s} &= \begin{bmatrix} s_0, \, s_1, \, \ldots, \, s_k, \, \ldots, \, s_{LN-1} \end{bmatrix} \\
&= \begin{bmatrix} c_1^{(0)}, \, \ldots, \, c_1^{(L-1)}, \, \ldots, \, c_n^{(0)}, \, \ldots, \, c_n^{(L-1)}, \, \ldots, c_N^{(0)}, \, \ldots, \, c_N^{(L-1)} \end{bmatrix}.
\end{aligned}
\tag{5.1}
$$

where $c_n^{(q)} = s_{(n-1)L+q}$. As an illustration, the chip sequence for a set of three consecutive SPPM symbols with $L = 4$ is depicted in Figure 5.1. The chips corresponding to each SPPM symbol are indicated in the figure.

The L-PPM data signal transmitted by each LED is obtained by passing the chip sequence $\mathbf{c}_n$ through a unit-energy rectangular pulse-shaping (transmitter) filter $p_\text{T}(t)$ of duration T_c.
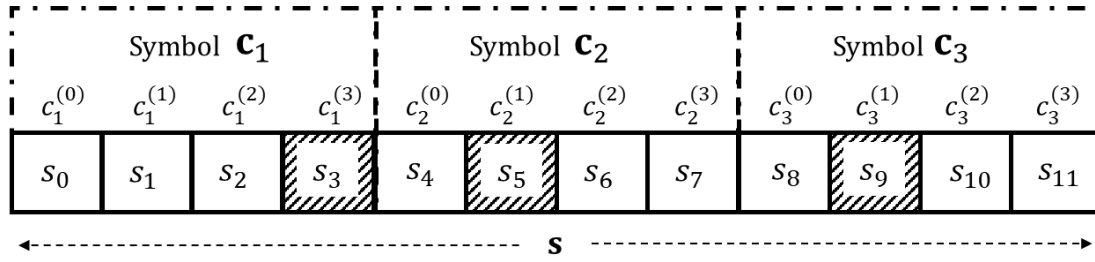
Figure 5.1: *A sample chip sequence consisting of three consecutive SPPM symbols, $\boldsymbol{c}_1, \boldsymbol{c}_2$ and $\boldsymbol{c}_3$, with $L = 4$ chips each. The shaded chips represent the pulse position of each symbol, i.e, the non-zero chips.*

The resulting signal is then scaled by the peak transmitted optical power $P_{\rm t}$. We consider a single detector at the receiver. The CIR of the subchannel from the Λ_n-th LED to the detector is denoted by $g_{\Lambda_n}(t)$, and it includes the LOS and the multipath components. Also, $g_{\Lambda_n}(t)$ is assumed to be fixed, positive, and of finite duration [124]. The MF receiver architecture employs a unit-energy receiver filter $p_{\rm R}(t)$, which is matched to $p_{\rm T}(t)$. For N transmitted SPPM symbols, the electrical signal at the output of the receiver filter is given by:

$$r(t) = RP_{\rm t} \sum_{\lambda=1}^{N} \sum_{k=(\lambda-1)L}^{\lambda L - 1} s_k \, \delta(t - kT_{\rm c}) \otimes p_{\rm T}(t) \otimes g_{\Lambda_\lambda}(t) \otimes p_{\rm R}(t) + \eta(t), \quad 0 \le t \le NT \quad (5.2)$$

where $\delta(.)$ is the Dirac delta function, $\otimes$ denotes convolution operation and R is the responsivity of the PD. The quantity $\eta(t)$ is the additive Gaussian noise at the receive filter output. By defining the combined impulse response of the channel, the transmitter filter and receiver filter as:

$$h_{\Lambda_\lambda}(t) = p_{\rm T}(t) \otimes g_{\Lambda_\lambda}(t) \otimes p_{\rm R}(t), \tag{5.3}$$

the output of the receive filter in (5.2) can thus be expressed as:

$$r(t) = RP_{\rm t} \sum_{\lambda=1}^{N} \sum_{k=(\lambda-1)L}^{\lambda L - 1} s_k \, h_{\Lambda_\lambda}(t - kT_{\rm c}) + \eta(t). \tag{5.4}$$

The MF output corresponding to each slot/chip of the transmitted symbols is obtained by

sampling at the chip rate $1/T_{\mathrm{c}}$, and is given by:

$$r_m = RP_{\mathrm{t}} \sum_{\lambda=1}^{N} \sum_{k=(\lambda-1)L}^{\lambda L-1} s_k \, h_{\Lambda_\lambda} \left((m-k)T_{\mathrm{c}} \right) + \eta_m$$

$$= RP_{\mathrm{t}} \sum_{\lambda=1}^{N} \sum_{k=(\lambda-1)L}^{\lambda L-1} s_k \, h_{\Lambda_\lambda}^{(m-k)} + \eta_m, \tag{5.5}$$

for $m = 1, 2, \ldots, LN$, where $h_{\Lambda_\lambda}^{(m-k)} = h_{\Lambda_\lambda}((m-k)T_{\mathrm{c}})$ is the discrete-time (DT) sample of the combined impulse response $h_{\Lambda_\lambda}(t)$, while the quantity $\eta_m = \eta(mT_{\mathrm{c}})$ is the DT noise sample at time $t = mT_{\mathrm{c}}$. For the nth received SPPM symbol, the MF samples corresponding to its L chips can be expressed as:

$$\mathbf{y}_n = \mathbf{x}_n + \mathbf{z}_n$$

$$[y_{n,q}]_{q=0}^{(L-1)} = [x_{n,q} + z_{n,q}]_{q=0}^{(L-1)}, \tag{5.6}$$

where $z_{n,q}$ denote Gaussian noise sample for slot q, having variance σ_z^2 and $x_{n,q}$ is the received signal sample in the absence of noise. By following (5.1), $y_{n,q}$ is obtained from (5.5) as:

$$y_{n,q} = r_{((n-1)L+q)}. \tag{5.7}$$

Therefore, the magnitude of the noise-free signal samples for the nth SPPM symbol are obtained from (5.5) as:

$$x_{n,q} = RP_{\mathrm{t}} \sum_{\lambda=1}^{n} \sum_{k=(\lambda-1)L}^{\lambda L-1} s_k \, h_{\Lambda_\lambda}^{((n-1)L+q-k)}. \tag{5.8}$$

The receiver makes decisions on the received symbol by determining the pulse position and the LED index combination which gives the minimum Euclidean distance metric from the received signal samples. That is, the estimate of the pulse position $\widehat{\ell}_n$ and the LED index $\widehat{\Lambda}_n$ are obtained as:

$$[\widehat{\ell}_n, \widehat{\Lambda}_n] = \arg\max_{q,\Lambda_n} f(\mathbf{y}_n|\mathbf{x}_n) = \arg\min_{q,\Lambda_n} \mathcal{D}\left(\mathbf{y}_n, \mathbf{x}_n \right). \tag{5.9}$$

The conditional PDF, $f(\mathbf{y}_n|\mathbf{x}_n)$ is expressed as:

$$f(\mathbf{y}_n|\mathbf{x}_n) = \frac{1}{(2\pi\sigma_z^2)^{L/2}} \exp\left[-\frac{\|\mathbf{y}_n - \mathbf{x}_n\|^2}{2\sigma_z^2}\right] \tag{5.10}$$

and the Euclidean distance metric is defined as

$$\mathcal{D}(\mathbf{y}_n, \mathbf{x}_n) = \|\mathbf{y}_n - \mathbf{x}_n\|^2. \tag{5.11}$$

5.2 Modelling ISI Due to Multipath Propagation

Let the DT combined impulse response for the LEDs, h_{n_t} for $n_t = 1,\ldots,N_t$, have equal number of taps, $K \geq 1$. For the purpose of this analysis, this assumption can be implemented by zero-padding the impulse response of the LEDs with smaller number of taps. The expression in (5.8) represents a convolution of the transmitted chip sequences from the first to the nth symbol with the DT combined impulse response of the LED that is activated to convey each symbol. This convolution operation implies that if $K > 1$, then, the pulse transmitted in any of the L slots of a symbol will spread into other time slots. That is, due to multipath propagation, the samples of any non-zero chip will interfere with the samples of other chips within the same symbol (intrasymbol interference). Moreover, depending on the number of channel taps and the number of chips in each symbol, the non-zero chip may also interfere with the chips in other neighbouring symbols (intersymbol interference) [124]. In this work, the term ISI refers to the collective effect of these two interference cases. In the following derivation, we present a model to account for the ISI incurred in a desired symbol due to pulse spreading.

Let $h_{n_t}^{(i)}$ for $i = 0,\ldots,(K-1)$, denote the amplitude of the i-th tap of the DT combined impulse response of the n_t-th LED. By defining the tap index as a non-negative integer in the range: $0 \leq i \leq K-1$, then, the limits of the second summation in (5.8) must satisfy the condition that:

$$0 \leq (n-1)L + q - k \leq K - 1. \tag{5.12}$$

That is,

$$(n-1)L + q - K + 1 \leq k \leq (n-1)L + q. \tag{5.13}$$

Therefore, the limits of (5.8) can be re-defined to satisfy (5.13), which yields:

$$x_{n,q} = RP_{\text{t}} \sum_{\lambda=1}^{n} \sum_{k=k_{\min}}^{k_{\max}} s_k \, h_{\Lambda_\lambda}^{(n-1)L+q-k}, \tag{5.14}$$

where

$$k_{\min} = \max\left((\lambda-1)L, \, (n-1)L+q-K+1\right) \tag{5.15a}$$

$$k_{\max} = \min\left((\lambda L - 1), \, (n-1)L+q\right). \tag{5.15b}$$

The functions $\max(a_1, a_2)$ and $\min(a_1, a_2)$ find the maximum and the minimum, respectively between two quantities a_1 and a_2. Furthermore, for a DT impulse response with K taps, the number of previously transmitted chips that are likely to interfere with a given chip is $(K-1)$. We refer to these as the *ISI chips*. Similarly, the number of previously transmitted symbols that can cause ISI in a given chip is $N_{\text{ISI}} = \left\lceil \frac{(K-1)}{L} \right\rceil$, where $\lceil \cdot \rceil$ denotes the ceiling function. Herein, these are referred to as the *ISI symbols*.

Consider a sequence of the first n consecutively transmitted symbols, $\mathbf{s} = \{\mathbf{c}_1, \ldots, \mathbf{c}_n\}$, where the nth symbol, $\mathbf{c}_n$, is the desired symbol received in the current symbol duration while the sequence $\mathbf{s}_{\text{ISI}} = \{\mathbf{c}_1, \ldots, \mathbf{c}_{n-1}\}$ represents the $(n-1)$ ISI symbols that are likely to interfere with symbol $\mathbf{c}_n$. That is, $n = N_{\text{ISI}} + 1$. For chip q of symbol $\mathbf{c}_n$, i.e., $c_n^{(q)}$, let $\mathbf{d}_{n,q}$ denote a sequence of K chips consisting of the chip $c_n^{(q)}$ and the $(K-1)$ ISI chips. Based on (5.14), the sequence $\mathbf{d}_{n,q}$ can be expressed as:

$$\mathbf{d}_{n,q} = \left[d_{n,q}^{(K-1)}, \, d_{n,q}^{(K-2)}, \ldots, d_{n,q}^{(i)}, \ldots, d_{n,q}^{(0)}\right] = \left[[s_k]_{k=k_{\min}}^{k_{\max}}\right]_{\lambda=1}^{n}. \tag{5.16}$$

Similarly, the sequence of DT impulse response samples for desired chip and the ISI chips is

written as:

$$\boldsymbol{\beta}_{n,q} = \left[\beta_{n,q}^{(K-1)}, \beta_{n,q}^{(K-2)}, \ldots, \beta_{n,q}^{(i)}, \ldots, \beta_{n,q}^{(0)}\right] = \left[\left[h_{\Lambda_\lambda}^{((n-1)L+q-k)}\right]_{k=k_{\min}}^{k_{\max}}\right]_{\lambda=1}^{n}. \quad (5.17)$$

As an illustration, considering the case of $n=3$, $L=4$ and $K=7$, then, $N_{\text{ISI}}=2$. The chips of the desired symbol $\mathbf{c}_3$ and the ISI symbols, $\mathbf{c}_1$ and $\mathbf{c}_2$, are depicted in Figure 5.2. For chip $c_3^{(1)}$, using (5.15), (5.16) and (5.17), the sequences $\mathbf{d}_{3,1}$ and $\boldsymbol{\beta}_{3,1}$ are obtained as:

$$\mathbf{d}_{3,1} = \left[d_{3,1}^{(6)}, d_{3,1}^{(5)}, \ldots, d_{3,1}^{(0)}\right] = [s_3, s_4, \ldots, s_9] \quad (5.18)$$

$$\boldsymbol{\beta}_{3,1} = \left[\beta_{3,1}^{(6)}, \beta_{3,1}^{(5)}, \ldots, \beta_{3,1}^{(0)}\right] = \left[h_{\Lambda_1}^{(6)}, h_{\Lambda_2}^{(5)}, h_{\Lambda_2}^{(4)}, h_{\Lambda_2}^{(3)}, h_{\Lambda_2}^{(2)}, h_{\Lambda_3}^{(1)}, h_{\Lambda_3}^{(0)}\right]. \quad (5.19)$$
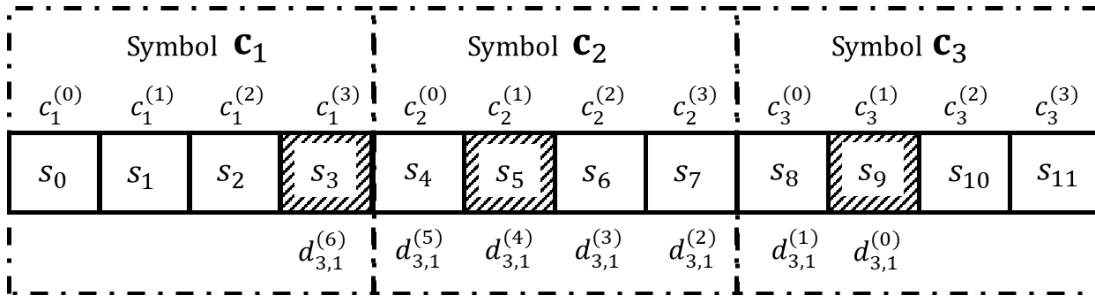
Figure 5.2: *A sample of chip sequence, $\mathbf{d}_{n,q}$, consisting of the chips of the desired symbol $\mathbf{c}_3$ and the chips of symbols $\mathbf{c}_1$ and $\mathbf{c}_2$ that are likely to cause ISI. $L=4$, $K=7$ and $n=3$. The shaded chips represent the pulse position of each symbol, i.e, the non-zero chips.*

Based on (5.14), (5.16) and (5.17), the magnitude of the noise-free signal sample received in slot $c_n^{(q)}$ can be expressed in term of the sequences $\mathbf{d}_{n,q}$ and $\boldsymbol{\beta}_{n,q}$ as:

$$x_{n,q} = RP_{\text{t}} \sum_{i=0}^{K-1} d_{n,q}^{(i)} \beta_{n,q}^{(i)}$$

$$= RP_{\text{t}} G_{n,q} + RP_{\text{t}} \widetilde{G}_{n,q}, \quad (5.20)$$

for $q \in [0, L-1]$, where

$$G_{n,q} = d_{n,q}^{(0)} \beta_{n,q}^{(0)} \quad (5.21)$$

$$\widetilde{G}_{n,q} = \sum_{i=1}^{K-1} d_{n,q}^{(i)} \beta_{n,q}^{(i)}, . \quad (5.22)$$

The quantity $G_{n,q}$ is the DT channel response of the ISI-free signal sample, while $\widetilde{G}_{n,q}$ is the combined DT channel responses of the interfering chip. The first term of (5.20), i.e., $\overline{x}_{n,q} = RP_{\mathrm{t}}G_{n,q}$, represents the magnitude of the ISI-free signal (without noise). The second term, $\widetilde{x}_{n,q} = RP_{\mathrm{t}}\widetilde{G}_{n,q}$, accounts for the multipath-induced ISI introduced by the previously transmitted symbols. Therefore, from (5.6), the MF samples corresponding to the L chips of the nth received SPPM symbol are obtained as:

$$y_{n,q} = RP_{\mathrm{t}}G_{n,q} \;+\; RP_{\mathrm{t}}\widetilde{G}_{n,q} + z_{n,q} \tag{5.23}$$

5.3 Error performance analysis

The correct detection of a transmitted SPPM symbol requires that both the pulse position and the LED index are correctly detected. Thus, the symbol error probability of SPPM is given by:

$$
\begin{aligned}
P_{\mathrm{e,sym}}^{\mathrm{SPPM}} &= 1 - P_{\mathrm{c,sym}}^{\mathrm{SPPM}} \\
&= 1 - \left(P_{\mathrm{c,scp}}^{\mathrm{SPPM}} \times P_{\mathrm{c,ppm}}^{\mathrm{SPPM}}\right)
\end{aligned}
\tag{5.24}
$$

where $P_{\mathrm{c,sym}}^{\mathrm{SPPM}}$ is the probability of correct SPPM symbol detection, $P_{\mathrm{c,ppm}}^{\mathrm{SPPM}} = \mathbb{P}(\hat{m} = m)$, is the probability of a correctly detected pulse position, and $P_{\mathrm{c,scp}}^{\mathrm{SPPM}} = \mathbb{P}(\hat{j} = j|\hat{m} = m)$, is the probability of correctly detecting the SCP (LED index), j, given that the pulse position has been correctly detected. The expressions for $P_{\mathrm{c,ppm}}^{\mathrm{SPPM}}$ and $P_{\mathrm{c,scp}}^{\mathrm{SPPM}}$ are obtained as follow.

5.3.1 Probability of correct pulse position detection

Considering that the desired symbol $\mathbf{c}_n$, is sent by activating LED Λ_n, the PEP that the receiver decides in favour of slot υ instead of slot ℓ_n, is the probability that the magnitude of the received signal sample in slot υ is greater than the magnitude of the sample in slot ℓ_n. That is,

$$
\begin{aligned}
\mathrm{PEP}_{\ell_n \to \upsilon}^{\Lambda_n} &= \mathbb{P}(y_{n,\upsilon} > y_{n,\ell_n}) \\
&= \mathbb{P}\Big(z_{n,\upsilon} - z_{n,\ell_n} > RP_{\mathrm{t}}(G_{n,\ell_n} + \widetilde{G}_{n,\ell_n} - G_{n,\upsilon} - \widetilde{G}_{n,\upsilon})\Big) \\
&= Q\left(\sqrt{\gamma_{\mathrm{s}}}\Big[G_{n,\ell_n} + \widetilde{G}_{n,\ell_n} - G_{n,\upsilon} - \widetilde{G}_{n,\upsilon}\Big]\right).
\end{aligned}
\tag{5.25}
$$

The symbol SNR, $\gamma_s = E_s/N_0$, the energy per symbol, $E_s = (RP_t)^2 T_c$, the noise variance $\sigma_z^2 = N_0 B/2$, and B is the bandwidth defined as the inverse of the slot duration, T_c. Using the union bound technique [106] with (5.25), the probability of error in the pulse position detection of the desired symbol sent by LED Λ_n, is obtained as:

$$
\begin{aligned}
P_{e,ppm}^{SPPM}(\Lambda_n) &\leq \sum_{\substack{v=0 \\ v \neq \ell_n}}^{L-1} PEP_{\ell_n \to v}^{\Lambda_n} \\
&= \sum_{\substack{v=0 \\ v \neq \ell_n}}^{L-1} Q\left(\sqrt{\gamma_s}\left[G_{n,\ell_n} + \widetilde{G}_{n,\ell_n} - G_{n,v} - \widetilde{G}_{n,v}\right]\right) \quad (5.26)
\end{aligned}
$$

Therefore, the probability of correct pulse position detection is expressed as:

$$
\begin{aligned}
P_{c,ppm}^{SPPM}(\Lambda_n) &= 1 - P_{e,ppm}^{SPPM}(\Lambda_n) \\
&\approx 1 - \sum_{\substack{v=0 \\ v \neq \ell_n}}^{L-1} Q\left(\sqrt{\gamma_s}\left[G_{n,\ell_n} + \widetilde{G}_{n,\ell_n} - G_{n,v} - \widetilde{G}_{n,v}\right]\right). \quad (5.27)
\end{aligned}
$$

5.3.2 Probability of correct LED detection

For a correctly detected pulse position of the desired symbol $\mathbf{c}_n$, i.e., $\widehat{\ell}_n = \ell_n$, the PEP that the receiver decides in favour of LED κ instead of Λ_n, is obtained as:

$$
PEP_{\ell_n}^{\Lambda_n \to \kappa} = \mathbb{P}\left(\left(y_{n,\ell_n} - RP_t G_{n,\ell_n}^{\Lambda_n}\right)^2 > \left(y_{n,\ell_n} - RP_t G_{n,\ell_n}^{\kappa}\right)^2\right) \quad (5.28)
$$

where $G_{n,\ell_n}^{\kappa} \neq G_{n,\ell_n}^{\Lambda_n}$, and the parameter $G_{n,\ell_n}^{\Lambda_n}$ is the value of G_{n,ℓ_n} obtained from (5.21) when the SPPM symbol is sent by activating the Λ_n-th LED. By applying (5.23) in (5.28), the PEP of the LED detection is obtained as:

$$
PEP_{\ell_n}^{\Lambda_n \to \kappa} = Q\left(\sqrt{\frac{\gamma_s}{2}}\left[\frac{\left(G_{n,\ell_n}^{\Lambda_n} - G_{n,\ell_n}^{\kappa}\right) \times \left(G_{n,\ell_n}^{\Lambda_n} - G_{n,\ell_n}^{\kappa} + 2\widetilde{G}_{n,\ell_n}^{\Lambda_n}\right)}{\left|G_{n,\ell_n}^{\kappa} - G_{n,\ell_n}^{\Lambda_n}\right|}\right]\right), \quad (5.29)
$$

where $\widetilde{G}_{n,\ell_n}^{\Lambda_n}$ is the value of $\widetilde{G}_{n,\ell_n}$ obtained from (5.22) if the symbol is sent by the Λ_n-th LED. Therefore, the union bound on the probability of error in detecting the LED index Λ_n, is

evaluated as:

$$P_{e,scp}^{SPPM}(\Lambda_n) \leq \sum_{\substack{\kappa=1 \\ \kappa \neq \Lambda_n}}^{N_t} \text{PEP}_{\ell_n}^{\Lambda_n \to \kappa}$$

$$= \sum_{\substack{\kappa=1 \\ \kappa \neq \Lambda_n}}^{N_t} Q \left(\sqrt{\frac{\gamma_s}{2}} \left[\frac{\left(G_{n,\ell_n}^{\Lambda_n} - G_{n,\ell_n}^{\kappa} \right) \times \left(G_{n,\ell_n}^{\Lambda_n} - G_{n,\ell_n}^{\kappa} + 2\widetilde{G}_{n,\ell_n}^{\Lambda_n} \right)}{\left| G_{n,\ell_n}^{\kappa} - G_{n,\ell_n}^{\Lambda_n} \right|} \right] \right).$$

$$(5.30)$$

Now, using (5.24), the error probability of the SPPM symbol that is transmitted by activating LED Λ_n to sent a pulse in PPM slot ℓ_n, is evaluated as:

$$P_{e,sym}^{SPPM}(\Lambda_n) = 1 - P_{c,scp}^{SPPM}(\Lambda_n) \times P_{c,ppm}^{SPPM}(\Lambda_n) \tag{5.31}$$

Finally, the average probability of symbol error is obtained by averaging $P_{e,sym}^{SPPM}(\Lambda_n)$ over: (i) the N_t equiprobable LEDs Λ_n that can be activated to sent the current symbol, (ii) the L possible positions of the transmitted pulse ℓ_n, (iii) the $(N_t)^{(n-1)}$ possible combinations of LEDs, $\Xi = \{ \boldsymbol{\Lambda} \mid \boldsymbol{\Lambda} = [\Lambda_1, \ldots, \Lambda_{n-1}] \}$, that are activated to send the ISI symbols, (iv) all the $L^{(n-1)}$ combinations of chip sequences for the ISI symbols, $\mathcal{S} = \{ \mathbf{s} \mid \mathbf{s} = [s_0, \ldots, s_{L(n-1)-1}] \}$. Thus, the average symbol error probability for SPPM in multipath channel is evaluated as:

$$P_{e,sym}^{SPPM}(\Lambda_n) = \mathbb{E}\left[P_{e,sym}^{SPPM}(\Lambda_n) \right]$$

$$\approx 1 - \frac{1}{(LN_t)^n} \sum_{\boldsymbol{\Lambda} \in \Xi} \sum_{\mathbf{s} \in \mathcal{S}} \sum_{\Lambda_n=1}^{N_t} \sum_{\ell_n=0}^{L-1} \left[P_{c,scp}^{SPPM}(\Lambda_n) \times P_{c,ppm}^{SPPM}(\Lambda_n) \right]. \tag{5.32}$$

5.3.3 Special case of LOS propagation of SPPM

For signal transmission involving only LOS propagation, the DT combined impulse response of the LEDs will have only one tap, i.e., $K = 1$. As such, $h_{\Lambda_n} = h_{\Lambda_n}^{(0)} \ \forall \Lambda_n$, where $h_{\Lambda_n}^{(0)}$ is the LOS DT impulse response of the Λ_n-th LED. Thus, $N_{ISI} = 0$, $n = 1$ and the desired symbol:

$\mathbf{c}_n \triangleq \mathbf{c}_1$. Also, (5.15) yields $k = k_{\min} = k_{\max} = q$, and (5.16) and (5.17) reduce to:

$$\mathbf{d}_{n,q} = d_{1,q}^{(0)} = s_q = c_1^{(q)}, \tag{5.33}$$

$$\boldsymbol{\beta}_{n,q} = \beta_{1,q}^{(0)} = h_{\Lambda_1}^{(0)}, \tag{5.34}$$

for $q \in [0, L-1]$. Therefore, (5.21) and (5.22) give:

$$G_{1,q} = h_{\Lambda_1}^{(0)} c_1^{(q)}; \quad \widetilde{G}_{1,q} = 0. \tag{5.35}$$

If the symbol $\mathbf{c}_1$ is conveyed by activating the LED Λ_n to transmit a pulse in slot ℓ_n, then the transmitted chip sequence is such that $c_1^{(q)} = 1$ if $q = \ell_n$, otherwise, $c_1^{(q)} = 0$. Thus, $G_{1,\ell_n} = h_{\Lambda_n}^{(0)}$ and $G_{1,q} = 0$, $\forall q, q \neq \ell_n$. Hence, for LOS propagation, by applying (5.35) in (5.25), the PEP that the receiver decides in favour of slot υ instead of ℓ_n, is:

$$\overline{\mathrm{PEP}}_{\ell_n \to \upsilon}^{\Lambda_n} = Q\left(G_{1,\ell_n} \sqrt{\gamma_{\mathrm{s}}}\right) = Q\left(h_{\Lambda_n}^{(0)} \sqrt{\gamma_{\mathrm{s}}}\right). \tag{5.36}$$

For L equally likely chips, the probability of correct pulse position detection in the LOS scenario is:

$$P_{\mathrm{c,ppm}}^{\mathrm{SPPM,LOS}}(\Lambda_n) = 1 - (L-1)Q\left(h_{\Lambda_n}^{(0)} \sqrt{\gamma_{\mathrm{s}}}\right). \tag{5.37}$$

Similarly, by using (5.35) in (5.29), the PEP that the receiver decides in favour of LED κ instead of LED Λ_n, is given by:

$$\overline{\mathrm{PEP}}_{\ell_n}^{\Lambda_n \to \kappa} = Q\left(\sqrt{\frac{\gamma_{\mathrm{s}}}{2}} \left|G_{1,\ell_n}^{\kappa} - G_{1,\ell_n}^{\Lambda_n}\right|\right) = Q\left(\left|h_{\kappa}^{(0)} - h_{\Lambda_n}^{(0)}\right| \sqrt{\frac{\gamma_{\mathrm{s}}}{2}}\right). \tag{5.38}$$

The probability of correctly decoding the LED index, conditioned on a correctly decoded pulse position, is:

$$P_{\mathrm{c,scp}}^{\mathrm{SPPM,LOS}}(\Lambda_n) \approx 1 - \sum_{\substack{\kappa=1 \\ \kappa \neq \Lambda_n}}^{N_{\mathrm{t}}} Q\left(\left|h_{\kappa}^{0} - h_{\Lambda_n}^{0}\right| \sqrt{\frac{\gamma_{\mathrm{s}}}{2}}\right). \tag{5.39}$$

By combining (5.37) and (5.39), the SER for an SPPM scheme involving only LOS propagation

is given by:

$$P_{\text{e,sym}}^{\text{SPPM,LOS}} \leq 1 - \frac{1}{N_{\text{t}}} \sum_{\Lambda_n=1}^{N_{\text{t}}} \left[\left[1 - \sum_{\substack{\kappa=1 \\ \kappa \neq \Lambda_n}}^{N_{\text{t}}} Q\left(\left| h_\kappa^{(0)} - h_{\Lambda_n}^{(0)} \right| \sqrt{\frac{\gamma_{\text{s}}}{2}} \right) \right] \times \left[1 - (L-1)Q\left(h_{\Lambda_n}^{(0)} \sqrt{\gamma_{\text{s}}} \right) \right] \right].$$

(5.40)

Clearly, (5.40) matches the SER expression for SPPM in LOS channel given by (3.27) in Chapter 3.

5.3.4 Analysis of SSK in multipath Channel

The analysis for SPPM presented above is now applied to obtain the SER of SSK in indoor multipath channel as follows. In SSK, since $L = 1$, then each symbol has just a single chip/slot, i.e., $q = 0$ and thus, $\mathbf{c}_u \triangleq c_u^{(0)}$, $\forall u$. Considering an n consecutively transmitted SSK symbol, $\mathbf{s} = \{\mathbf{c}_1, \ldots, \mathbf{c}_n\}$, the serialised sequence of the transmitted chips/symbols is written as:

$$\mathbf{s} = [s_0, s_1, \ldots, s_k, \ldots, s_{n-1}] = [c_1^{(0)}, c_2^{(0)}, \ldots, c_u^{(0)}, \ldots, c_n^{(0)}],$$

(5.41)

where $s_k = c_{k+1}^{(0)}$. Using the ISI model developed for SPPM in Section 5.2, for the DT combined impulse responses with $K \geq 1$ tap(s), the number of ISI symbols is equal to the number of interfering chips, and it is given by $N_{\text{ISI}} = K - 1$. Taking the nth SSK symbol, $c_n^{(0)}$, as the desired symbol received in the current symbol duration, where $n = N_{\text{ISI}} + 1 = K$, then, $\mathbf{s}_{\text{ISI}} = \{c_1^{(0)}, c_2^{(0)}, \ldots, c_{n-1}^{(0)}\}$ represents the $(K-1)$ previously transmitted ISI symbols. Therefore, using $L = 1$ and $q = 0$ in (5.15), we obtain:

$$k_{\min} = \max\left[\lambda - 1, n - K\right]$$

(5.42a)

$$k_{\max} = \min\left[\lambda - 1, n - 1\right].$$

(5.42b)

Now, since in (5.16), $1 \leq \lambda \leq n$, then $\lambda - 1 \leq n - 1$ and therefore, (5.42b) yields $k_{\max} = \lambda - 1$. Moreover, given that each symbol has just one chip, then $k = k_{\min} = k_{\max} = \lambda - 1$. This implies that in (5.42a), $\max\left[\lambda - 1, n - K\right] = \lambda - 1$. Hence, $\lambda - 1 \geq n - K$ and $\lambda \geq n - K + 1$. Consequently, (5.16) becomes:

$$\mathbf{d}_n = [d_n^{(K-1)}, d_n^{(K-2)}, \ldots, d_n^{(0)}] = \left[s_{(\lambda-1)} \right]_{\lambda=n-K+1}^{n}$$

(5.43)

Similarly, the sequence of the DT combined channel response corresponding to the desired and the ISI symbols is given by:

$$\boldsymbol{\beta}_n = [\beta_n^{(K-1)}, \beta_n^{(K-2)}, \ldots, \beta_n^{(0)}] = \left[h_{\Lambda_\lambda}^{(n-\lambda)}\right]_{\lambda=n-K+1}^{n}. \tag{5.44}$$

The desired symbol, $\mathbf{c}_n$ is sent by activating LED Λ_n. By using (5.43) and (5.44), the noise- and ISI-free magnitude of the MF sample for the desired symbol, is:

$$\bar{x}_n = RP_{\mathrm{t}}\, d_n^{(0)}\, \beta_n^{(0)} \;=\; RP_{\mathrm{t}} G_n. \tag{5.45}$$

and the ISI contributed by the previously transmitted symbols is expressed as:

$$\widetilde{x}_n = RP_{\mathrm{t}} \sum_{i=1}^{K-1} d_n^{(i)}\, \beta_n^{(i)} \;=\; RP_{\mathrm{t}} \widetilde{G}_n. \tag{5.46}$$

Combining (5.45) and (5.46), the magnitude of the MF sample for the desired symbol is:

$$y_n = \bar{x}_n + \widetilde{x}_n + z_n = RP_{\mathrm{t}}\,(G_n + \widetilde{G}_n) + z_n, \tag{5.47}$$

and the PEP that the receiver decides in favour of LED κ instead of Λ_n, is given by:

$$\mathcal{P}^{\Lambda_n \to \kappa} = \mathbb{P}\big((y_n - G_n^{\Lambda_n} RP_{\mathrm{t}})^2 \;>\; (y_n, -G_n^{\kappa} RP_{\mathrm{t}})^2\big)$$
$$= Q\left(\sqrt{\frac{\gamma_{\mathrm{s}}}{2}}\left[\frac{(G_n^{\Lambda_n} - G_n^{\kappa}) \times (G_n^{\Lambda_n} - G_n^{\kappa} + 2\widetilde{G}_n^{\Lambda_n})}{|G_n^{\kappa} - G_n^{\Lambda_n}|}\right]\right) \tag{5.48}$$

where $G_n^{\kappa} \neq G_n^{\Lambda_n}$. Since signal modulation is not transmitted by the activated LED in SSK, then, correct symbol detection implies correct LED detection. Thus, the symbol error probability of an SSK scheme is equal to the probability of error in detecting the LED. Now, considering the N_{t} equally likely LEDs, by averaging over all the $(N_{\mathrm{t}})^{(n-1)}$ possible combinations of the LEDs that can be activated to send the ISI symbols, $\Xi = \{\boldsymbol{\Lambda} \mid \boldsymbol{\Lambda} = [\Lambda_1, \ldots, \Lambda_{n-1}]\}$, the average SER of an SSK scheme in multipath channel is

given by:

$$P_{\text{e,sym}}^{\text{SSK}} \leq \frac{1}{(N_{\text{t}})^n} \sum_{\boldsymbol{\Lambda} \in \Xi} \sum_{\Lambda_n=1}^{N_{\text{t}}} \sum_{\substack{\kappa=1 \\ \kappa \neq \Lambda_n}}^{N_{\text{t}}} \mathcal{P}^{\Lambda_n \to \kappa}$$

$$= \frac{1}{(N_{\text{t}})^n} \sum_{\boldsymbol{\Lambda} \in \Xi} \sum_{\Lambda_n=1}^{N_{\text{t}}} \sum_{\substack{\kappa=1 \\ \kappa \neq \Lambda_n}}^{N_{\text{t}}} Q \left(\sqrt{\frac{\gamma_{\text{s}}}{2} \left[\frac{(G_n^{\Lambda_n} - G_n^{\kappa}) \times (G_n^{\Lambda_n} - G_n^{\kappa} + 2\widetilde{G}_n^{\Lambda_n})}{|G_n^{\kappa} - G_n^{\Lambda_n}|} \right]} \right) \quad (5.49)$$

For the LOS propagation of the SSK scheme, by setting $K = 1$, we obtain $\widetilde{G}_n^{\Lambda_n} = 0$, and the SER is given by:

$$P_{\text{e,sym}}^{\text{SSK,LOS}} \leq \frac{1}{N_{\text{t}}} \sum_{\Lambda_n=1}^{N_{\text{t}}} \sum_{\substack{\kappa=1 \\ \kappa \neq \Lambda_n}}^{N_{\text{t}}} Q \left(\left| h_{\kappa}^{(0)} - h_{\Lambda_n}^{(0)} \right| \sqrt{\frac{\gamma_{\text{s}}}{2}} \right). \quad (5.50)$$

5.4 Simulation and analytical results

The results of the performance evaluation of SPPM and SSK schemes in indoor multipath channel are presented in this section. The analytical results obtained from the expressions derived in Sections 5.3 are used to validate the simulation results obtained via MATLAB. The simulation procedure is outlined in Algorithm 1 of Appendix C.1. An OWC system with $N_{\text{t}} = 4$ LEDs is considered in an indoor multipath channel with LOS path as well as the first- and second-order reflections. The multipath CIR is obtained from simulations based on the ray-tracing algorithm [51] discussed in Chapter 2. The simulation parameters are provided in Table 5.1. The receiver is located at different coordinates across of the room. The values of reflectivity, ρ, are obtained from the typical measured values for different interior materials [121]. The setup configuration is designed in line with other papers on optical channel modelling [51, 121]. The configuration can however be varied to any dimension or number of sources.

The RMS delay spread, τ_{rms} is used to quantify the amount of dispersion experienced in the multipath channel, and it is given by (2.5). For a multiple LED system, the overall delay spread of the system is defined as: $\tau_{\text{rms}} = \max(\{\tau_{\text{rms}}^{n_{\text{t}}}\}_{n_{\text{t}}=1}^{N_{\text{t}}})$, where $\tau_{\text{rms}}^{n_{\text{t}}}$ is the RMS delay spread of the multipath link between the n_{t}-th LED and the detector. Furthermore, the CIRs of all the

Parameter	Value	Parameter	Value
Room dimension	$(5 \times 5 \times 3)$ m	PD Area (cm^2)	1.0
LED beaming angle, $\Phi_{1/2}$	60°	PD field of view	85°
LED separation	0.6 m	PD separation	0.05 m
LEDs orientation vector, $\hat{\mathbf{u}}_s$ (facing downward)	$[0,0,-1]$	PDs orientation vector, $\hat{\mathbf{u}}_r$ (facing upward)	$[0,0,1]$
$\rho_{\text{wall}}, \rho_{\text{ceiling}}, \rho_{\text{floor}}$	0.83, 0.48, 0.63		
LED coordinates (m)	LED1 - (1.25,1.25,3), LED2 - (1.25,3.75,3) LED3 - (3.75,1.25,3), LED4 - (3.75,3.75,3)		

Table 5.1: *OWC multipath channel simulation parameters.*

LEDs are normalised such that the impulse response of the LED with the highest path gain has unity area [51]. That is, $\max\limits_{n_{\text{t}} \in [1,N_{\text{t}}]} \left(\int_0^\infty g_{n_{\text{t}}}(t) \right) = 1$. With this assumption, if the LOS and all the multipath component signals are captured within a single symbol duration, then, for the LED with the best channel gain, the received optical power is equal to the peak transmitted optical power P_{t}.

5.4.1 SER performance results

To illustrate the performance of SPPM, we consider: $N_{\text{t}} = [2, 4]$ and $L = [2, 8]$, receiver coordinate: $(x, y, z) = (1.8, 2, 0)$m, and the LED coordinates as provided in Table 5.1. For a fair comparison, the system is designed to achieve equal bit rate for all values of L. For the case of $N_{\text{t}} = 2$, using LED1 and LED4, the plots of the SER against the SNR per bit, $\gamma_{\text{b}} = \gamma_{\text{s}}/\mathcal{M}$, are depicted in Figure 5.3. The number of bits/symbol, $\mathcal{M} = \log_2(LN_{\text{t}})$. It can be seen that the derived upper bound on the SER of SPPM in multipath channel is closely matched by the simulation results. The SER values greater than 1, as well as the slight deviations observed between the theoretical and simulation results at SER $> 10^{-2}$, is due to the union bound approximation used in the analysis. The closed form expression derived in Section 5.3 can therefore be used to study the performance of SPPM in more realistic indoor channel taking into account the multiple reflections of the transmitted signal.

At the specified LEDs and receiver locations, $\tau_{\text{rms}} = 2.32$ ns, which is equivalent to $0.14T_{\text{c}}$ and $0.29T_{\text{c}}$ for $L = 2$ and $L = 8$, respectively. The 3 dB bandwidth of the channel between the receiver and the LEDs, i.e., LED1 and LED4, is 50.5 MHz and 17.5MHz, respectively. Note that delay spread, τ_{rms}, as a function of T_{c}, amounts to the significance of the ISI. For example, $\tau_{\text{rms}} = 0$ implies the absence of ISI, while $\tau_{\text{rms}} > 0$ indicates the presence of ISI.
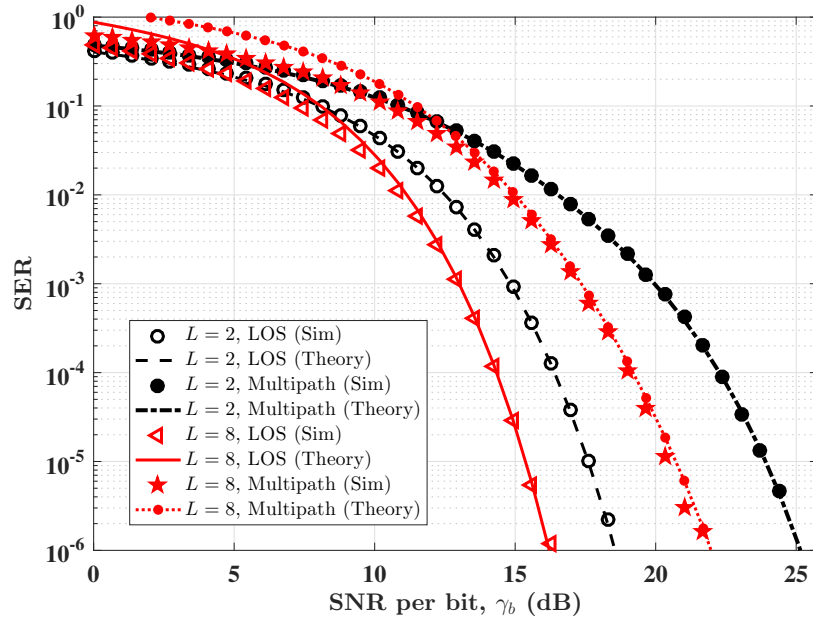
Figure 5.3: *Error performance of SPPM in LOS and multipath channel using $N_{\text{t}} = 2$, $L = [2, 8]$. $\tau_{\text{rms}} = 0.14 T_c$ and $0.29 T_c$ for $L = 2$ and $L = 8$, respectively. LOS channel gains: $[h_1^{(0)}, h_4^{(0)}] = [1, 0.3866]$.*

Due to the dispersion experienced in multipath channel, a higher value of SNR is required to achieve a given SER in multipath compared to LOS-only propagation. At a representative SER of 10^{-5}, due to ISI, multipath propagation incurs an SNR penalty of about 6.5 dB and 5.5 dB for $L = 2$ and $L = 8$, respectively. The SNR penalty is defined as $\Delta\gamma_{\text{b}} = \gamma_{\text{b,MP}} - \gamma_{\text{b,LOS}}$, where $\gamma_{\text{b,LOS}}$ and $\gamma_{\text{b,MP}}$ represent the SNR required to achieve a given value of SER under LOS and multipath propagation, respectively.

The error performance plots for the case of SPPM with $N_{\text{t}} = 4$ are shown in Figure 5.4. Evidently, the degradation in performance is more pronounced for $N_{\text{t}} = 4$ compared to $N_{\text{t}} = 2$. This is not unexpected because as the N_{t} increases, the spatial constellations become denser. This results in an increase in the SNR required to achieve a given SER. Moreover, as N_{t} increases, the requirement for a distinct channel response for all the LEDs becomes more stringent. Thus, there is an increasing likelihood that alteration in the actual channel response (due to ISI) will result in wrong LED detection. This can be observed in the case of $N_{\text{t}} = 4$ shown in Figure 5.4. Even at high SNR where the limiting effect of the noise has been greatly reduced, due to ISI, the receiver continually decodes some symbols erroneously, which results

in an irreducible SER.
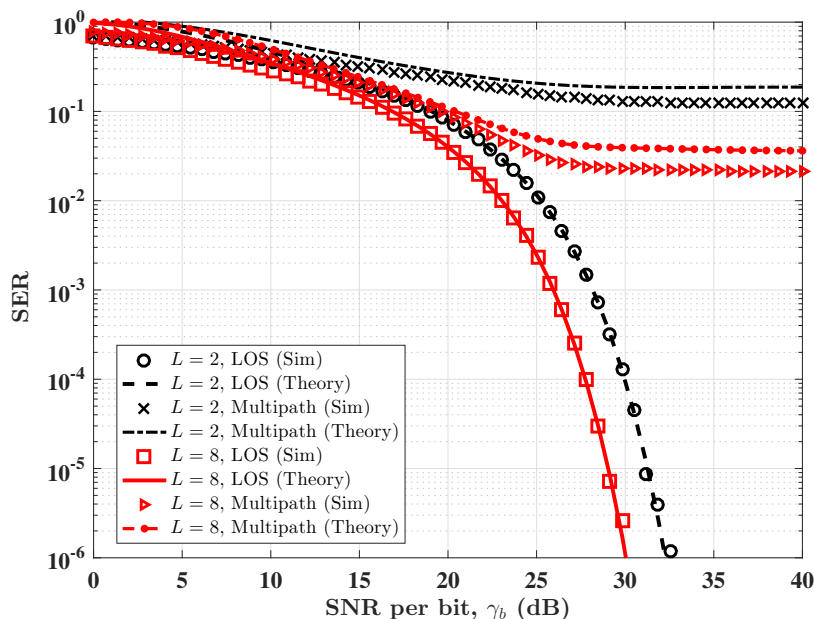
Figure 5.4: *Error performance of SPPM in LOS and multipath channel. $N_{\mathrm{t}} = 4$, $L = [2, 8]$. $\tau_{\mathrm{rms}} = 0.12 T_c$ and $0.29 T_c$ for $L = 2$ and $L = 8$, respectively. LOS channel gains: $[h_j^{(0)}]_{j=1}^{N_{\mathrm{t}}} = [1, 0.6365, 0.5448, 0.3866]$.*

Using the derived SER for SSK scheme (see Section 5.3.4), the SER plots for the case $N_{\mathrm{t}} = 2$ are shown in Figure 5.5. The RMS delay spread is normalised by the symbol duration T, and the SER plots for LOS propagation and two different symbol rates are shown. The derived analytical upper bound is closely matched by the simulation results. Expectedly, as the data rate increases, the error performance of the system degrades. This is because as the data rate increases, the symbol duration reduces, and thus the ISI caused by the spreading of the transmitted pulse becomes more significant.

5.4.2 SNR requirement versus delay spread

In Figure 5.6, the SNR, $\gamma_{\mathrm{b,MP}}$, required to achieve SER of 10^{-5} in multipath channel is plotted against the normalised RMS delay spread, $\tau_{\mathrm{rms}}/T_{\mathrm{c}}$. For this case, $N_{\mathrm{t}} = 2$, $L = [2, 4, 8]$ and receiver coordinate: $(x, y, z) = (0.6, 1.8, 0)$ m. All the schemes are implemented with the same bitrate and average transmitted optical power. As L increases from 2 to 8, SPPM benefits from the increasing energy efficiency in terms of SNR. However, the SNR penalty incurred in multipath channel also increases due to the shorter pulse duration. Moreover, As L increases,
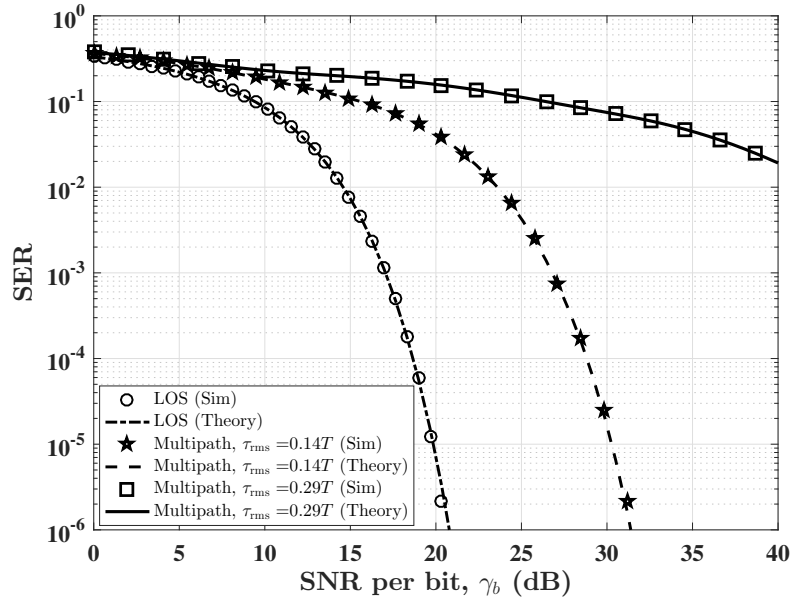
Figure 5.5: *Error performance of SSK in LOS and multipath channel. $N_\mathrm{t} = 2$, $\tau_\mathrm{rms} = 0.14T$ and $0.29T$. LOS channel gains: $[h_1^{(0)}, h_4^{(0)}] = [1, 0.3866]$, SNR per bit, $\gamma_\mathrm{b} = \gamma_\mathrm{s}/M$.*

the probability of intrasymbol interference due to pulse spreading increases. Consequently, the energy saving achieved by using a given value of L can be lost to multipath penalty if the delay spread exceeds a certain threshold. For instance, in Figure 5.6, for $\tau_\mathrm{rms} > 0.35T_\mathrm{c}$ and $\tau_\mathrm{rms} > 0.38T_\mathrm{c}$, the SNR required for $L = 8$ exceeds those for $L = 4$ and $L = 2$, respectively.

5.4.3 Impact of multipath CIR on performance

In SM, correct symbol detection requires an accurate detection of the LED index, hence, the system performance is highly dependent on the disparity of the CIR LEDs. In Figure 5.7, we illustrate how this impacts on performance in multipath channels. For an SPPM configuration with $L = 8$, using a pair of LEDs at different positions, Figure 5.7 depicts the SNR required to attain an SER of 10^{-5} in LOS and multipath channels. Also included in Figure 5.7, is the SNR penalty suffered in the multipath channel compared to the LOS channel. The normalised LOS path gain of the four LEDs are: $\{h_j^{(0)}\}_{j=1}^{N_\mathrm{t}} = [1, 0.6365, 0.5448, 0.3866]$. It is observed that for both LOS and multipath channels, as the difference between the channel responses of the two LEDs narrows, the required SNR increases. However, the increase in SNR is higher for multipath than for LOS channels. For instance, the difference between the required SNR for the gain sets A ($[h_1^{(0)}, h_2^{(0)}] = [1, 0.6365]$) and C ($[h_1^{(0)}, h_4^{(0)}] = [1, 0.3866]$) is about 3 dB
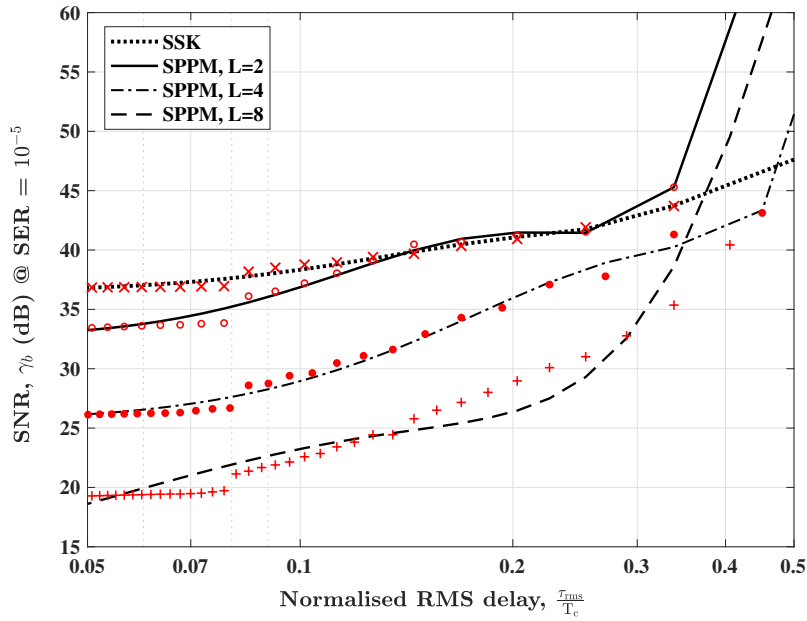
Figure 5.6: *SNR requirement in multipath channel ($\gamma_{b,MP}$) versus normalised RMS delay spread. The lines represent fifth-order polynomial fits to the data (Markers) for each scheme.*
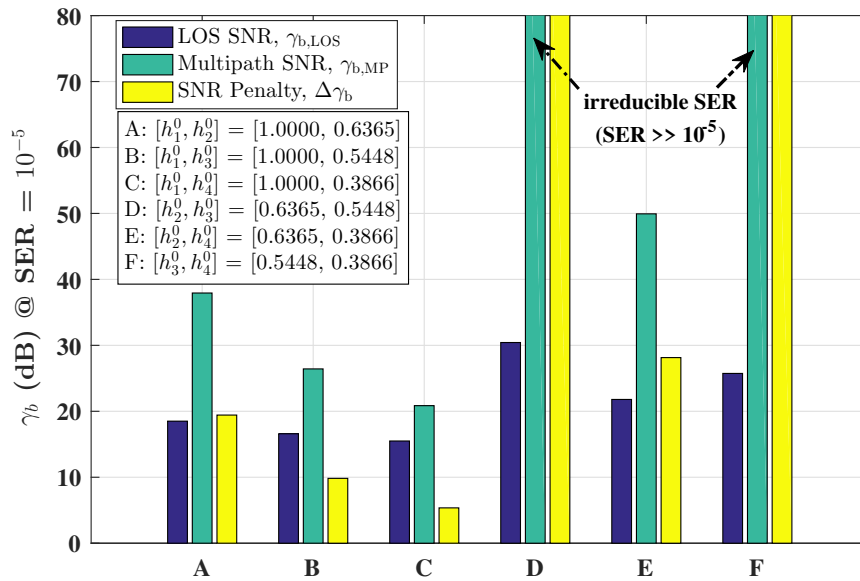
Figure 5.7: *SNR requirement in LOS and multipath channel for different LED pairs. $N_t = 2$, $L = 8$.*

for the LOS channel as against 14 dB for multipath channel. The higher SNR requirement in multipath can be attributed to the fact the ISI incurred in multipath channel also alters the actual channel response for the received signal, thereby making the received symbol appear as though it had been sent by another LED. Thus, even if the pulse position can be estimated from

the received amplitude when compared to the unfilled slots, the multipath-induced ISI could still cause erroneous LED detection. For less distinct channel responses, the incurred ISI can readily overcome the path gain difference to cause LED detection errors. As an example, for case D with a gain difference of $|h_2^{(0)} - h_3^{(0)}| = 0.0917$, LED2 can be wrongly detected as LED3 if the combined gain of all the interfering samples exceeds half of this gain difference. Hence, even at high SNR, the SER reaches an irreducible level because the receiver continues to decode the LED index of some sets of symbols erroneously. This corroborates the reported dependence of OSM schemes on path gain disparity [23, 93], and highlights the significant impact of multipath ISI on the system performance.

5.4.4 Mobility analysis using spatial distribution

As indoor OWC networks are to provide coverage and mobility, we explore the spatial distribution of system performance parameters such as channel response, delay spread and multipath-induced power penalty across the entire area of the room. We consider an SPPM scheme with $N_t = 2$ (LED1 and LED4) and $L = 8$. The receiver is positioned at different locations across the room. The spatial distributions of $\Delta\gamma_b$ and τ_{rms} are shown in Figure 5.8a and 5.8b, respectively. Also shown in Figure 5.8c is the absolute difference, Δh, between the normalised LOS channel gain of both LEDs, i.e., $\Delta h = |h_1^{(0)} - h_4^{(0)}|$. Given the symmetry of the configuration, similar plots can be obtained for LED2 and LED3. As observed in Figure 5.8, multipath propagation impacts differently at different locations. The delay spread is highest if the receiver is positioned in the vicinity of any of the two LEDs. This is because if the receiver is located close to LED1 for example, then even though LED1 will have a small value of τ_{rms}, the value of τ_{rms} will be bigger for LED4 because it is farther from the receiver. Thus, as shown in Figure 5.8a, the SNR penalty in the vicinity of both LEDs are very high due to the increase in multipath-induced ISI. Along the centre of the room where the receiver is equidistant from both LEDs, τ_{rms} has a relative smaller value (about 1.7 ns, see Figure 5.8b). However, because the LOS channel responses are identical in this area of the room, $0.1 \leq \Delta h \leq 0$ (see Figure 5.8c), the corresponding value of $\Delta\gamma_b$ shown in Figure 5.8a is very high. In fact, the SER lies in the range: $0.02 < SER \leq 0.5$. This observation is not unexpected since SM techniques, like most MIMO techniques, are highly dependent on the identifiability (disparity) of the multiple channels. As an SM technique, SPPM performs better when both Δh and the individual
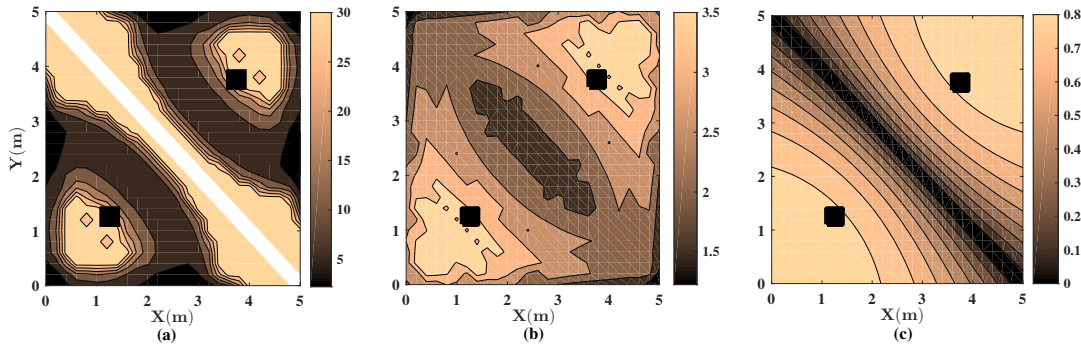
Figure 5.8: *Distribution of (a) SNR penalty, $\Delta\gamma_b$ (dB), (b) RMS delay spread τ_{rms} (nsec), and (c) Δh, across the room. $N_t = 2$, $L = 8$. The square markers indicate the position of transmitters LED1 and LED4. The white regions in (a) indicate the receiver locations at which SER $\gg 10^{-5}$*

channel response values are optimized [92, 93] as demonstrated in Chapter 3.

To further demonstrate how the interaction between channel response and multipath-induced ISI impacts on the performance, we extract the line plots in Figure 5.9 from the contour plots of Figure 5.8. The receiver is positioned at different points along the y-axis, while the x coordinate is fixed at 2.0 m. Figure 5.9a depicts Δh and τ_{rms} on the left and right y-axis, respectively. Figure 5.9b depicts the plot of $\gamma_{b,LOS}$ and $\gamma_{b,MP}$ required to achieve an SER of 10^{-5}. In Figure 5.9, it is observed that in the range: $0 \leq Y \leq 2$ m, as Δh reduces from 0.8 to 0.56, $\gamma_{b,LOS}$ reduces gradually from about 23 dB to its lowest value of 15 dB. However, in the same range, the graph of $\gamma_{b,MP}$, shows a trend that follows τ_{rms} rather than Δh. This is indicated by the similarity between the slopes of the graphs for $\gamma_{b,MP}$ and τ_{rms}. On the contrary, in the range: $2 \leq Y \leq 3$, even though τ_{rms} continued to decrease from about 2.2 to 1.6 ns, γ_b^{mp} shows an opposite trend by increasing from about 21 dB into the region of irreducible SER ($0.02 < \text{SER} \leq 0.5$). The observed trend for $\gamma_{b,MP}$ is similar to that of $\gamma_{b,LOS}$, and this indicates the dominance of the Δh component over the multipath ISI. As Δh decreases, the dissimilarity between the channel responses reduces, thereby making the transmitted symbol less distinguishable at the receiver. The performance of SPPM is largely dictated by the channel response values and the difference between these values. However, the ISI caused by multipath dispersion can adversely impact the identifiability of the subchannels by altering the channel response values.
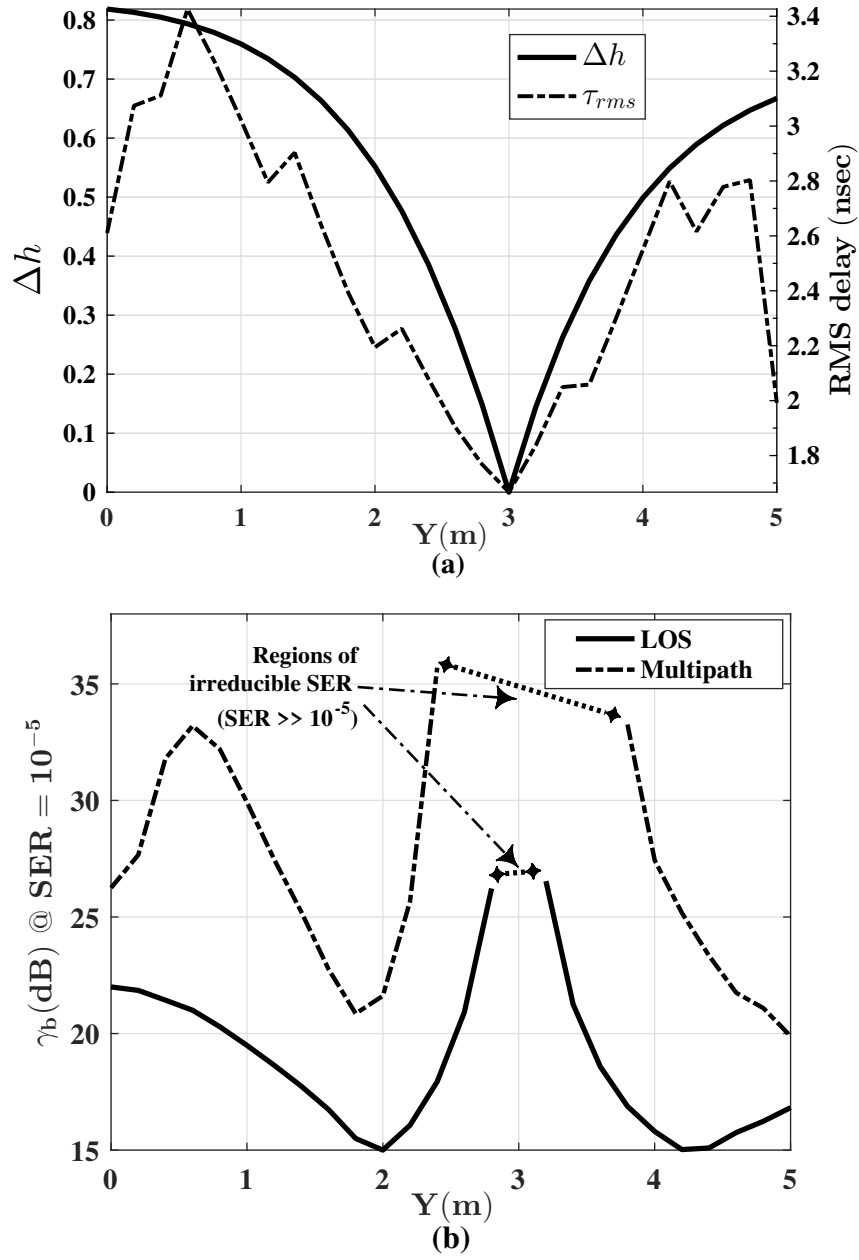
Figure 5.9: *(a) Plot of Δh and τ_{rms} (b) Plots of $\gamma_{\mathrm{b,LOS}}$ and $\gamma_{\mathrm{b,MP}}$, for different receiver locations along the y-axis at $X = 2.0\,m$. $N_{\mathrm{t}} = 2$ and $L = 8$.*

5.5 Summary

In this chapter, using SPPM and SSK as case studies, the performance of optical SM in an indoor multipath channel is studied. A model of the multipath-induced ISI in an OSM technique is presented. The model accounts for the spreading of the transmitted signal due to

multiple reflections from room surfaces. The ISI model is then used to derive the analytical upper bounds on the SER of SPPM and SSK under multipath propagation. Using a simulated indoor multipath channel with LOS and second-order reflections from the room surfaces, the theoretical derivations are used to verify the simulation results. The Multipath-induced ISI has significant impact on the performance of OSM schemes particularly on the detection of the activated transmitters. The incurred ISI can alter the actual channel response of the received symbol, thus making it appear as though it had been sent by a different transmitter source. In addition, to demonstrate how multipath propagation affects coverage and mobility, we presented the spatial distribution of channel gain, RMS delay spread and multipath-induced SNR penalty across the room. Results show how multipath propagation impacts system performance at different locations. The performance of SPPM is largely dictated by the channel response values and the difference between these values. However, the ISI caused by multipath dispersion can adversely impact the identifiability of the multiple channels by altering the actual channel response values.

Chapter 6

Pairwise coding for MIMO-OFDM VLC system

Although VLC technology provides access to a huge optical bandwidth resource, the electrical bandwidth of the VLC system is limited to several megahertz by the front-end devices, i.e., LEDs [13, 126]. As a result, for high data rate applications, spectrally efficient modulation techniques such as PAM [54] and OFDM [127] have been explored to increase throughput. However, as shown in the preceding Chapter 5, ISI due to the frequency selectivity of the LED response can significantly impair the performance of pulse modulation schemes such as PAM and PPM. Thus, as discussed in Chapter 2, the OFDM technique represents a viable solution in this regard. Besides, to achieve high data rates, SMP MIMO technique can also be employed to improve the capacity of VLC systems by exploiting the space domain of optical sources [23, 80]. Based on our review in Chapter 2, the performance of SMP MIMO technique is highly influenced by the degree of correlation among the spatially separated multiple links. Consequently, in typical indoor VLC systems where the MIMO channel matrix can be highly correlated, especially for direct LOS configurations [126], the achievable multiplexing gain is highly limited. Therefore, MIMO systems utilizing the singular value decomposition (SVD) architecture have been proposed to enhance system performance when channel state information (CSI) is known at the transmitter and receiver [128, 129]. The SVD architecture transforms the MIMO channel matrix into a set of parallel independent SCHs and it provides significant diversity gain [64, 130]. In an SVD-based MIMO-OFDM VLC system, the stronger the channel correlation, the more spread out the gains (singular values) of the independent SCHs created by the SVD, and the poorer the system performance [64]. The degree of channel correlation is quantified by the condition number, $\mathcal{C}_\mathrm{d}$, of the channel matrix, i.e., the ratio of the maximum to the minimum gains (singular values) of the independent SCHs. Higher the

value of C_d reflects a stronger channel correlation, and the bigger SNR imbalance between the independent SCHs. Similarly, the frequency selective fading due to the LED frequency response implies that the SCs in an OFDM frame are attenuated differently. This creates an imbalance in the received SNR of the SCs, and since the overall system performance is averaged across the SCs, then the system performance will be limited by the SCs with degraded SNR. As an illustration, considering the transmission of a 4-QAM OFDM signal with a bandwidth of 25 MHz using a 15 MHz LED modelled by a first order Butterworth low-pass filter (LPF) [22, 131]. From the power spectral density (PSD) values of the LED's input and output signals shown in Figure 6.1a, the SNR imbalance among the data-carrying SCs (indexed from 1 to 254) can be clearly observed. For instance, the LEDs' output shows a difference of about 44 dB between the best and the poorest SCs. The effect of this SNR imbalance is demonstrated by the bit error rate (BER) achieved at each SC. The BER plot obtained at average SNR per bit of 10 dB is shown Figure 6.1b. While the least attenuated SCs offer BER $< 10^{-4}$, the BER reaches about 0.9 at the most attenuated SCs. Consequently, on the average, the OFDM transmission could only achieve a BER of 2.94×10^{-2}.
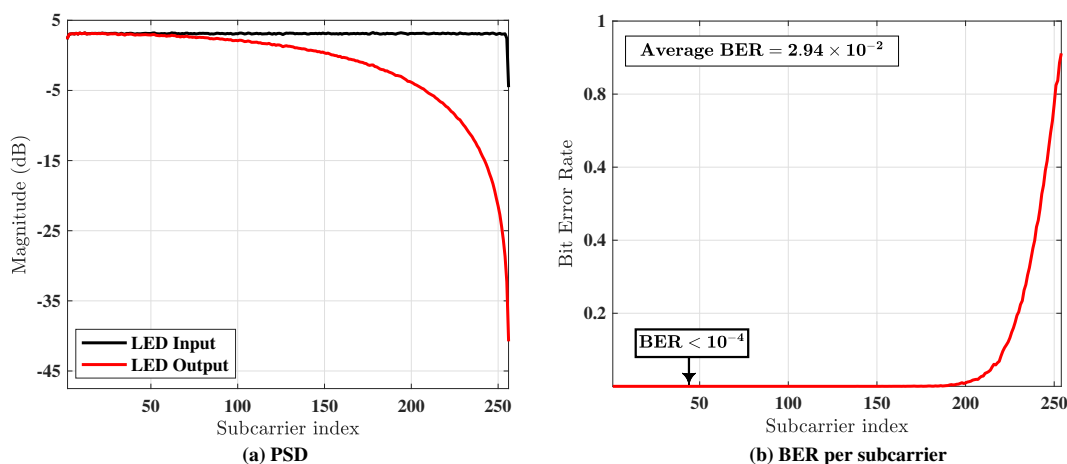
Figure 6.1: *Effect of SNR imbalance on error performance of OFDM SCs (a) PSD of LED's input and output signals (b) BER per SC. LED (LPF) bandwidth is 15 MHz and OFDM signal bandwidth is 25 MHz.*

In this chapter, we implement a joint coding of paired information symbols to mitigate the effect of the LEDs' bandwidth limitation and the strong correlation of the indoor VLC channel [23]. This coding technique, termed pairwise coding (PWC), is based on the rotated symbol constellation proposed in [132], and it is an effective method of improving overall

system performance when an SNR imbalance exists between channels [130, 133–136]. In RF communication over Rayleigh fading channels, the PWC technique was applied to improve the diversity gain of SISO systems in [132] and single-carrier MIMO systems in [130]. PWC has also been explored for optical OFDM over fibre channels to improve receiver sensitivity and reduce carrier power [133], to mitigate polarization dependent loss [137] and to decrease dispersion-induced power fading [135]. In SISO VLC systems, an adaptive scheme which combines PWC with selective SC loading is proposed in [138]. The merit of PWC is that for large SNR imbalance, significant improvement in system performance in terms of error rate, throughput or reliability can be achieved without additional power or bandwidth requirement.

In the following, an indoor MIMO-OFDM VLC system is modelled taking into account the LEDs' frequency selectivity, and the LOS channel impulse response of multiple LEDs and PDs. SVD-based precoding is employed to transforms the MIMO channel into independent SCHs, then PWC technique is applied across one or two dimensions, i.e., spatial and spectral dimensions, of the MIMO-OFDM VLC system to enhance system error performance by mitigating the effect of SNR imbalance across the OFDM SCs and MIMO SCHs. The BER plots show that high performance gains are achieved by using PWC compared to using only SVD precoding. Three different implementations of the PWC are compared in terms of SNR savings for different degrees of bandwidth limitation and MIMO channel conditions. Furthermore, the performance of the proposed DPWC scheme is investigated with experimental demonstration for different channel conditions and at varying data rates.

The remainder of this chapter is organized as follows. The system model and the SVD precoding scheme for the MIMO-OFDM VLC system are presented in Section 6.1. The encoding and decoding process for the PWC technique are then provided in Section 6.2. Section 6.3 presents and discusses the results of the performance evaluation via simulations. The experimental setup and results are provided in Section 6.4, while Section 6.5 gives the concluding remarks.

6.1 System description

We consider a MIMO-OFDM VLC system using N_t LEDs and N_r PDs for SMP MIMO setup, where $N_t \leq N_r$. The system block diagram is shown in Figure 6.2. By using the

OFDM technique, the frequency band of each MIMO transmitter SCH is divided into N_{sc} SCs, out of which N_d are data-carrying SCs on which information symbols are conveyed, while the rest are used as null SCs or Hermitian conjugate SCs. At the transmitter, first, the information bits are mapped into a specific M-ary QAM symbol constellation. Then, the S/P block converts the entire symbol stream into blocks of $N_t \times N_d$ complex symbols which are assigned to the N_d data-carrying SCs in the OFDM frames sent by the N_t LEDs. Next, on each SC, the frequency-domain MIMO channel is decomposed through the SVD operation, and the resulting singular values are then used to implement the PWC scheme which will be discussed in the next section. The CSI is known at both the transmitter and receiver. This is estimated using pilot symbols and the recursive least square (RLS) technique [139]. After the PWC block, the information symbols are precoded by multiplication with the SVD precoding matrix. As mentioned in Chapter 2, for VLC using IM/DD, real-time signals are required to modulate the LEDs' intensity. Hence, Hermitian symmetry is preserved by the IFFT operation on the precoded symbols in order to a obtain real-valued time domain signal. After adding the cyclic prefix (CP) and a suitable DC level, the time domain signal is then used to modulate the intensity of the LEDs.

At the receiver, the opto-electrical conversion of the incoming optical radiation is performed by the PDs. After post detection amplification and analogue-to-digital (A/D) conversion, the CP is removed and an FFT operation translates the received signal into its frequency domain equivalent. Then, the data symbols are extracted from the data-carrying SCs. The received signal is then decomposed into independent parallel SCHs by multiplying with the SVD decoding matrix. The estimates of the transmitted symbols are then obtained via the joint PWC decoding and MLD process detailed in Section 6.2.2. As stated above, for VLC systems, the time-domain transmitted and received signals as well as the channel gains are real-valued [63, 127]. Thus, in the frequency domain representation of the signals and the channel, the Hermitian conjugate SCs are mirror images of the data-carrying SCs. Therefore, in the following analysis, we focus on the data-carrying SCs.

6.1.1 SVD precoding

Considering the k-th data-carrying SC, the $N_r \times N_t$ frequency-domain MIMO channel matrix is given by $\mathbf{H}_k = [h_{i,j}^k]$, $i = 1, \ldots, N_r$, $j = 1, \ldots, N_t$, $k = 1, \ldots, N_d$, and $h_{i,j}^k$ corresponds to
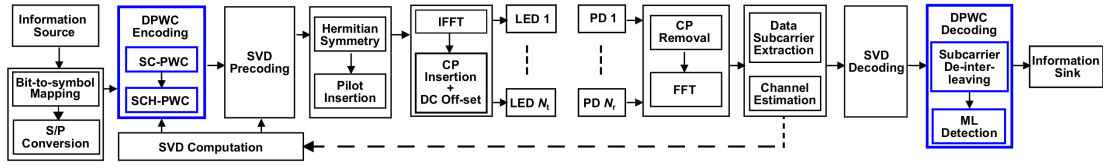
Figure 6.2: *Block diagram of MIMO-OFDM VLC system*

the channel coefficient of the SCH between the j-th LED and the i-th PD for the k-th OFDM SC. The precoding technique [64] is based on the SVD of the MIMO channel matrix of each SC, i.e., $\mathbf{H}_k = \mathbf{U}_k \mathbf{\Lambda}_k \mathbf{V}_k^*$, where $\mathbf{U}_k$ and $\mathbf{V}_k$ are unitary matrices of dimensions $N_r \times N_r$ and $N_t \times N_t$, respectively. The matrix $\mathbf{\Lambda}_k$ is the $N_r \times N_t$ rectangular diagonal matrix of the ordered non-negative singular values, i.e., $\lambda_{1,k} \geq \lambda_{2,k} \cdots \geq \lambda_{N_t,k} > 0$. Let the information symbols mapped to the N_t LEDs on the k-th SC be defined as $\mathbf{s}_k = [s_{1,k}, \ldots, s_{N_t,k}]^T$. The SVD-precoded symbol vector is given by $\mathbf{V}_k \mathbf{s}_k$, where $\mathbf{V}_k$ is the SVD precoding matrix. The received signal vector on the k-th data-carrying SC (in the frequency domain) is given by:

$$\mathbf{y}_k = \mathbf{H}_k \mathbf{V}_k \mathbf{s}_k + \mathbf{n}_k \tag{6.1}$$

where $\mathbf{n}_k$ is the i.d.d AWGN vector with variance, σ_n^2.

The received signal is then decomposed into independent parallel SCHs by multiplying with the matrix $\mathbf{U}_k^*$, and we obtain:

$$\mathbf{r}_k = \mathbf{U}_k^* \mathbf{H}_k \mathbf{V}_k \mathbf{s}_k + \mathbf{U}_k^* \mathbf{n}_k = \mathbf{\Lambda}_k \mathbf{s}_k + \mathbf{z}_k. \tag{6.2}$$

The final expression in (6.2) is obtained by exploiting the unitary properties of $\mathbf{U}_k$ and $\mathbf{V}_k$, i.e., $\mathbf{U}_k^* \mathbf{U}_k = \mathbf{I}_{N_r}$ and $\mathbf{V}_k^* \mathbf{V}_k = \mathbf{I}_{N_t}$. The Gaussian noise vector $\mathbf{z}_k = \mathbf{U}_k^* \mathbf{n}_k$ has the same statistics as $\mathbf{n}_k$, i.e., $\sigma_z^2 = \sigma_n^2$. Given that $\mathbf{\Lambda}_k$ is a diagonal matrix, then (6.2) represents the decomposition of the MIMO channels into N_t independent parallel SCHs. Therefore, for the SVD-based MIMO-OFDM system, the received symbol from the j-th transmitter SCH and the k-th OFDM SC is given by:

$$r_{j,k} = \lambda_{j,k} s_{j,k} + z_{j,k}. \tag{6.3}$$

Consequently, the singular value $\lambda_{j,k}$ corresponds to the equivalent channel gain associated
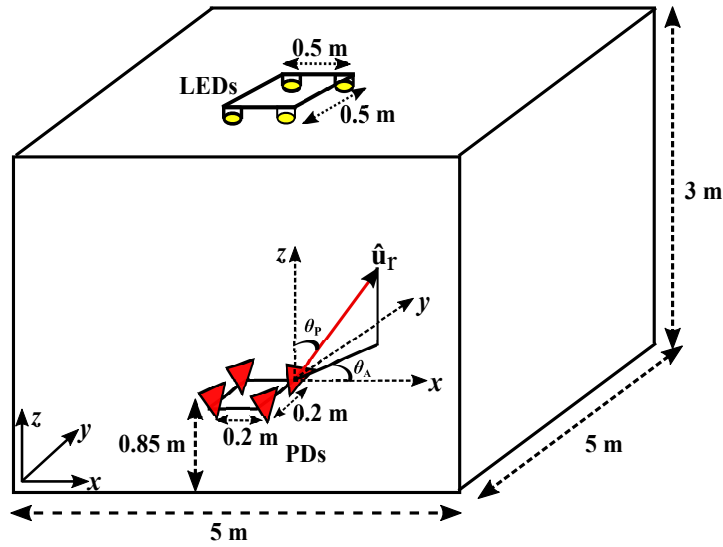
Figure 6.3: *Geometry of the indoor MIMO VLC system*

with the information symbol transmitted on the k-th SC by the j-th LED (transmitter SCH). From (6.3), the received SNR of the SCs on each of the parallel independent SCHs created by the SVD precoding is a factor of the SC gain, and it is given by $\gamma_{j,k} = \lambda_{j,k}^2 |s_{j,k}|^2 / \sigma_z^2$.

6.1.2 VLC channel model

The overall system response includes the LOS MIMO channel gain and the band-limiting LED response. The simulated LEDs' frequency response is modelled by a first order Butterworth LPF [22, 131]. The 3 dB bandwidth of the LEDs is set to be $B_{\text{LED}} = 15$ MHz (which is the measured 3 dB bandwidth of the experimental VLC link, as shown in Section 6.4). The configuration of the simulated indoor MIMO VLC link in a typical $5 \times 5 \times 3$ m room is depicted in Figure 6.3. In a 4×4 MIMO-OFDM system, the four LEDs are mounted on ceiling facing downward at 3 m above the floor, while the receiver plane is 0.85 m away from the floor. The VLC channel is simulated based on the source and receiver models in [51] and the simulation parameters used are provided in Table 6.1. Angular diversity is employed at the receiver to optimise the incident angle of the emitted intensity by varying polar and azimuthal angles of the PDs. Thus, using Figure 6.3, the orientation vector of the PDs are given by $\widehat{\mathbf{u}}_r = [\sin\theta_A \sin\theta_P, \sin\theta_A \sin\theta_P, \cos\theta_A \cos\theta_P]$ where θ_A is the azimuth angle on x-y plane and θ_P is the polar angle from the z-axis. The orientation vector of the LEDs which are facing downward vertically is obtained as $\widehat{\mathbf{u}}_t = [0, 0, -1]$. Using the azimuth angles of $45°$, $135°$,

225° and 315° for the four PDs, we obtain the optimal polar angles which ensure LOS channel gain to all the PDs and minimizes the off-diagonal values (cross channel gains) of the MIMO channel matrix.

Parameter	Value
LED beaming angle Φ	15° to 35°
LED separation	0.5 m
PD field of view	60°
PD separation	0.2 m
PD Area (cm^2)	1.0
Gain of optical filter	1.0
Concentrator refractive index	1.5
LEDs' coordinates (m)	(1.75,1.75,3), (1.75,2.25,3)
	(2.25,1.75,3), (2.25,2.25,3)
PDs' coordinates (m)	(1.9,1.9,0.85), (1.9,2.1,0.85)
	(2.1,1.9,0.85), (2.1,2.1,0.85)

Table 6.1: *VLC channel simulation parameters*

6.2 Implementation of pairwise coding for MIMO-OFDM VLC

As mentioned previously, PWC technique entails a joint coding of paired information symbols over the spectral and/or the spatial dimensions. This is illustrated in Figure 6.4 using 4-QAM. First, the information bits to be modulated onto a pair of SCs/SCHs are mapped into two complex QAM constellations, $\alpha = \alpha_r + \widetilde{i}\alpha_i$ and $\beta = \beta_r + \widetilde{i}\beta_i$, where α_r and β_r denote the real, i.e., in-phase (I) components, α_i and β_i denote the imaginary, i.e., quadrature (Q) components, and $\widetilde{i} = \sqrt{-1}$ is the imaginary unit. Then, a phase shift, ψ is applied to both constellations to obtain α_{rot} and β_{rot}, respectively. The phase rotation is then followed by I/Q component interleaving to generate the complex constellations α_{int} and β_{int} transmitted on each SC/SCH. The operators $\Re(\cdot)$ and $\Im(\cdot)$ provide the real and imaginary parts of a complex argument. This interleaving process transfers the SNR imbalance between the paired SC/SCH to the I and Q components of the symbols modulated onto the SCs/SCHs. The phase rotation transforms the classical symbol constellations such that a nonzero minimum distance exists between any two points. As such, with additive Gaussian noise, the ML detection error is reduced by maximising the minimum distance between the received symbols [130, 132]. The effectiveness of phase rotation is illustrated in Figure 6.5 with the diagram of classical (un-rotated) and rotated constellations for 4-QAM. With I/Q component interleaving, only one of the components
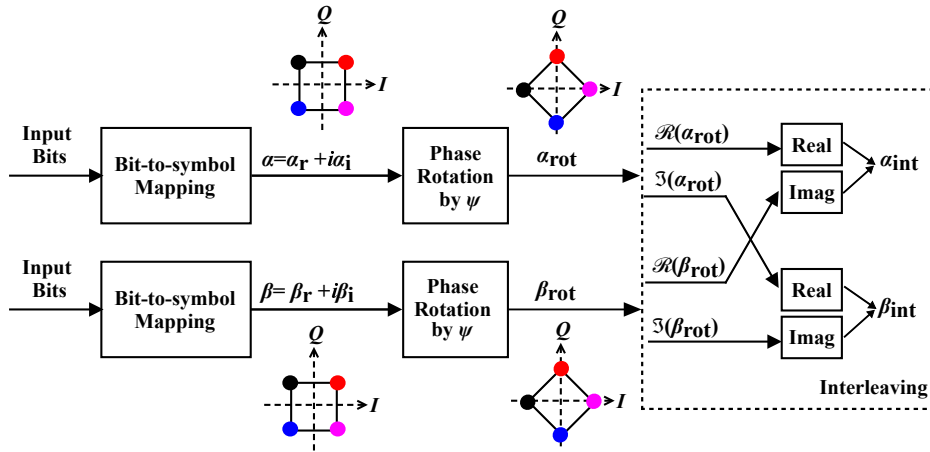
Figure 6.4: *Illustration of pairwise coding technique. The operators $\Re(\cdot)$ and $\Im(\cdot)$ provide the real and imaginary parts of a complex argument.*

(a) Classical constellation   *(b) Rotated constellation*
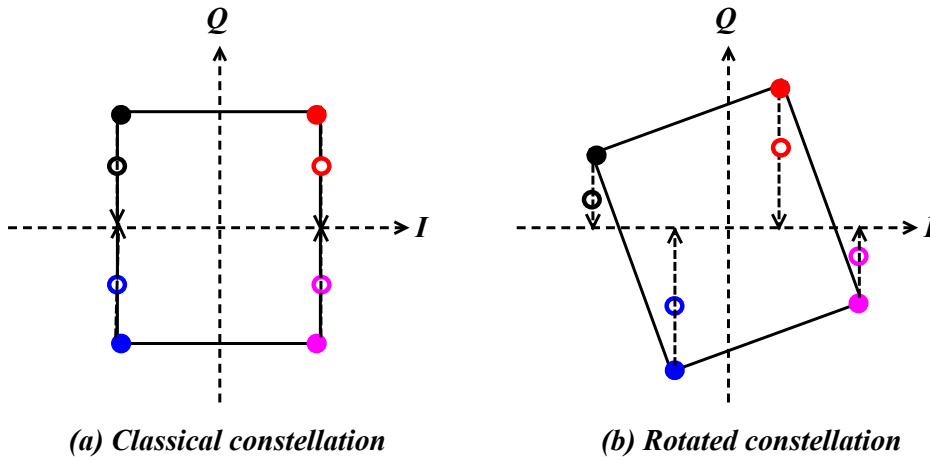
Figure 6.5: *Illustration of the effect of phase rotation in PWC: (a) classical (un-rotated) constellation diagram (b) rotated constellation diagram ($\psi = 20°$). The empty circles denote compressed constellation points due to low SNR of the Q-component, while the filled circles denote original (uncompressed) constellation.*

experiences a low SNR. As shown in Figure 6.5a for classical constellations, when the original constellation points (filled circles) are compressed due to low SNR on the Q component, it is possible for any two compressed points (empty circles) to merge together. This implies that a zero minimum distance and thus poor error performance will result. In contrast to the classical constellations, for the rotated constellations in Figure 6.5b, it can be seen that a non-zero minimum distance holds for the compressed points since no two points merges. Thus, the rotated constellation is more robust against the effects of noise.

When PWC is applied across the OFDM SCs (spectral dimension), the PWC scheme is termed

Subcarrier PWC (SC-PWC), and when PWC is applied over the transmitter SCHs (spatial dimension), it is referred to as Subchannel PWC (SCH-PWC). The generalised case is the dual PWC (DPWC) and it involve applying PWC both across the OFDM SCs and over the transmitter SCHs. Thus, both the SC-PWC and SCH-PWC schemes represent subsets of the DPWC technique. In this work, the focus is on the DWPC scheme while the SC-PWC and SCH-PWC schemes are treated as special cases of DPWC. The DPWC technique starts with the pairing of one OFDM SC having low SNR with another having high SNR. This is followed by the phase rotation and interleaving of the I and Q components of the information symbols on the paired SCs as described above. A similar procedure is then followed to encode the information symbols on the transmitter SCHs. The rest of this section details the encoding process for implementing the DPWC scheme by integrating SC-PWC and SCH-PWC. Later, we outline the procedure for decoding and estimating the transmitted symbols from the received signal.

6.2.1 DPWC encoding

To implement DPWC encoding, the information symbols to be modulated onto the data-carrying SCs are first encoded with SC-PWC, then the SCH-PWC is applied to the SC-PWC encoded symbols.

6.2.1.1 SC-PWC Encoding

Without loss of generality, we assume that N_d is an even number, and that the LEDs have similar frequency response profile. Let the data-carrying SCs be arranged in descending order of their channel gains, i.e., $\lambda_{j,1} \geq \lambda_{j,2} \cdots \geq, \lambda_{j,N_\mathrm{d}}$, for $j = 1, \ldots, N_\mathrm{t}$. Based on their gain, the N_d data-carrying SCs are grouped into two sets: those with high gains/SNR (good SCs), denoted by $\{\ell_p\}$, and those with small gains/SNR (bad SCs), denoted by $\{m_p\}$, where the pairing index, $p = 1, \ldots, N_\mathrm{d}/2$. The indices of the SCs corresponding to the p-th pair of good and bad SCs is given by: $(\ell_p, m_p) = (p, N_\mathrm{d} - p + 1)$. Hence, the vector of M-QAM information symbols mapped onto this pair of SCs are given by $(\mathbf{s}_{\ell_p}, \mathbf{s}_{m_p})$. After pairing, a constant phase shift, $\boldsymbol{\Psi}_p, \forall\, p$, is applied to the symbol vectors on the p-th SC pair, and the rotated symbol vectors are obtained as:

$$(\mathbf{s}_{\ell_p}^{\mathrm{rot}}, \mathbf{s}_{m_p}^{\mathrm{rot}}) = (e^{\widetilde{i\boldsymbol{\Psi}_p}}\, \mathbf{s}_{\ell_p},\, e^{\widetilde{i\boldsymbol{\Psi}_p}}\, \mathbf{s}_{m_p}), \tag{6.4}$$

where $\mathbf{\Psi}_p = \mathrm{diag}(\Psi_{1,p}, \ldots, \Psi_{N_t,p})$ is a diagonal matrix whose non-zero diagonal elements $\Psi_{j,p} \forall j$, denote the phase shift applied to the p-th SC pair on the j-th SCH. Next, I/Q component interleaving is applied over the rotated symbol vectors, and this entails exchanging the imaginary part of $\mathbf{s}_{\ell_p}^{\mathrm{rot}}$ and the real part of $\mathbf{s}_{m_p}^{\mathrm{rot}}$ [132]. The I/Q interleaving yields the two SC-PWC encoded symbol vectors on the p-th SC pair as:

$$\mathbf{w}_{\ell_p} = \Re(\mathbf{s}_{\ell_p}^{\mathrm{rot}}) + \Re(\mathbf{s}_{m_p}^{\mathrm{rot}}) = \Re(e^{\widetilde{i}\mathbf{\Psi}_p}\,\mathbf{s}_{\ell_p}) + \Re(e^{\widetilde{i}\mathbf{\Psi}_p}\,\mathbf{s}_{m_p}) \tag{6.5}$$

$$\mathbf{w}_{m_p} = \Im(\mathbf{s}_{\ell_p}^{\mathrm{rot}}) + \Im(\mathbf{s}_{m_p}^{\mathrm{rot}}) = \Im(e^{\widetilde{i}\mathbf{\Psi}_p}\,\mathbf{s}_{\ell_p}) + \Im(e^{\widetilde{i}\mathbf{\Psi}_p}\,\mathbf{s}_{m_p}) \tag{6.6}$$

The phase rotation (in (6.4)) and I/Q interleaving (in (6.5) and (6.6)) involved in the SC-PWC encoding can be combined into matrix-multiplication with an orthogonal matrix as:

$$\begin{bmatrix} \Re(\mathbf{w}_{\ell_p}) & \Im(\mathbf{w}_{\ell_p}) \\ \Re(\mathbf{w}_{m_p}) & \Im(\mathbf{w}_{m_p}) \end{bmatrix} = \begin{bmatrix} \cos\mathbf{\Psi}_p & -\sin\mathbf{\Psi}_p \\ \sin\mathbf{\Psi}_p & \cos\mathbf{\Psi}_p \end{bmatrix} \times \begin{bmatrix} \Re(\mathbf{s}_{\ell_p}) & \Re(\mathbf{s}_{m_p}) \\ \Im(\mathbf{s}_{\ell_p}) & \Im(\mathbf{s}_{m_p}) \end{bmatrix} \tag{6.7}$$

The proof of (6.7) is provided in Appendix D.1.

6.2.1.2 SCH-PWC Encoding

The SCH-PWC encoding is performed over the transmitter SCHs in a similar manner to the SC-PWC encoding of the OFDM SCs. With the SVD of the channel matrix, the channel gain obtained for the transmitter SCHs on the k-th SC are arranged in descending order. Therefore, considering an even N_t, by pairing the SCHs which have high gain/SNR with those with small gain/SNR, the SCHs pairing list is given by $(c_q, d_q) = (q, N_t - q + 1)$ for $q = 1, \ldots, N_t/2$, where c_q denote the index of high-gain SCHs while d_q denote the index of the small-gain SCHs. The corresponding SC-PWC encoded complex symbols mapped onto the paired SCHs are represented by $w_{c_q,k}$ and $w_{d_q,k}$. After pairing, phase rotation and I/Q component interleaving are applied to symbols $w_{c_q,k}$ and $w_{d_q,k}$. The phase rotation and component interleaving involved in SCH-PWC encoding of the q-th pair of SCHs can be

parameterised by the orthogonal matrix (SCH-PWC encoding matrix) [130]:

$$\mathbf{\Omega}_{q,k} = \begin{bmatrix} \Omega_{1,1}^{q,k} & \Omega_{1,2}^{q,k} \\ \Omega_{2,1}^{q,k} & \Omega_{2,2}^{q,k} \end{bmatrix} = \begin{bmatrix} \cos\phi_{q,k} & -\sin\phi_{q,k} \\ \sin\phi_{q,k} & \cos\phi_{q,k} \end{bmatrix}, \tag{6.8}$$

where $\phi_{q,k}$ is the angle by which the symbol on the q-th SCH pair of the k-th OFDM SC are rotated. Therefore, by applying SCH-PWC encoding, the DPWC encoded symbols on the q-th SCH pair are given by:

$$\begin{bmatrix} x_{c_q,k} \\ x_{d_p,k} \end{bmatrix} = \mathbf{\Omega}_{q,k} \times \begin{bmatrix} w_{c_q,k} \\ w_{d_p,k} \end{bmatrix}. \tag{6.9}$$

The SCH-PWC encoding process expressed by (6.9) translates to performing I/Q component interleaving and phase rotation of the complex symbol. The proof of this is provided in Appendix D.2. Using (6.9), the SCH-PWC encoding of all the N_t SCHs on the k-th SC can be written as:

$$\mathbf{x}_k = \mathbf{\Xi}_k \, \mathbf{w}_k, \tag{6.10}$$

where $\mathbf{\Xi}_k = \{\xi_{i,j}^k\}$ denote the $N_t \times N_t$ generalised SCH-PWC encoding matrix for all the N_t transmit SCHs on the k-th SC. Thus, the matrix $\mathbf{\Omega}_{q,k}$ corresponds to a sub-matrix of $\mathbf{\Xi}_k$, and the latter can be obtained from the former as follows:

$$\begin{aligned} \xi_{c_q,c_q}^k &= \Omega_{1,1}^{q,k}; \quad \xi_{c_q,d_q}^k = \Omega_{1,2}^{q,k} \\ \xi_{d_q,c_q}^k &= \Omega_{2,1}^{q,k}; \quad \xi_{d_q,d_q}^k = \Omega_{2,2}^{q,k}. \end{aligned} \tag{6.11}$$

We note that the $N_t \times N_d$ matrices of the user's information symbols and the DPWC encoded symbols are denoted by $\mathbf{S} = [\mathbf{s}_1, ..., \mathbf{s}_k, ..., \mathbf{s}_{N_d}]$ and $\mathbf{X} = [\mathbf{x}_1, ..., \mathbf{x}_k, ..., \mathbf{x}_{N_d}]$, respectively. The vectors $\mathbf{s}_k$ and $\mathbf{x}_k$ are the k-th columns (i.e., the k-th SC) of $\mathbf{S}$ and $\mathbf{X}$ respectively.

From (6.7) and (6.9), it can seen that the encoding process for the DPWC scheme can be defined completely in terms of the rotation angles. Hence, the design of the PWC technique is essentially dependent on using the optimal angles that maximize the minimum distance between the paired symbols constellations, which in turn minimizes the average error

probability. For an M-QAM symbol constellation, by maximizing the mutual information between a pair of information symbol vectors, the optimal rotation angles for SC-PWC encoding and SCH-PWC are given by [130]:

$$
\Psi_{j,p}^{\text{opt}} = \arg \max_{\Psi_{j,p} \in [0, \pi/4]} \left[\min_{(\mu,\upsilon) \in \mathbb{S}_M} \left[(\mu^2 + \upsilon^2) \Big(\lambda_{j,\ell_p}^2 \cos^2 \left(\Psi_{j,p} - \varphi_{\mu,\upsilon} \right) \right. \right.
$$
$$
\left. \left. + \lambda_{j,m_p}^2 \sin^2 \left(\Psi_{j,p} - \varphi_{\mu,\upsilon} \right) \Big) \right] \right] \quad (6.12)
$$

$$
\phi_{q,k}^{\text{opt}} = \arg \max_{\phi_{q,k} \in [0, \pi/4]} \left[\min_{(\mu,\upsilon) \in \mathbb{S}_M} \left[(\mu^2 + \upsilon^2) \Big(\lambda_{c_q,k}^2 \cos^2 \left(\phi_{q,k} - \varphi_{\mu,\upsilon} \right) \right. \right.
$$
$$
\left. \left. + \lambda_{d_q,k}^2 \sin^2 \left(\phi_{q,k} - \varphi_{\mu,\upsilon} \right) \Big) \right] \right]. \quad (6.13)
$$

where

$$
\mathbb{S}_M \triangleq \{ (\mu, \upsilon) \mid |\mu|, |\upsilon| \in [0, \sqrt{M} - 1], (\mu, \upsilon) \neq (0, 0) \} \quad (6.14)
$$

$$
\varphi_{\mu,\upsilon} = \tan^{-1} \left(\frac{\upsilon}{\mu} \right). \quad (6.15)
$$

The optimal angles in (6.12) and (6.13) are obtained by testing each candidate pair of (μ, υ) in set $\mathbb{S}_M$. However, since CSI is known at the transmitter, these computations can be performed before transmitting the user data. Also, for indoor optical wireless channel, which exhibits a relatively static channel condition, the optimisation of the angle does not require frequent update.

As stated above, the SC-PWC and SCH-PWC schemes can be treated as subsets of the DPWC scheme. Thus, by setting $\mathbf{\Xi} = \mathbf{I}_{N_t}$, the DPWC scheme becomes an SC-PWC scheme with PWC applied across the OFDM SCs only. Also, by setting $\mathbf{w}_k = \mathbf{s}_k$, $\forall k$, we derive the SCH-PWC scheme in which PWC is applied across the transmitter SCHs only. Furthermore, (6.7) and (6.9) indicate that DPWC encoding can be expressed in terms of multiplication with orthogonal matrices which can be readily inverted by finding its transpose.

6.2.2 PWC decoding and ML detection

At the receiver, with DPWC encoding applied at the transmitter, the expression in (6.2), for the received symbol vector on the k-th SC, becomes:

$$\mathbf{r}_k = \mathbf{\Lambda}_k \mathbf{x}_k + \mathbf{z}_k = \mathbf{\Lambda}_k \mathbf{\Xi}_k \mathbf{w}_k + \mathbf{z}_k$$
$$= \mathbf{G}_k \mathbf{w}_k + \mathbf{z}_k \tag{6.16}$$

where $\mathbf{G}_k = \mathbf{\Lambda}_k \mathbf{\Xi}_k$ is the effective channel gain matrix for the k-th SC. Next, the PWC decoding process is done on a per SC basis by first de-interleaving the I and Q components of received symbols on the paired SCs. That is, for the p-th SC pair, (ℓ_p, m_p), the de-interleaved complex symbols are obtained as:

$$\widetilde{\mathbf{r}}_{\ell_p} = \mathbf{G}_{\ell_p} \Re(\mathbf{s}_{\ell_p}^{\mathrm{rot}}) + \Re(\mathbf{z}_{\ell_p}) + \widetilde{i}(\mathbf{G}_{m_p} \Im(\mathbf{s}_{\ell_p}^{\mathrm{rot}}) + \Re(\mathbf{z}_{m_p}))$$
$$= \mathbf{G}_{\ell_p} \Re(e^{\widetilde{i}\mathbf{\Psi}_p}\mathbf{s}_{\ell_p}) + \Re(\mathbf{z}_{\ell_p}) + \widetilde{i}(\mathbf{G}_{m_p} \Im(e^{\widetilde{i}\mathbf{\Psi}_p}\mathbf{s}_{\ell_p}) + \Re(\mathbf{z}_{m_p})) \tag{6.17}$$
$$\widetilde{\mathbf{r}}_{m_p} = \mathbf{G}_{\ell_p} \Re(e^{\mathbf{\Psi}_p}\mathbf{s}_{m_p}) + \Im(\mathbf{z}_{\ell_p}) + \widetilde{i}(\mathbf{G}_{m_p} \Im(e^{\widetilde{i}\mathbf{\Psi}_p}\mathbf{s}_{m_p}) + \Re(\mathbf{z}_{m_p})) \tag{6.18}$$

The interpretation of (6.17) is that due to the I/Q interleaving of the paired SC at the transmitter, the I and Q components of the rotated symbol constellation on SC ℓ_p are transmitted though separate SCs with different gains/SNRs. That is, the real component, $\Re(e^{\mathbf{\Psi}_p}\mathbf{s}_{\ell_p})$ is sent on SC ℓ_p with effective channel gain matrix, $\mathbf{G}_{\ell_p}$, while the imaginary component, $\Im(e^{\mathbf{\Psi}_p}\mathbf{s}_{\ell_p})$, is sent via SC m_p which has an effective channel gain matrix $\mathbf{G}_{m_p}$. The noise vectors $\Re(\mathbf{z}_{\ell_p})$ and $\Re(\mathbf{z}_{m_p})$ are the respective noise terms associated with the real and imaginary components of the de-interleaved symbol $\widetilde{\mathbf{r}}_{\ell_p}$. A similar interpretation also holds for (6.18).

The MLD estimates of the transmitted symbols on the p-th SC pair are given by:

$$\widehat{\mathbf{s}}_{\ell_p} = \arg \min_{\mathbf{a} \in \mathcal{A}^{N_t}} \left\{ \|\widetilde{\mathbf{r}}_{\ell_p} - \mathbf{a}_{\ell_p}^{\mathrm{rot}}\|^2 \right\}$$
$$\widehat{\mathbf{s}}_{m_p} = \arg \min_{\mathbf{a} \in \mathcal{A}^{N_t}} \left\{ \|\widetilde{\mathbf{r}}_{m_p} - \mathbf{a}_{m_p}^{\mathrm{rot}}\|^2 \right\} \tag{6.19}$$

where $\mathbf{a}$ is an $N_t \times 1$ vector of M-QAM constellations drawn from the set $\mathcal{A}^{N_t}$, and $\mathbf{a}_{\ell_p}^{\mathrm{rot}}$ and

$\mathbf{a}_{m_p}^{\mathrm{rot}}$ are the rotated and scaled constellations obtained from:

$$
\begin{aligned}
\mathbf{a}_{\ell_p}^{\mathrm{rot}} &= \mathbf{G}_{\ell_p}\Re(e^{\widetilde{i}\boldsymbol{\Psi}_p}\mathbf{a}) + \widetilde{i}\mathbf{G}_{m_p}\Im(e^{\widetilde{i}\boldsymbol{\Psi}_p}\mathbf{a}) \\
\mathbf{a}_{m_p}^{\mathrm{rot}} &= \mathbf{G}_{\ell_p}\Re(e^{\widetilde{i}\boldsymbol{\Psi}_p}\mathbf{a}) + \widetilde{i}\mathbf{G}_{m_p}\Im(e^{\widetilde{i}\boldsymbol{\Psi}_p}\mathbf{a})
\end{aligned}
\tag{6.20}
$$

The set $\mathcal{A}^{N_t}$ is the Cartesian product of N_t sets of M-QAM constellations $\mathcal{A}$. The MLD expressed by (6.19) simultaneously estimates the N_t transmitted symbols modulated unto SCs ℓ_p and m_p of the OFDM frames sent on all the N_t transmitter SCHs. Thus, the ML search is performed over a $2N_t$ dimensional signal space. This can be reduced significantly into $N_t/2$ independent MLD steps over a 4-D signal space by performing MLD one pair of SCHs at a time. For instance, considering the q-th SCH pair, i.e., (c_q, d_q), let $\mathbf{G}_{\ell_p,q}$ and $\boldsymbol{\Psi}_{p,q}$ denote the 2×2 sub-matrices consisting of the entries in the c_q and d_q rows and columns of the matrices $\mathbf{G}_{\ell_p}$ and $\boldsymbol{\Psi}_p$, respectively. Also, let $\widehat{\mathbf{s}}_{\ell_p,q}$ and $\widetilde{\mathbf{r}}_{\ell_p,q}$ denote the 2×1 vectors consisting of the entries in rows c_q and d_q of the vector $\widehat{\mathbf{s}}_{\ell_p,q}$ and $\widetilde{\mathbf{r}}_{\ell_p}$, respectively. Then, the MLD estimates of the symbols modulated onto SCs ℓ_p and m_p, and sent over transmitter SCHs c_q and d_q are obtained from (6.19) as:

$$
\begin{aligned}
\widehat{\mathbf{s}}_{\ell_p,q} &= \arg\min_{\widetilde{\mathbf{a}}\in\mathcal{A}^2}\left\{\|\widetilde{\mathbf{r}}_{\ell_p,q} - \widetilde{\mathbf{a}}_{\ell_p}^{\mathrm{rot}}\|^2\right\} \\
\widehat{\mathbf{s}}_{m_p,q} &= \arg\min_{\widetilde{\mathbf{a}}\in\mathcal{A}^2}\left\{\|\widetilde{\mathbf{r}}_{m_p,q} - \widetilde{\mathbf{a}}_{m_p}^{\mathrm{rot}}\|^2\right\}
\end{aligned}
\tag{6.21}
$$

where $\widetilde{\mathbf{a}}$ is a 2×1 vector of M-QAM constellations drawn from the set $\mathcal{A}^2$, and $\widetilde{\mathbf{a}}_{\ell_p}^{\mathrm{rot}}$ and $\widetilde{\mathbf{a}}_{m_p}^{\mathrm{rot}}$ are obtained from (6.20) by substituting $\widetilde{\mathbf{a}}$ for $\mathbf{a}$.

6.3 Simulation results

In this section, the performance results obtained via Monte-Carlo simulations in MATLAB® are presented. The simulation procedure is outlined in Algorithm 2 of Appendix C.2. The basic MIMO-OFDM system with no pairwise coding is compared with the three PWC schemes: SC-PWC, SCH-PWC and DPWC. Note that SVD precoding is applied in all the configurations. To portray different levels of channel correlation and therefore different $\mathcal{C}_d$ values, the MIMO VLC channel is simulated using varying LED beaming angles, Φ. As Φ increases, the emitted light intensity spreads wider. This increases the correlation of the LOS channel gain matrix $\boldsymbol{\Gamma}$, and also reduces the gains of each desired LED-PD link i.e., the diagonal elements of $\boldsymbol{\Gamma}$. The

values of $\mathbf{\Gamma}$ and $\mathcal{C}_\mathrm{d}$ obtained for different channel case are provided in Table 6.2. Since $\mathbf{\Gamma}$ has a single tap for each MIMO subchannel, then $\mathbf{H}_k \ \forall\, k$, is equivalent to $\mathbf{\Gamma}$ multiplied by the gain of each OFDM SC. Hence, for each channel case, the value of $\mathcal{C}_\mathrm{d}$ is constant for $\mathbf{H}_k \ \forall\, k$.

Without loss of generality, a MIMO-OFDM system with $N_\mathrm{r} = N_\mathrm{t} = 4$ is considered for all simulations. Each OFDM frame has a total of $N_\mathrm{sc} = 512$ SCs, out of which $N_\mathrm{d} = 254$ are data-carrying SCs. Also, unless otherwise stated, the value of $\mathbf{\Gamma}$ for Case II in Table 6.2 is used as a representative MIMO channel case.

CASES	LED Beaming Angle, Φ	Channel Matrix, $\mathbf{\Gamma}$ $\times 10^{-4}$				Singular Values $\times 10^{-4}$	Condition Number $\mathcal{C}_\mathrm{d}$ (dB)
Case I	15°	$\begin{bmatrix} 1.1650 & 0.5880 & 0.5880 & 0.2950 \\ 0.5170 & 1.4140 & 0.1860 & 0.5170 \\ 0.6410 & 0.2410 & 1.2890 & 0.4640 \\ 0.2410 & 0.4640 & 0.6410 & 1.2890 \end{bmatrix}$				$\begin{bmatrix} 2.6357 \\ 1.1535 \\ 0.9778 \\ 0.4030 \end{bmatrix}$	8.16
Case II	20°	$\begin{bmatrix} 0.7776 & 0.5616 & 0.5616 & 0.4002 \\ 0.4938 & 0.9436 & 0.2532 & 0.4938 \\ 0.6125 & 0.3267 & 0.8606 & 0.4429 \\ 0.3267 & 0.4429 & 0.6125 & 0.8606 \end{bmatrix}$				$\begin{bmatrix} 2.2434 \\ 0.6311 \\ 0.4806 \\ 0.1139 \end{bmatrix}$	12.95
Case III	25°	$\begin{bmatrix} 0.5419 & 0.4620 & 0.4620 & 0.3874 \\ 0.4062 & 0.6575 & 0.2451 & 0.4062 \\ 0.5039 & 0.3163 & 0.5997 & 0.3644 \\ 0.3163 & 0.3644 & 0.5039 & 0.5997 \end{bmatrix}$				$\begin{bmatrix} 1.7850 \\ 0.3685 \\ 0.2500 \\ 0.0365 \end{bmatrix}$	17.25
Case IV	30°	$\begin{bmatrix} 0.3966 & 0.3700 & 0.3700 & 0.3389 \\ 0.3253 & 0.4812 & 0.2144 & 0.3253 \\ 0.4035 & 0.2767 & 0.4389 & 0.2918 \\ 0.2767 & 0.2918 & 0.4035 & 0.4389 \end{bmatrix}$				$\begin{bmatrix} 1.4117 \\ 0.2350 \\ 0.1457 \\ 0.0097 \end{bmatrix}$	21.61
Case V	35°	$\begin{bmatrix} 0.3026 & 0.2981 & 0.2981 & 0.2880 \\ 0.2621 & 0.3672 & 0.1822 & 0.2621 \\ 0.3251 & 0.2351 & 0.3349 & 0.2351 \\ 0.2351 & 0.2351 & 0.3251 & 0.3349 \end{bmatrix}$				$\begin{bmatrix} 1.3101 \\ 0.1619 \\ 0.0958 \\ 0.0023 \end{bmatrix}$	26.93

Table 6.2: *LOS VLC MIMO channel gain for different LED beaming angles*

6.3.1 BER performance

Using 4-QAM and 16-QAM, the plots of the BER versus SNR per bit γ_b (i.e., energy per bit to noise power spectral density ratio) for the basic and the PWC configurations are depicted in Figure 6.6. The signal has a representative bandwidth, B_s of 25 MHz, which is 10 MHz more than the 3-dB bandwidth of the LEDs, (i.e., B_LED of 15 MHz). The performance improvement achieved by applying the PWC schemes is apparent from the BER plots. It is observed that the DPWC scheme gives the best performance. For instance, at a representative BER of 10^{-5}, when 4-QAM is used, the DPWC scheme gives an SNR saving of about 37 dB, 23 dB and 12 dB over the basic, SCH-PWC and SC-PWC schemes, respectively. A similar result is obtained for 16-QAM where at a BER of 10^{-5}, the DPWC gives about 30 dB, 21 dB an 13 dB in SNR

saving over the basic, SCH-PWC and SC-PWC schemes, respectively. The SC-PWC scheme is effective in mitigating only the frequency selectivity caused by the LED's limited bandwidth, while the SCH-PWC scheme only addresses the ill-condition (SNR imbalance) due to the VLC MIMO channel correlation. In contrast, the DPWC provides robustness to mitigate the effect of both bandwidth limitation and channel correlation, and hence, the reason for its superior performance.
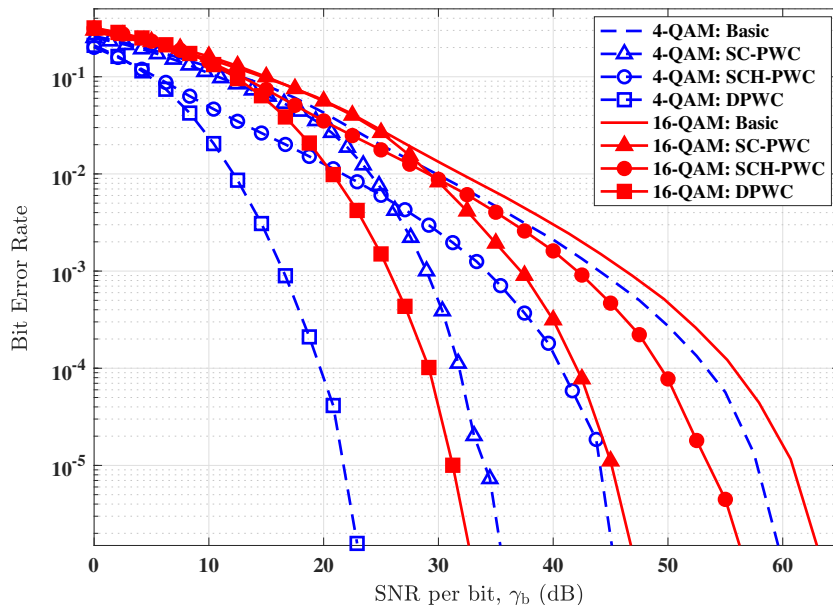
Figure 6.6: *Error performance of the basic and PWC configurations using 4-QAM and 16-QAM*

6.3.2 Performance for varying bandwidth limitation

With the $B_{\text{LED}} = 15$ MHz, as B_s increases, the number and the attenuation of the SCs beyond the LEDs' 3 dB bandwidth increases. This results in an increased SNR imbalance between the OFDM SCs. The variation in SNR imbalance with B_s value is illustrated in Figure 6.7 which shows the PSD of the LEDs' input and output OFDM signal for different B_s values. The data-carrying SCs are indexed from 2 to 255. The PSD magnitude is relatively constant for SC index between 2 and 50, hence the reason for their omission in the plots. From Figure 6.7, we observe that, as expected, the difference in the SC gain between the least attenuated and the most attenuated data-carrying SCs increases with the value of B_s. This difference in SC gain ranges from about 24 dB (for $B_s = 15.5$ MHz) to about 39 dB (for $B_s = 30$ MHz).
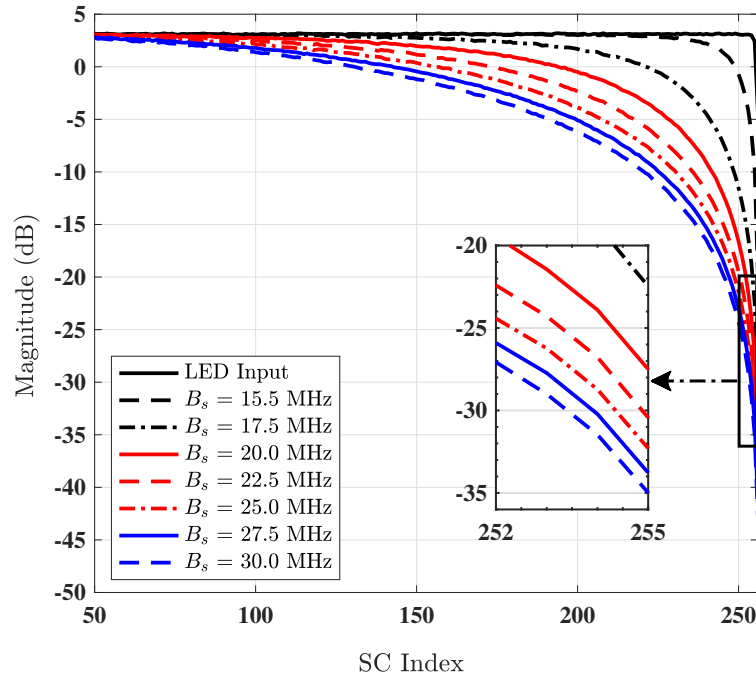
Figure 6.7: *PSD of LEDs' input signal and LEDs' output signals for different B_s values.*

In Figures 6.8a and 6.8b, the performance of the PWC schemes for different B_s is shown for 4-QAM and 16-QAM, respectively. For each scheme, the SNR savings achieved over the basic system at a BER of 10^{-5} is plotted against B_s. SNR saving is computed as the difference between the SNR required by a PWC scheme and the basic configuration to achieve a specific BER value. As expected the DPWC scheme gives the best SNR savings of up to 37 dB and 31 dB at $B_s = 30$ MHz for 4-QAM and 16-QAM, respectively. It can also be observed that the savings achieved by using SCH-PWC scheme is relatively constant for different B_s values. This is because in the SCH-PWC scheme, pairing is done among the SCHs only, and thus, SCH-PWC cannot mitigate the SNR imbalance among the SCs due to the LEDs. Hence, the gain achieved over the basic system will only vary significantly if the VLC MIMO channel condition varies.

6.3.3 Performance for varying channel condition

The performance of the PWC schemes in the different VLC channel conditions provided in Table 6.2 is depicted in Figure 6.9. The SNR savings achieved at a BER of 10^{-5} by the three PWC schemes over the basic configuration are plotted against $\mathcal{C}_d$ in Figure 6.9a (using 4-QAM)
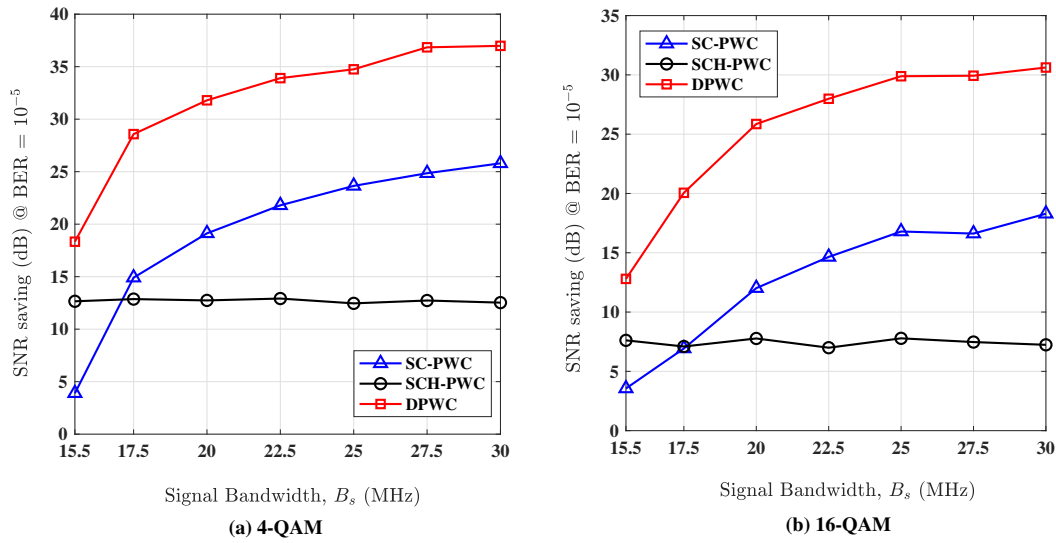
Figure 6.8: *Performance of PWC schemes for varying signal bandwidth. Plots of SNR savings of PWC schemes over basic MIMO-OFDM versus B_s using (a) 4-QAM, (b) 16-QAM.*

and Figure 6.9b (using 16-QAM). The superior performance of the DPWC scheme is obvious in Figure 6.9, since it has the capacity to mitigate SNR imbalance in both the spatial and the spectral domains. For instance, using 4-QAM, DPWC provides an SNR saving of about 21 dB and 31 dB (at $\mathcal{C}_\mathrm{d} = 26.93$ dB) over the SCH-PWC and SC-PWC schemes, respectively. While in the case of 16-QAM, DPWC achieved about 14.5 dB and 33 dB (at $\mathcal{C}_\mathrm{d} = 26.93$ dB) over the SCH-PWC and SC-PWC schemes, respectively. Also, since the SC-PWC scheme only benefits from mitigating SNR imbalance among the SCs, its SNR savings over the basic configuration remains relatively constant for varying $\mathcal{C}_\mathrm{d}$. Though the PWC configurations also suffer from the effect of the increasing channel correlation as $\mathcal{C}_\mathrm{d}$ increases, the degradation in performance is less severe compared to the basic configuration. Hence, the reason for the SNR savings achieved by the pairwise coding schemes.

6.4 Experimental demonstration

This section details the experimental setup and results which demonstrates the performance of PWC for MIMO-OFDM VLC system.
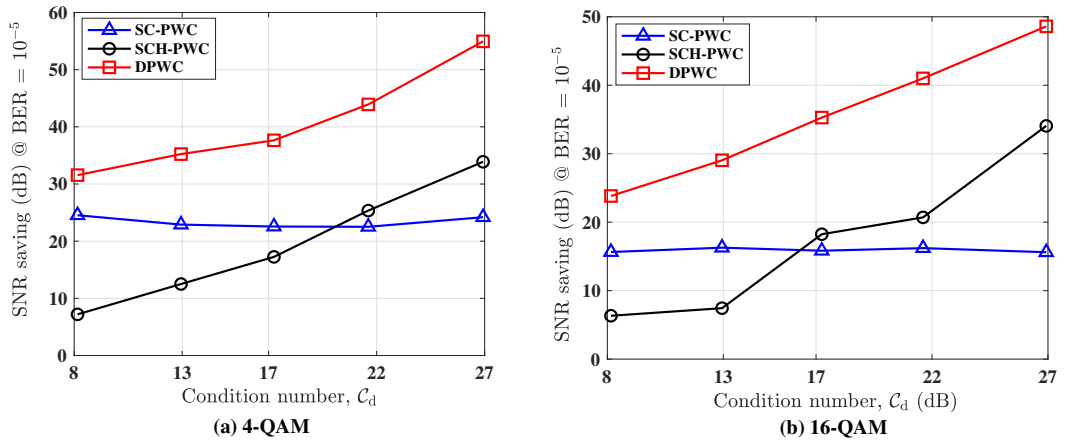
Figure 6.9: *Performance of the PWC schemes for varying condition number, $\mathcal{C}_d$. Plots of SNR savings of PWC schemes over basic configuration against $\mathcal{C}_d$, using (a) 4-QAM, (b) 16-QAM.*

6.4.1 Experimental setup

The experimental setup of a 2×2 MIMO-OFDM based VLC system over 1 m link is illustrated by Figure 6.10. The LED separation is 5 cm while that of the PDs is 7.5 cm. MATLAB® software installed on a personal computer is used to facilitate the digital signal processing (DSP) at the transmitter (TX-DSP) and the receiver (RX-DSP). The TX-DSP operations include generating bit streams, performing bit-to-symbol mapping and S/P conversion of the data symbols. Other TX DSP operations include the DPWC encoding, SVD precoding, IFFT operation, CP insertion and parallel-to-serial (P/S) conversion of the transmit symbols as described in Section 6.2. The data stream are then fed separately to the two channels of the arbitrary waveform generator (AWG) (Agilent 33600A) with sampling rate of 1 GSa/s and up to 120 MHz bandwidth. The waveform generated by the AWG is fed to a Bias-T which diplexes it with a DC bias. The output of the Bias-T is then used to modulate the intensity of the high power blue LEDs (Osram LD CN5M). Focusing lens are deployed at both the transmiting and receiving end of the VLC link to focus the data-bearing optical intensity on the receiving photodiode (PD). Lenses are used to collimate and focus the emitted intensity at the transmitter and the receiver ends, respectively.

At the RX, the transmitted signals are detected by the two Si Amplified PDs (Thorlabs PDA10A-EC) which feature built-in low-noise transimpedance amplifier (TIA), Noise
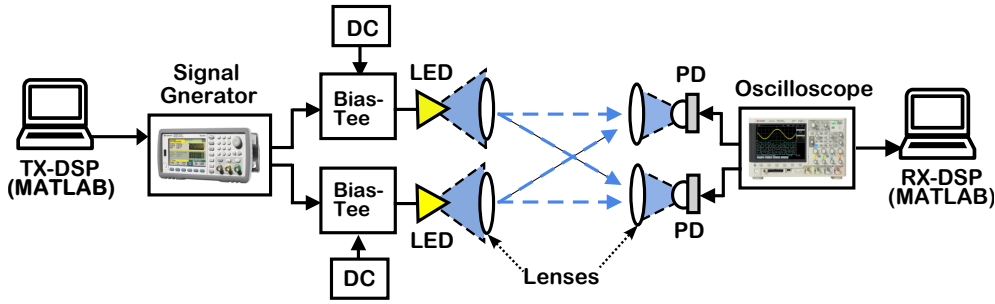
Figure 6.10: *Experimental setup of 2×2 MIMO-OFDM VLC system.*

equivalent power, NEP $= 3.5 \times 10^{-11}$ W/$\sqrt{\text{Hz}}$. The PDs have an active area of 0.8 mm^2 and a bandwidth of 150 MHz. The outputs of the PDs are captured on an oscilloscope (Agilent MSO7104B) with sample rate of 4 GSa/s and bandwidth of 1 GHz, and the acquired data is fed back into MATLAB$^{\circledR}$ software for offline processing. The RX-DSP operations in MATLAB$^{\circledR}$ include the FFT block, RLS channel estimation, SVD and pairwise decoding and demodulation of the received symbols.

6.4.2 Experimental results

The frequency responses of the VLC links between each LED-PD pair are shown in Figure 6.11. The frequency selective fading of the OFDM SCs caused mainly by the bandwidth limitation of each LEDs is obvious in Figure 6.11. The 3-dB bandwidth of both links is about 12 MHz and 15 MHz, respectively. In addition, two different channel conditions, denoted by Cases A and B, are obtained using different LED-PD alignment. The estimated and normalised time-domain MIMO VLC channel gain matrices are given in Table 6.3.

Table 6.3: *Measured LOS channel gain for 2×2 MIMO VLC experimental setup using different LED-PD alignment*

CASES	Channel Matrix, $\mathbf{\Gamma}$	Singular Values	Condition Number, $\mathcal{C}_{\text{d}}$ (dB)
Case A	$\begin{bmatrix} 1.0000 & 0.1225 \\ 0.0967 & 0.9657 \end{bmatrix}$	$\begin{bmatrix} 1.0914 \\ 0.8746 \end{bmatrix}$	0.9620
Case B	$\begin{bmatrix} 1.0000 & 0.1502 \\ 0.1256 & 0.2648 \end{bmatrix}$	$\begin{bmatrix} 1.0253 \\ 0.2398 \end{bmatrix}$	6.3105

Case A represents an almost ideal MIMO configuration in which the MIMO channels are less correlated as indicated by the small value of $\mathcal{C}_{\text{d}} = 0.9620$ dB. Thus, the major limitation is the
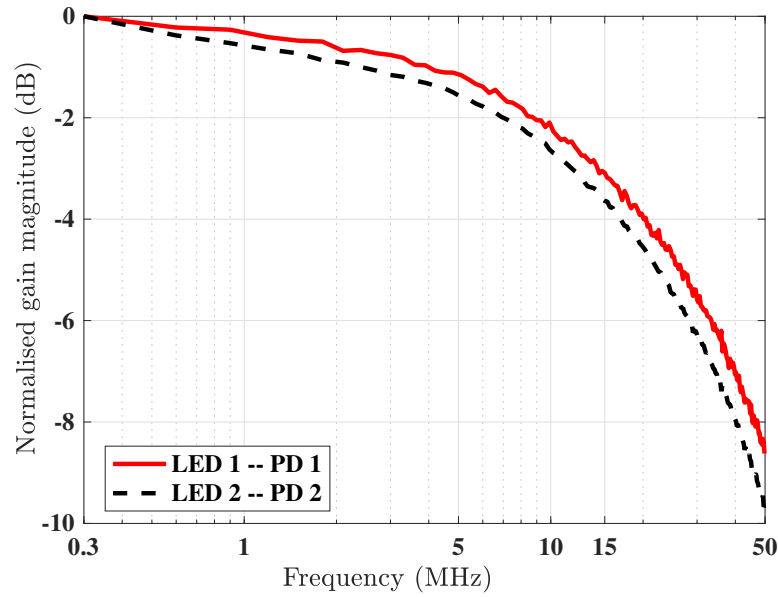
Figure 6.11: *Measured frequency responses of the MIMO VLC path between each LED-PD pair*

bandwidth of the LEDs. At a bit rate of 496 Mbps with 4-QAM, the error performance of the basic and PWC configurations are presented in Figure 6.12 with the plot of the BER against the average received electrical power per bit, P_{rec}. It can be seen that both the DPWC and the SC-PWC have superior performance compared to the basic and SCH-PWC. For instance, to achieve a BER of 10^{-4}, the DPWC and the SC-PWC schemes requires about 10 dB less than both the basic and SCH-PWC scheme. We note that due to limited hardware availability, a 2×2 MIMO setup is used for the experiment in contrast to the 4×4 MIMO setup used for the simulation. Also, by comparing Figure 6.7 and Figure 6.11, we observe that the attenuation incurred by the high-frequency SCs is smaller in the experiment than in the simulation. Hence, the difference in the performance gain achieved in both scenarios. The similarity of the BER plots for the DPWC and the SC-PWC schemes can be attributed to the fact that the MIMO channel is well-conditioned with a small difference in the singular values. Hence, there is no significant gain in applying PWC between the SCHs.

For Case B, the value of $\mathcal{C}_{\text{d}} = 6.3105$ dB shows that the MIMO channel experiences some degree of correlation and SNR imbalance in addition to the LEDs' bandwidth limitation. The error performance plots of the basic and PWC configurations at a bit rate of 248 Mbps are presented in Figure 6.13. It is observed that the DPWC scheme gives the best performance by
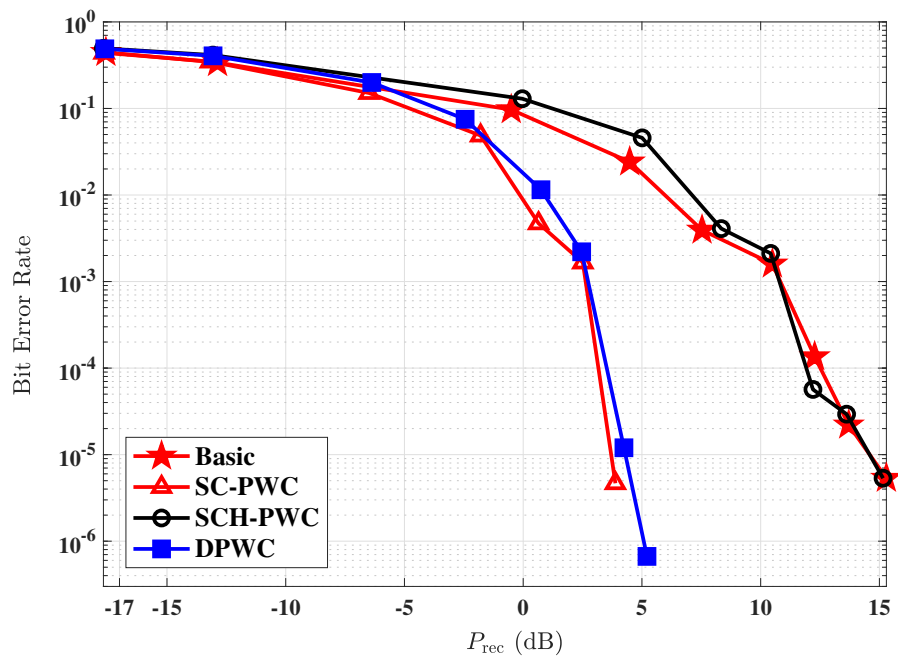
Figure 6.12: *Experimental BER plots for Case A:* $\mathcal{C}_d = 0.9620$ *dB, bit rate=496 Mbps.*
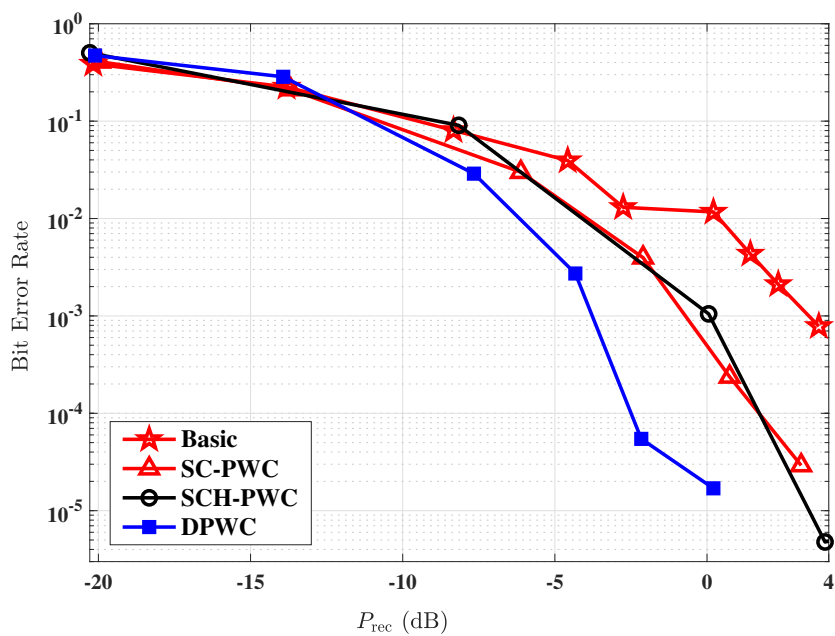
Figure 6.13: *Experimental BER plots for Case B:* $\mathcal{C}_d = 6.3105$ *dB, bit rate = 248 Mbps.*
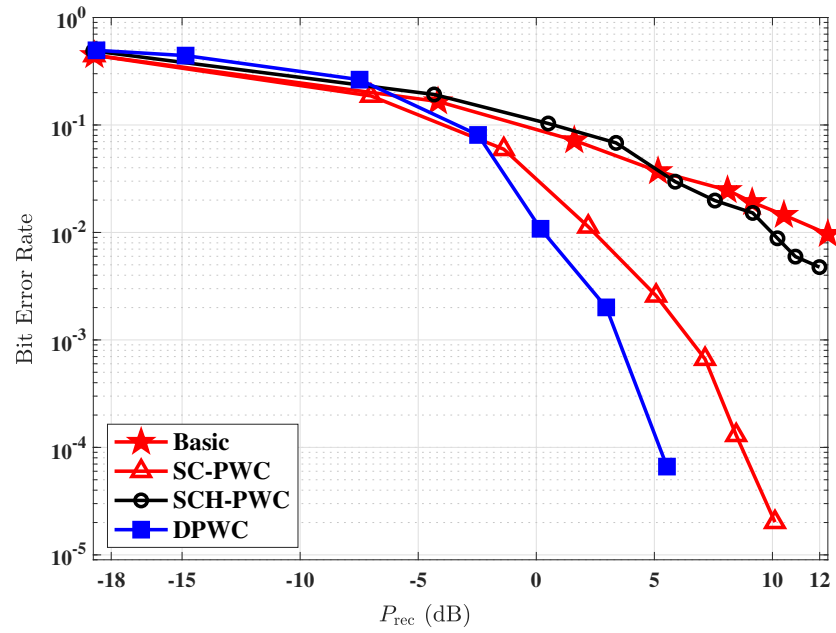
Figure 6.14: *Experimental BER plots for Case B: $C_d = 6.3105$ dB, bit rate = 496 Mbps.*

employing PWC to reduce the effect of the increased channel correlation. At a BER of 10^{-4}, DPWC provides a power saving of about 5 dB over the SC-PWC and the SCH-PWC, and a power saving of 8 dB over the basic system at BER $= 10^{-3}$. A similar performance trend is seen in Figure 6.14 for a bit rate of 496 Mbps. The DPWC again gives the best performance with power saving of about 3.5 dB over the SC-PWC scheme and even significantly higher gain over the SCH-PWC scheme and the basic configuration.

The benefits of applying PWC in the spectral/spatial dimension comes from averaging the BER across all SCs/SCHs such that the overall error performance of the system is improved. However, as a performance-enhancing technique, there is a level degradation beyond which the technique becomes ineffective with little or no gains. Such scenario in our observation is the case for SCH-PWC in Figure 6.14. The data rate, and hence the severity of the impact of LED bandwidth limitation, is increased from 248 Mbps in Figure 6.13 to 496 Mbps in Figure 6.14. While DPWC and SC-PWC leverage on the application of PWC in the spectral domain to reduce the impact of bandwidth limitation, the SCH-PWC scheme does not have such benefit. Furthermore, with just two LEDs, the gain that SCH-PWC can achieve by applying PWC in the spatial domain alone is very limited. Hence, the reason for the similarity in the performance of the SCH-PWC scheme and the basic configuration in Figure 6.14. The slight deviation

observed in the BER values can be attributed to errors in experimental measurements such as channel estimation.

6.5 Summary

A pairwise coding technique applied in MIMO-OFDM VLC system to mitigate the SNR imbalance created in the received information symbols due to the LEDs' frequency response and the strong correlation of the indoor VLC MIMO channel. PWC technique is implemented by the joint coding of information symbol pairs in the spatial and/or the spectral dimensions of MIMO-OFDM VLC. Three variants of the PWC technique are considered by implementing the joint coding over the spectral dimension (SC-PWC), over the spatial dimension (SCH-PWC), and over both spatial and spectral dimensions (DPWC) The overall error performance is improved in terms of bit error rate and throughput, without additional power or bandwidth is requirement. The BER plots show that high performance gains are achieved by using PWC compared the basic MIMO-OFDM. Simulation results show up to 35 dB reduction in SNR requirement (at $\text{BER} = 10^{-5}$) when DPWC is applied. Similarly, the experimental results indicate that SNR saving of more 10 dB can be achieved at a data rate of 496 Mbps in a 2×2 MIMO setup using LEDs with 3-dB bandwidth of 12 MHz and 15 MHz. Moreover, the DPWC achieves up to 5 dB in SNR saving over SC-PWC and more than 10 dB over the SCH-PWC for the same experimental 2×2 MIMO configuration.

Chapter 7
Conclusions and future work

This chapter summarises and concludes the body of research work presented in this thesis. The principal findings are captured along with the relevant conclusions. Finally, the chapter provides an outline of the limitations of this research work and recommends potential areas for future work.

7.1 Summary and major findings

In the global information and communication technology landscape, the proliferation of wireless communications has hit unexpected heights. A paradigm that, to a large extent, is driven by the ever increasing number and features of mobile devices and digital applications along with the rise of Internet of Things (IoT). As a result, the demand for the radio frequency (RF) spectrum employed in the wide-scale deployment of these devices and services is outstripping supply. To cater for the demands of emerging applications, the spotlight of research has been expanded to supplementary window of the electromagnetic spectrum (EM) where access to huge bandwidth is available. In this context, Optical wireless communications (OWC) has emerged as a promising solution to remedy the spectrum deficit. OWC opens the door to explore the optical range of the EM spectrum for wireless transmission, with a spectral resource that dwarfs that of the RF band. Accordingly, this research work was aimed at studying the OWC technology, in an attempt to harness its potential especially in indoor environment. Specifically, the research reported in this thesis addressed this objective by investigating, analysing and evaluating multiple-input multiple-output (MIMO) transmission techniques for OWC systems. This is motivated by the success recorded in the utilisation of MIMO in RF communications, where it has been used to improve system performance in terms capacity and/or reliability of wireless transmission. While MIMO techniques have proven to be highly beneficial, they are not without limitations, especially in the optical

domain where the channel is less disperse compared to the RF counterpart.

Detailed discussion on the motivation for this research work was presented in Chapter 1. The need to explore OWC as a complementary technology to the existing RF communication system was elucidated. Furthermore, the potentials for MIMO transmission in OWC was discussed, highlighting the wide-spread adoption and dense deployment of optical sources (LEDs) to meet the illumination requirements. A context which provides an opportunity to overlay communication on illumination with multiple transmitter sources that can enable MIMO systems. Besides, the finite bandwidth of optical sources, typically the off-the-shelf white LEDs [22] necessitates use of attractive techniques such as MIMO to enhance system capacity, while also benefiting from the low-power nature of these sources. The gains of MIMO in terms of increasing spectral efficiency and improving link range and reliability by the way of diversity were also outlined in Chapter 1. Moreover, the chapter also highlights the challenges faced in integrating MIMO technique into OWC systems. These include correlation of the indoor optical wireless channel, the synchronisation requirement and inter-channel interference (ICI) due to parallel data transmission, along with the intersymbol interference (ISI) in indoor multipath channels, particularly for supporting mobility and coverage.

In furtherance to achieving the objectives of this research, the background on OWC technology was provided in Chapter 2, starting with a brief account of the recent research works promoting the adoption of OWC. This was followed by an overview of the salient features of OWC, outlining the technical and operational advantages of the technology, such as vast bandwidth resource, simplicity of the system and cost effectiveness of the deployment, low power requirements and robustness to EM interference. Besides, the limitations of the OWC system in terms of adopting existing modulation format and supporting user mobility were given. Sequel to the outlined advantages, some of the application areas where OWC systems has been considered were summarised. Following this, the building blocks of a typical OWC link were described, stating the key components of the transmitter and receiver. The propagation modelling and characterization of the indoor optical wireless channel were also provided. In the concluding part of the chapter, we reviewed the widely used digital modulation format and MIMO technique for OWC, highlighting the unique features, advantages and limitations of each. In particular, three MIMO techniques were studied. The repetition coding (RC)

MIMO is used mainly for diversity gain, but requires large signal constellation sizes to achieve high data rates. In contrast, spatial multiplexing (SMP) MIMO offers capacity gains, but is highly sensitive to channel similarity. The third MIMO technique, termed spatial modulation (SM) provides provides a trade-off between capacity and reliability. SM is more robust to high channel symmetry than SMP, and achieves improved spectral efficiency compared to RC-MIMO. Considering the attributes of each MIMO technique, our investigation was in two folds. First, SM-MIMO is investigated in Chapters 3-5 with a focus on the impact of line-of-sight (LOS) channel path loss, system synchronisation and multipath-induced interference. Then, in Chapter 6, we explored SMP-MIMO for high data rate, employing techniques to address the high similarity of optical wireless channel and the small bandwidth of white LEDs.

On the backbone of the overview presented in the background chapter, an investigation of optical SM (OSM) as a low complexity MIMO technique for OWC was reported in Chapter 3. SM-MIMO is combined with energy-efficient pulse position modulation (PPM). A novel OSM scheme termed generalised spatial pulse position modulation (GSPPM) was devised to enhances the spectral efficiency of classical PPM by encoding additional information bits on the spatial domain (index) of optical sources. This scheme harnesses the spectral efficiency from SM technique and the energy efficiency of PPM. To this end, a general framework has been developed which provides analytical bounds on the error rate of PPM-based SM-MIMO schemes in indoor LOS channel path loss and additive white Gaussian noise (AWGN), assuming a perfectly synchronised system. The framework supports three other variants of SM, namely, optical space shift keying (SSK), generalised SSK (GSSK) and spatial pulse position modulation (SPPM). The derived bounds have been verified by closely-matching numerical simulations. The results show performance trade-offs of PPM-based SM techniques for indoor OWC systems. For instance, energy efficiency can be improved by increasing the number of PPM time slots per symbol interval, but doing that will also increase the bandwidth requirement of the system due to shorter pulse duration. Similarly, increasing the number of optical sources employed at the transmitter increases the spatial constellation size and thus, the spectral efficiency, but at the cost of higher signal-to-noise ratio (SNR). Therefore, the system parameters can be adjusted based on the requirement of the target application in terms of energy and throughput. The symbol error rate (SER) plots showed how the performance of

the SM schemes varies with SNR. But, we observed from the derived expressions that, typical of MIMO systems, the SER is also dependent on the differentiability (LED/PD alignment) of the multiple links. Analysis of the impact of channel gain showed that for GSPPM, GSSK and SPPM, the error performance is dictated by both the individual values of the channel gains and the disparity of the gains. Whereas, for SSK, performance is dependent on the dissimilarity of the gains. This analysis is relevant in the system setup in order to ensure that the LED/PD positioning and alignment are optimised for the best error performance (reliability). Furthermore, given that the general framework can be applied to any of the four variants of OSM, a comparison of these schemes was provided to highlight their benefits and limitations. SPPM and GSPPM profit from the energy efficiency of PPM, but also incurs the associated high bandwidth requirement. Thus, they can be considered for low data rate applications in wireless sensor networks which are constrained by energy resource. In contrast, GSSK provides the best spectral efficiency but require higher SNR. Finally, the performance of SPPM as a feasible scheme for OWC was demonstrated via proof-of-concept experiments, with a 2-LEDs SPPM setup over a distance of 1 m. For SPPM using $L = 2$ time slots, at data rate of 25.00 Mbps, an SER of 4×10^{-4} was achieved with $P_{\text{eb}} = -10$ dBm. While with $L = 4$ time slots, at the data rate of 18.75 Mbps and $P_{\text{eb}} = -12$ dBm, the achieved SER is 6×10^{-5}. Applying SM concept improved the achieved data rates over classical PPM by a factor of 2 and 2/3 for $L = 2$ and $L = 4$, respectively. It is worth mentioning that the achieved data rates were limited by the sampling rate of the signal generator (100Msa/s), and these results were obtained without any forward error correction codes.

Having investigated the performance of SM-MIMO scheme in an ideal system in which a complete synchronisation is assumed to have been maintained between the transmitter and receiver, in the subsequent chapter 4, we considered the implication of such assumption. This motivated by the fact that the presupposition of a perfect synchronisation does not hold for practical deployment. In a MIMO system which relies on the deployment of spatially separated multiple transmitter and receiver element, the sources of error in timing synchronisation considered include clock jitters in the transmitter and variation in path length due to spatial separation of the transmitter sources, multipath propagation in OWC channel and the mobility or orientation of the receiver. Thus, in Chapter 4, we examined the impact of timing synchronisation error on the performance of SM technique in OWC systems. The

timing errors were modelled as offset/displacement in the received signals with reference to the receiver's clock. By accounting the energy loss and energy spread due to timing offsets, the synchronisation error analyses of the four OSM schemes considered previously were formulated to derive the corresponding SER expressions. Error performance plots showed that these expressions were closely-matched by simulation results, and they provide insight into how error in synchronisation affect each SM scheme. Results show that error performance degrades with increasing synchronisation error. The SM schemes with digital modulation, i.e., PPM, showed more sensitivity to synchronisation errors. This was clearly indicated by the slope of the plot for each scheme. The plots showed a relatively rapid increase in the SER of SPPM and GSPPM as timing offset increases in contrast to SSK and GSSK. While SM technique relaxes synchronisation requirement by reducing the number of parallel data stream, accurate synchronisation is still critical for SM technique, particularly for SM schemes in which digital modulation is employed or multiple sources are activated simultaneously.

In the final part of our analysis and evaluation of SM-MIMO schemes, we considered the performance in multipath channel that include LOS and second-order reflected paths. The motivation for this study was to take forward our analysis of the LOS propagation considered in Chapter 3 which applies more to fixed configuration, to include non-LOS (NLOS) propagation which can support better coverage and mobility. Besides, the assumption of LOS channel is apt for low-speed transmission systems, where the symbol duration is long enough to capture the delayed signals NLOS signals. However, for high-speed Gigabits per second communication, the shorter symbol duration implies that the system will incur ISI due to pulse spreading. Consequently, in Chapter 5, the performance of two SM schemes, i.e., SPPM and SSK, in indoor multipath optical wireless was investigated. Based on a model devised to account for the multipath-induced ISI resulting from the dispersive NLOS paths, analytical approximations of the SER for the multipath propagation of SPPM and SSK were obtained. The error performance plots showed agreement between the simulation results and the analytical approximations. Due to the dispersion experienced in multipath channel, higher SNR was required to achieve a given SER compared to LOS-only propagation. The degree of dispersiveness of the channel was defined in terms of the root mean squared (RMS) delay spread, τ_{rms}. At a representative SER of 10^{-5}, the multipath-induced SNR penalty in a 2--LED SPPM setup is about 6.5 dB for $L = 2$ ($\tau_{\mathrm{rms}} = 0.14T_{\mathrm{c}}$) and 5.5 dB for $L = 8$ ($\tau_{\mathrm{rms}} = 0.29T_{\mathrm{c}}$), where L is the number of

PPM time slots per symbol interval and T_c is the pulse duration. As L increased from 2 to 4 and then 8, the SNR penalty incurred in multipath channel also increased due to the shortening of pulse duration. As a result, the energy saving achieved by using a given value of L can be lost to multipath penalty if the delay spread exceeds a certain threshold. For instance, for $\tau_{rms} > 0.35T_c$ and $\tau_{rms} > 0.38T_c$, the SNR required for $L = 8$ exceeds those $L = 4$ and $L = 2$, respectively. Moreover, the ISI incurred in multipath channel also alters the actual channel response for the received signal, thereby eroding the identifiability of the activated LED. For less distinct channel responses, the incurred ISI can readily diminish the path gain disparity to cause LED detection errors. As indoor OWC networks are to provide full coverage and mobility, we also explored the spatial distribution of system performance parameters such as channel path gain, delay spread and multipath-induced power penalty. This was used to illustrate the impact of each parameter on performance.

The second and final part of our investigation in Chapters 6 explored SMP-MIMO with Orthogonal frequency division multiplexing (OFDM) for high data rate VLC applications. The focal point here was to apply viable techniques to address the high symmetry of indoor optical wireless channel and the frequency selectivity due to the small bandwidth of the LEDs. Based on our understanding from the background work for this research, SMP requires high channel differentiability to achieve good error performance. Thus, in order to successfully utilise SMP in indoor optical wireless channel with high symmetry, we first considered angular diversity at the receiver by optimising the incident angle of the emitted intensity to minimizes the off-diagonal values (cross channel gains) of the MIMO channel matrix. Then, singular value decomposition (SVD) precoding was applied to transforms the MIMO channel matrix into a set of parallel independent subchannels (SCHs). With the SVD-based MIMO, the higher the degree of channel symmetry, the more spread out the gains (singular values) of the SCHs, and thus, the bigger the SNR imbalance between the SCHs. Similar SNR imbalanced exist between the OFDM subcarriers (SCs) as a result of the frequency selectivity of the small-bandwidth LEDs. To mitigate these two cases of SNR imbalance, joint coding of paired information symbols was applied via a technique termed pairwise coding (PWC). Three implementations of PWC were presented. One across the SCHs only (SCH-PWC), another across the SCs only (SC-PWC), and the third was across the both the SCHs and SCs, i.e., Dual PWC (DPWC). Results obtained from simulations showed that the PWC technique improves

the error performance of the system. Expectedly, SC-PWC was effective in mitigating only the frequency selectivity caused by the LED's limited bandwidth, while the SCH-PWC scheme only addressed the ill-condition (SNR imbalance) due to the VLC MIMO channel correlation. DPWC provides robustness to mitigate the effect of both bandwidth limitation and channel correlation, and hence offered the best performance. Experimental results also demonstrated the merits of the PWC technique. For instance, at a bit rate of 496 Mbps with 4-QAM and 2×2 MIMO setup using LEDs with 3-dB bandwidth of 12 MHz and 15 MHz, DPWC provided SNR saving of more 10 dB (at BER $= 10^{-4}$) over the basic MIMO-OFDM without PWC.

7.2 Limitations and recommendations for future work

The analysis and evaluation presented in this thesis have considered important aspect of optical MIMO transmission which hitherto have not been accounted for in most of the simplified models. For instance, in view of uncertainty expected in practical systems, the impact of non-perfect time synchronisation on the system performance has been examined. Similarly, effect of dispersion in multipath propagation, especially in mobile scenario has been presented. However, there are still areas where the scope of work reported in this thesis can be further investigated.

The simulations results presented in Chapter 3 applied realistic system parameters like transmitter and receiver element configuration. Thus, the results obtained can provide a useful insight into the performance of optical SM-MIMO techniques. However, as discussed in the chapter, the channel gain values play important role in determining the system performance. A knowledge of the channel state information (CSI) – channel gain – is needed for the detection algorithms to accurately estimate the transmitted symbol. while the work presented here assumes a perfect CSI estimation, there is need to investigate the impact imperfect estimation on the performance of the decoder. The analysis presented in Chapter 5 gave insights into how inaccurate CSI estimation can affect performance, where changes in the estimated channel gain due to interference results in erroneous detection of the activated source. Furthermore, given the significance of channel gain disparity on performance, it is imperative to research viable methods for improving the performance in optical wireless channel with high symmetry. Previous work in [23] proposed the use of power imbalance to enhance channel gain dissimilarity. However, this method is not optimal as it does not

incorporate the CSI information. It is effective when all the channel gains values are large but similar. Nevertheless, applying the power imbalance technique has the potential to further reduce the effective SNR of OWC links with smaller gain values. This observation is reported in our work on OSM technique in [80]. Therefore, further investigation can be done to optimise the power imbalance technique by taking the CSI into account. Although, such method will require that the CSI be avaliable at the transmitter, which imposes additional overhead. Alternatively, transmitter and receiver angle optimisation with theoretical support that can applied in different scenarios can be investigated as a means of reducing the symmetry of optical wireless channel. In addition, to further enhance the spectral efficiency of the PPM based OSM techniques, the signal constellation can be expanded by incorporating index modulation with other variant of PPM such as multipulse PPM (MPPM) and overlapping PPM (OPPM). Additional constellation points can be created based on the number and indices of pulse positions. However, detailed investigation will be required to determine the trade-offs in terms of power and complexity.

The work detailed in Chapter 4 provides insight on the effect of imperfect timing synchronisation due to a number factor such as clock jitters and propagation delays. The resulting timing offset has been modelled theoretical as predefined ratios of the pulse duration. In terms of expanding the scope of work, further studies can be conducted on accurately estimating the actual timing offset experienced in various scenarios. This is particularly important for dynamic setups where receiver mobility is supported and the orientation of devices can change due to the use techniques such as angular diversity. Nonetheless, when such estimation is successfully obtained, the analysis presented in this thesis will be useful as the predefined timing offsets can the replaced with the estimated values. In addition, delay-adaptive transmission techniques such as the one proposed in [140] can be investigated to address the variation in the propagation delays of multiple links. It is anticipated that such techniques can use the estimated timing offsets values to compensate for or correct synchronisation error.

It has been reported in this thesis that multipath-induced ISI can have significant impact on the error performance of OSM techniques, particularly those utilising pulsed modulation schemes. However, this investigation has been conducted for non-imaging receiver configuration. In this

context, application of imaging receivers is expected to provide a better performance. Thus, the analysis presented in this work can be extended to established their suitability in disperse NLOS links. In addition to multipath induced interference, performance of OSM techniques should also be studied in the presence of shadowing and blockage in indoor optical wireless channel. A solution to such effect may require a combination of SM with spatial diversity. Given the dense deployment and small form factor of light sources, they can be divided into groups, with the sources in each group employed in RC diversity mode, while each group can constitute a single index for SM transmission. Detailed investigation is required to ascertain the feasibility of such deployments.

Considering the PWC technique employed in 6, the optimal rotation angle is obtained by searching through the set of all possible constellation amplitudes scaled by the channel gain of the paired symbols. Thus, the complexity of the search process increases with size of the signal constellation diagram. In this regards, further investigation can be directed at optimising the search process, particularly with mathematical derivation that takes into account the appropriate parameters. Besides, future work can be done to provide a detailed comparison of the PWC scheme with other performance-enhancing techniques that are suitable for transmission channels with imbalanced SNR, such as bit and power loading. Preliminary results from simulation and experiment show a comparable BER performance for the PWC and the bit and power loading schemes when applied to OFDM technique in a SISO setup. However, for MIMO transmission, further investigation is required to apply the bit and power loading scheme simultaneous in both the spectral and spatial dimensions, as employed in the dual PWC scheme in Chapter 6. This is a challenge for the bit loading process in particular, given that once the bit resolution is fixed for optimal performance in either the spectral or spatial dimension, altering it for optimal performance in the other dimension may degrade the overall gain in performance improvement.

Moreover, the analysis and evaluation of optical MIMO techniques conducted in this work employed maximum likelihood (ML) detection at the receiver. As such, a considerable amount of computation will be required for larger constellation size. Therefore, the scope of work can be extended to investigate the use of suboptimal, but less complex schemes such as sphere decoding.

Appendix A
Computation complexity analysis

As explained in Section 2.4, assuming ML detection at the receiver, with $R = 1$ in (2.10), the estimate of the transmitted symbol vector is obtained from:

$$\widehat{\mathbf{s}} = \arg \min_{\mathbf{s}} \|\mathbf{r} - \mathbf{Hs}\|^2 \tag{A.1}$$

where the dimensions of $\mathbf{r}$, $\mathbf{H}$, and $\mathbf{s}$ are $N_r \times 1$, $N_r \times N_t$ and $N_t \times 1$, respectively.

Considering SMP based MIMO, for the matrix-vector product $\mathbf{v}_{\text{prod}} = \mathbf{Hs}$, each of the N_r rows of $\mathbf{v}_{\text{prod}}$ requires N_t multiplications and $(N_t - 1)$ additions. Therefore, the computation of $\mathbf{v}_{\text{prod}}$ involves $N_r(2N_t - 1)$ FLOPs. Also, evaluating the vector difference $\mathbf{v}_{\text{diff}} = \mathbf{r} - \mathbf{v}_{\text{prod}}$ requires N_r subtractions. Furthermore, the norm operation of the vector difference, $\|\mathbf{v}_{\text{diff}}\|^2$ requires N_r multiplications and $(N_r - 1)$ additions, which yields a total of $(2N_r - 1)$ FLOPs. Thus, for a given symbol vector $\mathbf{s}$, the computation of $\|\mathbf{r} - \mathbf{Hs}\|^2$ requires a total of $(2N_rN_t + 2N_r - 1)$ FLOPs. Moreover, if $\mathcal{M}$ bits are transmitted during a symbol interval, the total number of all possible symbol vector $\mathbf{s}$, is $2^{\mathcal{M}}$. Therefore, with ML detection, a total of $2^{\mathcal{M}}(2N_rN_t + 2N_r - 1)$ FLOPs are used to evaluate the Euclidean distance metric for all possible symbol vectors. The evaluation of FLOP counts for SMP MIMO receiver detection is summarised in Table A.1.

In the case of SM MIMO, the sparse structure of the SM transmission vector $\mathbf{s}$ given in (A.1) reduces the detection complexity of its ML detector in terms of the FLOPs count. The transmission vector $\mathbf{s}$, has only one non-zero element, thus, evaluating the matrix-vector product $\mathbf{v}_{\text{prod}} = \mathbf{Hs}$ requires only N_r multiplications. Similar to the SMP MIMO case, in SM MIMO, the vector difference $\mathbf{v}_{\text{diff}} = \mathbf{r} - \mathbf{v}_{\text{prod}}$ is computed using N_r subtractions, and the norm operation, $\|\mathbf{v}_{\text{diff}}\|^2$ requires N_r multiplications and $(N_r - 1)$ additions. Thus, the total

Operation	Expression	FLOPs
SMP MIMO		
Matrix-vector product	$\mathbf{v}_{\text{prod}} = \mathbf{Hs}$	$N_{\text{r}}(2N_{\text{t}} - 1)$
Vector subtraction	$\mathbf{v}_{\text{diff}} = \mathbf{r} - \mathbf{v}_{\text{prod}}$	N_{r}
Vector norm squared	$\|\mathbf{v}_{\text{diff}}\|^2$	$(2N_{\text{r}} - 1)$
Total per symbol vector, $\mathbf{s}$	$\|\mathbf{r} - \mathbf{Hs}\|^2$	$(2N_{\text{r}}N_{\text{t}} + 2N_{\text{r}} - 1)$
Total ($2^{\mathcal{M}}$ possible symbol vectors)		$2^{\mathcal{M}}(2N_{\text{r}}N_{\text{t}} + 2N_{\text{r}} - 1)$ $= L^{N_{\text{t}}}(2N_{\text{r}}N_{\text{t}} + 2N_{\text{r}} - 1)$
SM MIMO		
Matrix-vector product	$\mathbf{v}_{\text{prod}} = \mathbf{Hs}$	N_{r}
Vector subtraction	$\mathbf{v}_{\text{diff}} = \mathbf{r} - \mathbf{v}_{\text{prod}}$	N_{r}
Vector norm squared	$\|\mathbf{v}_{\text{diff}}\|^2$	$(2N_{\text{r}} - 1)$
Total per symbol vector, $\mathbf{s}$	$\|\mathbf{r} - \mathbf{Hs}\|^2$	$(4N_{\text{r}} - 1)$
Total ($2^{\mathcal{M}}$ possible symbol vectors)		$2^{\mathcal{M}}(4N_{\text{r}} - 1)$ $= LN_{\text{t}}(4N_{\text{r}} - 1)$
GSM (GSPPM) MIMO		
Matrix-vector product	$\mathbf{v}_{\text{prod}} = \mathbf{Hs}$	$N_{\text{r}}(2N_{\text{e}} - 1)$
Vector subtraction	$\mathbf{v}_{\text{diff}} = \mathbf{r} - \mathbf{v}_{\text{prod}}$	N_{r}
Vector norm squared	$\|\mathbf{v}_{\text{diff}}\|^2$	$(2N_{\text{r}} - 1)$
Total per symbol vector, $\mathbf{s}$	$\|\mathbf{r} - \mathbf{Hs}\|^2$	$(4N_{\text{r}} - 1)$
Total ($2^{\mathcal{M}}$ possible symbol vectors)		$2^{\mathcal{M}}(2N_{\text{r}}N_{\text{t}} + 2N_{\text{r}} - 1)$ $= L2^{N_{\text{t}}}(2N_{\text{r}}N_{\text{e}} + 2N_{\text{r}} - 1)$

Table A.1: *Evaluation of FLOPs count for MIMO receiver detection process.*

FLOPs count for SM MIMO with $2^{\mathcal{M}}$ possible transmission symbol vectors is $2^{\mathcal{M}}(4N_{\text{r}} - 1)$. A summary of the FLOPs count is shown in Table A.1

Much like the SM MIMO technique, GSM based MIMO schemes, such as GSSK and GSPPM (see Section 2.4), also benefits from the reduction in the number of active sources in order to reduce the detection complexity. For the GSPPM scheme, considering all the possible SCPs, the average number of activated sources per symbol is given by:

$$N_{\text{e}} = \frac{1}{2^{N_{\text{t}}}}\left[N_{\text{t}} + \sum_{k}^{N_{\text{t}}} k\binom{N_{\text{t}}}{k}\right]$$

$$= \frac{N_{\text{t}}}{2^{N_{\text{t}}}}\left(2^{N_{\text{t}}-1} + 1\right). \tag{A.2}$$

Therefore, for the GSPPM scheme, evaluating the matrix-vector product $\mathbf{v}_{\text{prod}} = \mathbf{H}\mathbf{s}$ requires an average of $N_{\text{r}}(2N_{\text{e}} - 1)$ FLOPs (multiplications and additions).

Like the SMP and SM MIMO cases, for the GSPPM scheme, the vector difference $\mathbf{v}_{\text{diff}} = \mathbf{r} - \mathbf{v}_{\text{prod}}$ is computed using N_{r} subtractions, and the norm operation, $\|\mathbf{v}_{\text{diff}}\|^2$ requires N_{r} multiplications and $(N_{\text{r}} - 1)$ additions. Thus, the total FLOPs count for GSM (GSPPM) MIMO with $2^{\mathcal{M}}$ possible transmission symbol vectors is $2^{\mathcal{M}}(2N_{\text{r}}N_{\text{e}} + 2N_{\text{r}} - 1)$. A summary of the FLOPs count is shown in Table A.1

Approximate error performance analysis in LOS channel

For the GSPPM symbol $\mathcal{A}_{j,m}$ which is transmitted by activating the LEDs based on SCP j, with the pulse in slot m, the PEP that receiver decides in favour of SCP k instead of SCP j is given by (3.16). Therefore, using the union bound approximation [106] with N_s equally likely SCPs, the probability of error in detecting the SCP is given by:

$$\widetilde{P}_{\mathrm{e,scp}}^{\mathrm{GSPPM}} \leq \frac{1}{N_\mathrm{s}} \sum_{j=1}^{N_\mathrm{s}} \sum_{\substack{k=1 \\ k \neq j}}^{N_\mathrm{s}} \mathrm{PEP}_m^{j \to k} = \frac{1}{N_\mathrm{s}} \sum_{j=1}^{N_\mathrm{s}} \sum_{\substack{k=1 \\ k \neq j}}^{N_\mathrm{s}} Q\left(\|\lambda_k \mathbf{H} \mathbf{v}_k - \lambda_j \mathbf{H} \mathbf{v}_j\| \sqrt{\frac{\gamma_\mathrm{s}}{2}} \right), \quad \text{(B.1)}$$

and the probability of correct SCP detection is expressed as:

$$\widetilde{P}_{\mathrm{c,scp}}^{\mathrm{GSPPM}} = 1 - P_{\mathrm{e,scp}}^{\mathrm{GSPPM}} = 1 - \frac{1}{N_\mathrm{s}} \sum_{j=1}^{N_\mathrm{s}} \sum_{\substack{k=1 \\ k \neq j}}^{N_\mathrm{s}} Q\left(\|\lambda_k \mathbf{H} \mathbf{v}_k - \lambda_j \mathbf{H} \mathbf{v}_j\| \sqrt{\frac{\gamma_\mathrm{s}}{2}} \right). \quad \text{(B.2)}$$

Similarly, for symbol $\mathcal{A}_{j,m}$, the PEP that the receiver decides in favour of pulse position q instead of m, is expressed by (3.21). Considering L equiprobable pulse positions and N_s equally likely SCPs, the probability of correct pulse position detection for the transmitted GSPPM symbol is given by:

$$\widetilde{P}_{\mathrm{c,ppm}}^{\mathrm{GSPPM}} = \frac{1}{N_\mathrm{s}} \sum_{j=1}^{N_\mathrm{s}} \left(1 - (L-1) Q\left(\|\lambda_j \mathbf{H} \mathbf{v}_j\| \sqrt{\gamma_\mathrm{s}} \right) \right). \quad \text{(B.3)}$$

Finally, combining (B.2) and (B.3) according to (3.11) and (3.12), and applying $N_\mathrm{s} = 2^{N_\mathrm{t}}$, the

average symbol error probability for GSPPM scheme in LOS channel can be approximated by:

$$\widetilde{P}_{\text{e,sym}}^{\text{GSPPM}} = 1 - \left[1 - \frac{1}{2^{N_{\text{t}}}} \sum_{j=1}^{2^{N_{\text{t}}}} \sum_{\substack{k=1 \\ k \neq j}}^{2^{N_{\text{t}}}} Q\left(\|\lambda_k \mathbf{H} \mathbf{v}_k - \lambda_j \mathbf{H} \mathbf{v}_j \| \sqrt{\frac{\gamma_{\text{s}}}{2}} \right) \right]$$

$$\times \left[\frac{1}{2^{N_{\text{t}}}} \sum_{j=1}^{2^{N_{\text{t}}}} \left(1 - (L-1) \times Q\left(\|\lambda_j \mathbf{H} \mathbf{v}_j \| \sqrt{\gamma_{\text{s}}} \right) \right) \right]. \quad \text{(B.4)}$$
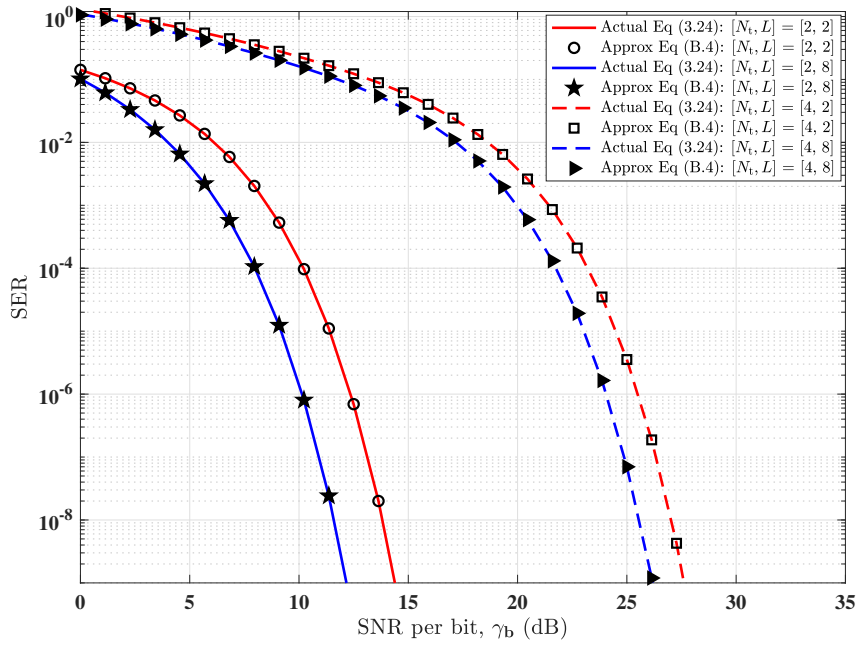
Figure B.1: *Error performance of GSPPM using approximate analysis, $N_{\text{t}} = \{2, 4\}$ and $L = \{2, 8\}$.*

Appendix C
Simulation procedures

C.1 Simulation procedure for OSM schemes

The simulation procedure for the OSM schemes in Chapters 3, 4 and 5 is outlined in Algorithm 1. The procedure provides the main routines employed in the Monte Carlo simulation of OSM schemes in LOS channel as considered in Chapters 3. For the simulation of the OSM schemes impaired by timing synchronisation errors in Chapter 4, an additional routine is required to incorporate the phenomenon of timing errors. This is applied to the transmitter signal before channel propagation, that is, between lines 19 and 20 in Algorithm 1. To implement the timing error routine, the transmitter signal (for the entire symbol stream) sent by each LED is delayed by the number of samples that is equivalent to the timing offset incurred in each LED-to-receiver path. Similarly, for the simulation of the OSM schemes in indoor multipath channel in Chapter 5, a channel estimation routine is implemented just before the matched filtering process. Unlike the LOS channel considered in Chapters 3 and 4 which has only one tap, the multipath channel in Chapter 5 has multiple taps. Hence, channel estimation routine is used to determine the effective channel coefficients that will be applied in the detection of the SCP index.

Algorithm 1 Simulation procedure for OSM schemes in Chapters 3, 4 and 5

Input : N_{t}, N_{r}, L, $\mathbf{H}$, γ_{b}: SNR per bit, N_{sym}: number of transmitted symbol
$\qquad$ N_{sps}: number of signal samples per symbol

1 **Transmitter**
$\quad$ Generate data symbols:
$\quad$ $\{\mathcal{A}_{j,m}^{1}, \ldots, \mathcal{A}_{j,m}^{N_{\text{sym}}}\} \leftarrow N_{\text{sym}}$ uniformly distributed pseudorandom symbols in $\{0, 1, \ldots, (2^{\mathcal{M}}-1)\}$
$\quad$ **for** $i \leftarrow 1$ **to** N_{sym} **do**
2 $\qquad$ Symbol-to-bit mapping (decimal-to-binary conversion): $[b_1, b_2, \ldots b_{\mathcal{M}}] \leftarrow \mathcal{A}_{j,m}^{i}$
3 $\qquad$ **if** $L > 1$ **then**
4 $\qquad\qquad$ Get PPM pulse position: $m \in [1, 2 \ldots, L] \leftarrow [b_{\log_2(N_{\text{s}})+1}, \ldots, b_{\mathcal{M}}]$
5 $\qquad\qquad$ Generate a sequence of L chips: assign a value of one to the m-th chip, and a value of zero to all other chips
6 $\qquad$ **else if** $L = 1$ **then**
7 $\qquad\qquad$ Generate only one chip with a value of one
8 $\qquad$ **end**
9 $\qquad$ **Transmitter pulse shaping**: signal samples, $\phi \leftarrow$ upsample all chip(s) by a factor of N_{sps}/L, and apply transmitter filter (rectangular pulse shape) with N_{sps}/L samples.
10 $\qquad$ **LED activation**: Get SCP index j, and activation vector $\mathbf{v}_j$, for symbol $\mathcal{A}_{j,m}^{i}$
$\qquad\qquad$ $\mathbf{v}_j = [v_{j,1} \ldots v_{j,N_{\text{t}}}] \leftarrow j \in [1, \ldots, N_{\text{s}}] \leftarrow [b_1, \ldots b_{\log_2(N_{\text{s}})}]$ $\qquad$ // SCP index
11 $\qquad$ Transmitter signal: $\mathbf{s}_{j,m} = [s_1, \ldots, s_{N_{\text{t}}}]^{\dagger}$
$\qquad$ Activate LEDs based on SCP:
$\qquad$ **for** $v_{j,n_{\text{t}}}$ *in* $\mathbf{v}_j$ **do**
12 $\qquad\qquad$ **if** $v_{j,n_{\text{t}}} = 1$ **then**
13 $\qquad\qquad\qquad$ $s_{n_{\text{t}}} \leftarrow$ signal samples, ϕ
14 $\qquad\qquad$ **else**
15 $\qquad\qquad\qquad$ $s_{n_{\text{t}}} \leftarrow N_{\text{sps}}$ zero-valued samples
16 $\qquad\qquad$ **end**
17 $\qquad$ **end**
18 $\qquad$ Append transmitter signal for symbol $\mathcal{A}_{j,m}^{i}$ to the transmitter signal of the entire symbol stream
19 **end**
20 **Channel propagation**: send signal through the channel by applying the channel response of each transmit-receive path, $h_{n_{\text{r}},n_{\text{t}}}$, for $n_{\text{r}} = 1, \ldots N_{\text{r}}, n_{\text{t}} = 1, \ldots N_{\text{t}}$, to filter the corresponding transmitter signal
21 **Receiver**
$\quad$ **Noise**: add Gaussian noise values with zero mean and variance: $\sigma^2 = \frac{E_{\text{s}}}{2\mathcal{M}\gamma_{\text{b}}}$
$\quad$ **Matched filtering**: apply the receiver filter response (rectangular pulse shape with N_{sps}/L samples), then downsample the filter output at the PPM chip rate (by a factor N_{sps}/L) to obtain the amplitude of the chip(s) for each received symbol.
$\quad$ **Detection**:
$\quad$ Initialise symbol error count: $e_{\text{cnt}} = 0$
$\quad$ **for** $i \leftarrow 1$ **to** N_{sym} **do**
22 $\qquad$ Get the MF samples corresponding to the chips of each received symbol
$\qquad\qquad$ **if** $L > 1$ **then**
23 $\qquad\qquad\qquad$ Estimate the PPM pulse position: $\hat{m} \in [1, \ldots, L] \leftarrow$ index of the chip/sample with the highest amplitude
24 $\qquad\qquad\qquad$ Convert the estimated chip index into bits: $[\hat{b}_{\log_2(N_{\text{s}})+1}, \ldots, \hat{b}_{\mathcal{M}}] \leftarrow \hat{m}$
25 $\qquad\qquad$ **end**
26 $\qquad$ Estimate the SCP index: $\hat{j} \leftarrow$ index of the SCP with the minimum Euclidean distance to the amplitude of the estimated chip, $\hat{m}$ (for SPPM and GSPPM) or the amplitude of the only chip (for SSK and GSSK)
27 $\qquad$ Convert the estimated SCP index into bits: $[\hat{b}_1, \ldots \hat{b}_{\log_2(N_{\text{s}})}] \leftarrow \hat{j}$
28 $\qquad$ Compute the received symbol alphabet (bit-to-symbol mapping): $\widehat{\mathcal{A}}_{j,m}^{i} \leftarrow [\hat{b}_1, \ldots \hat{b}_{\mathcal{M}}]$
29 $\qquad$ **if** $\widehat{\mathcal{A}}_{j,m}^{i} \neq \mathcal{A}_{j,m}^{i}$ **then**
30 $\qquad\qquad$ $e_{\text{cnt}} = e_{\text{cnt}} + 1$
31 $\qquad$ **end**
32 **end**
$\quad$ **Output:** Compute error rate: SER $\leftarrow e_{\text{cnt}}/N_{\text{sym}}$

146

C.2 Simulation procedure for MIMO-OFDM with PWC

The procedure for implementing the Monte Carlo simulation of MIMO-OFDM with PWC in Chapter 6 is outlined the following Algorithm 2. A brief description of the main routines employed in the simulation is provided.

Algorithm 2 Simulation procedure for implementing MIMO-OFDM with PWC in Chapters 6

Input : N_t, N_r, M, N_{sc}, γ_b: SNR per bit

1 **LED**: model LED response as first-order low-pass Butterworth filter with $B_{LED} = 15$ MHz
2 **Channel training**: estimate channel coefficient in frequency domain by using pilot symbols and RLS algorithm.
3 **SVD computation**: perform SVD to obtain the singular values for all the SCs on each transmitter channel.
4 Generate information bits: uniformly distributed pseudorandom bits
5 QAM modulation: bits to M-QAM symbol (constellation) mapping
6 S/P conversion: convert M-QAM symbol stream into blocks of N_d symbols
7 **PWC Encoding**: apply SC-PWC and/or SCH-PWC encoding in succession
   Symbol pairing: pair channels (SCs/SCHs) with low and high SNR based on the computed singular values
   Compute optimal rotation angle for each pair using the computed singular values
   Phase rotation: rotate the phase of the M-QAM constellations on the paired channels (SCs/SCHs)
   Interleaving: interleave the the real and imaginary components of the paired and rotated M-QAM constellations
8 **SVD precoding**: perform SVD precoding using the unitary matrix from the SVD computation
9 **OFDM SC modulation**: modulate the SVD precoded M-QAM symbols (constellations) unto the data-carrying OFDM SCs.
   Apply Hermitian symmetry: modulate the negative-frequency SCs with the conjugate of the constellations on the positive-frequency SCs in order to obtain real-valued signal after IFFT operation
   Perform IFFT operation to convert the OFDM frame from frequency-domain representation to time-domain samples
   Append cyclic prefix to eliminate ISI
10 **LED filtering**: apply the response of the LED modelled by first-order low-pass Butterworth filter to the time-domain samples
11 **Channel propagation**: send signal through the channel by applying the channel response of each transmit-receive path, h_{n_r,n_t}, for $n_r = 1, \ldots N_r$, $n_t = 1, \ldots N_t$, to filter the corresponding transmitter signal
12 **Receiver**
   Noise: add Gaussian noise values with zero mean and variance: $\sigma^2 = \frac{P_s}{M\gamma_b}$, P_s is the average power per symbol
   Remove CP prefix from the noisy time-domain received samples
   Perform FFT operation to convert the time-domain samples to the frequency domain representation of the received M-QAM constellations
   Extract the M-QAM data constellations from the data-carrying SCs
   SVD decoding: perform SVD decoding process to eliminate the channel effect
   PWC decoding and Detection:
   Perform SC pairwise de-interleaving
   Apply maximum likelihood detection to estimate the received symbols
   Received bits $\leftarrow M$-QAM symbol-to-bits mapping
Output: Compute error bit error rate by comparing the received and the transmitted bits

---

Appendix D
Matrix transformation for PWC

D.1 Matrix transformation for SC-PWC encoding

Considering two complex QAM constellation symbols $\alpha = \alpha_{\mathrm{r}} + \widetilde{i}\alpha_{\mathrm{i}}$ and $\beta = \beta_{\mathrm{r}} + \widetilde{i}\beta_{\mathrm{i}}$ to be modulated onto two paired SCs ℓ_1 and m_1, respectively, rotating the symbols by angle ψ yields:

$$
\begin{aligned}
\alpha_{\mathrm{rot}} &= e^{\widetilde{i}\psi}\alpha = (\alpha_{\mathrm{r}}\cos\psi - \alpha_{\mathrm{i}}\sin\psi) + \widetilde{i}(\alpha_{\mathrm{r}}\sin\psi + \alpha_{\mathrm{i}}\cos\psi) \\
\beta_{\mathrm{rot}} &= e^{\widetilde{i}\psi}\beta = (\beta_{\mathrm{r}}\cos\psi - \beta_{\mathrm{i}}\sin\psi) + \widetilde{i}(\beta_{\mathrm{r}}\sin\psi + \beta_{\mathrm{i}}\cos\psi).
\end{aligned}
\tag{D.1}
$$

By exchanging the imaginary part of α_{rot} and the real part of β_{rot}, the interleaved symbols are obtained as:

$$
\begin{aligned}
\alpha_{\mathrm{int}} &= (\alpha_{\mathrm{r}}\cos\psi - \alpha_{\mathrm{i}}\sin\psi) + \widetilde{i}(\beta_{\mathrm{r}}\cos\psi - \beta_{\mathrm{i}}\sin\psi) \\
\beta_{\mathrm{int}} &= (\alpha_{\mathrm{r}}\sin\psi + \alpha_{\mathrm{i}}\cos\psi) + \widetilde{i}(\beta_{\mathrm{r}}\sin\psi + \beta_{\mathrm{i}}\cos\psi).
\end{aligned}
\tag{D.2}
$$

Now, (D.2) can be written in matrix form as:

$$
\begin{bmatrix} \Re(\alpha_{\mathrm{int}}) & \Im(\alpha_{\mathrm{int}}) \\ \Re(\beta_{\mathrm{int}}) & \Im(\beta_{\mathrm{int}}) \end{bmatrix} = \begin{bmatrix} \cos\psi & -\sin\psi \\ \sin\psi & \cos\psi \end{bmatrix} \times \begin{bmatrix} \alpha_{\mathrm{r}} & \beta_{\mathrm{r}} \\ \alpha_{\mathrm{i}} & \beta_{\mathrm{i}} \end{bmatrix}
\tag{D.3}
$$

Thus, the expression in (6.7) represent a special form of (D.3) for a vector of information symbols.

D.2 Matrix transformation for SCH-PWC encoding

Considering two complex QAM constellation symbols $\alpha = \alpha_{\mathrm{r}} + \widetilde{i}\alpha_{\mathrm{i}}$ and $\beta = \beta_{\mathrm{r}} + \widetilde{i}\beta_{\mathrm{i}}$ to be modulated onto two paired SCHs c_1 and d_1, respectively, by exchanging the imaginary part of

α^{rot} and the real part of β^{rot}, the interleaved symbols are obtained as:

$$\alpha_{\text{int}} = \alpha_{\text{r}} + \widetilde{i}\beta_{\text{r}}$$
$$\beta_{\text{int}} = \alpha_{\text{i}} + \widetilde{i}\beta_{\text{i}}.$$

(D.4)

Rotating the symbols by angle ϕ yields:

$$\alpha_{\text{rot}} = (\alpha_{\text{r}}\cos\phi - \beta_{\text{r}}\sin\phi) + \widetilde{i}(\alpha_{\text{r}}\sin\phi + \beta_{\text{r}}\cos\phi)$$
$$\beta_{\text{rot}} = (\alpha_{\text{i}}\cos\phi - \beta_{\text{i}}\sin\phi) + \widetilde{i}(\alpha_{\text{i}}\sin\phi + \beta_{\text{i}}\cos\phi).$$

(D.5)

Then, by exchanging the imaginary part of α^{rot} and the real part of β^{rot}, the new interleaved symbols are obtained as:

$$\widehat{\alpha}_{\text{int}} = (\alpha_{\text{r}}\cos\phi - \beta_{\text{r}}\sin\phi) + \widetilde{i}(\alpha_{\text{i}}\cos\phi - \beta_{\text{i}}\sin\phi)$$
$$= (\alpha_{\text{r}} + \widetilde{i}\alpha_{\text{i}})\cos\phi - (\beta_{\text{r}} + \widetilde{i}\beta_{\text{i}})\sin\phi$$
$$\widehat{\beta}_{\text{int}} = (\alpha_{\text{r}}\sin\phi + \beta_{\text{r}}\cos\phi) + \widetilde{i}(\alpha_{\text{i}}\sin\phi + \beta_{\text{i}}\cos\phi)$$
$$= (\alpha_{\text{r}} + \widetilde{i}\alpha_{\text{i}})\cos\phi + (\beta_{\text{r}} + \widetilde{i}\beta_{\text{i}})\sin\phi$$

(D.6)

Now, (D.6) can be written in matrix form as:

$$\begin{bmatrix} \widehat{\alpha}_{\text{int}} \\ \widehat{\beta}_{\text{int}} \end{bmatrix} = \begin{bmatrix} \cos\phi & -\sin\phi \\ \sin\phi & \cos\phi \end{bmatrix} \times \begin{bmatrix} \alpha \\ \beta \end{bmatrix}$$

(D.7)

Thus, the expression in (6.9) is equivalent to (D.3)

Bibliography

[1] M. Uysal, C. Capsoni, Z. Ghassemlooy, A. Boucouvalas, and E. Udvary, *Optical wireless communications: an emerging technology*. Springer, 2016.

[2] P. J. Winzer and D. T. Neilson, "From scaling disparities to integrated parallelism: A decathlon for a decade," *Journal of Lightwave Technology*, vol. 35, no. 5, pp. 1099–1115, 2017.

[3] Cisco, "Cisco Visual Networking Index: Global Mobile Data Traffic Forecast Update, 2017–2022," Nov 2018. [Online]. Available: https://www.cisco.com/c/en/us/solutions/collateral/service-provider/visual-networking-index-vni/white-paper-c11-741490.html

[4] Ericsson, "Ericsson mobility report," Nov 2018. [Online]. Available: https://www.ericsson.com/en/mobility-report/reports/november-2018

[5] H. Haas, "LiFi is a paradigm-shifting 5G technology," *Reviews in Physics*, vol. 3, pp. 26–31, 2018.

[6] S. Dimitrov and H. Haas, *Principles of LED light communications: towards networked Li-Fi.* Cambridge University Press, 2015.

[7] Ofcom, "Report: Study on the future UK spectrum demand for terrestrial mobile broadband applications," April 2014.

[8] UK Spectrum Policy Forum, "Report: UK Spectrum Usage & Demand," April 2015.

[9] M. Z. Chowdhury, M. T. Hossan, A. Islam, and Y. M. Jang, "A comparative survey of optical wireless technologies: architectures and applications," *IEEE Access*, vol. 6, pp. 9819–9840, 2018.

[10] P. H. Pathak, X. Feng, P. Hu, and P. Mohapatra, "Visible light communication, networking, and sensing: A survey, potential and challenges," *IEEE Communications Surveys & Tutorials*, vol. 17, no. 4, pp. 2047–2077, 2015.

[11] United States Department of Energy, "Energy savings forecast of solid-state lighting in general illumination applications." September 2016, Available: https://www.energy.gov/sites/prod/files/2016/09/f33/energysavingsforecast16_2.pdf.

[12] D. Karunatilaka, F. Zafar, V. Kalavally, and R. Parthiban, "Led based indoor visible light communications: State of the art," *IEEE Communications Surveys & Tutorials*, vol. 17, no. 3, pp. 1649–1678, 2015.

[13] H. Burchardt, N. Serafimovski, D. Tsonev, S. Videv, and H. Haas, "VLC: Beyond point-to-point communication," *IEEE Communications Magazine*, vol. 52, no. 7, pp. 98–105, 2014.

[14] H. Le Minh, Z. Ghassemlooy, D. O'Brien, and G. Faulkner, "Indoor gigabit optical wireless communications: challenges and possibilities," in *Proceedings of the 12th International Conference on Transparent Optical Networks*, Munich, Germany, 2010, pp. 1–6.

[15] "Ieee standard for information technology– local and metropolitan area networks– specific requirements– part 11: Wireless lan medium access control (mac)and physical layer (phy) specifications amendment 5: Enhancements for higher throughput," *IEEE Std 802.11n-2009 (Amendment to IEEE Std 802.11-2007 as amended by IEEE Std 802.11k-2008, IEEE Std 802.11r-2008, IEEE Std 802.11y-2008, and IEEE Std 802.11w-2009)*, pp. 1–565, Oct 2009.

[16] 3rd Generation Partnership Project (3GPP), "LTE," http://www.3gpp.org/technologies/keywords-acronyms/98-lte, Accessed: 2019-02-19.

[17] J. Duplicy, B. Badic, R. Balraj, R. Ghaffar, P. Horváth, F. Kaltenberger, R. Knopp, I. Z. Kovács, H. T. Nguyen, D. Tandur *et al.*, "MU-MIMO in LTE systems," *EURASIP Journal on Wireless Communications and Networking*, vol. 2011, no. 1, p. 496763, 2011.

[18] J. Lee, J.-K. Han, and J. Zhang, "MIMO technologies in 3GPP LTE and LTE-advanced," *EURASIP Journal on Wireless Communications and Networking*, vol. 2009, p. 3, 2009.

[19] A. H. Azhar, T.-A. Tran, and D. O'Brien, "A gigabit/s indoor wireless transmission using MIMO-OFDM visible-light communications," *IEEE photonics technology letters*, vol. 25, no. 2, pp. 171–174, 2013.

[20] L. Zeng, D. C. O'Brien, H. Minh, G. E. Faulkner, K. Lee, D. Jung, Y. Oh, and E. T. Won, "High data rate multiple input multiple output (MIMO) optical wireless communications using white LED lighting," *IEEE Journal on Selected Areas in Communications*, vol. 27, no. 9, pp. 1654–1662, 2009.

[21] S. Rajbhandari, "Spatial and wavelength division multiplexing for high-speed VLC systems: An overview," in *Proceedings of the 2016 10th International Symposium on Communication Systems, Networks and Digital Signal Processing (CSNDSP)*, Prague, Czech Republic, 2016, pp. 1–6.

[22] H. Le Minh, D. O'Brien, G. Faulkner, L. Zeng, K. Lee, D. Jung, Y. Oh, and E. T. Won, "100-Mbps NRZ visible light communications using a postequalized white LED," *IEEE Photonics Technology Letters*, vol. 21, no. 15, pp. 1063–1065, 2009.

[23] T. Fath and H. Haas, "Performance comparison of MIMO techniques for optical wireless communications in indoor environments," *IEEE Transactions on Communications*, vol. 61, no. 2, pp. 733–742, 2013.

[24] O. Ergul, E. Dinc, and O. B. Akan, "Communicate to illuminate: State-of-the-art and research challenges for visible light communications," *Physical Communication*, vol. 17, pp. 72–85, 2015.

[25] The Flag Press, "History Behind Semaphore Flags," https://flagexpressions.wordpress.com/2010/03/23/history-behind-semaphore-flags/, March 2010, Accessed: 2019-02-22.

[26] M. A. Khalighi and M. Uysal, "Survey on free space optical communication: A communication theory perspective," *IEEE Communications Surveys & Tutorials*, vol. 16, no. 4, pp. 2231–2258, 2014.

[27] Z. Ghassemlooy, S. Arnon, M. Uysal, Z. Xu, and J. Cheng, "Emerging optical wireless communications - advances and challenges," *IEEE Journal on Selected Areas in Communications*, vol. 33, no. 9, pp. 1738–1749, 2015.

[28] Infrared Data Association (IrDA), http://www.irda.org, Accessed: 2019-02-16.

[29] Y. Tanaka, S. Haruyama, and M. Nakagawa, "Wireless optical transmissions with white colored led for wireless home links," in *Proceedings of the 11th IEEE International Symposium on Personal Indoor and Mobile Radio Communications. PIMRC 2000*, vol. 2, London, UK, 2000, pp. 1325–1329.

[30] Y. Tanaka, T. Komine, S. Haruyama, and M. Nakagawa, "Indoor visible light data transmission system utilizing white LED lights," *IEICE transactions on communications*, vol. 86, no. 8, pp. 2440–2454, 2003.

[31] Visible Light Communications Consortium (VLCC), http://www.vlcc.net/modules/xpage1/?ml_lang=en, 2007, Accessed: 2019-02-16.

[32] Home Gigabit Access (OMEGA) Project, https://cordis.europa.eu/project/rcn/85271/factsheet/en, Accessed: 2019-02-16.

[33] J. Vučić, C. Kottke, K. Habel, and K.-D. Langer, "803 Mbit/s visible light WDM link based on DMT modulation of a single RGB LED luminary," in *Proceedings of the 2011 Optical Fiber Communication Conference and Exposition and the National Fiber Optic Engineers Conference*, Los Angeles, California, USA, 2011, pp. 1–3.

[34] "IEEE Standard for Local and Metropolitan Area Networks–Part 15.7: Short-Range Wireless Optical Communication Using Visible Light," *IEEE Std 802.15.7-2011*, pp. 1–309, Sep. 2011.

[35] D. Tsonev, H. Chun, S. Rajbhandari, J. J. McKendry, S. Videv, E. Gu, M. Haji, S. Watson, A. E. Kelly, G. Faulkner *et al.*, "A 3-Gb/s Single-LED OFDM-Based Wireless VLC Link Using a Gallium Nitride μLED," *IEEE Photonics Technology Letters*, vol. 26, no. 7, pp. 637–640, 2014.

[36] Smart Lighting Engineering Research Center, "Synthesizing light for the benefit of humanity," http://www.bu.edu/smartlighting/, Accessed: 2019-02-17.

[37] Bourns College of Engineering, "Center for ubiquitous communication by light," https://www.uclight.ucr.edu/, Accessed: 2019-02-17.

[38] J. M. Kahn and J. R. Barry, "Wireless infrared communications," *Proceedings of the IEEE*, vol. 85, no. 2, pp. 265–298, 1997.

[39] Z. Tian, K. Wright, and X. Zhou, "The darklight rises: Visible light communication in the dark," in *Proceedings of the 22nd Annual International Conference on Mobile Computing and Networking*, New York City, New York, 2016, pp. 2–15.

[40] M. Biagi, T. Borogovac, and T. D. Little, "Adaptive receiver for indoor visible light communications," *Journal of Lightwave Technology*, vol. 31, no. 23, pp. 3676–3686, 2013.

[41] J. Song, W. Ding, F. Yang, H. Yang, B. Yu, and H. Zhang, "An indoor broadband broadcasting system based on PLC and VLC," *IEEE Transactions on Broadcasting*, vol. 61, no. 2, pp. 299–308, 2015.

[42] A. Sevincer, A. Bhattarai, M. Bilgi, M. Yuksel, and N. Pala, "LIGHTNETs: Smart LIGHTing and Mobile Optical Wireless NETworks—A Survey," *IEEE Communications Surveys & Tutorials*, vol. 15, no. 4, pp. 1620–1641, 2013.

[43] J. Luo, L. Fan, and H. Li, "Indoor positioning systems based on visible light communication: State of the art," *IEEE Communications Surveys & Tutorials*, vol. 19, no. 4, pp. 2871–2893, 2017.

[44] Y. Zhuang, L. Hua, L. Qi, J. Yang, P. Cao, Y. Cao, Y. Wu, J. Thompson, and H. Haas, "A survey of positioning systems using visible LED lights," *IEEE Communications Surveys & Tutorials*, vol. 20, no. 3, pp. 1963–1988, 2018.

[45] T. Cogalan, S. Videv, and H. Haas, "Inflight connectivity: deploying different communication networks inside an aircraft," in *Proceedings of the 2018 IEEE 87th Vehicular Technology Conference (VTC-Spring)*, Porto, Portugal, 2018, pp. 1–6.

[46] D. Tagliaferri, A. Matera, C. Capsoni, and U. Spagnolini, "Nonlinear visible light communications broadcast channel precoding: A new solution for in-flight systems," *IEEE Photonics Journal*, vol. 10, no. 4, pp. 1–14, 2018.

[47] B. Janjua, H. M. Oubei, J. R. D. Retamal, T. K. Ng, C.-T. Tsai, H.-Y. Wang, Y.-C. Chi, H.-C. Kuo, G.-R. Lin, J.-H. He *et al.*, "Going beyond 4 Gbps data rate by employing RGB laser diodes for visible light communication," *Optics express*, vol. 23, no. 14, pp. 18 746–18 753, 2015.

[48] V. Alwayn, *Optical network design and implementation*. Cisco Press, 2004.

[49] Z. Ghassemlooy, W. Popoola, and S. Rajbhandari, *Optical wireless communications: system and channel modelling with Matlab®*. CRC Press, 2012.

[50] S. Arnon, J. Barry, G. Karagiannidis, R. Schober, and M. Uysal, *Advanced optical wireless communication systems*. Cambridge university press, 2012.

[51] J. R. Barry, J. M. Kahn, W. J. Krause, E. A. Lee, and D. G. Messerschmitt, "Simulation of multipath impulse response for indoor wireless optical channels," *IEEE journal on selected areas in communications*, vol. 11, no. 3, pp. 367–379, 1993.

[52] J. M. Kahn, W. J. Krause, and J. B. Carruthers, "Experimental characterization of non-directed indoor infrared channels," *IEEE Transactions on Communications*, vol. 43, no. 2/3/4, pp. 1613–1623, 1995.

[53] H. Li, X. Chen, B. Huang, D. Tang, and H. Chen, "High bandwidth visible light communications based on a post-equalization circuit," *IEEE photonics technology letters*, vol. 26, no. 2, pp. 119–122, 2014.

[54] S. H. Lee, K.-I. Ahn, and J. K. Kwon, "Multilevel transmission in dimmable visible light communication systems," *Journal of Lightwave Technology*, vol. 31, no. 20, pp. 3267–3276, 2013.

[55] S. He, G. Ren, Z. Zhong, and Y. Zhao, "M-ary variable period modulation for indoor visible light communication system," *IEEE communications letters*, vol. 17, no. 7, pp. 1325–1328, 2013.

[56] B. Bai, Z. Xu, and Y. Fan, "Joint LED dimming and high capacity visible light communication by overlapping PPM," in *Proceedings of the 19th Annual Wireless and Optical Communications Conference (WOCC 2010)*, Shanghai, China, 2010, pp. 1–5.

[57] A. E. Morra, H. S. Khallaf, H. M. Shalaby, and Z. Kawasaki, "Performance analysis of both shot-and thermal-noise limited multipulse PPM receivers in gamma–gamma atmospheric channels," *Journal of Lightwave Technology*, vol. 31, no. 19, pp. 3142–3150, 2013.

[58] A. Goldsmith, *Wireless communications*. Cambridge university press, 2005.

[59] O. González, R. Perez-Jimenez, S. Rodriguez, J. Rabadán, and A. Ayala, "OFDM over indoor wireless optical channel," *IEE Proceedings-Optoelectronics*, vol. 152, no. 4, pp. 199–204, 2005.

[60] H. Elgala, R. Mesleh, H. Haas, and B. Pricope, "OFDM visible light wireless communication based on white LEDs," in *Proceedings of the 2007 IEEE 65th Vehicular Technology Conference VTC-Spring*, Dublin, Ireland, 2007, pp. 2185–2189.

[61] J. Armstrong and A. Lowery, "Power efficient optical OFDM," *Electronics letters*, vol. 42, no. 6, p. 1, 2006.

[62] R. Mesleh, H. Elgala, and H. Haas, "On the performance of different ofdm based optical wireless communication systems," *IEEE/OSA Journal of Optical Communications and Networking*, vol. 3, no. 8, pp. 620–628, 2011.

[63] J. Armstrong, "OFDM for optical communications," *Journal of lightwave technology*, vol. 27, no. 3, pp. 189–204, 2009.

[64] D. Tse and P. Viswanath, *Fundamentals of Wireless Communication*. Cambridge university press, 2005.

[65] J. Mietzner, R. Schober, L. H.-J. Lampe, W. H. Gerstacker, P. A. Hoeher *et al.*, "Multiple-antenna techniques for wireless communications-a comprehensive literature survey," *IEEE Communications Surveys and Tutorials*, vol. 11, no. 2, pp. 87–105, 2009.

[66] T. Fath and H. Haas, "Optical spatial modulation using colour LEDs," in *Proceedings of the 2013 IEEE International Conference on Communications (ICC)*, Budapest, Hungary, 2013.

[67] P. M. Butala, H. Elgala, T. D. Little, and P. Zarkesh-Ha, "Multi-wavelength visible light communication system design," in *Proceedings of the 2014 IEEE Globecom Workshops (GC Wkshps)*, Austin, Texas, USA, 2014, pp. 530–535.

[68] E. Bayaki, R. Schober, and R. K. Mallik, "Performance analysis of MIMO free-space optical systems in Gamma-Gamma fading," *IEEE Transactions on Communications*, vol. 57, no. 11, pp. 3415–3424, Nov 2009.

[69] M. R. Bhatnagar and Z. Ghassemlooy, "Performance Analysis of Gamma–gamma Fading FSO MIMO Links With Pointing Errors," *Journal of Lightwave Technology*, vol. 34, no. 9, pp. 2158–2169, May 2016.

[70] X. Song and J. Cheng, "Subcarrier Intensity Modulated MIMO Optical Communications in Atmospheric Turbulence," *Journal of Optical Communications and Networking*, vol. 5, no. 9, pp. 1001–1009, Sept 2013.

[71] R. Priyadarshani, M. R. Bhatnagar, Z. Ghassemlooy, and S. Zvanovec, "Effect of Correlation on BER Performance of the FSO-MISO System With Repetition Coding Over Gamma–Gamma Turbulence," *IEEE Photonics Journal*, vol. 9, no. 5, pp. 1–15, 2017.

[72] M. Safari and M. Uysal, "Do we really need OSTBCs for free-space optical communication with direct detection?" *IEEE Transactions on Wireless Communications*, vol. 7, no. 11, pp. 4445–4448, 2008.

[73] M. T. Dabiri, M. J. Saber, and S. M. S. Sadough, "On the performance of multiplexing FSO MIMO links in log-normal fading with pointing errors," *IEEE/OSA Journal of Optical Communications and Networking*, vol. 9, no. 11, pp. 974–983, 2017.

[74] A. Jaiswal, M. R. Bhatnagar, and V. K. Jain, "Performance evaluation of space shift keying in free-space optical communication," *IEEE/OSA Journal of Optical Communications and Networking*, vol. 9, no. 2, pp. 149–160, Feb 2017.

[75] M. Abaza, R. Mesleh, A. Mansour *et al.*, "Performance analysis of space-shift keying over negative-exponential and log-normal FSO channels," *Chinese Optics Letters*, vol. 13, no. 5, pp. 051 001–051 001, 2015.

[76] A. Jaiswal, M. R. Bhatnagar, and V. K. Jain, "BER analysis of optical space shift keying in atmospheric turbulence environment," in *Proceedings of the 2016 10th International Symposium on Communication Systems, Networks and Digital Signal Processing (CSNDSP)*, Prague, Czech Republic, 2016, pp. 1–6.

[77] T. Özbilgin and M. Koca, "Optical Spatial Modulation Over Atmospheric Turbulence Channels," *Journal of Lightwave Technology*, vol. 33, no. 11, pp. 2313–2323, 2015.

[78] K. P. Peppas and P. T. Mathiopoulos, "Free-Space Optical Communication With Spatial Modulation and Coherent Detection Over H-K Atmospheric Turbulence Channels," *Journal of Lightwave Technology*, vol. 33, no. 20, pp. 4221–4232, 2015.

[79] A. Jaiswal, M. R. Bhatnagar, and V. K. Jain, "Performance of Optical Space Shift Keying Over Gamma–Gamma Fading With Pointing Error," *IEEE Photonics Journal*, vol. 9, no. 2, pp. 1–16, April 2017.

[80] H. Olanrewaju, J. Thompson, and W. Popoola, "Performance Analysis of Optical Spatial Modulation in Atmospheric Turbulence Channel," *Photonics*, vol. 5, no. 4, 2018.

[81] G. Ntogari, T. Kamalakis, and T. Sphicopoulos, "Performance analysis of space time block coding techniques for indoor optical wireless systems," *IEEE Journal on Selected Areas in Communications*, vol. 27, no. 9, pp. 1545–1552, 2009.

[82] A. K. Gupta and A. Chockalingam, "Performance of MIMO modulation schemes with imaging receivers in visible light communication," *Journal of Lightwave Technology*, vol. 36, no. 10, pp. 1912–1927, 2018.

[83] D. O'Brien, R. Turnbull, H. Le Minh, G. Faulkner, O. Bouchet, P. Porcon, M. El Tabach, E. Gueutier, M. Wolf, L. Grobe *et al.*, "High-speed optical wireless demonstrators: conclusions and future directions," *Journal of Lightwave Technology*, vol. 30, no. 13, pp. 2181–2187, 2012.

[84] A. Burton, Z. Ghassemlooy, S. Rajbhandari, and S.-K. Liaw, "Design and analysis of an angular-segmented full-mobility visible light communications receiver," *Transactions on Emerging Telecommunications Technologies*, vol. 25, no. 6, pp. 591–599, 2014.

[85] J. Li, X. Huang, and N. Chi, "Enhanced performance of single-input multiple-output visible light communication system utilizing space diversity technology," *Optical Engineering*, vol. 54, no. 3, p. 036109, 2015.

[86] D. Takase and T. Ohtsuki, "Spatial multiplexing in optical wireless MIMO communications over indoor environment," *IEICE transactions on communications*, vol. 89, no. 4, pp. 1364–1371, 2006.

[87] ——, "Optical wireless MIMO communications (OMIMO)," in *Proceedings of the IEEE Global Telecommunications Conference*, Dallas, Texas, USA, 2004, pp. 928–932.

[88] Y. A. Chau and S.-H. Yu, "Space modulation on wireless fading channels," in *Proceedings of the 54th IEEE Vehicular Technology Conference (VTC-Fall)*, Atlantic City, New Jersey, USA, 2001, pp. 1668–1671.

[89] R. Y. Mesleh, H. Haas, S. Sinanovic, C. W. Ahn, and S. Yun, "Spatial modulation," *IEEE Transactions on Vehicular Technology*, vol. 57, no. 4, pp. 2228–2241, 2008.

[90] R. Mesleh, H. Elgala, and H. Haas, "Optical spatial modulation," *Journal of Optical Communications and Networking*, vol. 3, no. 3, pp. 234–244, 2011.

[91] M. Di Renzo, H. Haas, A. Ghrayeb, S. Sugiura, and L. Hanzo, "Spatial modulation for generalized MIMO: challenges, opportunities, and implementation," *Proceedings of the IEEE*, vol. 102, no. 1, pp. 56–103, 2014.

[92] W. O. Popoola, E. Poves, and H. Haas, "Spatial pulse position modulation for optical communications," *Journal of Lightwave Technology*, vol. 30, no. 18, pp. 2948–2954, 2012.

[93] W. O. Popoola and H. Haas, "Demonstration of the merit and limitation of generalised space shift keying for indoor visible light communications," *Journal of Lightwave Technology*, vol. 32, no. 10, pp. 1960–1965, 2014.

[94] H. G. Olanrewaju, J. Thompson, and W. O. Popoola, "Generalized Spatial Pulse Position Modulation for Optical Wireless Communications," in *Proceedings of the 2016 IEEE 84th Vehicular Technology Conference (VTC-Fall)*, Montréal, Canada, 2016.

[95] H. G. Olanrewaju and W. O. Popoola, "Effect of Synchronization Error on Optical Spatial Modulation," *IEEE Transactions on Communications*, vol. 65, no. 12, pp. 5362–5374, Dec 2017.

[96] H. G. Olanrewaju, J. Thompson, and W. O. Popoola, "Performance of Optical Spatial Modulation in Indoor Multipath Channel," *IEEE Transactions on Wireless Communications*, vol. 17, no. 9, pp. 6042–6052, 2018.

[97] T. Fath, M. Di Renzo, and H. Haas, "On the performance of space shift keying for optical wireless communications," in *Proceedings of the 2010 IEEE Globecom Workshops (GC Wkshps)*, 2010, pp. 990–994.

[98] W. Popoola, E. Poves, and H. Haas, "Generalised space shift keying for visible light communications," in *Proceedings of the 2012 8th International Symposium on Communication Systems Networks & Digital Signal Processing (CSNDSP)*, Poznan, Poland, 2012, pp. 1–4.

[99] S. Alaka, T. L. Narasimhan, and A. Chockalingam, "Generalized spatial modulation in indoor wireless visible light communication," in *Proceedings of the 2015 IEEE Global Communications Conference (Globecom)*, San Diego, California, USA, 2015, pp. 1–7.

[100] T. Bui, R. Singh, T. O'Farrell, and M. Biagi, "Performance Evaluation of Generalized Optical Spatial Modulation with Dimming Support," in *Proceedings of the 2018 IEEE Globecom Workshops (GC Wkshps)*, Abu Dhabi, UAE, 2018, pp. 1–6.

[101] X. Zhang, S. Dimitrov, S. Sinanovic, and H. Haas, "Optimal power allocation in spatial modulation OFDM for visible light communications," in *Proceedings of the 2012 IEEE 75th Vehicular Technology Conference (VTC-Spring)*, Yokohama, Japan, 2012, pp. 1–5.

[102] W. O. Popoola, E. Poves, and H. Haas, "Error performance of generalised space shift keying for indoor visible light communications," *IEEE Transactions on Communications*, vol. 61, no. 5, pp. 1968–1976, 2013.

[103] H. G. Olanrewaju, F. B. Ogunkoya, and W. O. Popoola, "Spatial modulation - a low complexity modulation technique for visible light communications," in *Visible Light Communications*, J.-Y. Wang, Ed. Rijeka: IntechOpen, 2017, ch. 1. [Online]. Available: https://doi.org/10.5772/intechopen.68888

[104] W. O. Popoola, S. Sinanovic, and H. E. Nistazakis, "Enhancing the error performance of optical SSK under correlated channel condition," in *Proceedings of the 2016 IEEE International Conference on Communications Workshops (ICC)*, Kuala Lumpur, Malaysia, 2016, pp. 7–11.

[105] K. Kiasaleh, "Performance of APD-based, PPM free-space optical communication systems in atmospheric turbulence," *IEEE transactions on communications*, vol. 53, no. 9, pp. 1455–1461, 2005.

[106] J. Proakis and M. Salehi, *Digital communications*, 5th ed. McGraw-Hill, 2008.

[107] F. Xu, M.-A. Khalighi, and S. Bourennane, "Impact of different noise sources on the performance of PIN-and APD-based FSO receivers," in *Proceedings of the 2011 11th International Conference on Telecommunications (ConTEL)*, Graz, Austria, 2011, pp. 211–218.

[108] H. G. Olanrewaju, J. Thompson, and W. O. Popoola, "On spatial pulse position modulation for optical wireless communications," in *Proceedings of the 2016 IEEE Photonics Society Summer Topical Meeting Series (SUM)*. IEEE, 2016, pp. 44–45.

[109] N. Serafimovski, A. Younis, R. Mesleh, P. Chambers, M. Di Renzo, C.-X. Wang, P. M. Grant, M. A. Beach, and H. Haas, "Practical implementation of spatial modulation," *IEEE Transactions on Vehicular Technology*, vol. 62, no. 9, pp. 4511–4523, 2013.

[110] J. Zhang, L. Tian, Y. Wang, and M. Liu, "Selection transmitting/maximum ratio combining for timing synchronization of MIMO-OFDM systems," *IEEE Transactions on Broadcasting*, vol. 60, no. 4, pp. 626–636, 2014.

[111] C. L. Wang and H. C. Wang, "Optimized Joint Fine Timing Synchronization and Channel Estimation for MIMO Systems," *IEEE Transactions on Communications*, vol. 59, no. 4, pp. 1089–1098, April 2011.

[112] M. Di Renzo, H. Haas, and P. M. Grant, "Spatial modulation for multiple-antenna wireless systems: a survey," *IEEE Communications Magazine*, vol. 49, no. 12, pp. 182–191, 2011.

[113] A. Younis, N. Serafimovski, R. Mesleh, and H. Haas, "Generalised spatial modulation," in *Proceedings of the 2010 Conference Record of the Forty Fourth Asilomar Conference on Signals, Systems and Computers (ASILOMAR)*, California, USA, 2010, pp. 1498–1502.

[114] S. Rajbhandari, H. Chun, G. Faulkner, K. Cameron, A. V. Jalajakumari, R. Henderson, D. Tsonev, M. Ijaz, Z. Chen, H. Haas *et al.*, "High-Speed Integrated Visible Light Communication

System: Device Constraints and Design Considerations," *IEEE Journal on Selected Areas in Communications*, vol. 33, no. 9, pp. 1750–1757, 2015.

[115] S. Zhang, S. Watson, J. J. McKendry, D. Massoubre, A. Cogman, E. Gu, R. K. Henderson, A. E. Kelly, and M. D. Dawson, "1.5 Gbit/s multi-channel visible light communications using CMOS-Controlled GaN-Based LEDs," *Journal of lightwave technology*, vol. 31, no. 8, pp. 1211–1216, 2013.

[116] R. M. Gagliardi and S. Karp, *Optical communications*, 2nd ed.   Wiley, 1995.

[117] S. Arnon, "The effect of clock jitter in visible light communication applications," *Journal of Lightwave Technology*, vol. 30, no. 21, pp. 3434–3439, 2012.

[118] Y. Fujiwara, "Self-synchronizing pulse position modulation with error tolerance," *IEEE Transactions on Information Theory*, vol. 59, no. 9, pp. 5352–5362, 2013.

[119] B. Ghimire, I. Stefan, H. Elgala, and H. Haas, "Time and frequency synchronisation in optical wireless OFDM networks," in *Proceedings of the IEEE 22nd International Symposium on Personal Indoor and Mobile Radio Communications (PIMRC)*, Toronto, Ontario, Canada, 2011, pp. 819–823.

[120] M. F. G. Medina, O. González, S. Rodríguez, and I. R. Martín, "Timing synchronization for OFDM-based visible light communication system," in *Proceedings of the Wireless Telecommunications Symposium (WTS)*, London, UK, 2016, pp. 1–4.

[121] K. Lee, H. Park, and J. R. Barry, "Indoor Channel Characteristics for Visible Light Communications," *IEEE Communications Letters*, vol. 15, no. 2, pp. 217–219, 2011.

[122] R. Mesleh, R. Mehmood, H. Elgala, and H. Haas, "Indoor MIMO optical wireless communication using spatial modulation," in *Proceedings of the 2010 IEEE International Conference on Communications (ICC)*, Cape Town, South Africa, 2010, pp. 1–5.

[123] N. A. Tran, D. Luong, T. C. Thang, A. T. Pham *et al.*, "Performance analysis of indoor MIMO visible light communication systems," in *Proceedings of the 2014 IEEE Fifth International Conference on Communications and Electronics (ICCE)*, Da Nang, Vietnam, 2014, pp. 60–64.

[124] M. D. Audeh, J. M. Kahn, and J. R. Barry, "Performance of Pulse-position Modulation on Measured Non-Directed Indoor Infrared Channels," *IEEE Transactions on Communications*, vol. 44, no. 6, pp. 654–659, 1996.

[125] Z. Zhou, C. Chen, and M. Kavehrad, "Impact Analyses of High-Order Light Reflections on Indoor Optical Wireless Channel Model and Calibration," *Journal of Lightwave Technology*, vol. 32, no. 10, pp. 2003–2011, May 2014.

[126] A. Nuwanpriya, S.-W. Ho, and C. S. Chen, "Indoor MIMO visible light communications: Novel angle diversity receivers for mobile users," *IEEE Journal on Selected Areas in Communications*, vol. 33, no. 9, pp. 1780–1792, 2015.

[127] W. O. Popoola, Z. Ghassemlooy, and B. G. Stewart, "Pilot-assisted PAPR reduction technique for optical OFDM communication systems," *Journal of Lightwave Technology*, vol. 32, no. 7, pp. 1374–1382, 2014.

[128] K.-H. Park, Y.-C. Ko, and M.-S. Alouini, "On the power and offset allocation for rate adaptation of spatial multiplexing in optical wireless MIMO channels," *IEEE Transactions on Communications*, vol. 61, no. 4, pp. 1535–1543, 2013.

[129] Y. Hong, T. Wu, L.-K. Chen *et al.*, "On the performance of adaptive MIMO-OFDM indoor visible light communications," *IEEE Photonics Technology Letters*, vol. 28, no. 8, pp. 907–910, 2016.

[130] S. K. Mohammed, E. Viterbo, Y. Hong, and A. Chockalingam, "MIMO Precoding With X-and Y-codes," *IEEE Transactions on Information Theory*, vol. 57, no. 6, pp. 3542–3566, 2011.

[131] G. Egecan, K. O. Akande, P. Anthony Haighy, and W. O. Popoola, "Frequency response modelling of cool and warm white leds in vlc systems," in *Proceedings of the First Western Conference on Wireless Telecommunications Western Asia*, Isfahan, Iran, 2017.

[132] J. Boutros and E. Viterbo, "Signal Space Diversity: A Power-and Bandwidth-efficient Diversity Technique for the Rayleigh Fading Channel," *IEEE Transactions on Information theory*, vol. 44, no. 4, pp. 1453–1467, 1998.

[133] Y. Hong, A. J. Lowery, and E. Viterbo, "Sensitivity Improvement and Carrier Power Reduction in Direct-Detection Optical OFDM Systems by Subcarrier Pairing," *Optics express*, vol. 20, no. 2, pp. 1635–1648, 2012.

[134] C. Zhu, B. Song, L. Zhuang, B. Corcoran, and A. J. Lowery, "Subband Pairwise Coding for Robust Nyquist-WDM Superchannel Transmission," *Journal of Lightwave Technology*, vol. 34, no. 8, pp. 1746–1753, 2016.

[135] B. Song, B. Corcoran, Q. Wang, L. Zhuang, and A. J. Lowery, "Subcarrier pairwise coding for short-haul L/E-ACO-OFDM," *IEEE photonics technology letters*, vol. 29, no. 18, pp. 1584–1587, 2017.

[136] I. N. Osahon, C. Ziyan, T. Adiono, and W. O. Popoola, "SI-POF transmission with OFDM and sub-carrier pairwise coding," in *Proceedings of the 2018 7th IEEE International Conference on Performance Evaluation and Modeling in Wired and Wireless Networks (PEMWN)*, Toulouse, Blagnac, France, Sept. 2018, pp. 1–5.

[137] C. Zhu, B. Song, B. Corcoran, L. Zhuang, and A. J. Lowery, "Improved Polarization Dependent Loss Tolerance for Polarization Multiplexed Coherent Optical Systems by Polarization Pairwise Coding," *Optics Express*, vol. 23, no. 21, pp. 27 434–27 447, 2015.

[138] J. He and J. Shi, "An enhanced adaptive scheme with Pairwise Coding for OFDM-VLC system," *IEEE Photonics Technology Letters*, 2018.

[139] P. S. Diniz, *Adaptive filtering*. Springer, 1997.

[140] A. T. Hussein and J. M. Elmirghani, "Mobile multi-gigabit visible light communication system in realistic indoor environment," *Journal of Lightwave Technology*, vol. 33, no. 15, pp. 3293–3307, 2015.